Turbulent regimes in the tokamak scrape-off layer

THÈSE Nᴼ 6197 (2014)

ÉCOLE POLYTECHNIQUE FÉDÉRALE DE LAUSANNE

POUR L'OBTENTION DU GRADE DE DOCTEUR ÈS SCIENCES

PAR

Annamaria MOSETTO

EPFL

ÉCOLE POLYTECHNIQUE
FÉDÉRALE DE LAUSANNE

Suisse
2014

e-mail: annamaria.mosetto@gmail.com
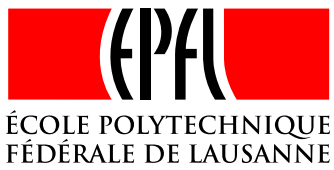
Abstract

The tokamak scrape-off layer (SOL) is the plasma region characterized by open field lines that start and end on the vessel walls. The plasma dynamics in the SOL plays a crucial role in determining the overall performance of a tokamak, since it controls the plasma-wall interactions, being responsible of exhausting the tokamak power, it regulates the overall plasma confinement, and it governs the plasma refueling and the removal of fusion ashes.

Scrape-off layer physics is intrinsically non-linear and characterized by phenomena that occur on a wide range of spatio-temporal scales. Free energy sources drive a number of unstable modes that develop into turbulence and lead to transport of particles and heat across the magnetic field lines. Depending on the driving instability, different SOL turbulent regimes can be identified. As the SOL turbulent regimes determine the plasma confinement properties and the SOL width (and, consequently, the power flux on the vessel wall, for example), it is of crucial importance to understand which turbulent regimes are active in the SOL, under which conditions they develop, and which are the main properties of the associated turbulent transport.

In the present thesis we define the SOL turbulent regimes, and we provide a framework to identify them, given the operational SOL parameters. Our study is based on the drift-reduced Braginskii equations and it is focused on a limited tokamak SOL configuration. We first describe the main SOL linear instabilities, such as the inertial and resistive branches of the drift waves, the resistive, inertial and ideal branches of the ballooning modes, and the ion temperature gradient mode. Then, we find the SOL turbulent regimes depending on the instability driving turbulent transport, assuming that turbulence saturates when the radial gradient associated to the pressure fluctuations is comparable to the equilibrium one. Our methodology for the turbulent regime identification is supported by the analysis of non-linear turbulence simulations performed with the GBS code, a flux-driven, 3D code that solves the drift-reduced Braginskii equations without separation between background and fluctuations. We find that drift waves drive transport at low resistivity and negative magnetic shear, while ballooning modes dominate at high resistivity and positive magnetic shear. The ion temperature gradient instability plays a negligible role in the SOL dynamics, since the ion temperature gradient is generally below the threshold necessary for the development of this instability.

Annamaria Mosetto – CRPP/EPFL

Version Abrégée

Le *scrape-off layer* (SOL) d'un tokamak est la région du plasma caractérisée par des lignes de champ ouvertes, qui commencent et terminent sur les parois de la chambre à vide. La dynamique du plasma dans le SOL joue un rôle crucial pour déterminer la performance d'ensemble d'un tokamak, car, en étant responsable de l'évacuation de la puissance produite par le tokamak, elle contrôle les interactions entre le plasma et les parois, elle régule le confinement du plasma et elle gouverne l'introduction de nouveau combustible et l'enlèvement des cendres produites par la fusion.

La physique du SOL est par nature non-linéaire et est caractérisée par des phénomènes dont les échelles spatio-temporelles varient fortement. Des sources d'énergie libre sont la cause de nombreuses instabilités, sont source de turbulence, et mènent au transport de particules et de chaleur à travers les lignes de champ magnétique. Selon l'instabilité qui les provoque, différents régimes de turbulence sont identifiés dans le SOL. Les régimes de turbulence déterminent les propriétés de confinement du plasma ainsi que l'épaisseur du SOL (et, par conséquence, le flux de puissance sur les parois de la chambre a vide, par exemple). L'identification des régimes actifs dans le SOL, des conditions dans lesquelles ils se développent, et des propriétés les plus importantes du transport associé sont d'importance cruciale.

Dans cette thèse nous définissons les régimes de turbulence dans le SOL, et nous fournissons un cadre pour leur identification, étant donnés les parametrès opérationnels du SOL. Notre étude est basée sur les équations *drift-reduced* de Braginskii et se concentre sur les configurations du SOL dites limitées. D'abord nous décrivons les instabilités linéaires les plus importantes dans le SOL, tel que les branches résistives et inertielles des ondes de dérive (*drift waves*), les branches résistives, intertielles et idéales du *ballooning mode*, et le mode du au gradient de température ionique (*ion temperature gradient mode*). Nous trouvons ensuite les régimes de turbulence dans le SOL après avoir identifié les instabilités qui sont la cause du transport turbulent, en supposant que la turbulence sature quand le gradient radial associé aux fluctuations de pression est comparable au gradient d'équilibre. Notre méthodologie pour l'identification du régime de turbulence est validée par l'analyse de simulations non-linéaires de la turbulence realisées avec le code GBS, un code *flux-driven*, 3D, qui résout les *drift-reduced* équations de Braginskii sans séparation entre les fluctuations et l'équilibre. Nous trouvons que

les *drift waves* sont la cause du transport lorsque la résistivité est faible et que le cisaillement magnétique est négatif, tandis que les *ballooning modes* dominent à haute résistivité lorsque le cisaillement magnétique est positif. L'instabilité liée au gradient de température ionique joue un rôle négligeable dans la dynamique du SOL, puisque le gradient de température ionique est généralement au dessous du seuil nécessaire pour le développement de cette instabilité.

Contents

Chapter 1

Introduction

Although the states of matter that are typically known are three, the solid, the liquid, and the gaseous state, which are characterized by an increasing mobility of the molecules and atoms, a fourth state of matter exists, the plasma state, which is attained when the temperature exceeds ~ 1 eV (1 eV$\simeq 11,000$ K). At this temperature the excitation of the atoms is so high that electrons are separated from the nuclei, and matter becomes an ensemble of charged particles. As a matter of fact, most of the matter visible in the universe, from high-density stars to the low-density interstellar gas, is in the plasma state. On Earth, plasmas can be observed during events like lighting and the aurora borealis or australis. Plasmas also play a role in technologies that impact our everyday life: neon tubes are lit up by light-emitting plasmas, plasma torches are used for precise cutting, thin films deposition used in semiconductor production is realized through plasma processes, and many more. Although constituted by an ensemble of electrically charged particles, plasmas appear to be quasi-neutral if observed on a scale larger than the Debye length, $\lambda_D = \sqrt{T/(4\pi n e^2)}$ (in CGS units), where T is the plasma temperature and n its density, since the single particle charges are shielded by collective effects.

Ions at high temperature can win their electrical repulsion, and fuse together. Nuclear fusion of two light nuclei releases energy until iron is obtained as product of the reaction. This is due to the fact that the mass of the product is inferior to the mass of the colliding nuclei; therefore an amount of energy equal to $E = mc^2$ is generated, where m is the mass difference between the colliding and the product nuclei, and c is the speed of light. Nuclear fusion is the process through which all the elements heavier than hydrogen are generated in the stars.

Among all the possible fusion reactions, few are interesting to use for energy production on an industrial scale, the reason being the high temperature at which the nuclear reaction has more probability to take place. The best candidate, having the largest cross-section around 100 KeV, is the reaction between deuterium (D) and tritium (T):

$$^2_1\text{D} + {}^3_1\text{T} \rightarrow \text{He}(3.5 \text{ MeV}) + {}^1_0\text{n}(14.1 \text{ MeV}) \tag{1.1}$$
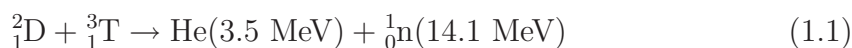
This reactions produces ~ 350 GJ of energy per gram of nuclear fuel. Comparing it to the energy released by burning a gram of fossil fuel, ~ 40 kJ, it is possible to understand the enormous interest of developing a technology capable of extracting energy from nuclear fusion and channeling it into an industrial scale production.

Unfortunately, achieving the conditions for the self-sustained thermonuclear reaction is a highly challenging task. It is required in fact that the amount of energy released by the fusion reactions is enough to keep the fuel at the necessary high temperature, compensating inevitable power losses. Fusion power is sufficient to maintain the plasma in the burning regime, when the Lawson *triple product* criterion $nT\tau_E \gtrsim 10^{20}$ m^3 keV s is satisfied, where τ_E is the energy confinement time, the ratio between the plasma total energy and the power losses from the fusion reaction. The physical meaning of the Lawson criterion can be easily understood. The larger n, the larger is the rate at which reactions take place, and therefore the thermonuclear power. A high temperature, as pointed out earlier, is necessary in order to have a large reaction probability. Finally, a long confinement time guarantees that the produced energy is not lost.

In order to reach self-sustained fusion conditions, two main approaches are currently followed. The first approach aims at reaching ignition by compressing fuel capsules of ~ 1 mm diameter using powerful lasers. Using this technology the National Ignition Facility (NIF) in Livermore, USA has showed significant progress recently (see Ref. [1]). The second approach, instead, aims at reaching ignition with lower density plasmas, $n \gtrsim 10^{20}$ m^3, heated to temperatures of the order of few keVs, and confined by a strong magnetic field in a torus shaped chamber. The next section is an overview of the confinement technologies used within the second approach, and in particular of the tokamak reactor.

1.1 The tokamak reactor

A tokamak is a toroidal chamber in which the plasma is confined by means of a magnetic field. The magnetic field is composed by a toroidal and a poloidal component, being the toroidal component around 10 times larger than the poloidal (see Fig. 1.1). The toroidal magnetic field is generated by a set of coils contained in a poloidal cross section of the machine. Since the toroidal magnetic field alone is not capable of confining the plasma as magnetic field curvature and gradient-induced drifts cause the loss of the plasma, a poloidal component of the magnetic field is added. The poloidal magnetic field is generated by an electric current induced in the plasma. The current is due to the action of the central solenoid, that works as the primary circuit of a transformer. The variation of the electric current in the central solenoid induces an electromotive force inside the plasma (secondary circuit of the transformer) that, in turn, drives the plasma current. Finally, additional outer poloidal field coils are necessary to control the vertical and the horizontal
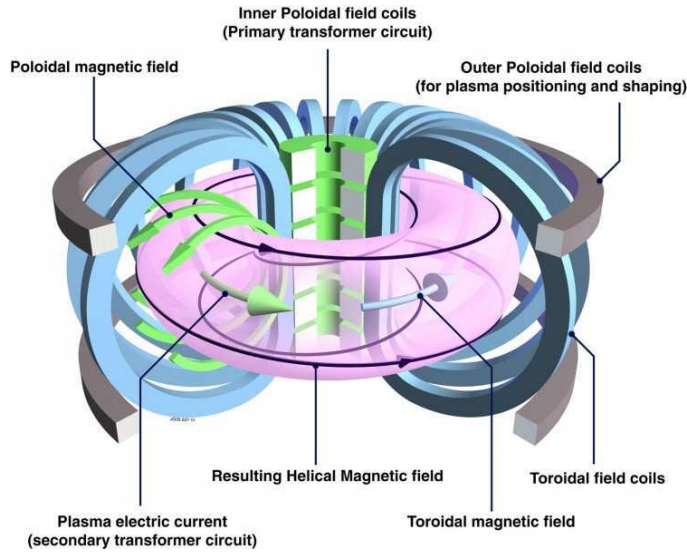
Figure 1.1: *Schematic representation of a tokamak. The main toroidal field is generated by toroidal field coils lying in poloidal planes, the smaller poloidal field is generated by a toroidal electric current induced by the central solenoid, that acts as a primary circuit of a transformer. Additional poloidal field coils are necessary for plasma shaping and positioning. Image source: EFDA.*

position of the plasma. The resulting magnetic field lines wind around the torus, defining toroidally nested surfaces of equal magnetic flux, called flux surfaces.

The contact of the plasma with a solid surface defines the last closed flux surface (LCFS, or separatrix) location. The poloidal cross section is therefore divided in two regions: the closed flux surface region, where the magnetic field lines wrap around the magnetic flux surfaces with no interruptions, and the open flux surface region, in which the field lines are open and end on machine vessel. The open flux surface region is called the scrape-off layer (SOL), since the plasma is *scraped off* from the hot core. The plasma particles entering the SOL are transported either along or across the field lines, determining the heat loads on the material constituting the first wall.

There are two methods of controlling the position of the LCFS. The oldest and simplest is used in the *limited* tokamak configuration and consists in introducing a barrier of few centimeters along the poloidal, or the toroidal cross section of the plasma, limiting it physically, and preventing the plasma from impacting directly onto the rest of the wall (see Fig. 1.2, left, for the cross section of a toroidally limited plasma). A more efficient strategy is used instead in the *diverted* configuration (see Fig. 1.2, right). By means of externally imposed magnetic fields, the magnetic topology is modified in such a way that the field lines of the SOL touch the wall in a well defined region of the tokamak separated from the main chamber, called divertor. The advantages of the diverted over the limited configuration is that it is more difficult for the first wall eroded materials to be reinjected into the hot core, it
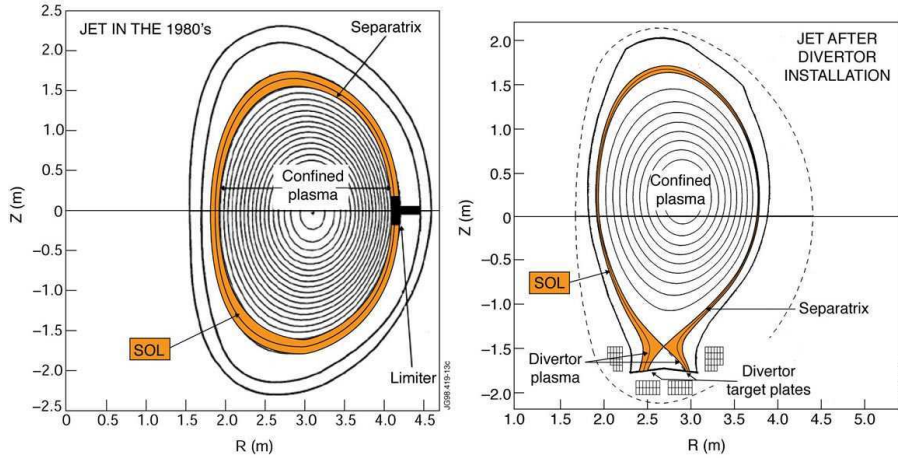
Figure 1.2: *Plasma flux surfaces poloidal cross section in a limited (left) and diverted configuration (right), example from the JET tokamak. The SOL region is highlighted in orange. Image source: EFDA.*

is easier to remove the fusion ashes (helium resulting from the fusion reactions), and, in general, it provides better confinement properties, allowing easier access to a high confinement mode; when the core plasma is heated above a certain threshold, the formation of a transport barrier is observed with the transition between a low (L) and a high (H) confinement mode, leading to an increase of the plasma confinement time. The H-mode is considered an attractive working scenario in future fusion reactors.

It is since the 1960s that experimental tokamak machines have entered into operation all over the world. Their increasing capability of achieving conditions closer to ignition (higher triple product) can be compared to the development of microchips by the electronic industry, see Fig. 1.3. Among the currently working tokamaks, we underline the Joint European Torus (JET), the world's largest tokamak, situated in Culham, UK. In 1997, JET produced 16 MW of fusion power from 24 MW of injected power, with a conversion factor (ratio between the energy produced by the fusion reactions and the energy injected in the tokamak by external sources) of around 65%.

Despite the undeniable progress of thermonuclear fusion research, a number of outstanding problems still need to be resolved. In fact, in order to be able to deliver fusion generated electricity on the grid, a conversion factor larger than 1 is needed, since the released fusion power needs to be transformed through a chain that involves energy losses at different stages. Moreover, present-day tokamaks are unable to guarantee a steady state power production. ITER, a tokamak machine of unprecedented capabilities, aims at addressing some of these open issues (see Fig. 1.4). Launched as a project in 1985, the ITER machine is currently under construction in Cadarache, France, and the first plasma is foreseen for 2020. The main goals of the ITER experimental campaign are (see Ref. [2]):

Figure 1.3: *Achieved triple product for different tokamaks compared to the development of computer chips. Image source: http://www.fusenet.eu.*

Figure 1.4: *Schematic of the ITER machine. Image source: http://www.fusion.kit.edu*

- to momentarily produce a conversion factor of 10;

- to produce a steady-state plasma with a conversion factor value greater than 5;

- to maintain a fusion pulse for up to 480 s;

- to ignite a self-sustaining plasma;

- to develop technologies and processes needed for a fusion power plant, including superconducting magnets and remote handling;

- to test tritium breeding concepts;

- to refine neutron shield/heat conversion technology (most of the energy in the deuterium-tritium fusion reaction is released in the form of fast neutrons).

The success of the ITER campaign is fundamental to prove that thermonuclear fusion will be capable of providing a reliable source of energy for the future.

1.2 Turbulence in the SOL

The tokamak SOL dynamics is of crucial importance in determining the overall performances of the machine, since it establishes the boundary conditions for the core plasma, it controls the impurity dynamics, the plasma refueling and it is responsible of exhausting the tokamak power [3]. The SOL width, for example, controls the wetted area of plasma facing components and, therefore, the maximum heat flux that needs to be evacuated. Scrape-off layer physics is believed to play a crucial role

in the L-H transition [4]. Improving the understanding and the predicting capabilities of tokamak SOL physics is therefore essential for the success of thermonuclear fusion.

Scrape-off layer plasma dynamics is particularly difficult to tackle because it is governed by highly non-linear turbulent processes, involving a large range of time and spatial scales. It is determined by the interplay between the plasma outflowing from the core, cross-field turbulent transport, and parallel streaming along the field lines. Since SOL plasma temperature is relatively low, it is possible to simplify its description by assuming that the collisionality is high enough to ensure to be close to thermodynamical equilibrium. The plasma can therefore be described by considering a few moments of the particle distribution function, obtaining a set of fluid equations, such as the ones derived by Braginskii in 1965 [5]. Afterwards, a number of models were deduced from the original work of Braginskii, considering the drift approximation, according to which the perpendicular velocity of the plasma particles is described as the sum of the plasma drifts: the $\boldsymbol{E} \times \boldsymbol{B}$ drift, the diamagnetic drift and the polarisation drift (see, *e.g.*, Ref. [6]). Based on the drift-reduced approximation, both 2D codes, capturing turbulence in the poloidal plane, (see, *e.g*, Refs. [7, 8, 9, 10]), and 3D codes, adding the dynamics parallel to the field lines (see, *e.g.*, Refs. [11, 12, 13, 14, 15, 16]) have been developed. At the same time, a number of gyrofluid models were derived including additional kinetic effects that are not comprised in the Braginskii equations, calculating moments of the gyrokinetic equations (see, *e.g.*, Refs. [17, 18, 19]). Some of the developed numerical tools are capable of simulating the SOL alone (*e.g.*, GBS [20]), some focus on the closed flux surface region (*e.g.*, EMEDGE3D [16]), while others consider a region across the separatrix. Among the latter, we mention the GEM code [19], the BOUT code [12], and the TOKAM3X code [13]. The passage from a closed to an open magnetic field lines region introduces physical phenomena whose analysis is far from being completed.

While the SOL turbulence regimes have not been the subject of a detailed analysis yet, in the 1990s a large effort has been devoted to the analysis of the turbulent regimes in the tokamak edge. Among the research groups who focused on this issue, we remind Scott [11, 21] and Rogers et al. [22, 23, 24]. Both groups use very similar systems of equations derived from the Braginskii model and both describe edge turbulence as the competition among different regimes: a self-sustained non-linear drift wave instability, two branches of the ballooning mode instability, the resistive and the ideal ballooning modes, and the ion temperature gradient instability.

Scott analyzes edge turbulence focusing on the energy transfer from the free energy source to the sinks, through a certain number of transfer channels [21, 25]. The free energy source is the background pressure gradient, advected by the $\boldsymbol{E} \times \boldsymbol{B}$ velocity. The sinks are the resistive current damping, and the dissipation of energy at small perpendicular scales [21]. Scott identifies the self-sustained non-linear drift wave instability as the main turbulent regime in the tokamak edge,

for standard experimental parameters [21]. This instability develops non-linearly, overpowering the underlying linear instability, if the fluctuations level overcomes a critical threshold. It is independent on the magnetic curvature, and it relies on the system non-linearities in order to be self-sustained. The main transfer channel for the non-linear drift wave instability is the *adiabatic coupling*, which couples the electric potential, the parallel current and the pressure in the parallel electron dynamics in Ohm's law. For the ballooning instabilities, instead, the main energy transfer channel is represented by the interchange drive, *i.e.* the curvature effect related to diamagnetic advection. This term directly relates the electric potential and the pressure, without involving the parallel dynamics. Finally, Scott introduces the role of the ion temperature dynamics by describing the ion temperature gradient instability, becoming increasingly important for steeper ion temperature gradients.

Rogers et al. also picture the edge turbulence as a competition among the forementioned regimes. Similarly, they describe a self-sustained, non-linear drift wave instability as the result of non-linear coupling between density and electric potential at different parallel wavelength, in the absence of magnetic shear [6]. They demonstrate that the non-linear drift wave mechanism is active also in the presence of magnetic shear [26]. As in Scott's work, they identify the threshold between drift wave and resistive ballooning mode regimes according to the importance of the adiabatic coupling [22]. In Ref. [22] they find that, for a series of ASDEX tokamak discharges, resistive ballooning mode is prevailing for Ohmic and L-mode discharges, while the non-linear self-sustained drift wave instability is driving transport in H-mode discharges. Both Scott and Rogers et al. eventually converge on a similar set of dimensionless control parameters for the description of the electromagnetic fluid drift turbulence: a parameter taking into account plasma $\beta = 8\pi n T_e / B^2$, *i.e.* the ratio between the kinetic pressure and the magnetic pressure (in Rogers et al. that is $\alpha_{MHD} = (q^2 R \beta)/L_{p_e}$), and a parameter including the effects of electron-ion collisions and the importance of the adiabatic coupling (in Rogers et al. that is $\alpha_d = (m_i/m_e)^{1/2} [(2R)/L_n]^{1/4} [c_s/(\nu q^2 R)]^{1/4} 1/(8\pi))$. We remark that the pressure gradient length, that sets the background pressure profile, is set a priori when gradient driven numerical simulations are performed, such at those carried out by Scott and Rogers et al. In experimental applications, instead, the pressure gradient length is the self-consistent result of the interplay between sources, plasma transport, and sinks. In Ref. [27] LaBombard et al. analyze a large number of Alcator C-Mod edge plasma states, studying the dependence of transport on parameters identified thanks to the drift-reduced analysis. Their results are summarized in Fig. 1.5. In L-mode discharges they find a one-to-one relationship between collisionality and α_{MHD}, suggesting that for each value of collisionality there is a critical value of α_{MHD} that cannot be overcome. For $\alpha_d \lesssim 0.35$ the upper α_{MHD} (or $\hat{\beta}$) limit corresponds to a dramatic increase in transport for decreasing α_d. H-mode discharges lie instead in a region where $\alpha_d \gtrsim 0.35$, and their α_{MHD} satisfies $\alpha_{MHD}\alpha_d^2 \simeq 0.15$. These experimentally defined limits show good agreement with a density limit for low α_d, and with an L-H threshold for high α_d identified in Refs. [24, 28]. The re-
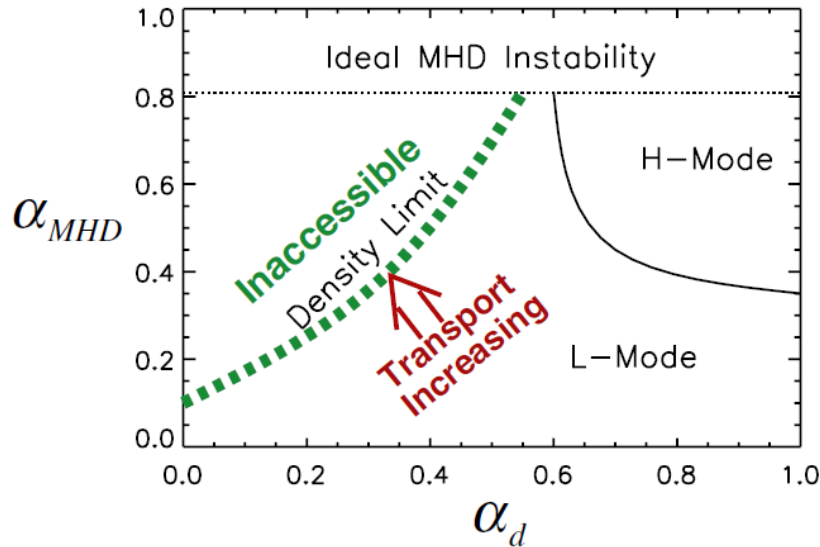
Figure 1.5: *Parameter space of edge turbulence within the electromagnetic fluid drift turbulence model, as identified in Ref. [24]. LaBombard et al. in Ref. [27] confirm experimentally the existence of the density limit at high collisionality (low α_d). Figure source: Ref. [27], Fig. 10.*

sults listed in Ref. [27] clearly suggest that the electromagnetic fluid drift turbulent model can be applied to the description of edge plasma turbulence, capturing some of its most important features.

1.3 Scope and outline of the thesis

The knowledge of the SOL turbulent regimes, of the conditions under which they develop, and of the characteristics of the transport they origin is of particular interest for the fusion community. This is necessary, in fact, to determine the SOL properties in order to predict, *e.g.*, the heat load on plasma facing components. In the present thesis we present analytical investigations supported by numerical GBS simulations of the plasma SOL aimed at improving the understanding of the main turbulent regimes active in the tokamak SOL. The GBS code represents a mature and developed tool capable of simulating SOL turbulent regimes. It is based on drift-reduced Braginskii equations, and it computes the plasma evolution self-consistently, without separation between background equilibrium and fluctuations. The plasma profiles are not fixed a priori, but they results from the non-linear interaction among the plasma outflow from the LCFS, the parallel streaming, and the radial transport due to the turbulence. Our goal is to provide a framework in which, given the operational SOL parameters, the turbulent regime driving SOL transport can be predicted without requiring expensive numerical analysis. The thesis is organized as follows.

In Chap. 2, starting from the fluid Braginskii equations, we derive the set of adimensionalized, drift-reduced, Braginskii equations used for our study of SOL turbulence and solved by GBS. We also derive a new set of boundary conditions to apply to these equations at the magnetic presheath entrance, including hot ion dynamics. The set of equations is then linearized and the linear solver used throughout our investigation is described.

In Chap. 3 we outline the main linear instabilities described by the linearized drift-reduced Braginskii equations, in the cold ion limit. We first identify the inertial and resistive branches of the drift wave and the inertial, resistive, and ideal branches of the ballooning mode instabilities, describing their main properties. We study their growth rate as a function of the main SOL parameters: the density gradient scale length, L_n, the ratio between the density and the temperature gradient length, $\eta_e = L_n/L_{T_e}$, the parallel resistivity, ν, the plasma beta, β, the magnetic shear, $\hat{s}$, the tokamak major and minor radii, R and a, and the safety factor q. We identify the threshold among the different instabilities as a function of the SOL parameters. Finally we verify our results against linear SOL calculations.

In Chap. 4 we identify the non-linear SOL turbulent regimes in the electrostatic limit, as a function of the SOL operational parameters: the safety factor, q, the magnetic shear, $\hat{s}$, the resistivity, ν and the ion to electron mass ratio, m_i/m_e. In order to estimate the pressure scale length, necessary to identify the instability that drives transport in the non-linear turbulence, among the ones introduced in Chap. 3, we use the *gradient removal* hypothesis. This says that turbulence is non-linearly saturated when the radial gradient of the background plasma pressure is of the same order of the radial gradient of the pressure fluctuations. By means of the gradient removal theory, we can build a map in the operational parameter space which defines the SOL turbulent regimes, *i.e.* the regions in which each linear instability drives transport. Finally, we check the validity of our methodology in identifying the non-linear prevailing regime in a set of non-linear GBS simulations.

In Chap. 5 we describe hot ion effects on SOL turbulence. We proceed to a detailed analysis of the linear instabilities in the presence of hot ions, describing both the changes on the linear instabilities existing in the cold ion limit, as described in Chap 3, and introducing the ion temperature gradient mode. We apply the gradient removal theory to SOL turbulence with hot ion dynamics and we outline the role of ion temperature gradient driven turbulence in the SOL turbulence. Finally we present the SOL turbulent regimes that include the hot ion effects.

In Chap. 6 we summarize the main findings of the present thesis and we outline the possible future developments of our work.

Chapter 2

The model equations for SOL turbulence and the GBS code

2.1 Introduction

Since the plasma is relatively cold at the edge of a tokamak device, the collisionality is high and allows the use of a fluid description. The Braginskii equations [5] were developed in the 1960s to describe the plasma dynamics in a highly collisional plasma. The original Braginskii equations are not suitable to describe and simulate turbulence in the tokamak SOL, since the spatial and temporal scale range they cover is too large to allow simulations at a reasonable computational cost. In order to circumvent this problem, a drift-reduced approach has been proposed soon following the derivation of the Braginskii equation. The drift-reduced approximation of Braginskii equations has been used by many authors (see, *e.g.*, Ref. [29]), neglecting ion or electron temperature, assuming an adiabatic electron response, or applying additional approximations [30,31,32,33]. For en early review, see Ref. [34]. We will consider the derivation of the drift-reduced Braginskii equations carried out by Zeiler [35, 6].

Based on the drift-reduced Braginskii equations, the Global Braginskii Solver (GBS) [20] is a three dimensional fluid code used to describe the evolution of the plasma density, electric potential, electron and ion parallel velocities, and electron and ion temperatures in the tokamak SOL. One of the key features of the code is the capability of advancing equilibrium and perturbations self-consistently, as an interplay among the plasma density and energy outflowing from the plasma core, the parallel losses at the limiter plates, and the cross-field transport due to turbulence.

The GBS code was initially conceived to describe the two dimensional plasma dynamics in basic plasma physics devices [36], and it was then developed to include the dynamics in the third dimension and progressively approach more complex configurations. At first GBS was successfully applied to simulate the LAPD linear

device [37]. Later, the code was employed to investigate the turbulent dynamics of the TORPEX device [38, 39, 40]. This is characterized by helicoidal field lines created by superposing a vertical and a toroidal magnetic field. The code has been validated against experiments in the TORPEX device [41, 42]. This machine is particularly suitable for the code validation, since it is equipped with a large number of diagnostics, allowing a detailed comparison with simulation results. With the addition of toroidal curvature and electromagnetic effects, the code was recently ported to the tokamak SOL geometry in a limited configuration [20, 43, 44]. Development of GBS have been carried out in the framework of the present thesis, in particular the inclusion of magnetic shear and hot ion temperature effects to provide a better description of tokamak SOL turbulence. Further developments of GBS are currently being carried out to describe more complex SOL scenarios.

We note that, beside GBS, a number of codes based on the drift-reduced Braginskii equations have been developed in the past years: the GEM code [19], the BOUT code [12], the TOKAM3D code [13], the CYTO code [14] and the EMEDGE3D code [15, 16]. As a matter of fact, those are based on a similar set of equations as GBS and similar numerical schemes.

The present chapter introduces the model that we employ to study the tokamak SOL turbulence. We first introduce the Braginskii equations, and we derive their drift-reduced limit. We then proceed with an explanation of the main features of the non-linear GBS code. Finally, we briefly describe the linear equations that we have considered and implemented in a linear solver to study the linear properties of the SOL instabilities.

2.2 The Braginskii equations

The description at a kinetic level of an ionized gas is given by the distribution function $f(t, \boldsymbol{r}, \boldsymbol{v})$ of all the particle species composing the plasma. The phase-space evolution of the distribution function is described by the Boltzmann equation:

$$\frac{\partial f}{\partial t} + \nabla \cdot (\boldsymbol{v}f) + \nabla \cdot \left(\frac{\boldsymbol{F}}{m}f\right) = C, \tag{2.1}$$

where $\boldsymbol{F}$ is the Lorentz force $\boldsymbol{F} = q\left(\boldsymbol{E} + \frac{1}{c}\boldsymbol{v} \times \boldsymbol{B}\right)$, m is the particle mass, q is the particle charge, and C is the collisional operator describing the evolution of the particle population due to collisions. Because of collisions, the distribution function approaches a Maxwellian distribution on a time scale of the same order of the collisional time.

In order to have a more amenable description of the plasma, we consider the time evolution of the first three moments of the Boltzmann equation. We introduce therefore the density,

$$n(t, \boldsymbol{r}) = \int f(t, \boldsymbol{r}, \boldsymbol{v}) \, d\boldsymbol{v}, \tag{2.2}$$

the mean velocity,

$$\boldsymbol{V}(t, \boldsymbol{r}) = \frac{1}{n} \int \boldsymbol{v} f(t, \boldsymbol{r}, \boldsymbol{v}) \, d\boldsymbol{v} = <\boldsymbol{v}>, \tag{2.3}$$

and the temperature,

$$T(t, \boldsymbol{r}) = \frac{1}{n} \int \frac{m}{3} (\boldsymbol{v} - \boldsymbol{V})^2 f(t, \boldsymbol{r}, \boldsymbol{v}) \, d\boldsymbol{v} = \frac{m}{3} < (\boldsymbol{v} - \boldsymbol{V})^2 > . \tag{2.4}$$

In the following, we assume that we are dealing with a plasma composed by electrons and one simple ion species, whose charge is Ze. The continuity equation, the momentum equation, and the temperature equation, describing the evolution of the density, of the average velocity, and of the temperature can be obtained by multiplying Eq. (2.1) by 1, by $m\boldsymbol{V}$, and by $mv^2/2$, respectively, and integrating over the velocity space. We obtain:

$$\frac{\partial n_e}{\partial t} + \nabla \cdot (n_e \boldsymbol{V_e}) = 0 \tag{2.5}$$

$$\frac{\partial n_i}{\partial t} + \nabla \cdot (n_i \boldsymbol{V_i}) = 0 \tag{2.6}$$

$$m_e n_e \frac{d_e \boldsymbol{V_e}}{dt} = -\nabla p_e - \nabla \cdot \pi_e - e n_e [\boldsymbol{E} + \frac{1}{c} \boldsymbol{V_e} \times \boldsymbol{B}] + \boldsymbol{R_e} \tag{2.7}$$

$$m_i n_i \frac{d_i \boldsymbol{V_i}}{dt} = -\nabla p_i - \nabla \cdot \pi_i + Z e n_i [\boldsymbol{E} + \frac{1}{c} \boldsymbol{V_i} \times \boldsymbol{B}] + \boldsymbol{R_i} \tag{2.8}$$

$$\frac{3}{2} n_e \frac{d_e T_e}{dt} + p_e \nabla \cdot \boldsymbol{V_e} = -\nabla \cdot \boldsymbol{q_e} - \pi_e : \nabla \boldsymbol{V_e} + Q_e \tag{2.9}$$

$$\frac{3}{2} n_i \frac{d_i T_i}{dt} + p_i \nabla \cdot \boldsymbol{V_i} = -\nabla \cdot \boldsymbol{q_i} - \pi_i : \nabla \boldsymbol{V_i} + Q_i, \tag{2.10}$$

where

$$\frac{d_e \boldsymbol{V_e}}{dt} = \frac{\partial}{\partial t} + \boldsymbol{V_e} \cdot \nabla \tag{2.11}$$

$$\frac{d_i \boldsymbol{V_i}}{dt} = \frac{\partial}{\partial t} + \boldsymbol{V_i} \cdot \nabla, \tag{2.12}$$

are the total derivatives for the electrons and the ions, respectively, $p_e = n_e T_e$ is the electron plasma pressure, and, analogously, $p_i = n_i T_i$, for the ions.

Equations (2.5) and (2.6) state the conservation of density. On the right hand side of Eqs. (2.7) and (2.8) the first two terms represent the change in momentum density due to the pressure tensor $P = pI + \pi$. Decomposing the particle velocity as the sum of the average, fluid, velocity and a random component, $\boldsymbol{v} = \boldsymbol{V} + \boldsymbol{v'}$, the plasma pressure p is the isotropic part of the pressure tensor,

$$p = nm < v'^2 > /3 = nT, \tag{2.13}$$

while the stress tensor,

$$\pi_{\alpha,} = nm < v'_\alpha v'_\beta - v'^2/3\delta_{\alpha,\beta} >, \tag{2.14}$$

is the anisotropic component. The third term on the right hand side of Eqs. (2.7) and (2.8) describes the effect of the electric and magnetic field, while the last term, $\boldsymbol{R}_{e,i}$ is the density of momentum per unit time exchanged due to collision with the other species:

$$\boldsymbol{R} = \int m\boldsymbol{v}'C d\boldsymbol{v}. \tag{2.15}$$

Eqs. (2.9) and (2.10) are the heat equations for electrons and ions, respectively. The vector $\boldsymbol{q}$ is the flux of heat density of a given species, due to the random motion of the particles:

$$\boldsymbol{q} = \int \frac{m}{2}v'^2\boldsymbol{v}f\left(t, \boldsymbol{r}, \boldsymbol{v}\right) d\boldsymbol{v}. \tag{2.16}$$

The scalar Q represents instead the heat density generated as a consequence of the collisions with the other species in the gas:

$$Q = \int \frac{m}{2}v'^2 C d\boldsymbol{v}. \tag{2.17}$$

Finally, we note that the Frobenius inner product, $\pi : \nabla\boldsymbol{V} = \pi_{\alpha\beta}\partial V_\alpha/\partial x_\beta$, has been used.

Equations (2.5)-(2.10) can be used to compute the time evolution of n, $\boldsymbol{V}$ and T, if an expression of $\boldsymbol{R}$, π, $\boldsymbol{q}$, and Q as a function of n, $\boldsymbol{V}$ and T can be formed. This is known as the *closure problem*: in order to solve the nth moment of the Boltzmann equation, the solution of the $n + 1$ moment is needed. Braginskii proposes to calculate the expressions for $\boldsymbol{R}$, π, $\boldsymbol{q}$, and Q, under the hypothesis that the distribution function f is close to a Maxwellian, as the plasma tends to thermodynamic equilibrium, because of collisions. As a matter of fact, a Maxwellian distribution function is reached if the gradients and the time derivative vanish identically. The presence of spatial and temporal gradients introduce deviations from a Maxwellian. These deviations are evaluated by the Braginskii equations in the case of spatial variations occurring on a scale that is much larger than the space travelled by a particle between two collisions and in the case of time scales of interest much longer than the collision time. Braginskii expresses $\boldsymbol{R}$, π, $\boldsymbol{q}$, and Q as proportional to n, $\boldsymbol{V}$ and T and their gradients. The proportionality coefficients are called transport coefficients. The next section is dedicated to the description of the relation between the transport coefficients and n, $\boldsymbol{V}$ and T and their gradients.

2.2.1 The transport coefficients

The transport coefficients described in the following are calculated under the hypothesis that the plasma is immersed in a strong magnetic field. Under this cir-

cumstances we suppose $\omega_{e,i}\tau_{e,i} \gg 1$, where $\omega_{e,i} = qB/m_{e,i}c$ are the electron/ion cyclotron frequencies, $\tau_{e,i}$ are the electron/ion collision times:

$$\tau_e = \frac{3\sqrt{m_e}T_e^{3/2}}{4\sqrt{2\pi}\lambda e^4 Z^2 n_i}, \tag{2.18}$$

$$\tau_i = \frac{3\sqrt{m_i}T_i^{3/2}}{4\sqrt{\pi}\lambda e^4 Z^4 n_i}, \tag{2.19}$$

and λ is the Coulomb logarithm.

The term $\boldsymbol{R}$ in the momentum equations (2.7) and (2.8) is the sum of two contributions: a friction force due to electron/ion collisions, and a thermal force, due to the coexistence of a temperature gradient in presence of electron/ion collision. These can be written as ($\boldsymbol{R_i} = -\boldsymbol{R_e}$):

$$\boldsymbol{R_e} = \boldsymbol{R_u} + \boldsymbol{R_t}, \tag{2.20}$$

$$\boldsymbol{R_u} = en_e\left(\frac{\boldsymbol{j}_\parallel}{\sigma_\parallel} + \frac{\boldsymbol{j}_\perp}{\sigma_\perp}\right), \tag{2.21}$$

$$\boldsymbol{R_t} = -0.71n_e\nabla_\parallel T_e - \frac{3}{2}\frac{n_e}{\omega_e\tau_e}\boldsymbol{b}\times\nabla_\perp T_e, \tag{2.22}$$

where $\boldsymbol{b}$ is the unit vector parallel to the magnetic field, $\boldsymbol{j}_{\parallel,\perp} = en_e\left(\boldsymbol{V}_{\parallel,\perp i} - \boldsymbol{V}_{\parallel,\perp e}\right)$ is the current in the parallel/perpendicular direction, and $\sigma_{\parallel,\perp}$ is the parallel/perpendicular conductivity:

$$\sigma_\perp = \frac{e^2 n_e \tau_e}{m_e}, \tag{2.23}$$

$$\sigma_\parallel = 1.96\sigma_\perp. \tag{2.24}$$

The electron heat flux $\boldsymbol{q_e}$ in the temperature equation (Eq. (2.9)) can be expressed as the sum of two terms, $\boldsymbol{q_u}$ and $\boldsymbol{q_t}$. The first term is directly related to the thermal force in $\boldsymbol{R}$, while the second is due to the presence of a temperature gradient:

$$\boldsymbol{q_u^e} = 0.71n_e T_e \boldsymbol{u}_\parallel + \frac{3}{2}\frac{n_e T_e}{\omega_e\tau_e}\boldsymbol{b}\times\boldsymbol{u}, \tag{2.25}$$

$$\boldsymbol{q_t^e} = -\chi_\parallel^e\nabla_\parallel T_e - \chi_\perp^e\nabla_\perp T_e - \frac{5}{2}\frac{cn_e T_e}{eB}\boldsymbol{b}\times\nabla T_e, \tag{2.26}$$

where $\boldsymbol{u} = \boldsymbol{V_e} - \boldsymbol{V_i}$ and the thermal conductivities are:

$$\chi_\parallel^e = 3.16\frac{n_e T_e \tau_e}{m_e}, \tag{2.27}$$

$$\chi_\perp^e = 4.66\frac{n_e T_e}{m_e\omega_e^2\tau_e}. \tag{2.28}$$

The ion heat flux $\boldsymbol{q_i}$ is, neglecting terms of order $\omega_i \tau_i$:

$$\boldsymbol{q_i} = -\chi_\parallel^i \nabla_\parallel T_i - \chi_\perp^i \nabla_\perp T_i + \frac{5}{2}\frac{c n_i T_i}{ZeB}\boldsymbol{b} \times \nabla T_i, \tag{2.29}$$

where the thermal conductivities are:

$$\chi_\parallel^i = 3.9\frac{n_i T_i \tau_i}{m_i}, \tag{2.30}$$

$$\chi_\perp^i = 2\frac{n_i T_i}{m_i \omega_i^2 \tau_i}. \tag{2.31}$$

The last term in Eqs. (2.26) and (2.29) is due to the interplay of Larmor radius effects and the presence of a temperature gradient.

If we consider $\omega\tau \gg 1$, and we align the z axis along the magnetic field, the stress tensor π can be written as:

$$\pi_{zz} = -\eta_0 W_{zz}, \tag{2.32}$$

$$\pi_{xx} = -\frac{\eta_0}{2}\left(W_{xx} + W_{yy}\right) - \frac{\eta_1}{2}\left(W_{xx} - W_{yy}\right) - \eta_3 W_{xy}, \tag{2.33}$$

$$\pi_{yy} = -\frac{\eta_0}{2}\left(W_{xx} + W_{yy}\right) - \frac{\eta_1}{2}\left(W_{yy} - W_{xx}\right) + \eta_3 W_{xy}, \tag{2.34}$$

$$\pi_{xy} = \pi_{yx} = -\eta_1 W_{xy} + \frac{\eta_3}{2}\left(W_{xx} - W_{yy}\right), \tag{2.35}$$

$$\pi_{xz} = \pi_{zx} = -\eta_2 W_{xz} - \eta_4 W_{yz}, \tag{2.36}$$

$$\pi_{yz} = \pi_{zy} = -\eta_2 W_{yz} - \eta_4 W_{xz}, \tag{2.37}$$

where the rate-of-strain tensor W is:

$$W_{\alpha,\beta} = \frac{\partial V_\alpha}{\partial x_\beta} + \frac{\partial V_\beta}{\partial x_\alpha} - \frac{2}{3}\delta_{\alpha,\beta}\nabla \cdot \boldsymbol{V}. \tag{2.38}$$

We remark that it is the presence of the magnetic field that introduces a different behaviour of the plasma in the directions parallel and perpendicular to the field itself. As a matter of fact, the parallel momentum is easily transported along the parallel direction, while the transport in the perpendicular direction is inhibited. For the perpendicular momentum, the transport is reduced in both the parallel and in the perpendicular directions, with respect to the parallel momentum transport. This is reflected in the fact that the viscosities η_1 and η_2 are smaller than η_0 by a factor $(\omega\tau)^2$, and the viscosities η_3 and η_4 by a factor $\omega\tau$. The expressions for the

electron and ion viscosities are:

$$\eta_0^e = 0.73 n_e T_e \tau_e, \tag{2.39}$$

$$\eta_1^e = 0.51 \frac{n_e T_e}{\omega_e^2 \tau_e}, \eta_2^e = 4\eta_1^e, \tag{2.40}$$

$$\eta_3^e = -\frac{n_e T_e}{2\omega_e}, \eta_4^e = 2\eta_3^e; \tag{2.41}$$

$$\eta_0^i = 0.96 n_i T_i \tau_i, \tag{2.42}$$

$$\eta_1^i = \frac{3}{10} \frac{n_i T_i}{\omega_i^2 \tau_i}, \eta_2^i = 4\eta_1^i, \tag{2.43}$$

$$\eta_3^e = \frac{n_i T_i}{2\omega_i}, \eta_4^i = 2\eta_3^i. \tag{2.44}$$

In the absence of magnetic field, the relation between π and W is simply $\pi = -\eta_0 W$. Finally, the heat generation Q appearing in Eqs. (2.9) and (2.10) can be written, for electrons and ions, respectively as:

$$Q_e = -\boldsymbol{R_e} \cdot \boldsymbol{u} - Q_i, \tag{2.45}$$

$$Q_i = \frac{3 m_e n_e}{m_i \tau_e} \left(T_e - T_i \right). \tag{2.46}$$

For the electrons, this is composed by the Joule heating due to friction with ions and a term due to the temperature difference between the two species. In the ion heat generation we keep the term related to the difference between T_e and T_i, while the Joule heating is neglected, since this is $\sim m_e/m_i$ times smaller than $\boldsymbol{R_e} \cdot \boldsymbol{u}$.

2.3   The drift reduced approximation

The Braginskii equations presented in the previous section, Eqs. (2.5)-(2.10), need to be further simplified to obtain a model that can be used to numerically investigate plasma turbulence in the SOL. In fact, the Braginskii equations describe the plasma dynamics occurring on a wide range of time and spatial scales, ranging from the fast cyclotron motion to the confinement time scale, and from the Larmor radius and the Debye length to the typical machine size. This makes their use to simulate SOL turbulence extremely challenging from a numerical point of view. However, turbulence in the SOL is characterized by time variations on a time scale much slower than the ion gyromotion and spatial variations on a scale of the order of $\rho_s = c_s/\omega_i$, the ion Larmor radius at the sound speed, c_s. Therefore, the drift ordering can be adopted, according to which we assume:

$$\frac{\partial}{\partial t} \sim \boldsymbol{V}_{E \times B} \cdot \nabla \sim \frac{\rho_s^2}{L_\perp^2} \omega_i \ll \omega_i, \tag{2.47}$$

as ρ_s is smaller than $L_\perp$, the typical equilibrium scale length, and $\boldsymbol{V}_{E \times B} = c/B$ $(-\nabla \phi \times \boldsymbol{b})$ is the $\boldsymbol{E} \times \boldsymbol{B}$ drift velocity. In the following we also assume the plasma to be quasi-neutral. In fact, we consider plasma turbulence taking place on a spatial scale $\rho_s \gg \lambda_D$, where $\lambda_D = \sqrt{T_e/(2\pi e^2 n)}$ is the Debye length. We can therefore assume $n_i = n_e \equiv n$.

The basic idea behind the drift-reduced approximation is to split the particles dynamics into the parallel and the perpendicular direction with respect to the magnetic field and express the electron and ion perpendicular velocities as:

$$\boldsymbol{V}_{\perp e} = \boldsymbol{V}_{E \times B} + \boldsymbol{V}_{*e}, \tag{2.48}$$

$$\boldsymbol{V}_{\perp i} = \boldsymbol{V}_{E \times B} + \boldsymbol{V}_{*i} + \boldsymbol{V}_{pol}, \tag{2.49}$$

where

$$\boldsymbol{V}_{*e} = -\boldsymbol{b} \times \nabla p_e c / (enB) \tag{2.50}$$

is the electron diamagnetic drift velocity, and

$$\boldsymbol{V}_{*i} = \boldsymbol{b} \times \nabla p_i c / (enB) \tag{2.51}$$

is the ion diamagnetic drift velocity. Together with the $\boldsymbol{E} \times \boldsymbol{B}$ drift, the diamagnetic drift provide the 0th order approximation of the perpendicular velocity, *i.e.* $\boldsymbol{V}_{\perp i0} = \boldsymbol{V}_{E \times B} + \boldsymbol{V}_{*i}$. The first order correction to the ion perpendicular velocity is called polarisation drift, $\boldsymbol{V}_{pol}$, and it is expressed as:

$$\boldsymbol{V}_{pol} = \frac{\boldsymbol{b}}{\omega_i} \times \frac{d}{dt} \boldsymbol{V}_{\perp i0} + \frac{1}{nm_i\omega_i} \left\{ \boldsymbol{b} \times \left[p_i \left(\nabla \times \frac{\boldsymbol{b}}{\omega_i} \right) \cdot \nabla \boldsymbol{V}_{\perp i0} \right] + \right.$$
$$+ \boldsymbol{b} \times \nabla_\perp \left[\frac{2p_i}{\omega_i} \nabla \cdot \boldsymbol{b} \times \boldsymbol{V}_{\perp i0} \right] - \nabla_\perp \left[\frac{p_i}{2\omega_i} \nabla_\perp \cdot \boldsymbol{V}_{\perp i0} \right] \right\} + \tag{2.52}$$
$$+ \frac{1}{nm_i\omega_i} \boldsymbol{b} \times \left[G\boldsymbol{\kappa} - \frac{\nabla G}{3} \right],$$

where $d/dt = \partial/\partial t + \left(\boldsymbol{V}_{E \times B} + \boldsymbol{V}_{\|i} \right) \cdot \nabla$, and $\boldsymbol{\kappa}$ is the field curvature, $\boldsymbol{\kappa} = \boldsymbol{b} \cdot \nabla \boldsymbol{b}$. The diamagnetic drift does not appear, since it cancels out with the first term on the right hand side of Eq. (2.55). In order to deduce Eq. (2.52), it has been necessary to further simplify Eqs. (2.7) and (2.8); the transfer of momentum from electrons to ions ($\boldsymbol{R_i}$) has been neglected, in the expression for $\boldsymbol{R_e}$ the perpendicular component of the frictional and thermal forces has been neglected too. Furthermore, the stress tensor π is divided in two contributions: a viscous part, π_{vis}, and a finite Larmor radius part (FLR), π_{FLR}. The viscous part can be written as:

$$\pi_{vis} = (\boldsymbol{bb} - I/3) \, G, \tag{2.53}$$

$$G = -\eta_0 \left(2\nabla_\| V_\| - \boldsymbol{\kappa} \cdot \boldsymbol{V} - \frac{1}{3} \nabla \cdot \boldsymbol{V} \right), \tag{2.54}$$

where G is the stress function. The FLR part of the stress tensor is such that:

$$\nabla \cdot \pi_{FLR} = -mn \left(\boldsymbol{V}_* \cdot \nabla \right) \boldsymbol{V} + p \left[\left(\nabla \times \frac{\boldsymbol{b}}{\omega} \right) \cdot \nabla \right] \boldsymbol{V} + \nabla_\perp \left(\frac{p}{2\omega} \nabla \cdot \boldsymbol{V} \right) +$$
$$+ \boldsymbol{b} \times \nabla \left(\frac{p}{2\omega} \nabla_\perp \cdot \boldsymbol{V} \right), \tag{2.55}$$

where $\boldsymbol{V}_*$ is the diamagnetic drift velocity. Just the terms related to η_3 have been kept, while η_1, η_2, and η_4 related terms have been neglected in Eqs (2.32)-(2.37). We remark that $\nabla \cdot \pi_{FLR}$ is smaller than $\nabla \cdot \pi_{vis}$ by a factor $\omega\tau \gg 1$. The complete derivation of π_{vis} and π_{FLR} can be found in [6] and references therein. It is possible to verify that $\boldsymbol{V}_{pol} \ll \boldsymbol{V}_{E \times B}$, by estimating $\boldsymbol{V}_{pol}$ through the first term of Eq. (2.52) as $\boldsymbol{V}_{pol} \simeq \frac{\boldsymbol{b}}{\omega_i} \times \frac{d}{dt} \boldsymbol{V}_{\perp i0} \simeq \boldsymbol{V}_{E \times B} \rho_s^2 / L_\perp^2 \ll \boldsymbol{V}_{E \times B}$ (according to Eq. (2.47), see Ref. [6] for details). The polarisation drift appears in the term $\nabla \cdot (n\boldsymbol{V}_{pol})$, which can be written as:

$$\nabla \cdot (n\boldsymbol{V}_{pol}) = \nabla_\perp \frac{nc}{B\omega_i} \frac{d}{dt} \left(\boldsymbol{E}_\perp - \frac{\nabla_\perp p_i}{en} \right) + \frac{1}{3m_i\omega_i} \boldsymbol{b} \times \boldsymbol{\kappa} \cdot \nabla G. \tag{2.56}$$

More details about the derivation of Eq. (2.56) can be found in Ref. [6]. The electron polarisation drift can be calculated similarly to the ions. It is nevertheless neglected, since, for electrons, the first term of Eq. (2.56) is smaller than the one for ions by a factor m_e; the second term is instead smaller than the ion one by a factor $\eta_{0e}/\eta_{0i} \simeq \sqrt{m_e/m_i}$.

2.3.1 The continuity and vorticity equations

Having separated the plasma motion along the perpendicular and the parallel directions, we can write the continuity equations for ions and electrons as follows:

$$\frac{\partial n_e}{\partial t} + \nabla \cdot \left[n \left(\boldsymbol{V}_{E \times B} + \boldsymbol{V}_{*e} + \boldsymbol{V}_{\parallel e} \right) \right] = 0, \tag{2.57}$$

$$\frac{\partial n_i}{\partial t} + \nabla \cdot \left[n \left(\boldsymbol{V}_{E \times B} + \boldsymbol{V}_{*i} + \boldsymbol{V}_{pol} + \boldsymbol{V}_{\parallel i} \right) \right] = 0. \tag{2.58}$$

The vorticity equation is derived by subtracting the ion and the electron continuity equations, and imposing quasi-neutrality by setting $n_e = n_i$. This is equivalent to impose $\nabla \cdot \boldsymbol{j} = 0$. This equation describes the evolution of the quantity $\omega = \nabla_\perp^2 \phi$, which is related to the fluid rotation in the plane perpendicular to the magnetic field. The name is derived from the analogy with the vorticity used in fluid dynamics, $\boldsymbol{\omega}_{fd} = \nabla \times \boldsymbol{V}$. In our case, in fact, it can be demonstrated that ω is proportional

to $\boldsymbol{b} \cdot \nabla \times \boldsymbol{V}_{E \times B}$. The vorticity equation reads as:

$$\frac{nc}{B\omega_i}\frac{d}{dt}\left(-\nabla_\perp^2\phi - \frac{1}{en}\nabla_\perp^2 p_i\right) + \frac{1}{3m_i\omega_i}\boldsymbol{b}\times\boldsymbol{\kappa}\cdot\nabla G_i + \nabla_\parallel\frac{j_\parallel}{e} + \nabla\cdot n\left(\boldsymbol{V}_{*i} - \boldsymbol{V}_{*e}\right) = 0, \tag{2.59}$$

where we have applied the Boussinesq approximation [45]:

$$\nabla_\perp \frac{nc}{B\omega_i}\frac{d}{dt}\left(\boldsymbol{E}_\perp - \frac{\nabla_\perp p_i}{en}\right) \simeq \frac{nc}{B\omega_i}\frac{d}{dt}\left(-\nabla_\perp^2\phi - \frac{1}{en}\nabla_\perp^2 p_i\right). \tag{2.60}$$

2.3.2   The semi-electrostatic limit

Braginskii equations retain both shear and compressional Alfvén waves. Since compressional Alfvén waves are several orders of magnitude faster than the turbulent fluctuations we are interested in, we want to exclude their dynamics from our system. This is achieved by choosing a vector potential $\boldsymbol{A}$ that is purely parallel to the magnetic field:

$$\delta\boldsymbol{A} = -\psi\boldsymbol{b}, \tag{2.61}$$

where ψ is the poloidal flux function. Within the assumption that $\beta = 8\pi(p_e + p_i)/B^2 \ll 1$ and observing that typical scale lengths in the parallel direction are much larger than the ones in the perpendicular direction, we can write the perturbed magnetic field as:

$$\delta\boldsymbol{B} = -\nabla\times(\psi\boldsymbol{b}) \simeq \boldsymbol{b}\times\nabla_\perp\psi = \delta\boldsymbol{B}_\perp. \tag{2.62}$$

The Ampere's law is therefore written as:

$$\nabla_\perp^2\psi = \frac{4\pi}{c}j_\parallel, \tag{2.63}$$

and the electric field is given by:

$$\boldsymbol{E} = -\nabla\phi + \frac{1}{c}\frac{\partial\psi}{\partial t}\boldsymbol{b}. \tag{2.64}$$

Beside entering Eq. (2.64), electromagnetic fluctuations play a role in the definition of the parallel derivative operator,

$$\nabla_\parallel = \boldsymbol{b}\cdot\nabla + \frac{\boldsymbol{b}}{B}\times\nabla_\perp\psi\cdot\nabla, \tag{2.65}$$

where the second term is the contribution to the parallel derivative due to magnetic perturbations.

2.3.3 Parallel motion

The parallel motion for the electron species can be derived by projecting Eq. (2.7) along the parallel direction. In this case, the parallel component of $\boldsymbol{R_e}$ is retained:

$$m_e \frac{d^e V_{\parallel e}}{dt} = -\frac{1}{n}\nabla_\parallel p_e - \frac{2}{3}\nabla_\parallel G_e + e\nabla_\parallel \phi - \frac{e}{c}\frac{\partial \psi}{\partial t} + e\frac{j_\parallel}{\sigma_\parallel} - 0.71\nabla_\parallel T_e. \qquad (2.66)$$

The total time derivative is expressed as: $d^e/dt = \partial/\partial t + \left(\boldsymbol{V_{E\times B}} + \boldsymbol{V_{\parallel e}}\right)\cdot\nabla$, being the diamagnetic contribution to the total derivative canceled out by the first term in the $\nabla\cdot\pi_{FLR,e}$ equation (see Eq. (2.55)). In deducing Eq. (2.66), we have used $\nabla\cdot\pi_e = 2/3\nabla_\parallel G_e$, where we have considered that the FLR part of the stress tensor is perpendicular to the magnetic field. The equation regulating the evolution of the ion parallel velocity can be obtained by adding the parallel components of the electron and the ion momentum equations:

$$m_i \frac{dV_{\parallel i}}{dt} = -\frac{1}{n}\nabla\left(p_i + p_e\right) - p_i\nabla\times\frac{\boldsymbol{b}}{\omega_i}\cdot\nabla V_{\parallel i} - \frac{2}{3}\nabla_\parallel G_i. \qquad (2.67)$$

In Eq. (2.67) the π_e tensor has been neglected since the $\pi_{FLR,e}$ and the $\pi_{vis,e}$ contributions are smaller than their ion counterpart by a factor m_e and $\sqrt{m_e}$ respectively.

2.3.4 Temperature equations

The electron temperature equation is obtained from Eq. (2.9) by neglecting, in the heat generation Q_e, the frictional part of the heating, the second term in Eq. (2.22), and the electron-ion heat transfer. In the heat flux term $\boldsymbol{q_e}$, we neglect the term proportional to $\chi_\perp^e$ and the second term in Eq. (2.25), since smaller than $\chi_\parallel^e$ by a factor $\omega_e\tau_e$. We therefore obtain:

$$\frac{3}{2}n\frac{d^e T_e}{dt} + \frac{3}{2}n\boldsymbol{V_{*e}}\cdot\nabla T_e + p_e\nabla\cdot\left(\boldsymbol{V_{\perp e}} + \boldsymbol{V_{\parallel e}}\right) - \frac{5}{2}\frac{c}{e}\nabla\cdot p_e\left(\frac{\boldsymbol{b}}{B}\times\nabla T_e\right)$$
$$-0.71 T_e\nabla_\parallel j_\parallel - \nabla\cdot\left(\chi_{\parallel e}\nabla_{\parallel T_e}\right) = 0. \qquad (2.68)$$

A similar equation is obtained for the ion temperature, starting from Eq. (2.10), by neglecting the electron-ion heat transfer ($Q_i = 0$) and the terms proportional to $\chi_\perp^i$ and to $\chi_\parallel^i$ in the heat flux $\boldsymbol{q_i}$; $\chi_\perp^i$ is smaller than $\chi_\parallel^i$ by a factor $\omega_i\tau_i$, and $\chi_\parallel^i$ is smaller than $\chi_\parallel^e$ by a factor $\sqrt{m_e/m_i}$. This leads to:

$$\frac{3}{2}n\frac{dT_i}{dt} + \frac{3}{2}n\boldsymbol{V_{*i}}\cdot\nabla T_i + p_i\nabla\cdot\left(\boldsymbol{V_{\perp i}} + \boldsymbol{V_{\parallel i}}\right) + \frac{5}{2}\frac{c}{e}\nabla\cdot p_i\left(\frac{\boldsymbol{b}}{B}\times\nabla T_i\right) = 0. \qquad (2.69)$$

We notice that in Eq. (2.69) the term $\nabla\cdot\boldsymbol{V_{pol}}$ has to be evaluated. This can be avoided by making use of the density equation (see Ref. [6]). We can in fact eliminate

the term $p_i \nabla \cdot \left(\boldsymbol{V}_{\perp i} + \boldsymbol{V}_{\|i} \right)$ using the ion continuity equation:

$$p_i \nabla \cdot \left(\boldsymbol{V}_{\perp i} + \boldsymbol{V}_{\|i} \right) = -T_i \left(\frac{dn}{dt} + \boldsymbol{V}_{*i} \cdot \nabla n \right) = -T_i \frac{dn}{dt} + n \boldsymbol{V}_{*i} \cdot \nabla T_i, \qquad (2.70)$$

where we notice that $\boldsymbol{V}_{*i} \cdot \nabla p_i = 0$. Moreover, we can rewrite the 4th term of Eq. (2.69) as:

$$\frac{5}{2} \frac{c}{e} \nabla \cdot p_i \left(\frac{\boldsymbol{b}}{B} \times \nabla T_i \right) = -\frac{5}{2} n \boldsymbol{V}_{*i} \cdot \nabla T_i + \frac{5}{2} \frac{c}{e} \left(\nabla \times \frac{\boldsymbol{b}}{B} \right) \cdot \nabla T_i. \qquad (2.71)$$

Substituting Eqs. (2.70) and (2.71) into Eq. (2.69), we obtain a new form for the ion temperature equation:

$$\frac{3}{2} n \frac{dT_i}{dt} - T_i \frac{dn}{dt} + \frac{5}{2} \frac{c}{e} p_i \left(\nabla \times \frac{\boldsymbol{b}}{B} \right) \cdot \nabla T_i = 0. \qquad (2.72)$$

In Eq. (2.72) we ignore $\boldsymbol{V}_{pol} \cdot \nabla$ in the total derivative, since much smaller than the other contributions, but we retain the term proportional to $\nabla \cdot \boldsymbol{V}_{pol}$, consistently with the derivation of Eq. (2.59), which is hidden in the dn/dt term. Substituting Eq. (2.57) into Eq. (2.72), we obtain the ion temperature equation that can be approached numerically:

$$\frac{3}{2} n \frac{dT_i}{dt} + T_i \left[n \cdot \nabla \left(\boldsymbol{V}_{E \times B} + \boldsymbol{V}_{\|e} \right) + \nabla \cdot (n \boldsymbol{V}_{*e}) \right] + \frac{5}{2} \frac{c}{e} p_i \left(\nabla \times \frac{\boldsymbol{b}}{B} \right) \cdot \nabla T_i = 0. \quad (2.73)$$

2.3.5 Summary of results

In the previous sections a set of drift-reduced equations describing the behaviour of plasma density, vorticity, electron and ion parallel velocities, electron and ion temperatures has been derived. Here we present a summary of the drift-reduced set

of equations that we will consider for the reminder of the present thesis:

$$\frac{\partial n}{\partial t} + \nabla \cdot \left(\boldsymbol{V}_{E\times B} + \boldsymbol{V}_{*e} + \boldsymbol{V}_{\|e} \right) = 0, \tag{2.74}$$

$$\frac{nc}{B\omega_i}\frac{d}{dt}\left(-\nabla_\perp^2 \phi - \frac{1}{en}\nabla_\perp^2 p_i \right) + \frac{1}{3m_i\omega_i}\boldsymbol{b}\times\boldsymbol{\kappa}\cdot\nabla G_i + \nabla_\| \frac{j_\|}{e} + \nabla \cdot n\left(\boldsymbol{V}_{*i} - \boldsymbol{V}_{*e} \right) = 0, \tag{2.75}$$

$$m_e\frac{d^e V_{\|e}}{dt} = -\frac{1}{n}\nabla_\| p_e - \frac{2}{3}\nabla_\| G_e + e\nabla_\|\phi - \frac{e}{c}\frac{\partial\psi}{\partial t} + e\frac{j_\|}{\sigma_\|} - 0.71\nabla_\| T_e, \tag{2.76}$$

$$m_i\frac{dV_{\|i}}{dt} = -\frac{1}{n}\nabla\left(p_i + p_e \right) - p_i\nabla\times\frac{\boldsymbol{b}}{\omega_i}\cdot\nabla V_{\|i} - \frac{2}{3}\nabla_\| G_i, \tag{2.77}$$

$$\frac{3}{2}n\frac{d^e T_e}{dt} + \frac{3}{2}n\boldsymbol{V}_{*e}\cdot\nabla T_e + p_e\nabla\cdot\left(\boldsymbol{V}_{\perp e} + \boldsymbol{V}_{\|e} \right) - \frac{5}{2}\frac{c}{e}\nabla\cdot p_e\left(\frac{\boldsymbol{b}}{B}\times\nabla T_e \right) +$$

$$-0.71 T_e\nabla_\| j_\| - \nabla\cdot\left(\chi_{\|e}\nabla_{\|T_e} \right) = 0, \tag{2.78}$$

$$\frac{3}{2}n\frac{dT_i}{dt} + T_i\left[n\cdot\nabla\left(\boldsymbol{V}_{E\times B} + \boldsymbol{V}_{\|e} \right) + \nabla\cdot\left(n\boldsymbol{V}_{*e} \right) \right] + \frac{5}{2}\frac{c}{e}p_i\left(\nabla\times\frac{\boldsymbol{b}}{B} \right)\cdot\nabla T_i = 0 \tag{2.79}$$

2.4 The GBS code

2.4.1 The GBS model

In order to express the system of Eqs. (2.74)-(2.79), summarized in Sec. 2.3.5, in an easy-to-handle form for numerical solution, we introduce some mathematical operators.

- Terms in the form $\nabla\cdot\left(n\boldsymbol{V}_{*e} \right)$ are developed as:

$$\nabla\cdot\left(n\boldsymbol{V}_{*e} \right) = -\frac{c}{e}\left(\nabla\times\frac{\boldsymbol{b}}{B} \right)\cdot\nabla p_e = -\frac{2c}{eB}C\left(p_e \right), \tag{2.80}$$

where C is the curvature operator, defined as:

$$C\left(f \right) = \frac{B}{2}\left(\nabla\times\frac{\boldsymbol{b}}{B} \right)\cdot\nabla f. \tag{2.81}$$

- Terms in the form $\nabla\cdot\left(n\boldsymbol{V}_{E\times B} \right)$ are developed as:

$$\nabla\cdot\left(n\boldsymbol{V}_{E\times B} \right) = c\nabla n\cdot\left(-\nabla\phi\times\frac{\boldsymbol{b}}{B} \right) + cn\nabla\cdot\left(\nabla\phi\times\frac{\boldsymbol{b}}{B} \right) = \frac{c}{B}\left[\phi, n \right] + \frac{2cn}{B}C\left(\phi \right), \tag{2.82}$$

where $\left[\phi, n \right]$ is the Poisson brackets operator, defined as:

$$\left[\phi, f \right] = \boldsymbol{b}\cdot\left(\nabla\phi\times\nabla f \right). \tag{2.83}$$

- Terms in the form $\nabla \cdot \left(n \boldsymbol{V}_{\parallel e} \right)$ are developed as:

$$\nabla \cdot \left(n \boldsymbol{V}_{\parallel e} \right) = \nabla n \cdot \boldsymbol{V}_{\parallel e} + n \nabla \cdot \boldsymbol{V}_{\parallel e} = n \nabla_{\parallel} V_{\parallel e} + V_{\parallel e} \nabla_{\parallel} n, \qquad (2.84)$$

where $\nabla \cdot \boldsymbol{b}$ has been neglected, *i.e.* finite aspect ratio effects are neglected, as in the reminder of the present work. The impact of finite aspect ratio effects on SOL turbulence has been the subject of one of our recent publications [46].

According to the operators previously introduced, Eqs. (2.74)-(2.79) can be written as:

$$\frac{\partial n}{\partial t} = -\frac{c}{B}[\phi, n] + \frac{2c}{eB}\Big[nC(T_e) + T_eC(n) - enC(\phi)\Big] +$$
$$-n\nabla_\parallel V_{\parallel e} - V_{\parallel e}\nabla_\parallel n + \mathcal{D}_n(n) + S_n, \tag{2.85}$$

$$\frac{\partial \omega}{\partial t} + \tau\frac{\partial \nabla_\perp^2 T_i}{\partial t} = -\frac{c}{B}[\phi, \omega] - \frac{c}{B}[\phi, \nabla_\perp^2 T_i] - V_{\parallel i}\nabla_\parallel \omega - V_{\parallel i}\nabla_\parallel \nabla_\perp^2 T_i +$$
$$+\frac{m_i\omega_{ci}^2}{e}\Bigg[\nabla_\parallel(V_{\parallel i} - V_{\parallel e}) + (V_{\parallel i} - V_{\parallel e})\frac{\nabla_\parallel n}{n}\Bigg] +$$
$$+\frac{2B}{cm_i}\Bigg[C(T_i) + \frac{T_i}{n}C(n) + C(T_e) + \frac{T_e}{n}C(n)\Bigg] +$$
$$+\frac{B}{3cm_in}C(G_i) + \mathcal{D}_\omega(\omega) + S_\omega, \tag{2.86}$$

$$m_en\frac{\partial V_{\parallel e}}{\partial t} + \frac{en}{c}\frac{\partial \psi}{\partial t} = -m_en\frac{c}{B}[\phi, V_{\parallel e}] - m_enV_{\parallel e}\nabla_\parallel V_{\parallel e} - \frac{2}{3}\nabla_\parallel G_e +$$
$$-\frac{e^2n^2}{\sigma_\parallel}(V_{\parallel e} - V_{\parallel i}) + en\nabla_\parallel\phi - T_e\nabla_\parallel n - 1.71n\nabla\|T_e + \mathcal{D}_{V_{\parallel e}}(V_{\parallel e}) + S_{V_{\parallel e}}, \tag{2.87}$$

$$m_in\frac{\partial V_{\parallel i}}{\partial t} = -m_in\frac{c}{B}[\phi, V_{\parallel i}] - m_inV_{\parallel i}\nabla_\parallel V_{\parallel i} - \frac{2}{3}\nabla_\parallel G_i +$$
$$-n\nabla_\parallel T_e - T_e\nabla_\parallel n - n\nabla_\parallel T_i - T_i\nabla_\parallel n + \mathcal{D}_{V_{\parallel i}}(V_{\parallel i}) + S_{V_{\parallel i}}, \tag{2.88}$$

$$\frac{\partial T_e}{\partial t} = -\frac{c}{B}[\phi, T_e] - V_{\parallel e}\nabla_\parallel T_e + \frac{4}{3}\frac{c}{eB}\Bigg[\frac{7}{2}T_eC(T_e) + \frac{T_e^2}{n}C(n) - eT_eC(\phi)\Bigg] +$$
$$+\frac{2}{3e}\Bigg\{T_e\Big[0.71\nabla_\parallel V_{\parallel i} - 1.71\nabla_\parallel V_{\parallel e}\Big] + 0.71T_e(V_{\parallel i} - V_{\parallel e})\frac{1}{n}\nabla_\parallel n\Bigg\} +$$
$$+\mathcal{D}_{T_e}(T_e) + \mathcal{D}_{T_e}^\parallel(T_e) + S_{T_e}, \tag{2.89}$$

$$\frac{\partial T_i}{\partial t} = -\frac{c}{B}[\phi, T_i] + \frac{4cT_i}{3eB}\Bigg[C(T_e) + \frac{T_e}{n}C(n)\Bigg] - \frac{4c}{3B}T_iC(\phi) +$$
$$+\frac{2}{3}\frac{T_i}{n}\left(V_{\parallel i} - V_{\parallel e}\right)\nabla_\parallel n - \frac{2}{3}T_i\nabla_\parallel V_{\parallel e} - V_{\parallel i}\cdot\nabla_\parallel T_i - \frac{10}{3}\frac{cT_i}{eB}C(T_i) +$$
$$+\mathcal{D}_{T_i}(T_i) + S_{T_i}, \tag{2.90}$$

which constitutes the system of equations solved by GBS. The gyroviscous term G_i can be written as (compare it with Eq. (2.53)):

$$G_i = -3\eta_{0i}\Bigg[\frac{2}{3}\nabla_\parallel V_{\parallel i} + \frac{1}{3}C(\phi) + \frac{c}{enB}C(p_i)\Bigg], \tag{2.91}$$

and similarly for G_e:

$$G_e = -3\eta_{0e}\Bigg[\frac{2}{3}\nabla_\parallel V_{\parallel e} + \frac{1}{3}C(\phi) - \frac{c}{enB}C(p_e)\Bigg]. \tag{2.92}$$

The diffusion operators, $\mathcal{D}$, have been introduced for numerical purpose. The diffusion coefficient $\mathcal{D}_{T_e}^{\parallel}$ is derived from the term $\nabla \cdot \left(\chi_{\parallel e} \nabla_{\parallel} T_e \right)$ in Eq. (2.78), supposing $\chi_{\parallel e}$ constant. The source terms are described in Sec. 2.4.5. Finally, Eqs. (2.85)-(2.90) are solved in a normalized form by GBS. More precisely, we normalize n to the reference density n_0, T_e to the reference temperature T_{e0}, T_i to the reference temperature T_{i0}, ϕ to T_{e0}/e, $V_{\parallel e}$ and $V_{\parallel i}$ to $c_{s0} = \sqrt{T_{e0}/m_i}$ (and therefore c_s to c_{s0}), ψ to $\beta c m_i c_{s0}/(2e)$ and time t to R/c_{s0}, where R is the major radius and $\beta = 8\pi n_0 T_{e0}/B^2$. Lengths in the perpendicular direction are adimensionalized to $\rho_{s0} = c_{s0}/\omega_i$ and in theparallel direction to R.

The system of Eqs. (2.85)-(2.90) in its adimensionalized form reads as:

$$\frac{\partial n}{\partial t} = -\frac{R}{B\rho_{s0}}[\phi, n] + \frac{2}{B}\Big[nC(T_e) + T_eC(n) - nC(\phi)\Big] +$$
$$-n\nabla_\parallel V_{\parallel e} - V_{\parallel e}\nabla_\parallel n + \mathcal{D}_n(n) + S_n, \tag{2.93}$$

$$\frac{\partial \omega}{\partial t} + \tau\frac{\partial \nabla_\perp^2 T_i}{\partial t} = -\frac{R}{B\rho_{s0}}[\phi, \omega] - \tau\frac{R}{B\rho_{s0}}[\phi, \nabla_\perp^2 T_i] - V_{\parallel i}\nabla_\parallel\omega - \tau V_{\parallel i}\nabla_\parallel\nabla_\perp^2 T_i +$$
$$+B^2\Big[\nabla_\parallel(V_{\parallel i} - V_{\parallel e}) + (V_{\parallel i} - V_{\parallel e})\frac{\nabla_\parallel n}{n}\Big] +$$
$$+2B\Big[\tau C(T_i) + \tau\frac{T_i}{n}C(n) + C(T_e) + \frac{T_e}{n}C(n)\Big] +$$
$$+\frac{B}{3n}C(G_i) + \mathcal{D}_\omega(\omega) + S_\omega, \tag{2.94}$$

$$\frac{\partial V_{\parallel e}}{\partial t} + \frac{m_i}{m_e}\frac{\beta}{2}\frac{\partial \psi}{\partial t} = -\frac{R}{B\rho_{s0}}[\phi, V_{\parallel e}] - V_{\parallel e}\nabla_\parallel V_{\parallel e} - \frac{m_i}{m_e}\frac{2}{3}\nabla_\parallel G_e +$$
$$-\frac{m_i}{m_e}\nu(V_{\parallel e} - V_{\parallel i}) + \frac{m_i}{m_e}\nabla_\parallel\phi - \frac{m_i}{m_e}\frac{T_e}{n}\nabla_\parallel n - 1.71\frac{m_i}{m_e}\nabla_\parallel T_e + \mathcal{D}_{V_{\parallel e}}(V_{\parallel e}) + S_{V_{\parallel e}}, \tag{2.95}$$

$$\frac{\partial V_{\parallel i}}{\partial t} = -\frac{R}{B\rho_{s0}}[\phi, V_{\parallel i}] - V_{\parallel i}\nabla_\parallel V_{\parallel i} - \frac{2}{3}\nabla_\parallel G_i +$$
$$-\nabla_\parallel T_e - T_e\frac{\nabla_\parallel n}{n} - \tau\nabla_\parallel T_i - \tau T_i\frac{\nabla_\parallel n}{n} + \mathcal{D}_{V_{\parallel i}}(V_{\parallel i}) + S_{V_{\parallel i}}, \tag{2.96}$$

$$\frac{\partial T_e}{\partial t} = -\frac{R}{B\rho_{s0}}[\phi, T_e] - V_{\parallel e}\nabla_\parallel T_e + \frac{4}{3}\frac{1}{B}\Big[\frac{7}{2}T_eC(T_e) + \frac{T_e^2}{n}C(n) - T_eC(\phi)\Big] +$$
$$+\frac{2}{3}\Big\{T_e\Big[0.71\nabla_\parallel V_{\parallel i} - 1.71\nabla_\parallel V_{\parallel e}\Big] + 0.71T_e(V_{\parallel i} - V_{\parallel e})\frac{\nabla_\parallel n}{n}\Big\} +$$
$$+\mathcal{D}_{T_e}(T_e) + \mathcal{D}_{T_e}^\parallel(T_e) + S_{T_e}, \tag{2.97}$$

$$\frac{\partial T_i}{\partial t} = -\frac{R}{B\rho_{s0}}[\phi, T_i] + \frac{4T_i}{3B}\Big[C(T_e) + \frac{T_e}{n}C(n)\Big] - \frac{4}{3B}T_iC(\phi) +$$
$$+\frac{2}{3}T_i\Big(V_{\parallel i} - V_{\parallel e}\Big)\frac{\nabla_\parallel n}{n} - \frac{2}{3}T_i\nabla_\parallel V_{\parallel e} - V_{\parallel i}\cdot\nabla_\parallel T_i - \tau\frac{10}{3B}T_iC(T_i) +$$
$$+\mathcal{D}_{T_i}(T_i) + S_{T_i}. \tag{2.98}$$

In Eqs. (2.93)-(2.98) we introduce the adimensionalized resistivity, $\nu = e^2 nR/\left(m_i\sigma_\parallel c_{s0}\right)$, and the ion to electron temperature ratio, $\tau = T_{i0}/T_{e0}$. We note that the curvature operator (see Eq. (2.81)), appearing in Eqs. (2.93)-(2.98), has been multiplied by R because of the adimensionalization, resulting in Eq. (2.100).

2.4.2 Geometry

The mathematical operators introduced in Sec. 2.4 have to be specified for the geometry of interest. For simplicity, we consider the system of Eqs. (2.93)-(2.98) in $s - \alpha$ circular geometry [47] with a toroidal limiter positioned on the high field side equatorial midplane of the device. In this geometry, operators are computed in the large aspect ratio limit $\epsilon = a/R \to 0$ (a is the tokamak minor radius). We use a right handed coordinate system $[y, x, z]$, where x is the flux coordinate and corresponds, in a circular magnetic flux surface configuration, to the radial direction, while y is the coordinate perpendicular to x and $\mathbf{B}$, see Fig. 2.1. In the $\epsilon \to 0$ limit, the plane (x, y) coincides with the poloidal plane and, as a consequence, $y = a\theta$, where $0 < \theta < 2\pi$ is the poloidal angle, with $\theta = 0$ and $\theta = 2\pi$ at the outer midplane; z is the direction parallel to the magnetic field, $0 < z < 2\pi q$, where $q = aB_\varphi/(RB_\theta)$ is the safety factor. Therefore, the Poisson brackets (defined in Eq. (2.83)), the curvature (defined in Eq. (2.81)), the Laplacian and the parallel derivative (defined in Eq. (2.65)) operators, reduce to:

$$[f, g] = \partial_y f \partial_x g - \partial_x f \partial_y g, \tag{2.99}$$

$$C(f) = \sin\theta \partial_x f + \cos\theta \partial_y f, \tag{2.100}$$

$$\nabla_\perp^2 f = \partial_x^2 f + \partial_y^2 f, \tag{2.101}$$

$$\nabla_\parallel f = \partial_z f + R\beta/2 [\psi, f]. \tag{2.102}$$

While convenient, the $[y, x, z]$ coordinate system has the disadvantage that, in the presence of magnetic shear, defined as $\hat{s} = (a/q) \, dq/dx$, the pitch of the field line varies radially. This cannot be easily handled by the numerical algorithm implemented in GBS. For this purpose the introduction of the magnetic shear in the GBS code is realized by means of a coordinate transformation:

$$\begin{aligned} x' &= x, \\ y' &= y\left(1 + \frac{x\hat{s}}{a}\right), \\ z' &= z. \end{aligned} \tag{2.103}$$

The derivative operators change consequently, taking the form:

$$\begin{aligned} \partial_x &= \partial_{x'} + \frac{y\hat{s}}{a}\partial_{y'}, \\ \partial_y &= \left(1 + \frac{x\hat{s}}{a}\right)\partial_{y'}, \\ \partial_z &= \partial_{z'}, \end{aligned} \tag{2.104}$$
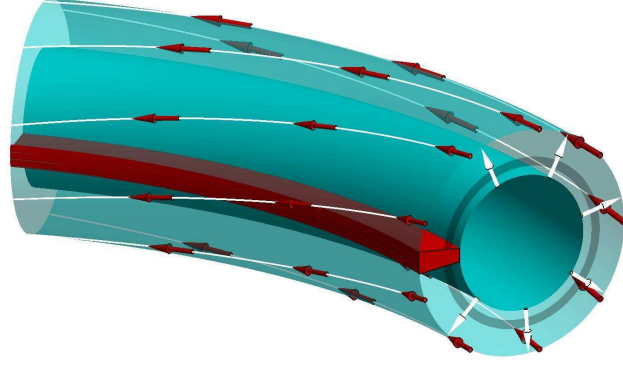
Figure 2.1: *Sketch of the SOL geometry considered in the present thesis. The magnetic field lines (in white) wrap around the torus in the direction indicated by the red arrows. The white arrows indicate the direction in which the plasma is perpendicularly transported from the core to the periphery of the device, by turbulent transport. The source is represented by the grey shaded surface.*

leading to the following expression of the Poisson brackets,

$$[f, g] = \left(1 + \frac{x'\hat{s}}{a}\right) [f, g]_{x', y'}, \tag{2.105}$$

of the curvature operator,

$$C(f) = \sin\theta \partial_{x'} f + \left[\sin\theta \frac{y'\hat{s}}{a + x'\hat{s}} + \cos\theta \left(1 + \frac{x'\hat{s}}{a}\right)\right] \partial_{y'} f, \tag{2.106}$$

and of the Laplacian in the perpendicular direction,

$$\nabla_\perp^2 f = \partial_{x'}^2 f + 2\frac{y'\hat{s}}{a + x'\hat{s}} \partial_{x', y'}^2 f + \left(\frac{y'\hat{s}}{a + x'\hat{s}}\right)^2 \partial_{y'}^2 f + \tag{2.107}$$
$$\left(1 + \frac{x'\hat{s}}{a}\right)^2 \partial_{y'}^2 f.$$

The previous expressions are further simplified according to the assumption $x'/a \ll 1$, *i.e.* for the SOL width much smaller than a. The Poisson brackets becomes therefore $[f, g] = \partial_{y'} f \partial_{x'} g - \partial_{x'} f \partial_{y'} g$, while the curvature operator and the Laplacian

operator in the perpendicular direction become:

$$C(f) = \sin\theta \partial_{x'} f + \left(\sin\theta \frac{y'\hat{s}}{a} + \cos\theta \right) \partial_{y'} f, \tag{2.108}$$

$$\nabla_{\perp}^2 f = \partial_{x'}^2 f + 2\frac{y'\hat{s}}{a}\partial_{x',y'}^2 f + \left[1 + \left(\frac{y'\hat{s}}{a} \right)^2 \right] \partial_{y'}^2 f. \tag{2.109}$$

A detailed derivation of the operators including finite aspect ratio effects can be found in Ref. [46] and a generalization to take into account plasma elongation and triangularity is being carried out.

2.4.3 Numerics

In GBS the domain is discretized along the x, y and z_φ direction, where z_φ is the coordinate along the toroidal direction, $0 < z_\varphi < 2\pi$. The grid points are defined as $x_i = (i - 1/2)\Delta x$, for $i = 0, \ldots, N_x + 1$, being the width of the interval $\Delta_x = L_x/N_x$. The $i = 0$ and the $i = N_x + 1$ points of the grid are the ghost cells. Similar definitions are valid for the y direction, $y_j = (j - 1/2)\Delta y$. In the toroidal direction the n, T_e, T_i, ϕ and ω variables are defined on $z_{\varphi,k} = k\Delta z_\varphi$, while $V_{\parallel e}$, $V_{\parallel i}$ and ψ are shifted by half a cell, $z_{\varphi,k} = (k - 1/2)\Delta z_\varphi$, $\Delta z_\varphi = 2\pi/N_{z_\varphi}$, $k = 0, \ldots, N_{z_\varphi} + 1$, due to numerical stability reasons. Each quantity $A(x,y,z)$ is then discretized as $A_{i,j,k} \equiv A(x_i, y_j, z_{\varphi,k})$. We can take advantage of the fact that turbulence is mostly aligned in the direction parallel to the field to reduce the computational cost of the simulations. For this purpose we choose N_y and N_{z_φ} in such a way that the discretization points fall on the field lines, *i.e.* we impose Δ_j to be an integer, where $\Delta_j = N_y/(N_{z_\varphi}q)$. This allows us to use a low resolution in the toroidal direction. The parallel derivative is then approximated as:

$$(\boldsymbol{b} \cdot \nabla) A|_{i,j,k} \simeq \frac{1}{2\Delta z_\varphi} \left(A_{i,j+\Delta j,k} - A_{i,j-\Delta j,k} \right). \tag{2.110}$$

The derivatives in the x and y directions are performed using a standard centered finite difference scheme, such as:

$$\left. \frac{\partial A}{\partial x} \right|_{i,j,k+1} \simeq \frac{A_{i+1,j,k} - A_{i-1,j,k-1}}{2\Delta x}, \tag{2.111}$$

except for the Poisson brackets, that are discretized according to the Arakawa scheme [48].

The Laplacian operator is discretized using a standard second order centered finite difference scheme. The obtained matrix can be solved either by matrix inversion, or it can be reduced to the solution of a set of tridiagonal systems, by applying the fast Fourier transform (FFT) algorithm in the x direction. The first

approach is applied for a simulation with magnetic shear, the second is suitable for a shearless simulation. The time stepping is realized with a standard fourth order Runge-Kutta scheme. Finally, we remark that Eqs. (2.93)-(2.98) are rewritten in terms of $\theta_n = \log n$, $t_e = \log T_e$, and $t_i = \log T_i$, to ensure the positivity of n, T_e, and T_i.

The GBS code is parallelized through a domain decomposition using standard MPI techniques. The parallelization is performed in the x and z_φ directions, along which the domain is partitioned in N_{px} and N_{pz_φ} parts, respectively. The total number of processors used to perform a simulation is therefore $N_p = N_{px}N_{pz_\varphi}$. An additional ghost cell along both the domain-decomposed directions has to be added. An array containing a physical quantity has therefore size $(N_x/N_{px} + 2) \times \left(N_{z_\varphi}/N_{pz_\varphi} + 2\right) \times N_y$ on each processor. A more detailed description of GBS numerics can be found in Ref. [20].

2.4.4 Boundary conditions at the magnetic presheath entrance

The boundary conditions for GBS, applied at the magnetic pre-sheath entrance, have been derived in the cold ion limit in Ref. [49]. In the following, we extend the study presented in Ref. [49] to the $T_i \neq 0$ case. The GBS code solves Eqs. (2.93)-(2.98) in a domain that is periodic in the toroidal direction, but that covers a finite extension in the radial and poloidal directions. Therefore, it has to be provided by a proper set of boundary conditions. In the poloidal direction, the plasma touches the conducting limiter and spontaneously generates a thin layer contiguous to the wall, the so-called sheath, where quasi-neutrality and the drift approximations are broken. Due to their higher mobility, electrons tend to reach the wall at a higher rate than ions. In order to prevent an electron loss to the wall larger than the ion loss, the plasma naturally builds up a potential drop between the bulk plasma and the wall. Consequently, an electric field in the direction perpendicular to the wall is generated on a ρ_s scale length, and, in closest proximity of the wall, on a λ_D length, accelerating the ions towards the wall and slowing the electrons. When the magnetic field is oblique with respect to an absorbing wall (which happens in most of the cases, since $B_\varphi \gg B_\theta$), three regions can be identified at the plasma-wall transition: the collisional presheath (CP), the magnetic presheath (MP), and the Debye sheath (DS). Although in all these three regions a potential drop proportional to T_e is observed, they are characterized by very different length scales. In the CP, whose size scales with the ion mean free path, λ_{mfp}, the ions are magnetized, *i.e.* they are accelerated towards the wall following the magnetic field lines, and the plasma is quasi-neutral. At the MP entrance the ions reach the sound speed. The width of the MP scales as ρ_s. In this region the plasma is still quasi-neutral, but the amplitude of the electric field increases to the point that ions are demagnetized and accelerated in the direction perpendicular to the wall. The DS scales as the Debye length, λ_D,
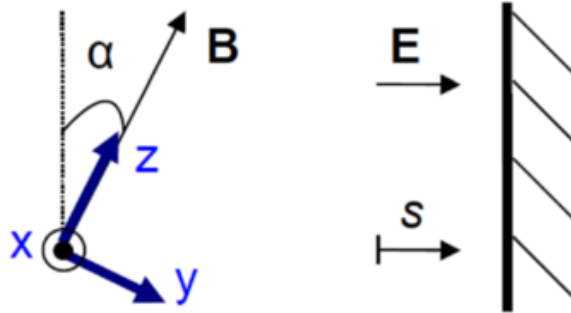
Figure 2.2: *Coordinate system used for the description of the plasma-wall transition. The magnetic field $\boldsymbol{B}$ impacts the wall at an angle α. The wall is represented on the right with the sheath electric field $\boldsymbol{E}$, along the normal direction s. Source: Ref. [49].*

being in this region quasi-neutrality violated. Plasma turbulence fluid codes, such as GBS, are based on both the quasi-neutrality and the ion drift approximations. Since quasi-neutrality is violated in the DS and the ion drift approximation loses its validity in the MP, the validity of the drift-reduced Braginskii equations stops at the MP entrance, where boundary conditions that properly describe the sheath physics have to be applied. In the following, in agreement with the hypothesis used in the derivation of the drift-reduced Braginskii equations, we neglect ion FLR effects. In particular, we assume that ions are lost to the wall when their gyrocenters are. We also assume that the ion distribution function remains Maxwellian throughout the plasma-wall transition.

The dynamics at the plasma-wall transition is described by using the same coordinate system (x, y, z) used in Ref. [49]: z is the direction along $\boldsymbol{B}$, x is perpendicular to $\boldsymbol{B}$ and parallel to the wall, and y is perpendicular to both x and z, pointing towards the wall. We also define the coordinate $s = y \cos\alpha + z \sin\alpha$, normal to the wall, being α the angle of incidence of the magnetic field to the wall (see Fig. 2.2). The magnetic field is assumed constant.

To describe the steady-state dynamics of the plasma in the CP we use the ion continuity, the parallel ion velocity, and the electron parallel velocity equations. We consider plasma gradients in the x direction with an ordering $\epsilon = \rho_s/L_n \sim \rho_s/L_T \sim \rho_s/L_\phi \ll 1$. The plasma dynamics is split into the directions parallel and perpendicular to the magnetic field (see Sec. 2.3). In the context of the ion drift approximation, the perpendicular velocity can be written as $\boldsymbol{V}_{\perp i} = \boldsymbol{V}_{E \times B} + \boldsymbol{V}_{*i} + \boldsymbol{V}_{pol}$, where the polarization drift contains first order corrections in $(1/\omega_i)d/dt$. The equations are adimensionalized as follows: electron temperature, $T_e \to T_e/T_{e0}$, electric potential, $\phi \to e\phi/T_{e0}$, space $x \to x/\rho_{s0}$, and velocities, $V \to V/c_{s0}$. The steady-state ion continuity equation reads as $\nabla \cdot (n\boldsymbol{V}_i) = S_{p,i}$, where $S_{p,i}$ represents the ion density source. In the evaluation of $\nabla \cdot (n\boldsymbol{V}_i) = S_{p,i}$, the perpendicular components of $\boldsymbol{V}_i$ ($V_{x,i}$ and $V_{y,i}$) are computed by neglecting $\boldsymbol{V}_{pol}$, as in Ref. [49],

therefore retaining only 0th order terms in $(1/\omega_i)d/dt$, and assuming $\partial_s T_i = 0$:

$$V_{x,i} = V_{x,Ei} + V_{x,*i} = -\partial_y \phi - \tau \frac{T_i}{n}\partial_y n, \qquad (2.112)$$

$$V_{y,i} = V_{y,Ei} + V_{y,*i} = \partial_x \phi + \tau \frac{T_i}{n}\partial_x n, \qquad (2.113)$$

The validity of the isothermal ion assumption as well as $\partial_s T_e = 0$, used later, are discussed in Appendix A. The first terms on the right hand side of Eqs. (2.112) and (2.113) represent the $\boldsymbol{E} \times \boldsymbol{B}$ drift contribution to the ion velocity, while the second terms are due to the diamagnetic drift. Using the relation $V_{s,i} = V_{\parallel,i}\sin\alpha + V_{y,i}\cos\alpha$, we obtain, for the ion continuity equation:

$$\nabla \cdot (n\mathbf{V}_i) =$$
$$n\partial_x V_{x,Ei} + n\cos\alpha\partial_s V_{y,Ei} + V_{s,i}\partial_s n - V_{y,*i}\cos\alpha\partial_s n + n\sin\alpha\partial_s V_{\parallel i} + V_{x,Ei}\partial_x n =$$
$$S_{p,i}. $$
$$(2.114)$$

The first and the second terms on the right hand side cancel out since $n\cos\alpha\partial_s V_{y,Ei} = n\cos\alpha\partial_s\partial_x\phi = -n\partial_x V_{x,Ei}$. The third and fourth terms are gathered together introducing $V'_{s,i} = V_{s,i} - V_{y,*i}\cos\alpha$. We remark that the diamagnetic contribution appearing in the fourth term cancels out with the identical term appearing in the definition of $V_{s,i}$, since the ion diamagnetic flux is divergence free, $i.e.$ $\nabla \cdot (n\boldsymbol{V}_{*i}) = 0$. For the sixth term we have $V_{x,Ei}\partial_x n = -\partial_x n\cos\alpha\partial_s\phi$. Accordingly, Eq. (2.114) is simplified as:

$$V'_{s,i}\partial_s n + n\sin\alpha\partial_s V_{\parallel,i} - \partial_x n\cos\alpha\partial_s\phi = S_{p,i}, \qquad (2.115)$$

which constitutes the form of the ion continuity equation that we consider for our analysis. The steady state ion momentum equation reads as:

$$n\left(\boldsymbol{V}_i \cdot \nabla\right)\boldsymbol{V}_i = n\mathbf{E} + n\mathbf{V}_i \times \mathbf{b} - \nabla p_i + \boldsymbol{S}_{m_i}, \qquad (2.116)$$

where $\boldsymbol{S}_{m_i}$ represents the ion momentum source. For sake of simplicity, we write the total derivative $d_t = \partial_t + (\boldsymbol{V}_{\parallel i} + \boldsymbol{V}_{E\times B}) \cdot \nabla$, by neglecting the polarization drift, since smaller than the other contributions. We note that the diamagnetic velocity does not appear in the convective derivative due to diamagnetic cancellation. The parallel component of Eq. (2.116) can be written therefore as:

$$n\left(V'_{si}\partial_s + V_{xi}\partial_x\right)V_{\parallel i} = -n\partial_s\phi\sin\alpha - \tau T_i\partial_s n\sin\alpha + S_{\parallel m_i}. \qquad (2.117)$$

Substituting Eq. (2.112) into Eq. (2.117), we find:

$$nV'_{si}\partial_s V_{\parallel i} + \sin\alpha\left(n\partial_s\phi + \tau T_i\partial_s n\right) - n\partial_x V_{\parallel i}\cos\alpha\partial_s\phi = S_{\parallel m_i}, \qquad (2.118)$$

where the third term represents the ion pressure contribution. Finally, the momen-

tum equation for the electrons reads as:

$$n \left(\boldsymbol{V}_e \cdot \nabla \right) \boldsymbol{V}_e = -\mu \left(n\boldsymbol{E} + n\boldsymbol{V}_e \times \boldsymbol{b} + \nabla p_e \right) + \boldsymbol{S}_{m_e}, \qquad (2.119)$$

where $\boldsymbol{S}_{m_e}$ is the electron momentum source, and $\mu = m_i/m_e$. Equation (2.119) is simplified assuming $\mu \gg 1$ and isothermal electrons in the CP, $i.e.$ $\partial_s T_e = 0$. The parallel component of Eq. (2.119) reads therefore as:

$$\mu \sin \alpha T_e \partial_s n - \mu \sin \alpha n \partial_s \phi = S_{\|m_e}. \qquad (2.120)$$

Equations. (2.115), (2.118), and (2.120) can be written in the form of a system of linear equations, $M\boldsymbol{X} = \boldsymbol{S}$, where $\boldsymbol{X} = \left[\partial_s n, \partial_s V_{\|i}, \partial_s \phi \right]$, $\boldsymbol{S} = \left[S_{p,i}, S_{\|m_i}, S_{\|m_e} \right]$, and:

$$M = \begin{pmatrix} V'_{si} & n \sin \alpha & -\partial_x n \cos \alpha \\ \sin \alpha \tau T_i & n V'_{si} & n \left(\sin \alpha - \partial_x V_{\|i} \cos \alpha \right) \\ \mu \sin \alpha T_e & 0 & -\mu n \sin \alpha \end{pmatrix}. \qquad (2.121)$$

In the $T_i = 0$ limit, we retrieve the system of equations reported in Eq. (11) of Ref. [49]. When T_i dynamics is included, a new term, due to the ion pressure, appears in Eq. (2.121) and $V_{s,i}$ is redefined as $V'_{s,i}$, to take into account the presence of the ion diamagnetic drift. Equations (2.115), (2.118), and (2.120) are valid in the CP, up to the MP entrance. In the CP the source terms are responsible for the small plasma gradients. Approaching the MP entrance, gradients become large, while the intensity of the source terms remains the same as in the main SOL plasma. Non-zero gradients in the MP exist therefore with negligible sources, leading to $M\boldsymbol{X} \simeq 0$ to define the location of the MP entrance. This condition requires that $\det M = 0$ is satisfied, resulting in:

$$V'_{s,i} = \sqrt{T_e} \sin \alpha \left[\theta_n + \sqrt{\left(1 + \tau \frac{T_i}{T_e} \right) + \theta_n^2 - \frac{\partial_x V_{\|i}}{\tan \alpha}} \right], \qquad (2.122)$$

in the case of the coordinate s increasing towards the wall, corresponding to the boundary condition at the upper side of the limiter plate in the GBS simulations, and where

$$\theta_n = \frac{\sqrt{T_e}}{2 \tan \alpha} \frac{\partial_x n}{n}, \qquad (2.123)$$

has been defined. Recalling $V_{s,i} = V_{\|,i} \sin \alpha + V_{y,i} \cos \alpha$ and $V_{y,i} \sim \mathrm{O}\left(\epsilon \right)$, from Eq. (2.122) we have $\partial_x V_{\|i} = \partial_x \sqrt{T_e} + \mathrm{O}\left(\epsilon^2 \right)$. We can therefore write Eq. (2.122) as:

$$V'_{s,i} = \sqrt{T_e} \sin \alpha \left[\theta_n + \sqrt{\left(1 + \tau \frac{T_i}{T_e} \right) + \theta_n^2 - \theta_T} \right], \qquad (2.124)$$

where

$$\theta_T = \frac{\sqrt{T_e}}{2\tan\alpha}\frac{\partial_x T_e}{T_e}. \qquad (2.125)$$

In the following, we neglect terms of order $O(\epsilon^2)$. By introducing $F_T = 1 + \tau T_i/T_e$, the condition for $V'_{s,i}$ becomes therefore:

$$V'_{s,i} = \sqrt{T_e}\sin\alpha\left(\theta_n + \sqrt{F_T} - \frac{1}{2\sqrt{F_T}}\theta_T\right), \qquad (2.126)$$

and the boundary conditions for $V_{\parallel i}$ are derived from Eq. (2.124), using the relation:

$$V_{\parallel i}\sin\alpha = V_{s,i} - V_{y,i}\cos\alpha. \qquad (2.127)$$

In the evaluation of $V_{\parallel i}$, we remark that the ion diamagnetic contributions in $V_{y,i}$ and in $V'_{s,i}$ cancel out, so that only $V_{y,Ei}$ appears in Eq. (2.128). The boundary condition for $V_{\parallel i}$ reads as:

$$V_{\parallel i} = \sqrt{T_e}\left(\theta_n + \sqrt{F_T} - \frac{1}{2\sqrt{F_T}}\theta_T - \frac{2\phi}{T_e}\theta_\phi\right), \qquad (2.128)$$

where

$$\theta_\phi = \frac{\sqrt{T_e}}{2\tan\alpha}\frac{\partial_x\phi}{\phi}, \qquad (2.129)$$

and, therefore, the fourth term in Eq. (2.128) is the contribution to $V_{\parallel i}$ of the $\boldsymbol{E}\times\boldsymbol{B}$ drift. The boundary conditions for the density n and the potential ϕ can be derived by solving for $\det M = 0$, the linear system of equations $M\boldsymbol{X} = 0$, obtaining:

$$\partial_s n = \frac{n}{T_e}\partial_s\phi, \qquad (2.130)$$

and

$$\partial_s\phi = -\frac{V'_{s,i}\partial_s V_{\parallel i}}{\sin\alpha F_T - \cos\alpha\partial_x V_{\parallel i}}. \qquad (2.131)$$

Keeping only first order terms in ϵ, Eq. (2.130) and Eq. (2.131) can be written as:

$$\partial_s n = -\frac{n}{\sqrt{T_e}}\left(\frac{1}{\sqrt{F_T}} + \frac{\theta_n}{F_T} + \frac{\theta_T}{2F_T^{3/2}}\right)\partial_s V_{\parallel i},$$

$$\partial_s\phi = -\sqrt{T_e}\left(\frac{1}{\sqrt{F_T}} + \frac{\theta_n}{F_T} + \frac{\theta_T}{2F_T^{3/2}}\right)\partial_s V_{\parallel i}. \qquad (2.132)$$

For what concerns the boundary condition for the vorticity, this is derived from the

boundary condition for ϕ:

$$\omega = \nabla_\perp^2 \left(\phi + \tau T_i\right) = \partial_y^2 \phi + \partial_x^2 \phi = \partial_y^2 \phi + \mathrm{O}(\epsilon^2), \qquad (2.133)$$

where ϵ^2 terms are neglected, as well as $\partial_s T_i$. Moreover, we can use $\partial_y^2 \phi = \cos^2 \alpha \partial_s^2 \phi$, where we estimate $\partial_s^2 \phi$ at the MP entrance deriving Eq. (2.131) with respect to s. Finally, neglecting second order terms in ϵ, and substituting $V'_{s,i}$ with its expression in Eq. (2.126), we obtain:

$$\omega = -\cos^2 \alpha \left[\left(\frac{1}{F_T} + \frac{1}{F_T^2}\theta_T\right) \left(\partial_s V_{\|i}\right)^2 + \partial_s^2 V_{\|i} \sqrt{T_e} \left(\frac{1}{\sqrt{F_T}} + \frac{\theta_n}{F_T} + \frac{\theta_T}{2F_T^{3/2}}\right) \right]. \qquad (2.134)$$

The $V_{\|e}$ boundary condition is derived by using a detailed kinetic treatment of the electron dynamics in the sheath region, including gradients in the x direction, (see Ref. [49] and references therein) and reads as:

$$V_{\|e} = \sqrt{T_e} \left(\pm \exp\left(\Lambda - \eta_m\right) - \frac{2\phi}{T_e}\theta_\phi + 2\left(\theta_n + \theta_T\right) \right), \qquad (2.135)$$

where $\eta_m = \left(\phi_{MPE} - \phi_{wall}\right)/T_e$, being $\phi_{MPE} - \phi_{wall}$ the potential drop between the MP entrance and the wall, and $\Lambda = \log\sqrt{\mu/2\pi}$. Equation (2.135) is valid in the limit $\rho_e \ll \lambda_D$, i.e. when electrons are magnetized all the way to the wall. The case $\rho_e \gtrsim \lambda_D$ leads to complex electron trajectories in the DS, preventing us from obtaining a simple expression of the $V_{\|e}$ boundary conditions, such as the one in Eq. (2.135).

To summarize, the set of boundary conditions at the magnetic presheath entrance, generalized to the case of hot ions, are:

$$V_{\|i} = \sqrt{T_e} \left(\theta_n \pm \sqrt{F_T} \mp \frac{1}{2\sqrt{F_T}}\theta_T - \frac{2\phi}{T_e}\theta_\phi \right), \qquad (2.136)$$

$$V_{\|e} = \sqrt{T_e} \left(\pm \exp\left(\Lambda - \eta_m\right) - \frac{2\phi}{T_e}\theta_\phi + 2\left(\theta_n + \theta_T\right) \right), \qquad (2.137)$$

$$\partial_s n = -\frac{n}{\sqrt{T_e}} \left(\pm\frac{1}{\sqrt{F_T}} + \frac{\theta_n}{F_T} \pm \frac{\theta_T}{2F_T^{3/2}} \right) \partial_s V_{\|i}, \qquad (2.138)$$

$$\partial_s \phi = -\sqrt{T_e} \left(\pm\frac{1}{\sqrt{F_T}} + \frac{\theta_n}{F_T} \pm \frac{\theta_T}{2F_T^{3/2}} \right) \partial_s V_{\|i}, \qquad (2.139)$$

$$\partial_s T_e = 0, \qquad (2.140)$$

$$\partial_s T_i = 0, \qquad (2.141)$$

$$\omega = -\cos^2 \alpha \left[\left(\frac{1}{F_T} + \frac{1}{F_T^2}\theta_T\right) \left(\partial_s V_{\|i}\right)^2 + \partial_s^2 V_{\|i} \sqrt{T_e} \left(\pm\frac{1}{\sqrt{F_T}} + \frac{\theta_n}{F_T} \pm \frac{\theta_T}{2F_T^{3/2}} \right) \right], \qquad (2.142)$$

where the upper signs are for the case when the coordinate s increases towards the wall and the lower signs are for the opposite case, corresponding to the upper and the lower side of the limiter for GBS simulations, respectively. In the $\tau = 0$ limit, we retrieve Eqs. 33-38 of Ref. [49].

The calculation of the $\partial_s T_e, \partial_s T_i \neq 0$ effects on the GBS boundary conditions is presented in Appendix A.

In the radial direction the SOL boundaries correspond to the tokamak vessel wall and to the separatrix. Since most of the particles are lost at the limiter plates, preventing them from reaching the vessel wall because of cross-field transport, the conditions applied to the outer edge of the simulation domain do not significantly impact the turbulence. Ad-hoc boundary conditions are therefore applied at this location. On the other hand, at the separatrix, the hot plasma reaches the SOL from the core. In GBS a particle and heat source mimic the plasma outflow from the core (see Fig. 2.1 and a more detailed description in Sec. 2.4.5). This source is located at a finite distance from the inner boundary of the domain. The region of the domain between the source and the inner boundary acts as a buffer region and it has not to be taken into account for turbulence analysis. Therefore, also in this case, ad hoc boundary conditions (Dirichlet or Neumann boundary conditions can be chosen) can be used as the impact on turbulence properties is not significant.

2.4.5 Initial conditions and sources

In GBS simulations n, T_e, T_i, ϕ, and ω are initialized as $f(t_0) = f_0 + \tilde{f}(x, y, z)$, where f_0 is a constant value and $\tilde{f}$ is a fluctuation randomly generated. For $V_{\|e}$ and $V_{\|i}$ a profile that varies linearly from $-c_s$ to c_s, going from one side of the limiter to the other side, is used, instead. The source term for the field $f = n, T_e, T_i$ is defined as

$$S_f = A_f \exp\left\{ - \left[(x - x_s)^2 / \sigma_s^2 \right] \right\}, \tag{2.143}$$

where x_s represents the radial position of the source, A_f its strength, and σ_s its width. Typically $A_f = 1$ $x_s = 30$, and $\sigma_s = 2.5$. We note that this corresponds to a poloidally symmetric source, and it implies that no ionisation process takes place in the SOL. As a matter of fact, transport in the tokamak edge is expected to be larger on the low-field side with respect to the high-field side, which corresponds to a non-poloidally symmetric plasma source. To test the importance of a non-poloidally symmetric source, we also performed simulations with a source localized on the low-field side and we compared it with a simulation carried out with a poloidally symmetric source. In the cases analyzed, the two scenarios resulted in a similar pressure profile and similar turbulence properties. Therefore, the results presented in the present thesis should not depend on the details of the source used.

The sources inject particle and heat in the domain, building up a pressure gradient, until an instability is triggered and turbulence sets in. Turbulence drives

transport, also through plasma coherent structures that move in the radial direction and stream along the field lines until they are lost on the limiter plates or at the vessel walls. After a transient, a quasi-stationary phase is reached, during which there is a quasi-stationary balance between injected plasma, turbulent transport, and losses. Our analysis is typically focused on this quasi-stationary phase.

2.5 The linearized drift-reduced Braginskii equations and the linear solver

The set of Eqs. (2.93)-(2.98) is linearized assuming that the equilibrium n and T can be described as $f = f_{00}\left(1 + x/L_f\right)$, where f_{00} represents the equilibrium value. All the other equilibrium fields vanish. For the perturbed quantities, the set of linearized equations that we consider are:

$$\frac{1}{n_{00}T_{e00}}\frac{\partial n}{\partial t} = \frac{R}{L_n}\frac{1}{T_{e00}}\frac{\partial \phi}{\partial y} + \frac{2}{BT_{e00}}\hat{C}\left(T_e\right) + \frac{2}{Bn_{00}}\hat{C}\left(n\right) - \frac{2}{BT_{e00}}\hat{C}\left(\phi\right) - \frac{1}{T_{e00}}\nabla_{\parallel}V_{\parallel e}$$
(2.144)

$$\frac{\partial\left(\nabla_{\perp}^2\phi + \tau\nabla_{\perp}^2 T_i\right)}{\partial t} = 2B\left[\hat{C}(T_e) + \frac{T_{e00}}{n_{00}}\hat{C}(n)\right] + 2B\tau\left[\hat{C}(T_i) + \frac{T_{i00}}{n_{00}}\hat{C}(n)\right] +$$
$$+ \frac{B^2}{T_{e00}}\left(\nabla_{\parallel}V_{\parallel i} - \nabla_{\parallel}V_{\parallel e}\right)$$
(2.145)

$$\frac{\partial\left[V_{\parallel e} + (m_i\beta)/(2m_e)\psi\right]}{\partial t}\frac{1}{T_{e00}} = -\frac{m_i}{m_e}\frac{1}{n_{00}}\nabla_{\parallel}n + \frac{m_i}{m_e}\frac{1}{T_{e00}}\nabla_{\parallel}\phi - 1.71\frac{m_i}{m_e}\frac{1}{T_{e00}}\nabla_{\parallel}T_e +$$
$$+ \frac{m_i}{m_e}\nu\frac{1}{T_{e00}}\left(V_{\parallel i} - V_{\parallel e}\right)$$
(2.146)

$$\frac{\partial V_{\parallel i}}{\partial t} = -\frac{T_{e00}}{n_{00}}\nabla_{\parallel}n - \nabla_{\parallel}T_e - \tau\left(\frac{T_{i00}}{n_{00}}\nabla_{\parallel}n + \nabla_{\parallel}T_i\right)$$
(2.147)

$$\frac{\partial T_e}{\partial t}\frac{1}{T_{e00}} = \frac{R}{L_{Te}}\frac{\partial \phi}{\partial y} + \frac{4}{3B}\left[\frac{7}{2}\hat{C}(T_e) + \frac{T_{e00}}{n_{00}}\hat{C}(n) - \hat{C}(\phi)\right] +$$
$$+ \frac{2}{3}0.71\left(\nabla_{\parallel}V_{\parallel i} - \nabla_{\parallel}V_{\parallel e}\right) - \frac{2}{3}\nabla_{\parallel}V_{\parallel e}$$
(2.148)

$$\frac{\partial T_i}{\partial t}\frac{1}{T_{i00}} = \frac{R}{L_{Ti}}\frac{\partial \phi}{\partial y} + \frac{4}{3B}\hat{C}(T_e) + \frac{4}{3B}\frac{T_{e00}}{n_{00}}\hat{C}(n) - \frac{4}{3B}\hat{C}(\phi) - \frac{2}{3}\nabla_{\parallel}V_{\parallel e} - \frac{10}{3B}\tau\hat{C}(T_i).$$
(2.149)

According to non-local, linear studies of curvature driven modes and drift waves (see Refs. [50,36]), the scale length of the turbulence in the radial direction is larger than in the poloidal direction, i.e. $k_y/k_x \sim \sqrt{k_x L_p} \gg 1$. Therefore, we ignore the radial mode dependence and assume $k_y \gg k_x$. As a consequence, the curvature

operator is defined as:

$$\hat{C} = \left[\cos\frac{y}{a} + \frac{y}{a}\hat{s}\sin\frac{y}{a}\right]\partial_y, \tag{2.150}$$

and the Laplacian operator as:

$$\nabla_\perp^2 = \left[1 + \left(\frac{y}{a}\hat{s}\right)^2\right]\partial_y^2. \tag{2.151}$$

In general, the perturbed quantities can be written in the form $f_n(y, z, t) = f_n(y)\exp(inz_\varphi + \gamma t)$, where n is the toroidal mode number, γ is the linear growth rate of the mode, and z_φ is the toroidal angle. This allows to reduce Eqs. (2.144)-(2.149) to a one-dimensional eigenvalue problem in the y direction for γ, as the parallel derivative can be evaluated as a combination of the poloidal derivative and the toroidal mode number, as $\nabla_\parallel f_n = [(a/q)\partial_y f_n + inf_n]\exp(inz_\varphi + \gamma t)$.

We have developed a toroidal modes decomposition code that solves the resulting eigenvalue problem. We discretize $y = [0, L_y]$ with N_y points, $y_1, \cdots, y_i, \cdots, y_{N_y}$, with $y_i = (i-1)L_y/(N_y - 1)$ and we evaluate n, ϕ, T_e and T_i at these points. The quantities ψ and $V_{\parallel i}$ are evaluated on $N_y - 1$ points, $y_1, \cdots, y_i, \cdots, y_{N_y-1}$, with $y_i = (i - 1/2)L_y/(N_y - 1)$ for ψ and $V_{\parallel i}$. We denote the grid on which we evaluate n, ϕ, T_e and T_i as the unshifted grid, while the grid for ψ and $V_{\parallel i}$ is referred to as the shifted grid. We also denote $\Delta_y = L_y/(N_y - 1)$. We introduce the vector $\boldsymbol{x} = [n_1, \cdots, n_{N_y}, \phi_1, \cdots, \phi_{N_y}, \psi_1, \cdots, \psi_{N_y-1}, V_{\parallel i,1}, \cdots, V_{\parallel i,N_y-1}, T_{e,1}, \cdots, T_{e,N_y}, T_{i,1}, \cdots, T_{i,N_y}]$, and rewrite Eqs. (2.144)-(2.149) as:

$$L\frac{\partial}{\partial t}\boldsymbol{x} = M\boldsymbol{x}, \tag{2.152}$$

where:

$$L = \begin{pmatrix} U_u & Z_{u,u} & Z_{s,u} & Z_{s,u} & Z_{u,u} & Z_{u,u} \\ Z_{u,u} & D_{u,u}^{y,2} & Z_{s,u} & Z_{s,u} & Z_{u,u} & \tau D_{u,u}^{y,2} \\ Z_{u,s} & Z_{u,s} & -m_e/m_i D_{s,s}^{y,2} - \beta/2 & Z_{s,s} & Z_{u,s} & Z_{u,s} \\ Z_{u,s} & Z_{u,s} & Z_{s,s} & U_s & Z_{u,s} & Z_{u,s} \\ Z_{u,u} & Z_{u,u} & Z_{s,u} & Z_{s,u} & U_u & Z_{u,u} \\ Z_{u,u} & Z_{u,u} & Z_{s,u} & Z_{s,u} & Z_{u,u} & U_u \end{pmatrix}, \tag{2.153}$$

and

$$M = \begin{pmatrix} 2C_{u,u} & R/L_n D_{u,u}^{y,1}+ & D_{s,u}^{z,1}D_{s,u}^{y,2} & -D_{s,u}^{z,1} & 2C_{u,u} & Z_{u,u} \\ & -2C_{u,u} & & & & \\ 2C_{u,u} & Z_{u,u} & D_{s,u}^{z,1}D_{s,u}^{y,2} & Z_{s,u} & 2C_{u,u} & \tau 2C_{u,u} \\ -D_{u,s}^{z,1} & D_{u,s}^{z,1} & \nu D_{s,s}^{y,2}+ & Z_{s,s} & -1.71D_{u,s}^{z,1} & Z_{u,s} \\ & & +\left[(1+1.71\eta_e)\beta/2R/L_n\right]D_{s,s}^{y,2} & & & \\ -D_{u,s}^{z,1} & Z_{u,s} & \left[(1+\eta_e)\beta/2R/L_n\right]D_{s,s}^{y,2}+ & Z_{s,s} & -D_{u,s}^{z,1} & -\tau D_{u,s}^{z,1} \\ & & +\left[\tau(1+\eta_i)\beta/2R/L_n\right]D_{s,s}^{y,2} & & & \\ 4/3C_{u,u} & R/L_n\eta_e D_{u,u}^{y,1}+ & 2/3\,1.71D_{s,u}^{z,1} & -2/3D_{s,u}^{z,1} & 14/3C_{u,u} & Z_{u,u} \\ & -4/3C_{u,u} & & & & \\ 4/3C_{u,u} & R/L_n\eta_i D_{u,u}^{y,1}+ & 2/3D_{s,u}^{z,1} & -2/3D_{s,u}^{z,1} & 4/3C_{u,u} & -10/3C_{u,u} \\ & -4/3C_{u,u} & & & & \end{pmatrix}.$$

(2.154)

We note that U is the identity matrix, Z is the empty matrix, while the D matrices are discretized differential operators for which the first superscript indicates the variable with respect to which the derivative is calculated, the second superscript indicates the order of the derivative. For every matrix the first subscript indicates the shifted (s) or unshifted (u) grid on which the operator is acting, the second subscript indicates the grid type or the resulting variable. Both $D_{u,u}$ and $D_{s,s}$ are square matrices, the first with $N_y \times N_y$ dimensions and the second with $(N_y - 1) \times (N_y - 1)$ dimensions. The generic differential operators are written as:

$$D^{k,p}B_i = \left.\frac{\partial^k B}{\partial y^k}\right|_{y=y_i} \simeq \frac{1}{(\Delta y)^k} \sum_{n=-p/2}^{p/2} A_n^{k,p} B_{i+n},$$

(2.155)

where p is the accuracy order of the scheme. Coefficients for $D_{u,u}$ and $D_{s,s}$ are similar. Coefficients A_k^n are obtained by Taylor expanding $B_{i+n} = B(y_{i+n})$ around y_i. Coefficients for $D_{u,s}$ and $D_{s,u}$ are obtained in a similar way by replacing i by $i + 1/2$. The C matrix is the curvature operator, constructed by combining the appropriate differential operators defined above, according to Eq. (2.150). We remark that the parallel derivative is calculated as $\partial_z f_n = a/q\partial_y f_n + inf_n$.

The eigenvalue problem is solved using three different approaches. The first one is the direct solution of the problem associated to Eq. (2.152), providing the whole spectrum of eigenmodes and eigenvalues of the system. This was accomplished by using the LAPACK library [51]. The second method is an iterative solver that integrate the time evolution of the system (2.152) by discretizing it with an implicit scheme in the form:

$$\frac{\boldsymbol{x}_{t+\Delta t} - \boldsymbol{x}_t}{\Delta t} = (1-\Theta)L^{-1}M\boldsymbol{x}_t + \Theta L^{-1}M\boldsymbol{x}_{t+\Delta t},$$

(2.156)

where the choice of $\Theta = 0$ leads to a fully explicit scheme, while $\Theta \neq 0$ leads to an implicit scheme. The growth rate is calculated by comparing the solution at two different time steps. The third approach is based on considering the time evolution

of the system (2.152) and evaluating the exponential of the matrix $L^{-1}M\Delta t$, having fixed a desired time step Δt. The employed method is the Padé approximation described in Ref. [52]. The growth rate can be calculated comparing the solution at two different time steps. The calculation of the exponential matrix is costly, but the successive iterations are extremely fast. The iterative solver is usually faster than the other two methods. We have verified that the three methods, applied to the same set of parameters, give similar results. For the linear global calculations presented in the present thesis we use the spectral solver with a fourth order finite difference scheme.

The linear problem can also be solved by a field line following approach. In this case each perturbed quantity is Fourier decomposed in the y direction: $f(y, z, t) \propto \exp(ik_y y + \gamma t)$. The ∂_y operator is substituted by ik_y and the parallel derivative is calculated directly on the discretized parallel direction z with a finite difference scheme. Within this approach, the Laplacian operator is:

$$\nabla_\perp^2 = -k_\perp^2 = -k_y^2 \left[1 + \left(\frac{z}{q} \hat{s} \right)^2 \right], \tag{2.157}$$

and the curvature operator is defined as $\hat{C} = ik_y C$, where $C = \cos(z/q) + (z/q)\,\hat{s}\sin(z/q)$.

Chapter 3

Linear modes in the tokamak SOL

3.1 Introduction

Ballooning modes (BM) and drift waves (DW) are thought to be the instabilities that play the major role in the edge and SOL dynamics. The linear and non-linear properties of BM and DW have been studied extensively (see, for example, Refs. [11,26,22,6,53,54,55,56,57,58,59,60,61,25,39,40,62,63,64,65,66]). Ballooning modes are driven unstable in the bad curvature region [53,54,55,56,57,58], in the presence of resistivity or finite electron mass, or, in their absence, if the plasma β is sufficiently high. Drift waves, on the other hand, arise from $\boldsymbol{E} \times \boldsymbol{B}$ convection of the electron density profile, and they become destabilized in the presence of a non-adiabatic electron response, due to, *e.g.*, resistivity or finite electron mass [62,63,64,65,66].

In agreement with experimental results, past studies carried out with low-frequency non-linear electromagnetic models (both fluid and gyro-fluid) have showed that DW and BM instabilities determine the plasma turbulent dynamics [67, 11, 26, 22, 6], without, however, clarifying their relative importance, and non-linear simulations of edge and SOL turbulent dynamics have addressed both instabilities. The SOL region, in particular, is characterized by a wide range of density gradients and resistivities [68, 69, 70, 71, 67, 72, 73, 74, 75], allowing the interplay between $\boldsymbol{E} \times \boldsymbol{B}$ convection and curvature effects to change considerably, depending on the plasma scenario.

The present chapter constitutes a first step in the understanding of the relative importance of DW and BM, and of their branches, by defining the linear-mode regimes in the SOL parameter space, *i.e.* pointing out the fastest growing linear instability once the parameters that characterize a SOL scenario are given, in particular the SOL plasma width. Leveraging the study presented here, in Chap. 4 we study the turbulent regimes, *i.e.* we identify the linear instability driving non-linear transport, considering a plasma gradient that is not fixed a priori, but it is

the self-consistent result of the interplay between turbulent transport and plasma losses at the vessel wall. It is noted that modes other than BM and DW could become unstable in the edge and SOL regions of tokamak plasmas. Among those, we mention peeling-ballooning modes, external kinks, and sheath modes [76, 77, 78], while trapped electron modes are stable in the SOL due to the fact that the bounce frequency of trapped electrons is smaller than the collision frequency. To start with a relatively simple system, we consider the cold-ion regime, therefore ion temperature gradient modes [6, 60] are excluded. The description of these modes, and, in general, the role of finite ion temperature will be the subject of Chap. 5.

Our study provides a simple way of identifying the underlying instabilities for a given set of parameters, a starting point for the interpretation of non-linear simulations. Our stability study is based on a linearization of the drift-reduced Braginskii fluid equations described in Chap. 2, in $s - \alpha$ geometry, in the cold ion limit, with a toroidal limiter placed on the tokamak high-field side. The relative simplicity of the model chosen allows to capture the fundamental properties of both BM and DW by retaining density and temperature gradients, magnetic field curvature, magnetic shear, resistivity, electron inertia, and finite β effects. Within this linear fluid framework, we remark that the main parameters characterizing the SOL are: the typical gradient scale length, L_n, the ratio between the density and the electron temperature gradient length, $\eta_e = L_n/L_{T_e}$, the plasma β, the parallel resistivity, ν, the magnetic shear, $\hat{s}$, the tokamak major and minor radii, R and a, and the safety factor q.

The chapter is organized as follows: in Sec. 3.2 we present the main characteristics of BM and DW. Sec. 3.3 is focused on the transition among the different instabilities, in order to define the linear-mode regimes in the SOL parameter space, while Sec. 3.4 demonstrates how our analysis can be used to interpret the results of SOL studies. Finally, we draw our conclusions in Sec. 3.5. The study presented in this chapter has been the subject of a recent publication [79].

3.2   The linear SOL instabilities

To study the plasma instabilities present in the SOL, we consider the drift-reduced linearized Braginskii equations, in the cold ion limit:

$$\frac{\partial n}{\partial t} = \frac{R}{L_n}\frac{\partial \phi}{\partial y} + 2\hat{C}\left(T_e + n - \phi\right) + \nabla_\parallel \nabla_\perp^2 \psi - \nabla_\parallel V_{\parallel i},$$

$$\frac{\partial \nabla_\perp^2 \phi}{\partial t} = 2\hat{C}\left(n + T_e\right) + \nabla_\parallel \nabla_\perp^2 \psi,$$

$$\frac{\partial \psi}{\partial t}\frac{\beta}{2} - \frac{m_e}{m_i}\frac{\partial}{\partial t}\nabla_\perp^2 \psi = \nu\nabla_\perp^2 \psi + \nabla_\parallel\left(\phi - n - 1.71T_e\right) + (1 + 1.71\eta_e)\frac{\beta}{2}\frac{R}{L_n}\nabla_\perp^2 \psi,$$

$$\frac{\partial T_e}{\partial t} = \eta_e\frac{R}{L_n}\frac{\partial \phi}{\partial y} + \frac{2}{3}2\hat{C}\left(\frac{7}{2}T_e + n - \phi\right) + \frac{2}{3}1.71\nabla_\parallel\nabla_\perp^2 \psi - \frac{2}{3}\nabla_\parallel V_{\parallel i},$$

$$\frac{\partial V_{\parallel i}}{\partial t} = -\nabla_\parallel\left(n + T_e\right) + \frac{\beta}{2}\frac{R}{L_n}\left(1 + \eta_e\right)\nabla_\perp^2 \psi,$$

(3.1)

where we have used $V_{\parallel e} = -\nabla^2\psi$. A number of instabilities are described by the system of Eqs. (3.1). In the following two sections, Sec. 3.2.1 and 3.2.2, we concentrate our attention on the BM and DW.

Ballooning modes are interchange-like modes driven by the curvature of the magnetic field lines and plasma pressure gradient, unstable in the presence of collisions or finite electron mass, or, in their absence, if the plasma β is sufficiently high to allow magnetic field lines bending. A simple explanation of the mechanism leading to the ballooning mode instability can be found in Ref. [6]. We can split the electron diamagnetic drift defined by Eq. (2.50) in two contributions:

$$\boldsymbol{V}_{*e} = +\frac{c}{en}\nabla \times \frac{p_e\boldsymbol{b}}{B} - 2\frac{cT_e}{eB}\boldsymbol{b} \times \boldsymbol{\kappa}, \tag{3.2}$$

where we have used the identity $\nabla \times (\boldsymbol{b}/B) = 2/B\left(\boldsymbol{b} \times \boldsymbol{\kappa}\right)$ [6]. Since the diamagnetic velocity appears in terms of the form $\nabla \cdot (n\boldsymbol{V}_{*e})$ in the continuity equation, the first term on the right hand side of Eq. (3.2) does not contribute to the first equation of the system of Eqs. (3.1). The second term leads to a drift in the direction perpendicular to both $\boldsymbol{b}$ and $\boldsymbol{\kappa}$, which is responsible for the ballooning instability on the low field side of a tokamak (see Fig. 3.1 from Ref. [6]). On the left of the figure the plasma is more dense, leading to a density gradient pointing to the left. The magnetic field points towards the figure, generating a diamagnetic drift shifting the electrons downwards. In presence of a small density perturbation (represented by the waves), a charge separation is generated, resulting in an electric field. The electric field is in turn responsible for the appearance of an $\boldsymbol{E} \times \boldsymbol{B}$ drift that amplifies the original density perturbation, leading to an instability. The opposite situation at the high field side of the torus, where $\boldsymbol{\kappa}$ and ∇n point into opposite directions is, instead, stable, because the initial density perturbation is damped by the particle flow due to the generated $\boldsymbol{E} \times \boldsymbol{B}$ drift. It is clear from
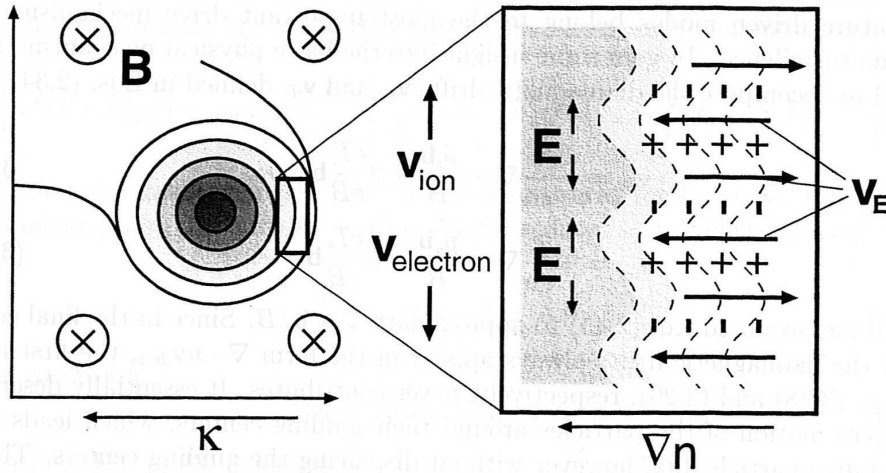
Figure 3.1: *Rosenbluth-Longmire picture of curvature driven instabilities. The initial density perturbation results in a charge separation due to the diamagnetic drifts. This leads to the generation of an electric field, that in turn creates a $E \times B$ drift that amplifies the original perturbation. Source: Ref. [6].*

this picture that the instability requires a non-vanishing phase shift between the density and the potential perturbations. For the shift to exist, the adiabaticity has to be broken by finite resistivity, finite electron mass, or electromagnetic effects, giving rise to resistive ballooning modes (RBM), inertial ballooning modes (InBM), or ideal ballooning modes (IdBM). A similar scenario describes the rising of temperature driven instabilites, but the density is replaced by the temperature. A more complete description of the ion temperature gradient mode will be given in Chap. 5.

The DW instability is caused by $E \times B$ convection of the plasma pressure accompanied by the breaking of the electron adiabaticity in Ohm's law, which is due to resistivity or finite electron mass [39,40]. A simple picture of the mechanism driving the DW instability is described in Ref. [80]. In Fig. 3.2 we consider a plasma with a density gradient pointing downwards. In presence of a density perturbation, if we assume a plasma close to adiabaticity, zones of high density correspond to zone of high electric potential and viceversa. The modulation of the electric potential causes the rise of an electric field and, consequently, of an $E \times B$ drift. The $E \times B$ velocity, in presence of the density gradient, convects high density plasma to the left of density peak in the perturbation and low density plasma to the right of the density peak, generating a propagation of the density perturbation to the left, in the same direction of the electron diamagnetic velocity. In the presence of finite resistivity or finite electron mass the DW is destabilized, giving rise to the resistive drift wave (RDW) or the inertial drift wave (InDW). Electromagnetic effects stabilize the DW instability, as shown in Sec. 3.3.5. For DW typically $\gamma \sim \omega_*$, $k_y \sim 1$, while $k_\parallel$ takes
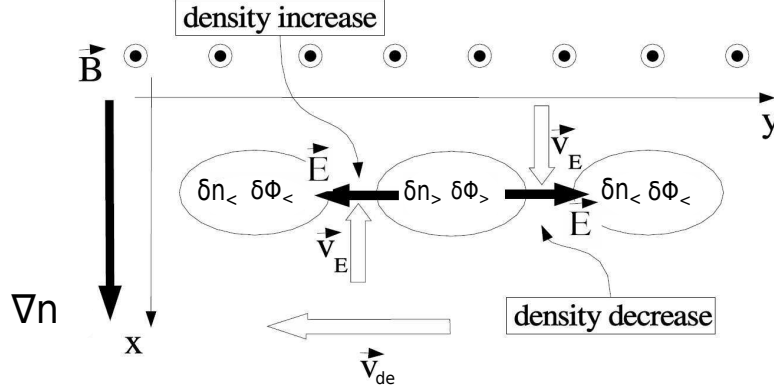
Figure 3.2: *Mechanism for the generation of the drift wave. In adiabatic conditions, in presence of a density perturbation, an electric field is generated. In turn, this creates an $E \times B$ velocity that, in presence of a density gradient, convects high density plasma to the left of a peak in the density perturbation, and low density plasma to the right of a peak. This results in a movement of the density perturbation to the left, giving rise to a wave that moves in the electron diamagnetic velocity direction, the so called drift wave. Source: Ref. [80].*

a finite value.

In the following we describe separately the main properties of BM and DW in detail. This is fundamental in order to identify the parameter regime where those modes dominate, which is the subject of Sec. 3.3.

3.2.1 Ballooning instabilities

For the study of BM, we simplify the system of Eqs. (3.1), avoiding the coupling with sound waves, *i.e.* by considering the limit $k_\parallel \ll \gamma$ (in dimensional units $c_{s0}k_\parallel \ll \gamma$), and therefore neglecting the $V_{\parallel i}$ dynamics. We also drop the compressibility terms due to magnetic curvature, ascribed to $\boldsymbol{V}_{E \times B}$ and $\boldsymbol{V}_{*e}$ convection, in the continuity and temperature equations, because they are much smaller than the R/L_n terms. Finally, we neglect the $\nabla_\parallel$ terms in the continuity and in temperature equations and the diamagnetic term, $\nabla_\parallel (n + 1.71 T_e)$, in Ohm's law, to avoid coupling with DW, therefore assuming $\omega_* < \gamma$, where $\omega_* = k_y R/L_n$ is the diamagnetic frequency. In the fluxtube geometry, Eqs. (3.1) reduce to:

$$\gamma n = \frac{R}{L_n} i k_y \phi,$$

$$-k_\perp^2 \gamma \phi = 2\hat{C}\left(n + T_e\right) - k_\perp^2 \nabla_\parallel \psi,$$

$$\gamma \psi \frac{\beta}{2} + k_\perp^2 \frac{m_e}{m_i} \gamma \psi = -k_\perp^2 \nu \psi + \nabla_\parallel \phi + i k_\perp \left(1 + 1.71\eta_e\right) \frac{\beta}{2} \frac{R}{L_n} \psi,$$

$$\gamma T_e = \eta_e \frac{R}{L_n} i k_y \phi$$

$$(3.3)$$

In the following subsections we detail the main characteristics of the resistive, the inertial, and the ideal branches of the BM (RBM, InBM and IdBM, respectively). We find that in all cases the maximum growth rate is $\gamma_B^{max} = \sqrt{2R/L_p}$. The RBM and InBM have $\gamma \to \gamma_B^{max}$ for $k_\parallel \to 0$, therefore the fastest growing mode has the smallest possible $k_\parallel$, approaching the minimum allowed value $k_\parallel \sim 1/(2\pi q)$. The poloidal mode number k_y can vary within a range set by the competition between parallel and perpendicular dynamics (lower k_y limit) and by the plasma compressibility (upper k_y limit). On the other hand, the IdBM is a global instability that develops with the maximum growth rate at smallest possible k_y.

Resistive ballooning mode

The resistive branch of the ballooning mode is destabilized by finite parallel resistivity. If electron inertia and electromagnetic effects are neglected, the system of Eqs. (3.3) can be reduced to the following equation for ϕ:

$$\hat{\gamma}\phi\left[1 + (\hat{z}\hat{s})^2\right] = \sigma_R\frac{\partial^2\phi}{\partial\hat{z}^2} + \frac{2C}{2\hat{\gamma}}\phi, \tag{3.4}$$

where we define $\hat{z} = z/q$ ($0 \le \hat{z} \le 2\pi$), $\hat{\gamma} = \gamma/\gamma_B^{max}$ and $\sigma_R = 1/(\gamma_B^{max}k_y^2q^2\nu)$, which describes the damping of the mode due to the resistive parallel spread.

Figure 3.3a shows the growth rate as a function of the magnetic shear $\hat{s}$ and the σ_R parameter obtained solving the eigenvalue problem of Eq. (3.4). We observe that the peak of the growth rate is at $\hat{s} \simeq 0.5$ and it decreases asymmetrically moving away from this value. This result agrees with the observations reported in Refs. [6] and [81]: for curvature driven modes, positive magnetic shear has a destabilizing effect, while negative shear reduces the region in which the instability can be driven. Moreover, in agreement with our findings, in Ref. [56] it was found that a branch of the resistive ballooning instability was highly unstable up to $\hat{s} = 1$. Negative shear stabilization of RBM has been invoked as one of the possible mechanisms behind the formation of transport barriers in the L-H transition (see Ref. [82]) as it reduces the fluxes of particles [11, 61], globally enhancing plasma confinement. The reduction of the growth rate for high values of the σ_R parameter is due to the competition between the parallel dynamics and the ballooning drive, *i.e.* the two terms appearing on the right hand side of Eq. (3.4). The ballooning drive prevails on the parallel dynamics for $k_\parallel^2\sigma_R \lesssim 1$, leading to an estimate of the value of k_y below which the growth rate is reduced by the parallel dynamics, given by $k_y^{min} = 1/(2\pi q\sqrt{\gamma_B^{max}\nu})$ (see Ref. [6]).

An analytical estimate for the eigenvalues of Eq. (3.4) can be calculated in the strong ballooning regime (see, *e.g.*, Refs. [6] and [56]). Assuming strong ballooning character of the mode, *i.e.* a strong localization of the solution near the outer mid

plane, we can Taylor expand the curvature operator around that location and derive a Weber-type equation for ϕ, of the form:

$$a\frac{d^2\phi}{dz^2} + \left(b + cz^2\right)\phi = 0, \tag{3.5}$$

where $a = \sigma_R\hat{\gamma}$, $b = 1 - \hat{\gamma}^2$ and $c = -\hat{\gamma}^2\hat{s}^2 + \hat{s} - 1/2$. The solution of Eq. (3.5) is $\phi = \exp\left(-\lambda^2 z^2/2\right)$, where $\lambda^2 = -c/b$, for $\lambda^2 > 0$. Since the coefficients a, b and c have to satisfy $b^2 + ac = 0$, the relation between $\hat{\gamma}$, $\hat{s}$ and σ_R is:

$$\sigma_R = \frac{2\hat{\gamma}^2 - \hat{\gamma}^4 - 1}{\hat{\gamma}\hat{s} - \hat{\gamma}/2 - \hat{\gamma}^3\hat{s}^2}. \tag{3.6}$$

The accuracy of Eq. (3.6) is higher for localized modes, *i.e.* with large λ, which is the case at strong positive and strong negative shear. In Fig. 3.3a the black line shows the relation between σ_R and $\hat{s}$ evaluated from Eq. (3.6) for $\hat{\gamma} = 0.7$. Compared to the numerical solution of Eq. (3.4), one sees that Eq. (3.6) is able to describe the effect of magnetic shear on the RBM for $\hat{s} \lesssim 0$ and for $\hat{s} \gtrsim 2$. In fact for $0 \lesssim \hat{s} \lesssim 2$ the strong ballooning assumptions are not satisfied and the analytical solution is not accurate. We remark that, according to Eq. (3.6), the system is unstable even for $\sigma_R \to 0$.

According to the evaluation of the eigenvalues of Eq. (3.4), $\gamma \to \gamma_B^{max}$ for $k_y \to \infty$. However, the solution of Eqs. (3.1) shows that $\gamma \to 0$ for $k_y \to \infty$. We find that this is due to magnetic curvature induced plasma compressibility, that is not included in the simplified system (3.3). This effect can be understood by considering a relatively simple model, Eqs. (3.1) in the $k_\parallel = 0$ limit and assuming constant curvature evaluated at the outer mid plane. The linear dispersion relation associated to such a system is [40] $b_0 + b_1\gamma + b_2\gamma^2 + b_3\gamma^3 = 0$, where $b_0 = 20ik_y^3\left(2 - R/L_n\right)/3$, $b_1 = 20\left(k_y^2 - 1\right)k_y^2/3 + 2\left(1 + \eta_e\right)k_y^2 R/L_n$, $b_2 = 20ik_y^3/3$, $b_3 = -k_y^2$. The solution of this dispersion relation shows reduction of the growth rate for $k_y \gtrsim 0.3\gamma_B^{max}$; our numerical tests show that this reduction is due to the compressibility terms in the density and temperature equations. In conclusion, the RBM grows for $k_y^{min} < k_y < k_y^{max}$, being $k_y^{min} = 1/(2\pi q\sqrt{\gamma_B^{max}\nu})$ and $k_y^{max} = 0.3\gamma_B^{max}$.

In a previous study (see Ref. [6]) BM analysis demonstrated that their growth rate is reduced by diamagnetic effects when $\alpha_D = Rk_y^{min}/(L_n\gamma_B^{max}) > 1$. We observe a reduction of the growth rate at high k_y due to compressibility effects, ascribed to both the diamagnetic terms ($\hat{C}T_e$ and $\hat{C}n$) and the potential term ($\hat{C}\phi$) in the density and temperature equations. Our approach separates the compressibility damping from the diamagnetic effects in Ohm's law, while in Ref. [6] the two contributions were not clearly separated.

Inertial ballooning mode

In the limit of negligible resistivity and negligible electromagnetic effects, one finds the inertial branch of the BM instability. In this limit Eqs. (3.3) can be reduced to the following equation for ϕ:

$$\hat{\gamma}\phi\left[1+(\hat{z}\hat{s})^2\right] = \frac{\sigma_{In}^2}{\hat{\gamma}}\frac{\partial^2\phi}{\partial\hat{z}^2} + \frac{2C}{2\hat{\gamma}}\phi, \qquad (3.7)$$

where $\sigma_{In} = \sqrt{m_i}/\left(\gamma_B^{max}k_y q\sqrt{m_e}\right)$, which describes the damping of the mode due to the inertial parallel spread. In Fig. 3.3b we show the growth rate as a function of $\hat{s}$ and σ_{In}, solution of the eigenvalue problem of Eq. (3.7). We observe that the reduction of γ due to the magnetic shear is asymmetric with respect to the peak value occurring at $\hat{s} \simeq 0.5$. As for the RBM, we remark that the diminution of the growth rate with σ_{In} is due to the competition between the ballooning drive and the parallel dynamics terms appearing on the right hand side of Eq. (3.7). By comparing the two terms on the right hand side of Eq. (3.7), we find the minimum value of k_y, below which we have a considerable suppression of the growth rate, which is $k_y^{min} = \sqrt{m_i}/(2\pi q\gamma_B^{max}\sqrt{m_e})$. As in the case of RBM, it is possible to solve the Eq. (3.7) within the strong ballooning limit (see Refs. [6] and [56]). In this case the coefficients of the Weber equation, Eq. (3.5), are $a = \sigma_{In}^2$, $b = -\hat{\gamma}^2 + 1$ and $c = -\hat{\gamma}^2\hat{s}^2 + \hat{s} - 1/2$ and the relation between σ_{In}, $\hat{s}$ and $\hat{\gamma}$ is given by:

$$\sigma_{In} = \sqrt{\frac{2\hat{\gamma}^2 - \hat{\gamma}^4 - 1}{\hat{s} - 1/2 - \hat{\gamma}^2\hat{s}^2}}. \qquad (3.8)$$

In Fig. 3.3b the black line shows the relation between σ_{In} and $\hat{s}$ given by Eq. (3.8) for $\hat{\gamma} = 0.7$ compared to the numerical solution of Eq. (3.7), as in the RBM case. We notice that the agreement between the analytical and the numerical solution is good for $\hat{s} \lesssim 0$ and for $\hat{s} \gtrsim 2$. In fact for $0 \lesssim \hat{s} \lesssim 2$ the strong ballooning assumption is not valid and the analytical solution, Eq. (3.8), is not accurate. We remark that, according to Eq. (3.8), the system is unstable even for $\sigma_{In} \to 0$. As stated for the RBM case, also for the InBM the compressibility reduces the growth rate for $k_y \gtrsim 0.3\gamma_B^{max}$ [40].

Ideal ballooning mode

The ideal ballooning instability persists in the absence of plasma resistivity and electron inertia, and it is characterized by magnetic field lines bending outward in the bad curvature region due to interchange drive. In the limit of negligible

resistivity, ν, and negligible electron mass, m_e, the system of Eqs. (3.3) can be reduced to the following equation for ϕ:

$$-\hat{\gamma}\phi\left[1+(\hat{z}\hat{s})^2\right] = -\frac{\left[1+(\hat{z}\hat{s})^2\right]}{\alpha_{MHD}\hat{\gamma}}\frac{\partial^2\phi}{\partial\hat{z}^2} - \frac{2C}{2\hat{\gamma}}\phi, \qquad (3.9)$$

where $\alpha_{MHD} = q^2\beta(1+\eta_e)R/L_n$ and it represents the ratio between interchange drive and parallel spread. The growth rate as a function of $\hat{s}$ and α_{MHD} is shown in Fig. 3.3c, as a solution of the eigenvalue problem of Eq. (3.9). When the parallel stabilization is overcome, *i.e.* for $\alpha_{MHD} \sim 1$, the IdBM is unstable independently of k_y (see Ref. [6]), since α_{MHD} is independent of k_y. The magnetic shear has a stabilizing effect that is not symmetric with respect to the peak value occurring at $\hat{s} \simeq 0.5$, the damping of the growth rate for $\hat{s} < 0$ being more effective than for $\hat{s} > 0$. In the strong ballooning regime the coefficients of the Weber equation, Eq. (3.5), associated with Eq. (3.9) are: $a = 1$, $b = \alpha_{MHD}(1-\gamma^2)$, $c = \alpha_{MHD}(-\hat{s}^2+\hat{s}-1/2)$. For the IdBM case the analytical solution in the strong ballooning limit leads to the relation among α_{MHD}, $\hat{s}$ and $\hat{\gamma}$ given by:

$$\alpha_{MHD} = \frac{\hat{s}-1/2-\hat{s}^2}{2\hat{\gamma}^2-\hat{\gamma}^4-1}. \qquad (3.10)$$

The black continuous line in Fig. 3.3c shows the relation between α_{MHD} and $\hat{s}$, Eq. (3.10), for $\hat{\gamma} = 0$ (marginal ideal stability), while the dotted line shows the same relation for $\hat{\gamma} = 0.5$, compared to the numerical solution of Eq. (3.9). The numerical solution of Eq. (3.9) shows good agreement with the solid curve in Fig. 1 of Ref. [53], which was obtained following the hypothesis described in Ref. [83]. In that case the marginal ideal stability was computed from the ideal MHD energy principles, imposing zero boundary conditions in the poloidal direction. We remark that, according to Eq. (3.10), the system is stable for $\alpha_{MHD} \to 0$, showing the existence of a pressure threshold for the destabilization of the IdBM. As in the RBM and InBM cases, when compressibility effects are retained in Eqs. (3.1), we verified a reduction of the growth rate with increasing k_y that becomes important for $k_y \gtrsim 0.3\gamma_B^{max}$ [40]. Therefore the maximum growth rate of the IdBM develops for $k_y \to 0$.

3.2.2 Drift Wave instability

In order to model the DW instability we simplify Eqs. (3.1) by neglecting the sound waves coupling, *i.e.* by assuming $\gamma \gg k_\parallel$. Moreover, we turn off the ballooning drive, *i.e.* the curvature terms in the vorticity equation, in order to exclude BM from the system. We also neglect the compressibility terms in the continuity and temperature equations, since they have a stabilizing effect that we ignore for
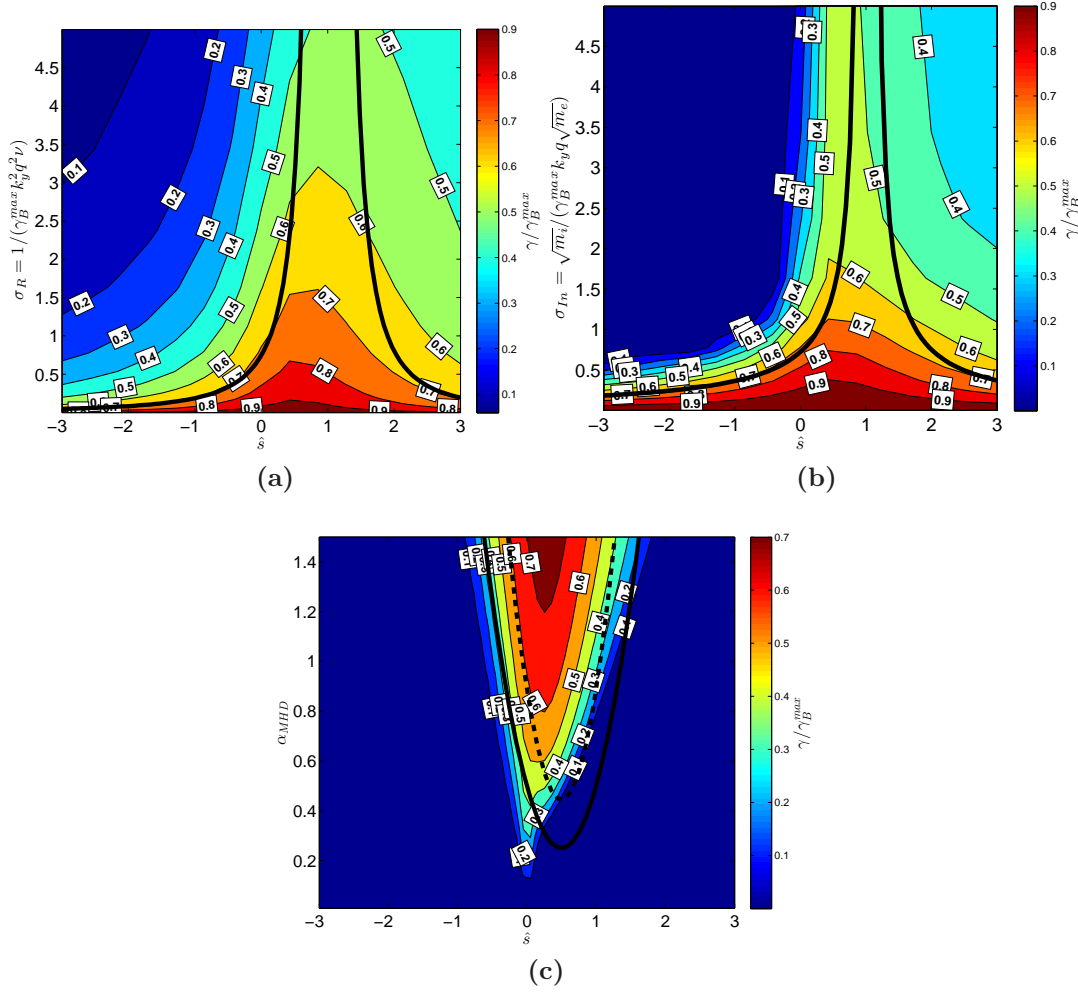
Figure 3.3: *The normalized growth rate of the resistive ballooning mode (a), γ/γ_B^{max}, solution of Eq. (3.4), is plotted as a function of $\hat{s}$ and σ_R; the black line shows the analytical solution given by Eq. (3.6) for $\gamma/\gamma_B^{max} = 0.7$. The normalized growth rate of the inertial ballooning mode (b), γ/γ_B^{max}, solution of Eq. (3.7), is plotted as a function of $\hat{s}$ and σ_{In}; the black line shows the analytical solution given by Eq. (3.8) for $\gamma/\gamma_B^{max} = 0.7$. The normalized growth rate of the ideal ballooning mode (c), γ/γ_B^{max}, solution of Eq. (3.9), is plotted as a function of $\hat{s}$ and α_{MHD}; the dotted black line shows the analytical solution for $\gamma/\gamma_B^{max} = 0.5$, while the continuous black line shows the ideal marginal stability, $\gamma = 0$, both given by Eq. (3.10).*

sake of simplicity. The reduced system of equations able to take into account the fundamental elements of the DW is:

$$\gamma n = ik_y \frac{R}{L_n}\phi - k_\perp^2 \nabla_\parallel \psi,$$

$$-k_\perp^2 \gamma \phi = -k_\perp^2 \nabla_\parallel \psi,$$

$$\gamma\psi\frac{\beta}{2} + \frac{m_e}{m_i}\gamma k_\perp^2\psi = -k_\perp^2\nu\psi + \nabla_\parallel(\phi - n - 1.71T_e) + ik_\perp(1 + 1.71\eta_e)\frac{\beta}{2}\frac{R}{L_n}\psi,$$

$$\gamma T_e = ik_y\eta_e\frac{R}{L_n}\phi - k_\perp^2\frac{2}{3}1.71\nabla_\parallel\psi.$$

$$(3.11)$$

We analyze this system in more detail by separating the resistive and the inertial branches of the DW.

Resistive drift waves

In the case of resistive DW (RDW) the adiabaticity is broken by the presence of a finite parallel resistivity. Neglecting electron inertia and electromagnetic effects, the system of Eqs. (3.11) can be reduced to the following equation for ϕ:

$$\check{\gamma}k_\perp^2\phi = \frac{\partial^2\phi}{\partial\check{z}^2} + 2.94\frac{\partial^2(k_\perp^2\phi)}{\partial\check{z}^2} - \frac{1}{\check{\gamma}}\left[ik_y(1 + 1.71\eta_e)\right]\frac{\partial^2\phi}{\partial\check{z}^2}, \qquad (3.12)$$
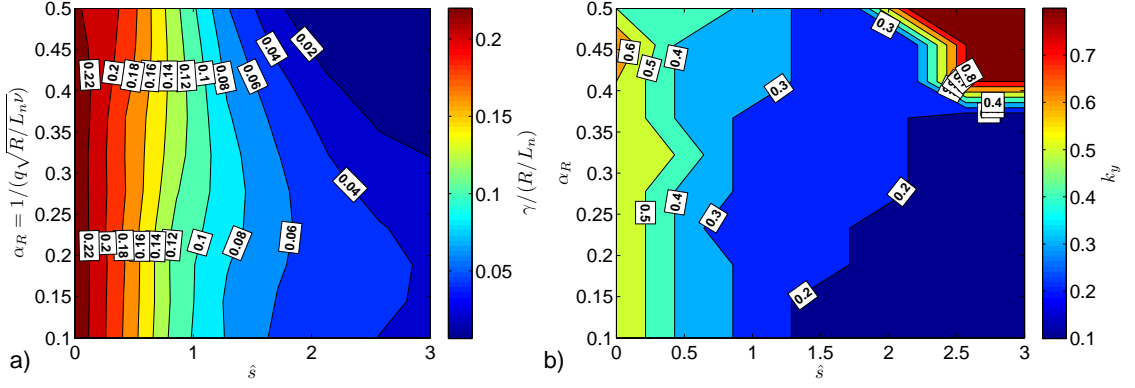
where $\check{z} = z\sqrt{\nu R/L_n}$, $\check{\gamma} = \gamma L_n/R$, $k_\perp^2 = k_y^2[1 + (\check{z}\alpha_R\hat{s})^2]$, and $\alpha_R = \sqrt{L_n}/(q\sqrt{\nu R})$. In Fig. 3.4 the growth rate of the fastest growing mode, found from Eq. (3.12) and the corresponding k_y are shown as a function of $\hat{s}$ and α_R, assuming $\eta_e = 1$. Magnetic shear damps the instability almost independently of α_R in the observed range of values, with the maximum growth rate at $\hat{s} = 0$. The typical wavenumber of the fastest growing mode is in the range $0.2 < k_y < 0.8$. We remark that for $\hat{s} = 0$, with the substitution $\partial/\partial z \rightarrow ik_\parallel$, Eq. (3.12), can be reduced to an algebraic equation, $\nu k_y^2\gamma^2 + k_\parallel^2\left(1 + 2.94k_y^2\right)\gamma - (1 + 1.71\eta_e)ik_\parallel^2 k_y R/L_n = 0$, with a maximum growth rate of $\gamma_{RDW}^{max} \simeq 0.085(1 + 1.71\eta_e)R/L_n$ at $k_y \simeq 0.57$ and $k_\parallel \simeq 0.24\sqrt{\nu R/L_p}$ [40]. We note that the influence of magnetic shear on the RDW has been discussed, for example, in Ref. [84], in the collisionless limit, and in Ref. [85], with the inclusion of resistivity. For a constant value of R/L_n, in both cases it has been found that the DW instability in a sheared slab geometry is unconditionally stable. We find that the growth rate of DW is suppressed by shear effects, but the instability is not unconditionally stable for $\hat{s} \neq 0$. In Refs. [84] and [85] the radially non-local DW dispersion relation is studied, neglecting the electron temperature dynamics and assuming $k_\parallel = 0$ at the center of the flux tube. In our approach we allow $k_\parallel \neq 0$, leading to the development of an unstable DW instability, even in the presence of magnetic shear.

Inertial drift waves

In the inertial branch of the DW (InDW) the electron adiabaticity is broken by the presence of a finite electron mass. Neglecting resistivity and electromagnetic effects, the system of Eqs. (3.11) can be reduced to the following equation for ϕ:

$$\check{\gamma}^2 k_\perp^2 \phi = \frac{\partial^2 \phi}{\partial \bar{z}^2} + 2.94 \frac{\partial^2 (k_\perp^2 \phi)}{\partial \bar{z}^2} - \frac{1}{\check{\gamma}} \left[ik_y \left(1 + 1.71\eta_e\right)\right] \frac{\partial^2 \phi}{\partial \bar{z}^2}, \qquad (3.13)$$

where $\bar{z} = zR\sqrt{m_e}/(L_n\sqrt{m_i})$, $k_\perp^2 = k_y^2 \left[1 + (\check{z}\alpha_I \hat{s})^2\right]$ and $\alpha_I = L_n\sqrt{m_i}/(qR\sqrt{m_e})$. In Fig. 3.5 the solution of Eq. (3.13) and the k_y related to the maximum growth rate are shown as a function of $\hat{s}$ and α_I, assuming $\eta_e = 1$. As for the RDW, the maximum growth rate is reached for $\hat{s} = 0$ and magnetic shear causes a damping of the instability, almost independently of α_I in the observed range of values. We note that the magnetic shear damps more efficiently the RDW instability than the InDW instability. For example, the growth rate of the InDW is reduced approximately to 30% of the shearless value at $\hat{s} = \pm 3$ while, in the RDW case, the growth rate is reduced to approximately 10%. The typical wavenumber of the fastest growing mode is in the range $0.35 < k_y < 0.6$. For the $\hat{s} = 0$ case, Eq. (3.13) can be reduced to an algebraic equation, $m_e/m_i k_y^2 \gamma^3 + k_\parallel^2 \left(1 + 2.94 k_y^2\right) \gamma - (1 + 1.71\eta_e) i k_\parallel^2 k_y R/L_n = 0$, with a maximum growth rate given by $\gamma_{InDW}^{max} \simeq 0.17 \left(1 + 1.71\eta_e\right) R/L_n$, at $k_y \simeq 0.57$ and $k_\parallel \simeq 0.2R\sqrt{m_e}/(L_p\sqrt{m_i})$ [40]. The maximum growth rate is double the value obtained for RDW.

# 3.3 Parameter space of the linear instabilities

We now identify the parameter space of the previously described linear instabilities. Our goal is to provide a framework according to which, given the set of parameters necessary to characterize the SOL, it is possible to state which is the dominant linear mode, *i.e.* the one that has the fastest growth rate. Within our model, the parameters necessary to characterize the SOL are: R/L_n, ν, m_e/m_i, β, $\hat{s}$, and q. In Fig. 3.6 the different regimes of linear instabilities are schematically identified in the parameter space. Our analysis starts from the electrostatic limit, $\beta = 0$, represented in Fig. 3.6a. Since DW have a growth rate of the order $\gamma \sim \omega_* \sim R/L_n$, while BM growth rate scales as $\sqrt{R/L_n}$, we expect the DW to overcome the BM growth rate for sufficiently steep density gradients. In fact, four regimes can be distinguished: at high values of R/L_n the DW is the dominant instability, the resistive branch prevailing at high resistivity and the inertial branch at low resistivity. For low values of R/L_n BM dominate, in particular the resistive branch at high resistivity and inertial branch at low resistivity. Finite β effects are described in Fig. 3.6b. At high values of R/L_n, for increasing values of β, first DW suppression due to electromagnetic effects is observed and then the IdBM becomes unstable, once the

Figure 3.4: *The normalized growth rate of the resistive drift wave, $\gamma L_n/R$, maximized over k_y, (a) and k_y of the maximum growth rate (b), solution of Eq. (3.12), are plotted as a function of $\hat{s}$ and α_R. $\hat{s} > 0$ is represented, since Eq. (3.12) is invariant for $\hat{s} \to -\hat{s}$ transformation.*
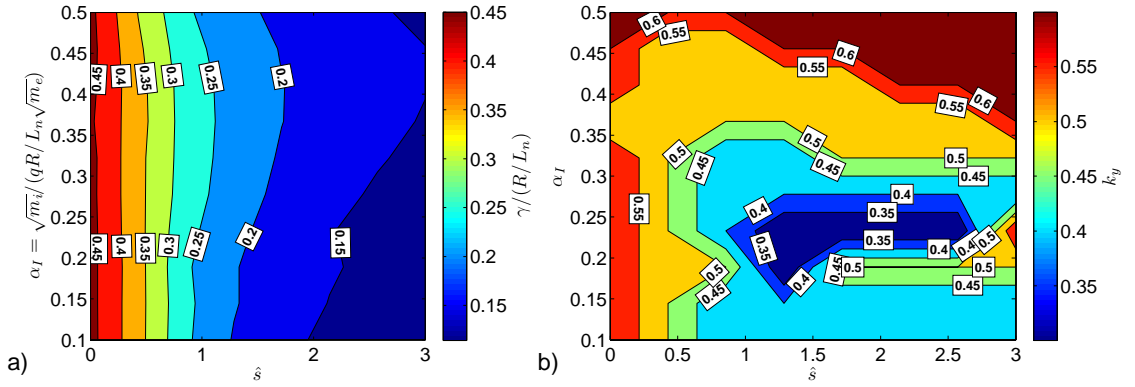
Figure 3.5: *The normalized growth rate of the inertial drift wave, $\gamma L_n/R$, maximized over k_y, (a) and k_y of the maximum growth rate (b), solution of Eq. (3.13), are plotted as a function of $\hat{s}$ and α_I. $\hat{s} > 0$ is represented, since Eq. (3.13) is invariant for $\hat{s} \to -\hat{s}$ transformation.*

α_{MHD} threshold is overcome. For small values of R/L_n, the RBM and the InBM dominate at small β and the IdBM at high β.

In the following paragraph we first provide a description of the transition among the different instabilities in the electrostatic case. We then discuss the role of electromagnetic effects.

3.3.1 Transition between resistive ballooning mode and resistive drift wave

An estimate of the transition between the RDW and RBM can be obtained by comparing their maximum growth rates. In the shearless case, a very simple estimate can be obtained by equating the maximum growth rate for RDW, γ_{RDW}^{max}, defined in Sec. 3.2.2, to the maximum growth rate for RBM, γ_B^{max}, defined in Sec. 3.2.1. One obtains a transition value of R/L_n, that is $R/L_n = 2(1 + \eta_e)/[0.085(1 + 1.71\eta_e)]^2 \simeq 75.2$ at $\eta_e = 1$.

In the general case, the threshold value of R/L_n depends on $\hat{s}$, σ_R and α_R and is obtained by comparing the solutions of Eqs. (3.4) and (3.12), namely γ_{RBM} and γ_{RDW}, respectively. We identify the R/L_n threshold in correspondence to $\gamma_{RDW}/\gamma_{RBM} = 1$. In the following analysis we fix $\alpha_R = 0.35$, since the DW depend weakly on this parameter. In Fig. 3.7a we show the R/L_n threshold as a function of $\hat{s}$ and σ_R. The R/L_n threshold decreases for increasing σ_R, since the RBM is suppressed by the parallel dynamics. For $\hat{s} = 0$, while at $\sigma_R \simeq 0$ the transition between RDW and RBM occurs at $R/L_n \simeq 75$ (in agreement with our analytical estimate), at $\sigma_R \simeq 0.5$ the RDW grows faster than the RBM for $R/L_n \gtrsim 45$. The R/L_n threshold decreases to $R/L_n \simeq 15$ for $\hat{s} = 0$ at $\sigma_R \simeq 3$. The decrease of the R/L_n threshold is more noticeable for $\hat{s} < 0$, as the RBM is more efficiently suppressed by negative shear (see Fig. 3.3a) and the asymmetry with respect to $\hat{s} = 0$ becomes evident at high values of σ_R. In the white region the R/L_n threshold is at values greater than 300 and the RBM always prevails on the RDW.

3.3.2 Transition between inertial ballooning mode and inertial drift waves

In order to estimate the threshold value of R/L_n above which the InDW grows faster than the InBM we can proceed as for the resistive case. For $\hat{s} = 0$, a simple analytical estimate of the threshold can be obtained by equating the maximum growth rate for InDW, γ_{InDW}^{max}, defined in Sec. 3.2.2, to the maximum growth rate for InBM, γ_B^{max}, defined in Sec. 3.2.1. The normalized gradient below which the InBM growth rate is larger than the one for the InDW is $R/L_n = 2(1 + \eta_e)/[0.17(1 + 1.71\eta_e)]^2 \simeq 18.8$ at $\eta_e = 1$. In general, the threshold depends on $\hat{s}$, σ_{In} and α_I and can be evaluated comparing the solution of Eqs. (3.7) and (3.13), γ_{InBM} and γ_{InDW}, respectively,

identifying the R/L_n threshold in correspondence to $\gamma_{InDW}/\gamma_{InBM} = 1$. In Fig. 3.7b we show the R/L_n threshold as a function of $\hat{s}$ and σ_{In}, for $\alpha_I = 0.30$. The R/L_n threshold decreases for increasing σ_{In}, since the InBM is suppressed by the parallel dynamics. As for the RBM, the decrease is more evident for $\hat{s} < 0$. For $\sigma_{In} \simeq 0$ we observe that the R/L_n threshold is very close to the analytical estimate previously calculated for $\hat{s} = 0$ and that, because of the shear damping of the InDW, at $\hat{s} = \pm 1$ the transition occurs at $R/L_n \simeq 55$. The threshold decreases to $R/L_n \simeq 10$, due to the smaller growth rate of the InBM at $\sigma_{In} \simeq 0.5$ and $\hat{s} = 0$. In the white region of Fig. 3.7b the InDW always prevails on the InBM.

3.3.3 Transition between resistive drift wave and inertial drift wave

In the parameter space region where R/L_n is sufficiently high, and therefore the DW are the dominant instability, the relative influence of the resistive term with respect to the inertial term governs the transition between the RDW and the InDW. The threshold value of resistivity for the transition between these two branches of the DW can be roughly estimated by balancing the resistive term and the inertial term in Ohm's law: if $\nu > \gamma m_e/m_i$, resistive effect dominates, leading therefore to the development of the RDW instability, otherwise inertial effects do, *i.e.* the InDW prevail.

A more precise estimate of the transition value of the resistivity can be obtained by studying the behaviour of the system of Eqs. (3.11), considering the $\beta = 0$ limit, as a function of $\delta = \nu L_n m_i/(R m_e)$, which defines the ratio between the resistive and inertial effects. In Fig. 3.8a, we plot the growth rate of DW as a function of δ, for different values of $\hat{s}$. From low to high values of δ, one observes the transition from the InDW to the RDW region. The maximum RDW growth rate is half the one for the InDW for $\hat{s} = 0$. In general, it is always smaller than the one for InDW, even for $\hat{s} \neq 0$. Therefore one can obtain the value of δ at which the transition takes place, by evaluating the value of δ at which the growth rate is the average of the growth rates for RDW and InDW. We observe that, for increasing $\hat{s}$, the value of δ at which the transition from InDW to RDW occurs decreases. This is plotted in Fig. 3.8b: the δ threshold passes from $\delta \sim 3.55$ for $\hat{s} = 0$ to $\delta \sim 1.12$ for $\hat{s} = 5$.

3.3.4 Transition between resistive ballooning mode and inertial ballooning mode

The threshold between RBM and InBM has been calculated by comparing the growth rate of the two linear modes, solutions of Eqs. (3.4) and (3.7), γ_{RBM} and γ_{InBM}, respectively. In the resistive limit, γ is a function of $\hat{s}$ and σ_R and, in the inertial limit, it depends on $\hat{s}$ and σ_{In}, therefore the ratio $\gamma_{InBM}/\gamma_{RBM}$ has to be
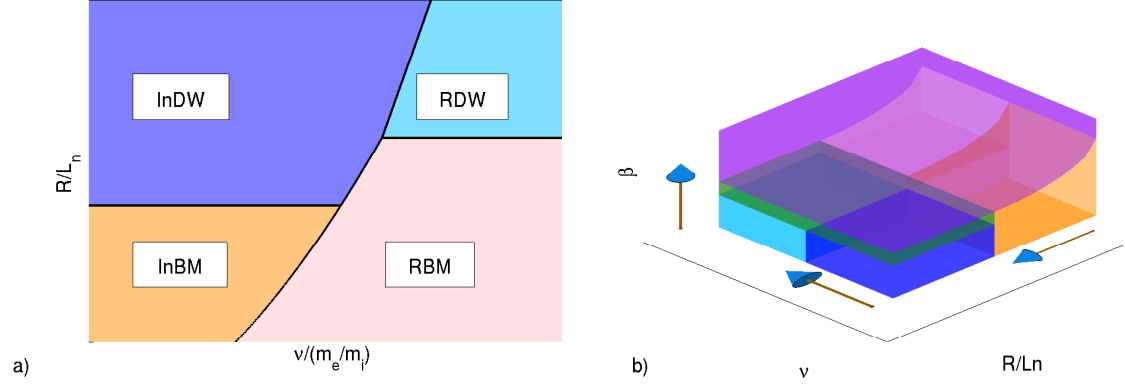
Figure 3.6: *Sketch of the linear instability regimes in the parameter space: electrostatic limit (a) and full electromagnetic analysis (b): different colours identify the region of influence of different instabilities: resistive ballooning (pink), inertial ballooning (orange), resistive drift wave (light blue), inertial drift wave (dark blue), ideal ballooning (violet), region of suppression of drift waves (green).*
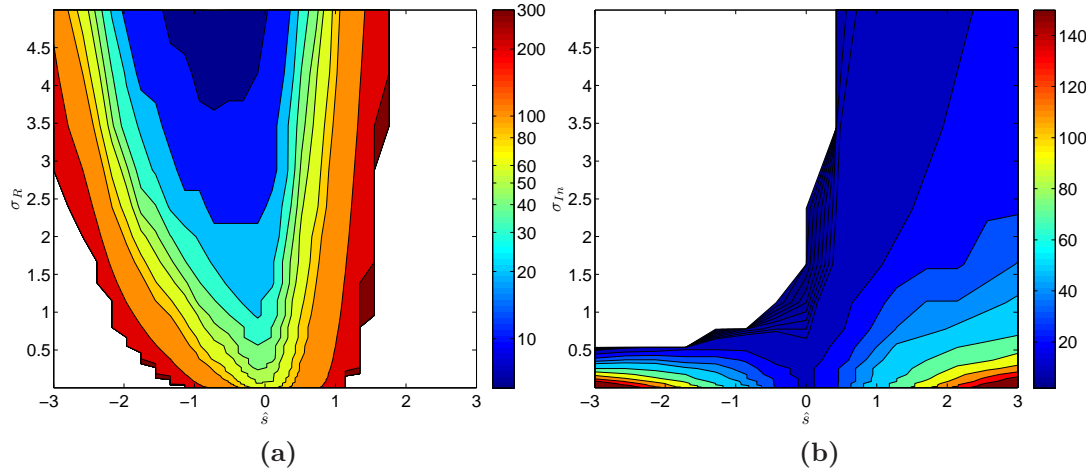
Figure 3.7: *Transition between resistive drift waves and resistive ballooning mode (a). The R/L_n value for which the growth rate of the RDW, solution of Eq. (3.12), and of the RBM, solution of Eq. (3.4), are equal, $\gamma_{RDW} = \gamma_{RB}$, is plotted as a function of $\hat{s}$ and σ_R. In the white region the RBM always prevails on the RDW for $R/L_n > 300$. Transition between inertial drift waves and inertial ballooning mode (b). The R/L_n value for which the growth rate of the InDW, solution of Eq. (3.13), and of the InBM, solution of Eq. (3.7), are equal, $\gamma_{InDW} = \gamma_{InB}$, is plotted as a function of $\hat{s}$ and σ_{In}. In the white region the InDW always prevail on the InBM.*

evaluated as a function of σ_R, σ_{In}, and $\hat{s}$. We observe that the ratio is larger or smaller than 1, independently of $\hat{s}$, in a wide region of the plane (σ_R, σ_{In}). In Fig. 3.9 the red surface identifies the region in which the ratio $\gamma_{InBM}/\gamma_{RBM}$ is larger than 1 for all values of $\hat{s}$, *i.e.* the InBM prevails, while the blue surfaces identify the region where the ratio $\gamma_{InBM}/\gamma_{RBM}$ is smaller than 1, *i.e.* the RBM prevails, independently of $\hat{s}$. The narrow regions of the plane (σ_R, σ_I) in which the threshold depends on $\hat{s}$ are colored in white. The value of σ_R for which we observe the transition depends on σ_{In} as $\sigma_R \simeq 0.56\sigma_{In}^{1.82}$, which provides therefore a simple estimate of the transition between RBM and InBM.

3.3.5 The role of electromagnetic effects

We extend the analysis of the linear instability regime to finite β plasmas and therefore we consider the effect of the electromagnetic terms on the system of Eqs. (3.1). Two main phenomena are observed related to finite β: suppression of the DW instability, and the appearance of the IdBM, when the ideal limit is overcome.

In order to describe the effect of the electromagnetic terms, the simplest model to consider consists of the system of Eqs. (3.1), excluding the coupling with sound waves, *i.e.* $k_{\parallel} \ll \gamma$ and analyzing the resistive $(m_e/m_i = 0)$ and inertial $(\nu = 0)$ limits. The system can be reduced to the following eigenvalue equation for ϕ:

$$\gamma k_{\perp}^2 \phi = -2\hat{C}\left\{A_0 + \frac{1}{A_1}\left[A_0 2\hat{C}\left(\frac{1}{1.71} - 1\right) + A_2\right]\right\}\phi +$$
$$+ \frac{k_{\perp}^2}{A_3}\left\{1 - A_0 - \frac{1.71}{A_1}\left[A_0 2\hat{C}\left(\frac{1}{1.71} - 1\right) + A_2\right]\right\}\frac{\partial^2 \phi}{\partial \hat{z}^2}, \tag{3.14}$$

where $A_0 = Rik_y/(\gamma L_n) - k_{\perp}^2 - 2\hat{C}/\gamma$, $A_1 = 0.88\gamma - 2.09\hat{C}$, and $A_2 = -k_{\perp}^2\gamma + 0.88\eta_e Rik_y/L_n + 1.17\hat{C}$. In the resistive case $X = \beta/(2\nu)$, $0 < \hat{z} < 2\pi q\sqrt{\nu}$, and $A_3 = \gamma X + k_{\perp}^2 + k_{\perp}^2 XR(1 + 1.71\eta_e)/L_n$, while in the inertial case $X = \beta m_i/(2m_e)$, $0 < \hat{z} < 2\pi q\sqrt{m_e/m_i}$, and $A_3 = \gamma X + \gamma k_{\perp}^2 + k_{\perp}^2 XR(1 + 1.71\eta_e)/L_n$.

In order to illustrate the role of electromagnetic effects, we consider two specific cases, which reflect the typical impact of $\beta \neq 0$ on the instabilities. The maximum growth rate of the instability, solution of Eq. (3.14), is plotted in Fig. 3.10 in the resistive limit for $\nu = 0.01$ and $q = 4$, and in Fig. 3.11 in the inertial limit, for $m_e/m_i = 2.72 \times 10^{-4}$ and $q = 4$. In both cases $\eta_e = 1$. Focusing on the resistive case, a number of observations can be made. For $\hat{s} = 0$ (Fig. 3.10a), at high values of R/L_n, the RDW is suppressed. As it will be demonstrated in the following, this occurs for $\beta/(2\nu) \simeq 1.17L_n/[R(1 + 1.71\eta_e)]$. We also observe the appearance of the IdBM instability once the α_{MHD} threshold is overcome. Since α_{MHD} is proportional to $\beta R/L_n$, the β threshold for IdBM is inversely proportional to R/L_n, *i.e.* the IdBM develops at lower β for higher values of R/L_n. For $\hat{s} \neq 0$ the suppression of the RDW and the appearance of the IdBM is also observed (see Figs. 3.10b and

3.10c, that consider $\hat{s} = 1$ and $\hat{s} = -1$, respectively). With respect to the $\hat{s} = 0$ case we also point out: (i) a reduction of the RDW growth rate (high R/L_n) to half of the shearless value, as expected from Fig. 3.4; (ii) an increase of the RBM growth rate for $\hat{s} = 1$ and a decrease for $\hat{s} = -1$ with respect to the shearless value, as expected from Fig. 3.3a; (iii) an increase of the IdBM growth rate for $\hat{s} = 1$ and a decrease for $\hat{s} = -1$ with respect to the shearless value, as expected from Fig. 3.3b. We finally note that for $\hat{s} < 0$ IdBM is less suppressed by magnetic shear than RBM. This is due to the fact that for the characteristic values of α_{MHD} in Fig. 3.10, the $\hat{s}$ damping is minimum: for example, for $\beta = 2 \times 10^{-3}$, $R/L_n = 50$, we have $\alpha_{MHD} = 3.2$, consequently the mode is highly unstable for any value of the magnetic shear (see Fig. 3.3c). On the other hand, we are considering the RBM instability at high values of σ_R and the dependence of the growth rate on the shear is more evident: for the same set of parameters $\sigma_R = 1.77$ and $\hat{s}$ reduces the growth rate (see Fig. 3.3a). In the inertial case (Fig. 3.11) similar observations as in the resistive case can be made. For $\hat{s} = 0$ (see Fig. 3.11a), at high values of R/L_n, the InDW instability is suppressed for $\beta m_i/(2m_e) \gtrsim 0.17$, as it will be shown in the following. We also observe the appearance of the IdBM instability, at β value that is inversely proportional to R/L_n. For $\hat{s} = \pm 1$ the remarks made for the resistive case remain valid.

Now we analyze in details the suppression of the DW instability due to the electromagnetic effects by considering a relatively simple model. We reduce the system of Eqs. (3.11) to an algebraic dispersion relation by considering the $\hat{s} = 0$ case and substituting $\partial/\partial z \rightarrow ik_{\parallel}$, and we consider electromagnetic effects acting on both the InDW (by setting $\nu = 0$) and the RDW (with $m_e/m_i = 0$). Within these hypothesis, the dispersion relation has the form $\bar{\gamma}^3 b_3 + \bar{\gamma}^2 b_2 + \bar{\gamma} b_1 + b_0 = 0$, where $\bar{\gamma} = \gamma/\left[(1 + 1.71\eta_e)R/L_n\right]$. In the resistive case the coefficients in the dispersion relation are: $b_3 = iX$, $b_2 = ik_y^2 + Xk_y$, $b_1 = iZ^2\left[(1 + 2.95k_y^2)\right]$, $b_0 = Z^2 k_y$, being $X = (1 + 1.71\eta_e)\beta R/(2\nu L_n)$ and $Z = k_{\parallel}\sqrt{L_n}/\sqrt{\nu R(1 + 1.71\eta_e)}$. In Fig. 3.12a we show the maximum growth rate over k_y and $k_{\parallel}$ as a function of X. Numerically we verify that the growth rate is reduced to half of the maximum for $X > 1.17$, *i.e.* the RDW is suppressed by electromagnetic effects for $\beta > 2.34\nu L_n/\left[R(1 + 1.71\eta_e)\right]$. On the other hand, in the inertial case, $b_3 = ik_y^2 + iX$, $b_2 = Xk_y$, $b_1 = iZ^2(1 + 2.95k_y^2)$, $b_0 = Z^2 k_y$, with $X = \beta m_i/(2m_e)$ and $Z = k_{\parallel}L_n\sqrt{m_i}/\left[R\sqrt{m_e}(1 + 1.71\eta_e)\right]$. In Fig. 3.12b we show the maximum growth rate over k_y and $k_{\parallel}$ as a function of X: the growth rate is reduced to the half of the maximum for $X > 0.17$, *i.e.* the InDW is suppressed for $\beta > 0.34 m_e/m_i$.

To summarize, with the introduction of electromagnetic effects we observe two main phenomena in our system. At high values of R/L_n the RDW and the InDW are suppressed at $\beta > 2.34\nu L_n/\left[R(1 + 1.71\eta_e)\right]$ and $\beta > 0.34 m_e/m_i$, respectively. When the α_{MHD} threshold is overcome, then the IdBM starts to play a role and we expect the shift of the instability from finite k_y values to the smallest allowed k_y value.

3.4 Examples of linear stability analysis

In this section we use the framework built in Sec. 3.3 to identify and analyze the linear instability present in three typical SOL scenarios. For this purpose we use a linear code that solves the system of Eqs. (3.1) as a function of the toroidal mode number n (see Sec. 2.5 for details) and we identify the dominant instability according to our parameter space, testing the reliability of our analysis by exploring the dependence of the instability on $\hat{s}$ and β. We focus our attention on the following sets of parameters: first, a parameter set with $R/L_n = 10$, $L_y = 1000$, $q = 4$, $\nu = 0.1$, $m_e/m_i = 2.72 \times 10^{-4}$, called "low-gradient"; second, a "high-gradient" parameter set, with $R/L_n = 90$, $\nu = 0.01$, being the other parameters the same as in the first set; third, we apply our analysis to a TCV tokamak [86] L-mode discharge, where the plasma with approximately circular flux surfaces is created close to the high-field side of the machine, creating a scenario that reproduces the toroidal limiter configuration considered here: $R/L_n = 25$, $R/L_T = 35$ $L_y = 1610$, $R = 1025$, $q = 3$, $\nu = 3.16 \times 10^{-3}$, $m_e/m_i = 2.72 \times 10^{-4}$. The parameter sets used are summarized in Table 3.1.

We first consider the low-gradient set of parameters. Our analysis indicates that the SOL corresponding to this parameter set is in the BM dominated regime. In fact, R/L_n is smaller than the threshold value between RBM and RDW, as calculated in Sec. 3.3.1, and it is also smaller than the threshold between InBM and InDW, as calculated in Sec. 3.3.2. Moreover, according to the results shown in Fig. 3.9, since $\sigma_R \simeq 0.44$ and $\sigma_I \simeq 5.25$, the instability belongs to the resistive branch of the BM. We first consider the effect of $\hat{s}$ on the instability. In Fig. 3.13a we show γ as a function of n, for different values of the magnetic shear, in the $\beta = 0$ limit. Our analysis (see Sec. 3.2.1) shows that the maximum expected growth rate is for $1/(2\pi q \sqrt{\gamma_B^{max} \nu}) < k_y < 0.3\gamma_B^{max}$, that in our case corresponds to $0.052 < k_y < 1.73$, therefore, the peak growth rate is expected at $k_y \simeq 1$. Since $k_\parallel \ll k_y$, we can estimate the toroidal mode number as $n \simeq m/q$, where m is the poloidal mode number, thus the interval can also be expressed as $2 < n < 69$. Effectively, the results of the linear code shows that the maximum growth rate, $\gamma \simeq 0.53\gamma_B^{max}$, is reached for $k_y \simeq 0.50$, which corresponds to a toroidal mode number $n \simeq 20$, in agreement with our estimate. We also observe, as expected from the analysis in Sec. 3.2.1, the maximum of the growth rate for $\hat{s} \simeq 1$ (see Fig. 3.3a). The influence of electromagnetic effects is studied in Fig. 3.13b, where we show γ as a function of n for different values of β. We verify the development of the IdBM when the ideal threshold is overcome. At $\hat{s} = 0$ the IdBM growth rate rises up to $0.5\gamma_B^{max}$ when $\alpha_{MHD} \simeq 0.58$, according to the results shown in Fig. 3.3c, and consequently the limit for the development of the IdBM is overcome when $\beta > 1.8 \times 10^{-3}$. According to our observations, we remark a shift of the maximum growth rate from finite k_y towards $k_y \to 0$, typical of the IdBM instability, at the expected β threshold.

Considering the high-gradient parameter set, from the analysis in Sec. 3.3 we conclude that it falls in the parameter space region where the RDW is the fastest
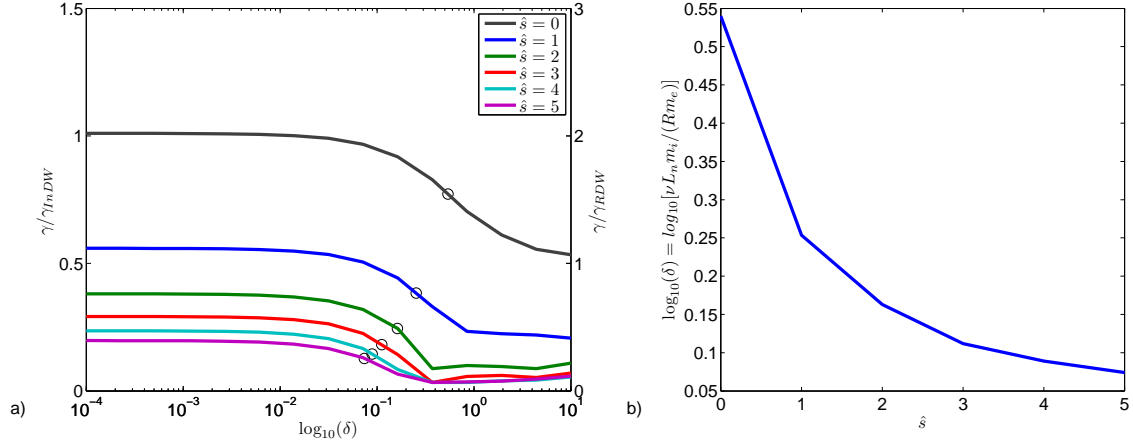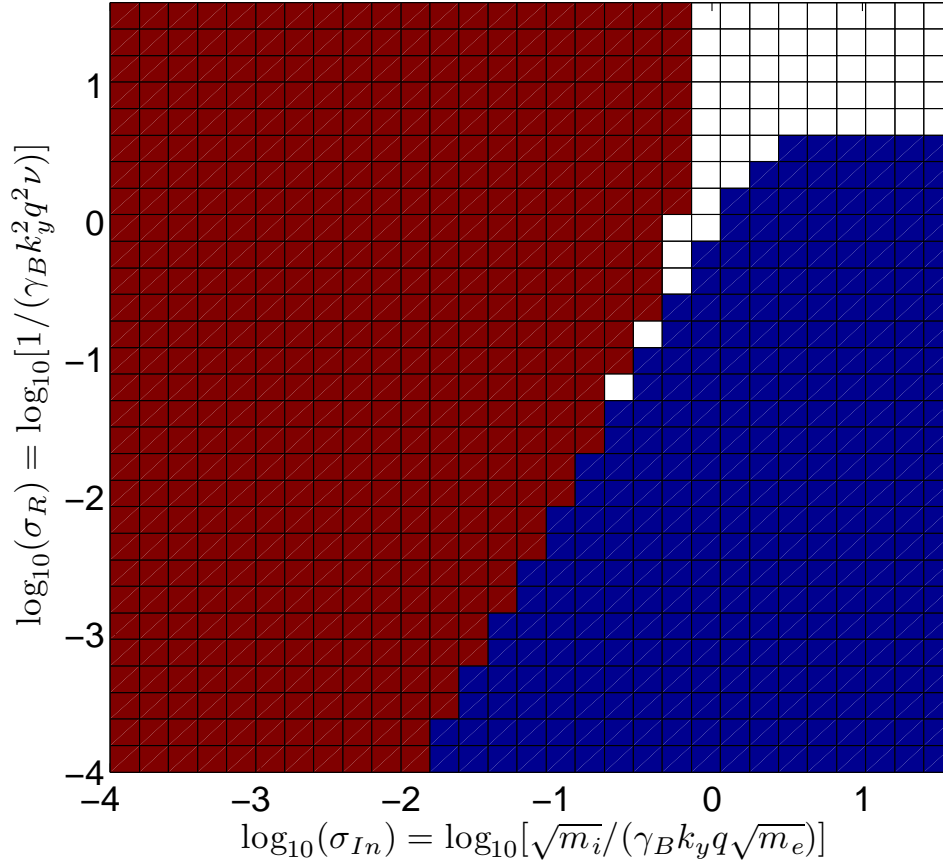
Figure 3.8: *The transition between inertial and resistive drift waves. The drift wave instability growth rate, γ, solution of Eq. (3.11), is plotted as a function of $\delta = \nu L_n m_i / (R m_e)$ and $\hat{s}$ (a) and the value of δ at the transition is plotted as a function of $\hat{s}$ (b)(in (a) the bullets indicate the threshold between the two modes).*

name	$2\pi a$	q	ν	m_e/m_i	R/L_n	η_e
low-gradient	1000	4	0.1	2.72×10^{-4}	10	1
high-gradient	1000	4	0.01	2.72×10^{-4}	90	1
TCV L-mode	1610	3	3.16×10^{-3}	2.72×10^{-4}	25	0.71

Table 3.1: List of the parameters for the three cases analyzed in the linear stability analysis. The TCV L-mode parameter set reflects the equilibrium of shot #42237.

Figure 3.9: *The transition between resistive and inertial ballooning modes. The ratio $\gamma_{InBM}/\gamma_{RBM}$ between the growth rate of RBM, solution of Eq. (3.4), and of the InBM, solution of Eq. (3.7), is plotted as a function of σ_{In} and σ_R; in the red area $\gamma_{InBM}/\gamma_{RBM} > 1$, in the blue area $\gamma_{InBM}/\gamma_{RBM} < 1$, while the white area shows the region where the ratio depends on $\hat{s}$.*
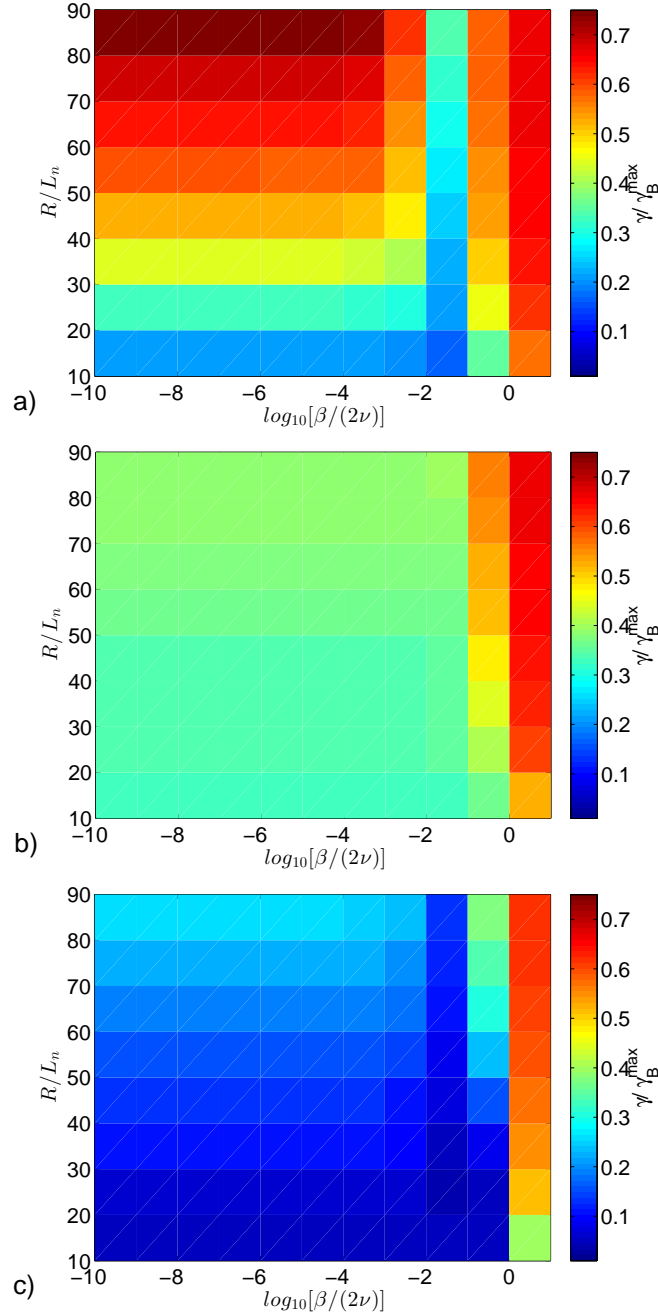
Figure 3.10: *Role of electromagnetic effects on the resistive instabilities. The normalized growth rate γ/γ_B^{max}, solution of Eq. (3.14), is plotted as a function of $\beta/(2\nu)$, R/L_n for $\hat{s} = 0$ (a), $\hat{s} = 1$ (b), and $\hat{s} = -1$ (c).*
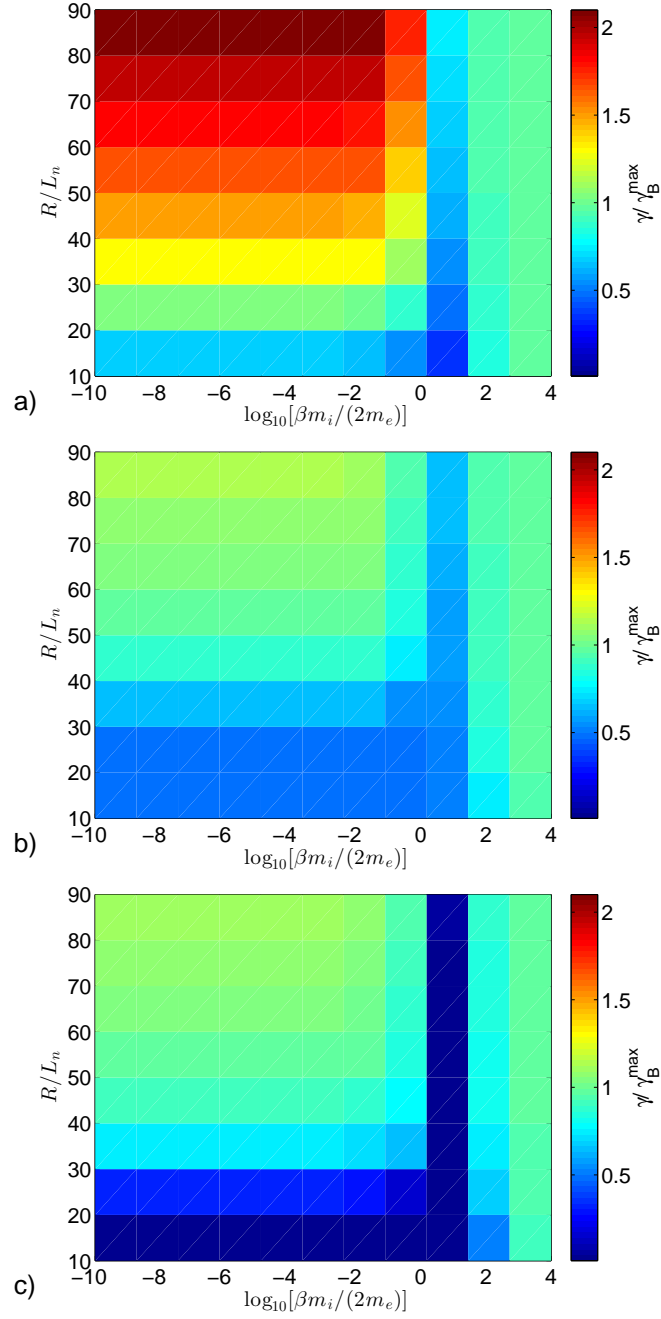
Figure 3.11: *Role of electromagnetic effects on the inertial case. The normalized growth rate γ/γ_B^{max}, solution of Eq. (3.14), is plotted as a function of $\beta m_i/(2m_e)$, R/L_n for $\hat{s} = 0$ (a), $\hat{s} = 1$ (b), and $\hat{s} = -1$ (c).*

growing instability. In fact R/L_n is above both the threshold between RBM and RDW (see Sec. 3.3.1) and the threshold between InBM and InDW (see Sec. 3.3.2). Moreover, according to the results shown in Fig. 3.8, for $\delta \simeq 0.41$ ($\gamma \simeq 34.20$) the DW is in the parameter range of the resistive branch, although marginal influence by inertial effects may be expected. In Fig. 3.14a we show γ as a function of n, for different values of $\hat{s}$, as calculated by the linear code. The maximum growth rate is $\gamma \simeq 32.15$, while, with the considered parameters $\gamma_{RDW}^{max} \simeq 20.73$. The difference is due to the presence of inertial effects, which increases the growth rate with respect to the purely resistive case. The analysis in Sec. 3.2.2 shows that the peak growth rate is expected at $k_y \simeq 0.57$ and, since $k_\parallel \ll k_y$, corresponding to $n \simeq m/q \simeq 22$. The linear code confirms that the maximum growth rate is reached at $k_y \simeq 0.57$ and $n \simeq 22$, close to the poloidal and toroidal mode number estimate. The peak growth rate is observed at $\hat{s} = 0$ and, for both $\hat{s} > 0$ and $\hat{s} < 0$, we remark a decrease of the growth rate, according to the results in Fig. 3.4. We underline that in the linear code the curvature term is retained in all the equations, while in the simplified fluxtube model used to compute the results in Fig. 3.4 it is neglected. This introduces an asymmetric behaviour of the solutions with respect to $\hat{s} > 0$ and $\hat{s} < 0$. Finally, we analyse electromagnetic effects on the RDW instability that we are considering here. In Fig. 3.14b we show γ as a function of n, for different values of β. For $\beta = 1 \times 10^{-4}$ we observe that the growth rate decreases to about $1/3$ of the maximum value obtained for $\beta = 1 \times 10^{-5}$. This is due to the electromagnetic damping of the RDW. The effect starts to be noticeable for $\beta > 2.34 L_n \nu / \left[R(1 + 1.71\eta_e) \right] \simeq 9.59 \times 10^{-5}$, according to Sec. 3.3.5. Since, for the parameters under consideration, the α_{MHD} limit for the IdBM is overcome when $\beta \gtrsim 2.01 \times 10^{-4}$, we note that there is a window of β values in which the RDW instability is suppressed and the IdBM is not unstable. For $\beta = 1 \times 10^{-3}$ we observe the appearance of the IdBM instability, where we note the shift of the maximum growth rate from finite k_y to $k_y \to 0$, as expected for the IdBM instability. The maximum growth rate decreases to $\gamma \simeq \gamma_B^{max} \simeq 18.52$, close to the maximum growth rate of BM instabilities.

Finally we analyze the L-mode discharge in the TCV tokamak. We find that, according to the parameter space analysis, the SOL of this configuration is in the InDW region. In fact, for this set of parameters we evaluate $\delta \simeq 0.46$, $\sigma_R \simeq 20.54$, and $\sigma_{In} \simeq 5.10$, therefore inertial effects partially dominate over resistive effects, as shown in Fig. 3.8. Moreover, since $R/L_n \simeq 25$, we are in the regime where the DW grow faster. The highest growth rate of $\gamma = 10.58$ is reached at $n = 39$ and $m = 112$, corresponding to $k_y = 0.44$; for comparison we note that the maximum InDW growth rate for the considered parameters is $\gamma_{InDW}^{max} = 9.44$ at $k_y = 0.57$. The nature of the instability changes with $\hat{s}$. In fact, at $\hat{s} = 2$ the InBM prevails, with the maximum growth rate of $\gamma = 3.42$ at $n = 13$ and $m = 40$, corresponding to $k_y = 0.16$. At this k_y value, $\sigma_{In} = 43.06$, causing a damping of the growth rate for InBM to $\gamma \simeq 0.3\gamma_B^{max} \simeq 2.78$, according to the parameter space analysis. At $\hat{s} = -2$ both the InBM and the InDW are suppressed.
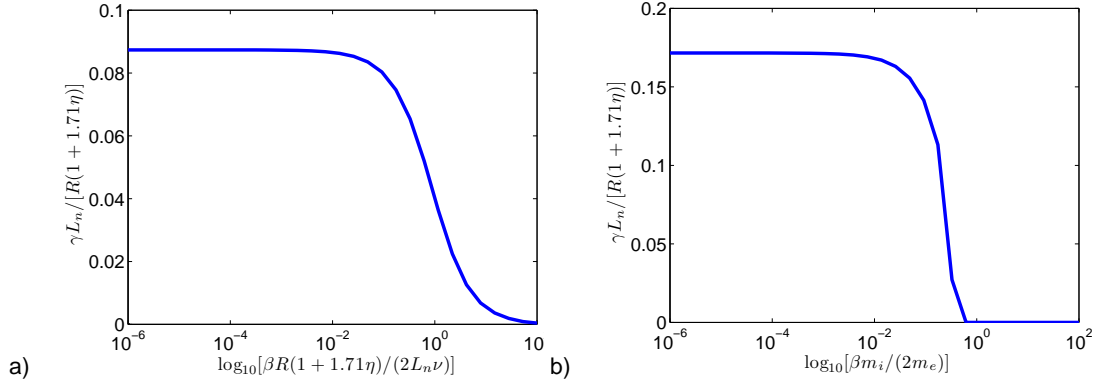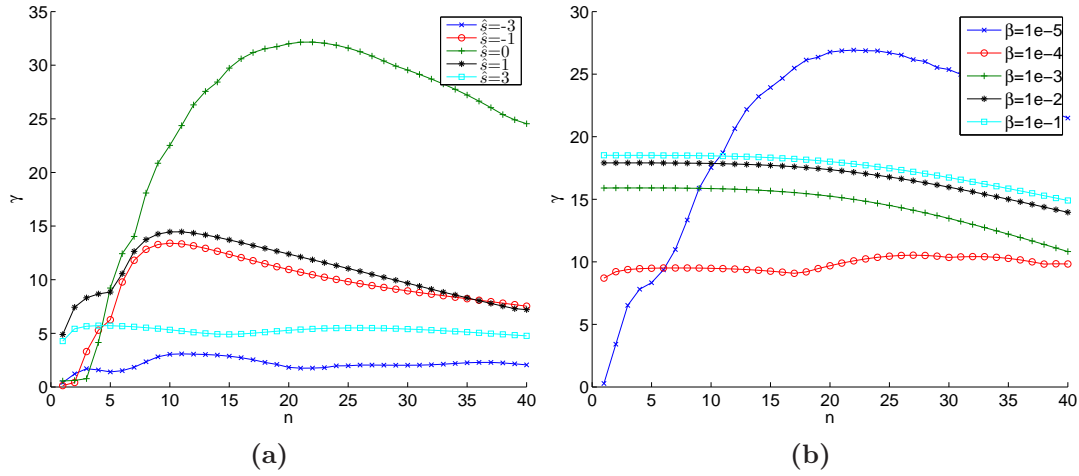
Figure 3.12: *Role of electromagnetic effects on the drift waves: suppression of the drift waves growth rate in the resistive limit (a) and in the inertial limit (b) for increasing β.*
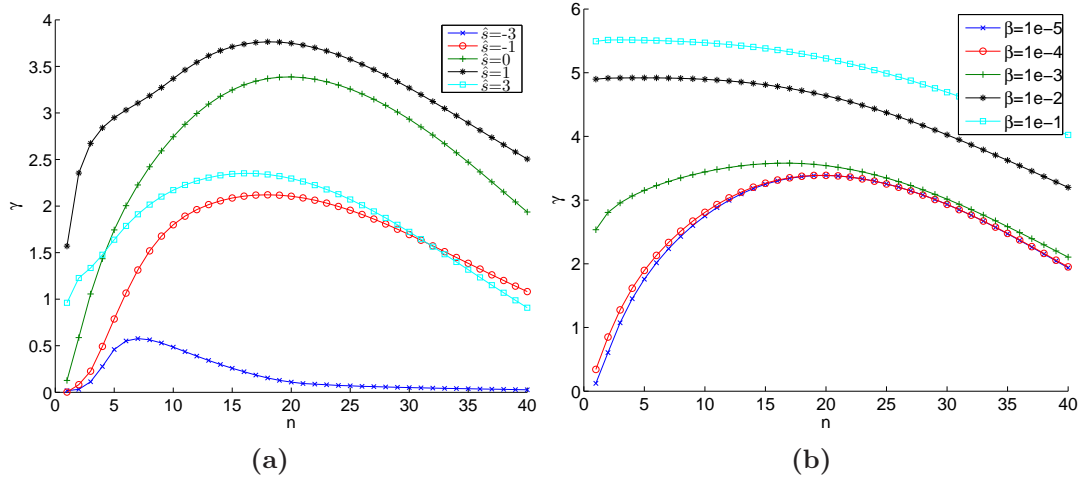
Figure 3.13: *Linear growth rate γ, solution of Eqs. (3.1), as a function of the toroidal mode number n, for different values of $\hat{s}$ (a), and for different value of β (b), for the "low-gradient" set of parameters.*

Figure 3.14: *Linear growth rate γ, solution of Eqs. (3.1), as a function of the toroidal mode number n, for different values of $\hat{s}$ (a), and for different value of β (b), for the "high-gradient" set of parameters.*

3.5 Conclusions

In this chapter we provide a framework to identify the fastest growing instabilities as a function of the parameters characterizing the tokamak SOL region. We have identified the regimes of linear instabilities due to the presence of the resistive and inertial branches of the DW and the resistive, inertial, and ideal branches of the BM. Starting from a detailed analysis of each instability, we have identified the boundaries of the SOL parameter space regions dominated by each mode.

In the electrostatic limit, we observe that DW dominates over the BM at steep gradients. In general, the R/L_n threshold depends on $\sigma_R = 1/(\gamma_B^{max} k_y^2 q^2 \nu)$, $\sigma_{In} = \sqrt{m_i}/\left(\gamma_B^{max} k_y q \sqrt{m_e}\right)$, and $\hat{s}$ (Figs. 3.7a and 3.7b). The transition between RDW and InDW is governed by the $\delta = \nu L_n m_i/(R m_e)$ parameter and it occurs at $\delta \simeq 3.55$ for $\hat{s} = 0$, with the transition value of δ decreasing with the increase of $|\hat{s}|$ (Fig. 3.8). The regions of influence of the RBM and the InBM has been evaluated as a function of σ_R and σ_{In}, the boundary between those is independent of $\hat{s}$ for most of the values of σ_R and σ_{In} and the transition occurs for $\sigma_R \simeq 0.56 \times \sigma_{In}^{1.82}$ (Fig. 3.9). Electromagnetic effects cause, at high R/L_n, the damping of the DW instability at $\beta/(2\nu) \simeq 1.17 L_n/\left[R(1 + 1.71\eta_e)\right]$ in the resistive case, and at $\beta m_i/(2m_e) \simeq 0.17$ in the inertial case (Fig. 3.12). The appearance of the IdBM instability is observed when the $\alpha_{MHD} = q^2 \beta(1 + \eta_e)R/L_n$ threshold is overcome (Figs. 3.10 and 3.11).

We have used our framework to interpret the results of a linear code that evaluates the growth rate of the SOL instabilities. By considering three different sets of SOL parameters, we have identified the main instability governing the physical system in each scenario, showing that we can predict the dependence of each instability on magnetic shear and plasma β.

We notice that in existing tokamaks R/L_n spans one order of magnitude and ν two orders of magnitude (see, *e.g.* Refs. [68, 69, 70, 71, 67, 72, 73, 74, 75]). Both DW and BM instabilities can exist in this range of R/L_n and both resistive and inertial effects are important, and therefore we expect the behaviour of the SOL to change remarkably in these wide intervals of parameters. Our parameter space analysis has been conceived as a first stage tool to be used in the understanding of turbulence in the SOL of tokamaks, necessary to interpret the results of non-linear simulations. This is the subject of Chap. 4 of the present thesis.

Chapter 4

Tokamak SOL turbulence regimes in the cold ion limit

4.1   Introduction

The turbulent regimes in the tokamak SOL are identified according to the linear instability responsible for the perpendicular transport. Four regions of the SOL operational parameters are determined where turbulence is driven by the inertial or resistive branches of the ballooning mode or of drift waves. The linear and non-linear behavior of these modes have been extensively studied [11, 26, 22, 6, 53, 54, 55, 56, 57, 58, 59, 60, 61, 25, 39, 40, 62, 63, 64, 65, 66].

In this chapter we identify the SOL turbulent regimes, determining the instability driving turbulent transport, as a function of the SOL operational parameters. In Chap. 3, we have presented a detailed description of the linear properties of the BM and DW modes, providing also a tool to identify the nature of the fastest growing linear modes, once the SOL pressure gradient length is known. This is a starting point of the present work, where we determine the instability dominating the nonlinear plasma dynamics, *i.e.* the mode that leads to the major contribution to turbulent transport. Here, our analysis considers the pressure scale length as the self-consistent result of the interplay between plasma losses and turbulent transport, and that the mode dominating the nonlinear plasma dynamics does not necessarily correspond to the fastest growing mode. Our study requires therefore the understanding of the mechanism leading to the saturation of the linearly unstable modes. These have been subject of a detailed analysis presented in Ref. [87].

For typical SOL parameters, the saturation is provided by the *gradient removal* mechanism, *i.e.* the saturation of the linear mode due to the non-linear flattening of the driving plasma gradients. The gradient removal theory provides an estimate of the plasma pressure scale length as a function of the SOL operational parameters, in quantitative good agreement with simulation [87] and experimental results [88].

As a consequence, it also allows us to identify the instability that dominates the non-linear dynamics. By studying the nature of this instability, we can determine the SOL turbulent regimes as a function of the SOL operational parameters, *i.e.* the safety factor, q, the magnetic shear, $\hat{s}$, the resistivity, ν and the ion to electron mass ratio, m_i/m_e. With respect to Chap. 3, we consider only the electrostatic limit. As in the rest of the present thesis, our work concentrates on a relatively simple, circular, inner-wall limited configuration. Understanding a circular configuration is a starting point for studying more complicated geometries and regimes. We also report on a set of non-linear simulations that support our methodology to identify the SOL turbulent regimes. The simulations are performed by using the GBS code.

The chapter is organized as follows. After the Introduction, in Sec. 4.2 we describe the gradient removal saturation mechanism at play in the SOL, using which we estimate the equilibrium pressure scale length depending on the SOL operational parameters. In Sec. 4.3 we describe the SOL turbulent regimes, and we present the investigation of the transitions among those. Sec. 4.4 is focused on the description of non-linear simulations carried out with the GBS code, supporting the methodology previously outlined. Finally, we draw our conclusions in Sec. 4.5. The study presented in this chapter has been the object of a recent publication [43].

4.2 Estimate of the SOL plasma gradient length

In the SOL, the plasma pressure scale length results from a balance between turbulent radial transport and parallel losses. Different possible mechanisms have been proposed to provide saturation of the linear modes during the non-linear phase (see, *e.g.*, Refs. [87, 25, 26, 8]), therefore setting the amplitude of the plasma fluctuations and the related radial turbulence level. In Ref. [87], two saturation mechanisms are shown to play a role in the SOL: the growth of the Kelvin-Helmholtz (secondary) instability and the *gradient removal* mechanism, *i.e.* the local flattening of the plasma gradients and associated removal of the instability drive. Analytical estimates and numerical simulations show that the gradient removal saturation mechanism is at play in the typical regime of SOL turbulence [87]. In the following we summarize the main features of the gradient removal mechanism.

Starting from the continuity equation, Eq. (2.93), and the electron temperature equation, Eqs. (2.97), we can derive a relation between the pressure flux and the parallel losses at the limiter plates. Ignoring the curvature terms, and the diffusion, as they are smaller terms in comparison to the $\boldsymbol{E} \times \boldsymbol{B}$ convection and the parallel terms, in the SOL we have:

$$\frac{\partial p}{\partial t} = -R\left[\phi, p\right] - \frac{\partial \left(pV_{\|e}\right)}{\partial z}, \tag{4.1}$$

where the Poisson bracket can be written as $[\phi, p] = \nabla \cdot \Gamma$, being $\Gamma = p\partial_y \phi \boldsymbol{e}_x - p\partial_x \phi \boldsymbol{e}_y$ the adimensionalized pressure flux. Equation (4.1) can be time averaged during the quasi-steady state phase and along the toroidal and poloidal directions. All quantities are written as $f = \overline{f} + \tilde{f}$, being $\overline{f}$ the time average, and $\tilde{f}$ the fluctuating component. As $\partial_z = a/q\partial_y + \partial_{z_\varphi}$, we therefore obtain:

$$\frac{\partial \overline{\Gamma}_x}{\partial x} + \frac{1}{2\pi a} \left. \overline{\Gamma}_y \right|_{\text{limiter}} = -\frac{1}{2\pi qR} \left. \overline{pV_{\|e}} \right|_{\text{limiter}}, \tag{4.2}$$

$\left. \overline{\Gamma}_y \right|_{\text{limiter}}$ and $\left. \overline{pV_{\|e}} \right|_{\text{limiter}}$ are the pressure flux in the poloidal direction and the parallel losses averaged over time and in the toroidal direction, evaluated at the limiter plates. Estimating the parallel losses as

$$\left. \overline{pV_{\|e}} \right|_{\text{limiter}} \simeq \overline{p}\, \overline{c_s}, \tag{4.3}$$

and neglecting the Γ_y, since considerably smaller with respect to Γ_x, we finally obtain:

$$\frac{\partial \overline{\Gamma}_x}{\partial x} \simeq -\frac{1}{2\pi qR} \overline{p}\, \overline{c_s}, \tag{4.4}$$

Equation (4.4) is the balance between radial flux and parallel losses, and it can be estimated as:

$$\frac{\overline{\Gamma}_x}{L_p} \sim \frac{\overline{p}\, \overline{c_s}}{Rq}, \tag{4.5}$$

where L_p is the radial length of the background pressure. We write the radial flux as:

$$\overline{\Gamma}_x = \overline{p}\frac{\partial \overline{\phi}}{\partial y} + \overline{\tilde{p}\frac{\partial \tilde{\phi}}{\partial y}}, \tag{4.6}$$

being the first term on the right hand side of Eq. (4.6) the equilibrium component of the radial flux, and the second term the turbulent part. The equilibrium component of the $\boldsymbol{E} \times \boldsymbol{B}$ flux is negligible compared to the turbulent one, and therefore it is neglected here. We can therefore approximate the radial flux as:

$$\overline{\Gamma}_x \simeq \overline{\frac{\partial \tilde{\phi}}{\partial y}\tilde{p}} \sim k_y \overline{\tilde{\phi}\tilde{p}}, \tag{4.7}$$

being k_y the typical poloidal wavelength of the mode driving transport. We assume that the growth of the linearly unstable modes saturates when the radial gradient of the perturbed pressure becomes comparable to the radial gradient of the background pressure:

$$\frac{d\tilde{p}}{dx} \sim \frac{d\overline{p}}{dx}, \tag{4.8}$$

which can also be written as

$$k_x \tilde{p} \sim \frac{\overline{p}}{L_p}, \tag{4.9}$$

where k_x denotes the typical radial wavevector of the instability. From Eq. (4.9) we obtain an estimate of the perturbed pressure:

$$\tilde{p} \sim \frac{\overline{p}}{L_p k_x}. \tag{4.10}$$

From the leading term of the pressure equation, Eq. (4.1), we can derive an estimate for $\tilde{\phi}$:

$$\gamma \tilde{p} \sim \frac{R}{L_p} k_y \tilde{\phi}, \tag{4.11}$$

from which we obtain:

$$\tilde{\phi} \sim \frac{\gamma \tilde{p} L_p}{R k_y} \tag{4.12}$$

Following non-local linear theory methods outlined in Refs. [39], [36], and [50], we can derive an estimate for k_x for DW and BM that reads as:

$$k_x \sim \sqrt{\frac{k_y}{L_p}}. \tag{4.13}$$

Plugging Eqs. (4.10), (4.12) and (4.13) into Eqs. (4.5) and (4.7), we finally obtain the gradient removal theory estimate for the pressure scale length:

$$L_p \sim \frac{q}{c_s} \left(\frac{\gamma}{k_y} \right). \tag{4.14}$$

Equation (4.14) allows us to predict L_p as a function of the SOL operational parameters: m_e/m_i, ν, q, R/ρ_s, and $\hat{s}$. For this purpose, we first evaluate the growth rate of the linear modes described by the system of Eqs. (2.144)-(2.149), considering the cold ion limit for the present chapter, as a function of k_y and R/L_p, having fixed the SOL operational parameters. We then maximize γ/k_y over k_y, obtaining $(\gamma/k_y)_{\max}$ as a function of R/L_p (with all the other parameters fixed). We then seek for the value of R/L_p that satisfies Eq. (4.14), obtaining our L_p prediction. For simplicity, in the following we assume $\eta_e = 1$. This is justified by simulation and experimental results showing that η_e is of order unity. In fact, in the non-linear simulation results presented herein, $\eta_e \simeq 0.7$, which corresponds to the typical value observed in the simulations [36]. Moreover, limited plasmas realized in the JET, Alcator C-MOD, COMPASS, and Tore Supra tokamaks (Ref. [44] and references therein), covering a wide range of parameter, show $0.3 \lesssim \eta_e \lesssim 1.25$.

The R/L_p estimate as a function of ν and $\hat{s}$ is showed for $q = 4$ in Fig. 4.1a and for $q = 8$ in Fig. 4.1b ($m_i/m_e = 1836$). We observe that the gradient is steeper for negative $\hat{s}$ and low ν, for both the $q = 4$ and the $q = 8$ case. Moreover, for $q = 4$,
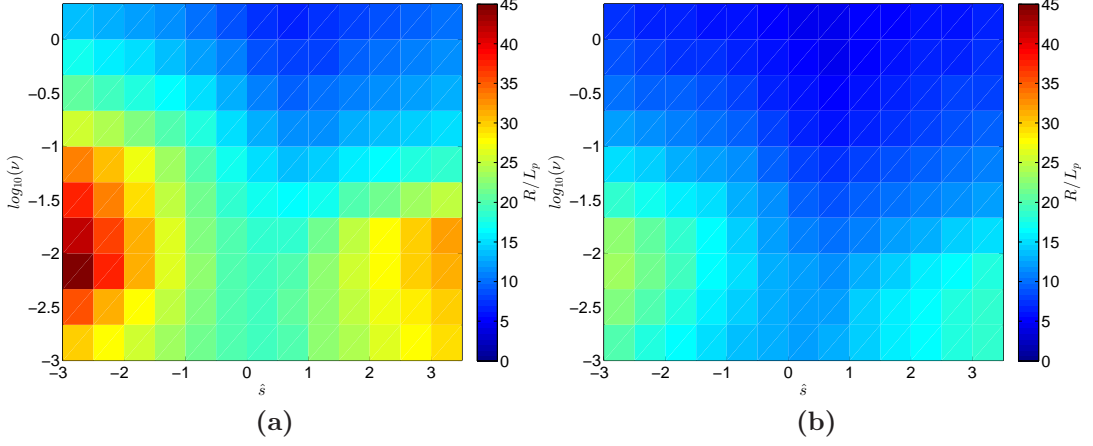
Figure 4.1: *Gradient removal estimate of R/L_p, as a function of $\hat{s}$ and ν for $q = 4$ (a), and for $q = 8$ (b).*

R/L_p is higher than in the $q = 8$ case.

The L_p estimates obtained by the methodology outlined in this paragraph has been successfully compared to experimental data for different tokamaks, showing good agreement, in Ref. [44]. Moreover, Ref. [44] and [89] also report remarkable agreement between the gradient removal L_p estimates and a large set of GBS numerical simulation results.

4.3 The SOL turbulent regimes

As pointed out by our analysis of the SOL linear modes (see Chap. 3), the main instabilities expected to play a role in the SOL are the resistive and inertial branches of the ballooning modes (RBM and InBM) and of the drift waves (RDW and InDW). Ballooning modes have an interchange character and are driven by the presence of magnetic field line curvature and plasma pressure gradients. The dispersion relation that describes the fundamental properties of BMs can be obtained from Eqs. (2.144)-(2.149), in the cold ion limit, by neglecting coupling with sound waves, plasma compressibility, parallel flows in the density and temperature equations, and the $\nabla_\parallel(n + 1.71 T_e)$ term in Ohm's law. The obtained boundary value problem for ϕ reads as:

$$\left[1 + \left(\frac{z}{q}\hat{s}\right)^2\right]\phi\gamma = 2C\frac{R}{L_n}\frac{(1 + \eta_e)}{\gamma}\phi + \frac{1}{\hat{\nu}k_y^2}\frac{\partial^2\phi}{\partial z^2}, \qquad (4.15)$$

where $\hat{\nu} = \nu + \gamma m_e/m_i$. In the limit $\nu \to 0$, Eq. (4.15) reduces to the dispersion relation for the InBM, while for $m_e/m_i \to 0$ the RBM dispersion relation is retrieved, corresponding to Eqs. (3.7) and (3.4) in Sec. 3.2.1, respectively. Both the RBM and InBM growth rates are such that $\gamma/\gamma_I \to 1$, where $\gamma_I = \sqrt{2R/L_p}$, respectively for

$\sigma_R = 1/(\gamma_I k_y^2 q^2 \nu) \to 0$, and $\sigma_I = m_i/(\gamma_I k_y q \sqrt{m_e}) \to 0$ (see Chap. 3). Stabilization of BMs is observed for $k_y \gtrsim 0.3\gamma_I$, due to plasma compressibility. The effect of magnetic shear is a reduction of the growth rate for $\hat{s} \lesssim 0$ and $\hat{s} \gtrsim 1$ (see Ref. [79] and Chap. 3).

The DW instability is driven by the $\mathbf{E} \times \mathbf{B}$ convection of the background pressure gradient, coupled with the breaking of the electron adiabaticity due to finite resistivity or finite electron mass. In order to describe the fundamental properties of the DW, the following equation for ϕ can be used:

$$\gamma k_\perp^2 \phi = \frac{1}{\hat{\nu}} \frac{\partial^2 \phi}{\partial z^2} + \frac{2.94}{\hat{\nu}} \frac{\partial^2 (k_\perp^2 \phi)}{\partial z^2} - \frac{R}{L_n \hat{\nu} \gamma} \left[i k_y \left(1 + 1.71\eta_e \right) \right] \frac{\partial^2 \phi}{\partial z^2}, \qquad (4.16)$$

where the curvature terms in Eqs. (3.1) are neglected as well as the coupling with sound waves. In Eq. (4.16), we retrieve the dispersion relation for the InDW, in the limit $\nu \to 0$, and the RDW dispersion relation for $m_e/m_i \to 0$, corresponding to Eqs. (3.13) and (3.12) in Sec 3.2.2, respectively. Typically $\gamma \sim \omega_*$, where $\omega_* = k_y R/L_n$ is the diamagnetic frequency, $k_y \sim 1$ and $k_\parallel$ assumes a finite value.

Which of these instabilities drives the SOL turbulent dynamics? The goal of the present chapter is to describe the non-linear turbulent regimes as a function of the SOL operational parameters, *i.e.* to understand the nature of the instability responsible for the largest fraction of the radial transport. This is achieved by evaluating the growth rate of InBM, RBM, InDW, and RDW, the inertial and resistive limits of Eqs. (4.15) and (4.16), as a function of the SOL operational parameters, at the k_y and R/L_p given by Eq. (4.14). The turbulent regime is defined according to the instability among those four that has the highest γ/k_y value.

In Fig. 4.2 different colors are used to represent the non-linear turbulent regimes at $q = 4$ and $q = 8$. At both values of q we retrieve some of the linear results of Chap. 3: DWs are the dominant instability at low ν and negative $\hat{s}$, where R/L_n is high. At $\nu \lesssim 10^{-2}$ the dominant instability is the InDW. On the other hand, the BM regime extends in the region where gradients are more relaxed, ($\hat{s} > 0$ and large ν). We also remark that, with respect to $q = 4$, the safety factor $q = 8$ favours BMs. This is in agreement with Chap. 3, which shows that the R/L_n value at which the transition from BMs to DWs occurs is a decreasing function of σ_R and σ_I, meaning that, at higher q, steeper gradients are needed to develop DWs. We finally note that, at $q = 8$, the InBM dominates at the lowest values of ν and positive $\hat{s}$, while it is not present at $q = 4$.

In order to provide a complete and general estimate of the parameter ranges where the different instabilities dominate, we proceed to a more detailed analysis of the transition between the instabilities. More precisely, we evaluate the location in the operational parameters space of the five transitions observed in Fig. 4.2: RBM and InBM, RBM and InDW, RBM and RDW, RDW and InDW, and InDW and InBM.
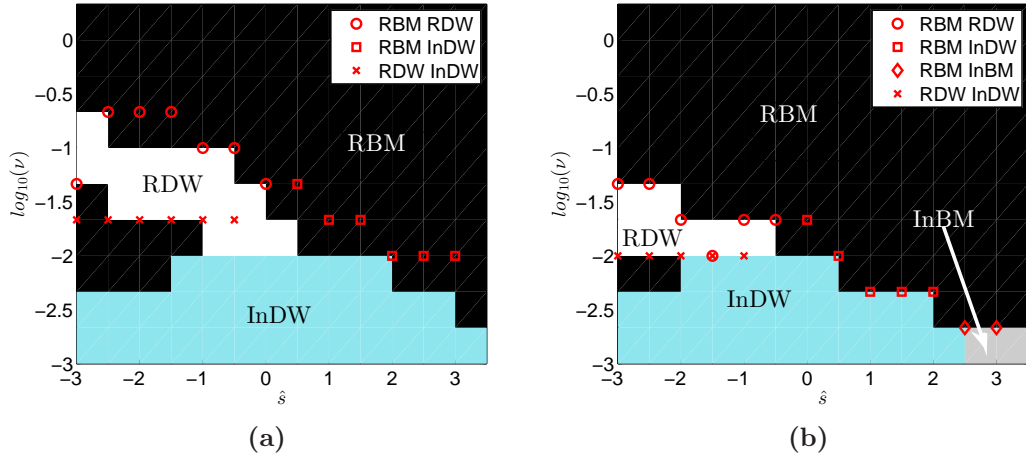
Figure 4.2: *Turbulent regimes for q = 4 (a), and for q = 8 (b); different colors identify different regimes: RBM (black), InBM (grey), InDW (light blue), and RDW (white). The red symbols indicate the estimate of the transition between regimes obtained in Sec. 4.3.*

We first consider the transition between the RBM and the InBM. We use the dispersion relations of the RBM and InBM (the resistive and inertial limits of Eq. (4.15)) to obtain, separately for these two branches, the expected R/L_n and the γ/k_y of the mode dominating the non-linear dynamics. The transition between the RBM and InBM regimes takes place when their γ/k_y are equal, at a ν value that depends on $\hat{s}$ and q, which is plotted in Fig. 4.3a. We note that the white region in Fig. 4.3a represents the parameter region in which the RBM dominates over the InBM independently of ν. This region extends at $\hat{s} < 0$. BMs are, in fact, suppressed by negative shear, and the stabilisation is more efficient for the InBM than for the RBM. For $\hat{s} > 0$, as the threshold occurs at $\nu \sim 1 \times 10^{-3}$, we expect the RBM to prevail over the InBM in typical experimental conditions, where $\nu \sim 10^{-2} - 10^{-3}$.

Following a similar procedure and considering the resistive and inertial limits of Eqs. (4.15) and (4.16) respectively, it is possible to evaluate the transition between the RBM and the InDW. This is shown in Fig. 4.3b, which provides the value of ν above which the RBM prevails over the InDW. We observe that the RBM dominates at positive values of $\hat{s}$ and high q, which are favourable to its growth, as previously noted.

In Fig. 4.3c, we also show the value of ν above which the RBM prevails over the RDW. This is evaluated considering the resistive limit of Eqs. (4.15) and (4.16). The ν threshold diminishes with increasing q and $\hat{s}$. In Chap. 3 it is noticed that the RBM dominates over the RDW for highly positive and highly negative values of $\hat{s}$, and for high values of q, which corresponds to low σ_R. These predictions agree with the findings showed in Fig. 4.3c. In the white region the RBM prevails on the RDW for all values of ν.

In order to accurately describe the transition between RDW and InDW, we follow a slightly different procedure. In fact, as the growth rate of InDW is sensitive to k_y, and k_y can be affected by the inclusion of even a small resistivity, we cannot decouple the two instabilities. Therefore, we compute the expected R/L_n by considering, for the gradient removal mechanism, the linear growth rate given by Eq. (4.16), which includes both RDW and InDW. At the R/L_n and k_y found, we then calculate the RDW and InDW growth rates, which we compare, finding the value of ν above which the RDW prevail over the InDW, as a function of $\hat{s}$ and q. This is shown in Fig. 4.3d. We note that the transition is symmetric with respect to $\hat{s} = 0$, as a consequence of the symmetry of Eq. (4.16). The RDW onsets at values of ν decreasing with q. This is different than the conclusions reported in Chap. 3, where the transition between the peak growth rate of two instabilities was shown to depend on $\hat{s}$ and to be independent of q.

Finally, we consider the transition between the InBM and the InDW. To estimate this transition, we consider the inertial limits of Eqs. (4.15) and (4.16), which are independent of ν, as it is our estimate of the transition between these two instabilities. We find that, for $\hat{s} \lesssim 1$, the InDW prevail over the InBM for all the values of q. For $\hat{s} \gtrsim 1$ InBM dominates over InDW above a q values that varies approximately linearly from $q \simeq 10$ at $\hat{s} = 1$ to $q \simeq 7$ at $\hat{s} = 3$. The InBM is therefore the leading instability for high q and for $\hat{s} > 0$; this generally agrees with the observations presented in Chap. 3.

We can now use the transition estimates discussed above to explain the SOL non-linear regimes displayed in Fig. 4.2. Our estimates are plotted by using red symbols, showing a good agreement with the observed transitions. For $q = 4$ and for $q = 8$, for $\hat{s} < 0$, from low to high values of ν, we essentially observe the transition between three regimes: InDW, RDW and RBM. According to the results in Figs. 4.3d and 4.3c, the transition between the InDW and the RDW, and between the RDW and the RBM, respectively, occur at higher ν for $q = 4$ with respect to $q = 8$.

For $\hat{s} > 0$ we observe that the RDW regime disappears as the RBM prevails on the RDW (see Fig. 4.3c). At $q = 4$, we observe the presence of two regimes; InDW and RBM from low to high ν, while at $q = 8$, at the highest $\hat{s}$ and lowest ν values, also the InBM instability appears, in agreement with the results in Fig. 4.3a. We also observe that the RBM prevails on the InDW for smaller values of ν with respect to the $q = 4$ case (see Fig. 4.3b, where the ν threshold between RBM and InDW decreases with increasing q). Finally, we note that the application of our SOL turbulent regime analysis for predicting the turbulent regime of a typical L-mode discharge in the TCV tokamak [86] (for $\nu \simeq 10^{-2}$, $q \simeq 5$ and $\hat{s} \simeq 2$) points to the RBM regime.
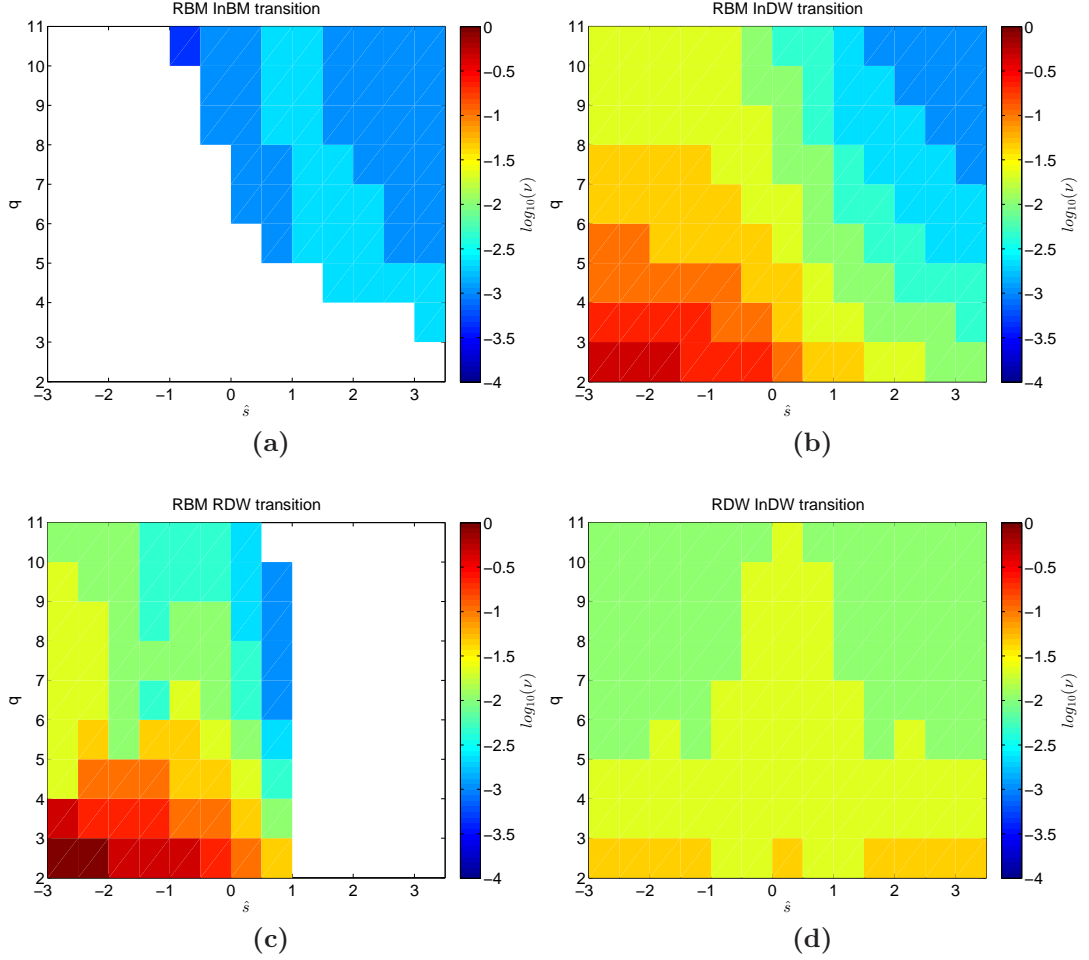
Figure 4.3: *Value of ν, as a function of $\hat{s}$ and q, of the transition between RBM and InBM (in the white region RBM prevails on InBM independently of ν) (a), transition between RBM and InDW (b), transition between RBM and RDW (in the white region RBM prevails on RDW independently of ν) (c), and transition between RDW and InDW (d). In all cases the first instability prevails over the second one at ν values larger than the ones plotted.*

4.4 Non-linear simulations

In Secs. 4.2 and 4.3 the equilibrium gradient length, L_p, and the instability regimes are predicted, based on the gradient removal theory and the evaluation of the linear growth rate. Here we present the results of non-linear simulations of SOL turbulence that support our methodology to determine the SOL turbulent regimes. The simulations have been performed using the GBS code, described in Chap. 2.

Typical SOL simulations results are described in Ref. [20]. The plasma outflow from the core is mimicked by a density and a temperature source, S_n and S_T, defined as $S_{n,T} = \exp\left\{-\left[(x-x_s)^2/\sigma_s^2\right]\right\}$, with $x_s = 30$ and $\sigma_s = 2.5$. Other simulation parameters are the major radius, $R = 500$, and the domain dimensions, $L_x = 100$ and $L_y = 800$. After an initial transient, a non-linear quasi-steady regime is reached, as a balance between plasma outflow from the core, turbulent transport and parallel losses at the vessel. Our analysis is focused on this quasi-steady state regime. Among a number of simulations that we have carried out, we focus and we present the results of four simulations that belong to the four predicted instability regimes: RBM, InBM, RDW, and InDW. The plasma parameters of these four simulations are listed in Table 4.1. We first estimate the equilibrium R/L_p, using the gradient removal theory, and we compare our prediction with the results of the non-linear simulations. As reported in Table 4.1, our estimates show reasonable agreement with the simulations results, the maximum relative error being approximately 40%. In Table 4.1 we also compare the gradient-removal predicted k_y of the dominant mode with the time averaged k_y of the mode leading to the maximum turbulent flux in the simulations. The uncertainty affecting k_y is estimated by considering a 10% variation of the γ/k_y value with respect to its maximum at the predicted R/L_p (for comparison, we note that the standard deviation of the time averaged particle flux, proportional to γ/k_y, is approximately 25% of the time averaged particle flux). We verify that all the non-linear simulations studied herein satisfy the inequality $\sqrt{k_y L_p} < 3$ [87], and that they belong to the regime where the gradient removal mechanism is responsible for turbulence saturation. In Table 4.1, we list the growth rate of each instability separately, in order to identify the regime of the four simulations. A detailed description and analysis of the properties of the non-linear simulations follows, in order to identify and discuss the nature of the transport.

Figs. 4.4-4.7 show the pressure equilibrium profiles, $\overline{p}$, and typical snapshots of the pressure fluctuation, $\tilde{p}$, in the (x, y) plane, for the identified RBM, InBM, RDW and InDW simulations, respectively. We define $\overline{p}$ as the time and toroidal average of the pressure, evaluated during the quasi-steady state phase of the simulation, and we calculate the fluctuating part of the pressure as $\tilde{p} = p - \overline{p}$. We now discuss a number of tests that show that it is justified to identify the turbulent regime according to the procedure used in Sec. 4.3.

First, for an identified resistive mode, a simulation with a reduced value of m_e/m_i is performed, or, for an identified inertial mode, we carry out a simulation

with reduced ν. As shown in Figs. 4.4-4.7, the change in the radial equilibrium gradient length and the radial extent of the fluctuations is small, confirming our prediction of being in a resistive or inertial regime.

Second, in the four simulations considered, we turn off the interchange drive (ID), *i.e.* the curvature terms in the vorticity equation. We can infer the BM nature of turbulence, by observing major effects following the ID turn off, while small changes point to a DW regime. For BM simulations we remark that the average profiles in Figs. 4.4 and 4.5 lose their ballooning character once the ID is turned off, R/L_p becomes steeper, and the long streamers are broken into smaller structures in the case without ID (therefore k_x increases). This is due to the fact that, while k_y does not change significantly, L_p decreases from the base case to the case without ID, and therefore k_x increases, according to the non-local estimate of the radial eddy extension. For DW simulations, instead, there is no observable difference between the equilibrium profiles, following the ID turn off, and the nature of the fluctuations is very similar (see Figs. 4.6 and 4.7). Moreover, in the simulation with and without ID, the plasma profile is weakly dependent on the poloidal angle, showing a non-ballooning character. We conclude from this analysis that our simulations can be classified as BM or DW dominated, as pointed out by our methodology.

Finally, in order to reinforce the validity of our analysis, we analyze the relation between potential and density fluctuations, according to the methods proposed in Refs. [11] and [25]. For BMs, the vorticity equation imposes a $\pi/2$ phase shift between ϕ and n fluctuations, which are not correlated. In case of DWs, the electrons are close to adiabaticity and the amplitudes of ϕ and n fluctuations are clearly correlated [22], [25]. Following Ref. [25], we introduce two analysis techniques to investigate the relation between ϕ and n: the phase shift probability and the cross coherence analysis.

The phase shift probability is calculated at a fixed radial position, by considering the FFT along y of the ϕ and n fluctuations, as a function of toroidal position and time. From the FFT, we then compute the phase shift, $-\pi \leq \chi < \pi$, corresponding to each k_y, and we bin them as a function of the toroidal position and time, with the proper weight given by the power spectral density of the ϕ and n fluctuations. The phase shift probability between ϕ and n is showed in Fig. 4.8. As expected, for the BM simulations (Figs. 4.8a and 4.8b), the phase shift has a maximum at $\chi \approx 0.5\pi$ for the dominant mode $k_y \approx 0.1$. For DW simulations (Figs. 4.8c and 4.8d), we observe a phase shift with a maximum at $\chi \approx 0$ for the dominant mode $k_y \approx 0.1$.

The cross coherence is computed at a fixed radial position. The ϕ and n fluctuations are considered as a function of the poloidal and toroidal directions, and time, and normalized to their standard deviation. We then evaluate the probability of finding both fluctuations at a certain ordered pair of amplitudes and we display it in Fig. 4.9. The cross coherence in Figs. 4.9a, for the RBM, and 4.9b, for the InBM, does not show correlation between ϕ and n, while the cross coherence in Figs. 4.9c,

for the RDW, and 4.9d, for the InDW, shows a high correlation between ϕ and n fluctuations. This additional analysis supports our methodology to identify the turbulent regime of the non-linear simulations.

4.5   Conclusions

In the present chapter we have identified the non-linear SOL turbulent regimes as a function of the SOL operational parameters (q, ν, $\hat{s}$, and m_i/m_e) depending on the instability responsible for the non-linear transport. We have assumed that the linear instabilities are saturated when the plasma pressure gradient is non-linearly flattened by the growth of the unstable modes. This has allowed us to predict the time-averaged plasma gradient length, which is proportional to γ/k_y, where γ is the linear growth rate and k_y the poloidal wavenumber of the instability that dominates the non-linear dynamics.

We note that a number of modes are possibly unstable in the edge and SOL regions of tokamak plasmas. While the instabilities playing a major role in the tokamak SOL are believed to be the resistive and inertial branches of BMs and DWs, peeling-ballooning modes, external kinks, and sheath modes [76,77,78] might also become unstable. In the cold-ion regime considered here, ion temperature gradient modes [6,60] are excluded, while trapped electron modes are also stable in the SOL due to the fact that the bounce frequency of trapped electrons is smaller than the collision frequency.

In the present study we have focused our attention exclusively on the resistive and inertial branches of BMs and DWs. Using simplified models that retain the basic linear characteristics of these instabilities, we have built a map in the operational parameter space, defining the region in which each instability drives transport (see Figs. 4.2a and 4.2b for $q = 4$ and $q = 8$). We have observed that DWs prevail at negative shear, InDW dominates at low ν, while positive shear and high q are favourable for BMs. We have investigated the transition among the different instabilities (the RBM-InBM, the RBM-InDW, the RBM-RDW, and the RDW-InDW transitions) determining, in general, the threshold value of ν at which they take place. This is shown in Fig. 4.3. Being the transition between InBM and InDW independent of ν, we have estimated the value of q at which this transition takes place as a function of $\hat{s}$. The estimates are in good agreement with the transitions observed with the full model.

In order to verify the validity of our methodology, we have performed a set of non-linear simulations, and we have presented four of those, each belonging to a different instability regime. The simulations have been carried out with GBS. For each set of SOL parameters of the non-linear simulations, we have predicted the instability regime, R/L_p, and the k_y of the saturated non-linear mode, according

to the gradient removal hypothesis. The predictions and the results of the non-linear simulations show reasonable agreement. In particular, the analysis of the turbulence character (see Figs. 4.4-4.9) supports our methodology to identify the non-linear turbulent regimes.

We remark that our analysis leads not only to the identification of the SOL turbulence regimes, but also to the prediction of the steady state gradient and poloidal wavelength at saturation, and therefore to the prediction of the main turbulence properties. The model that we have presented is relatively simple and constitutes a framework which can be generalized to the analysis of more complicated SOL configurations.

(a)

(b)
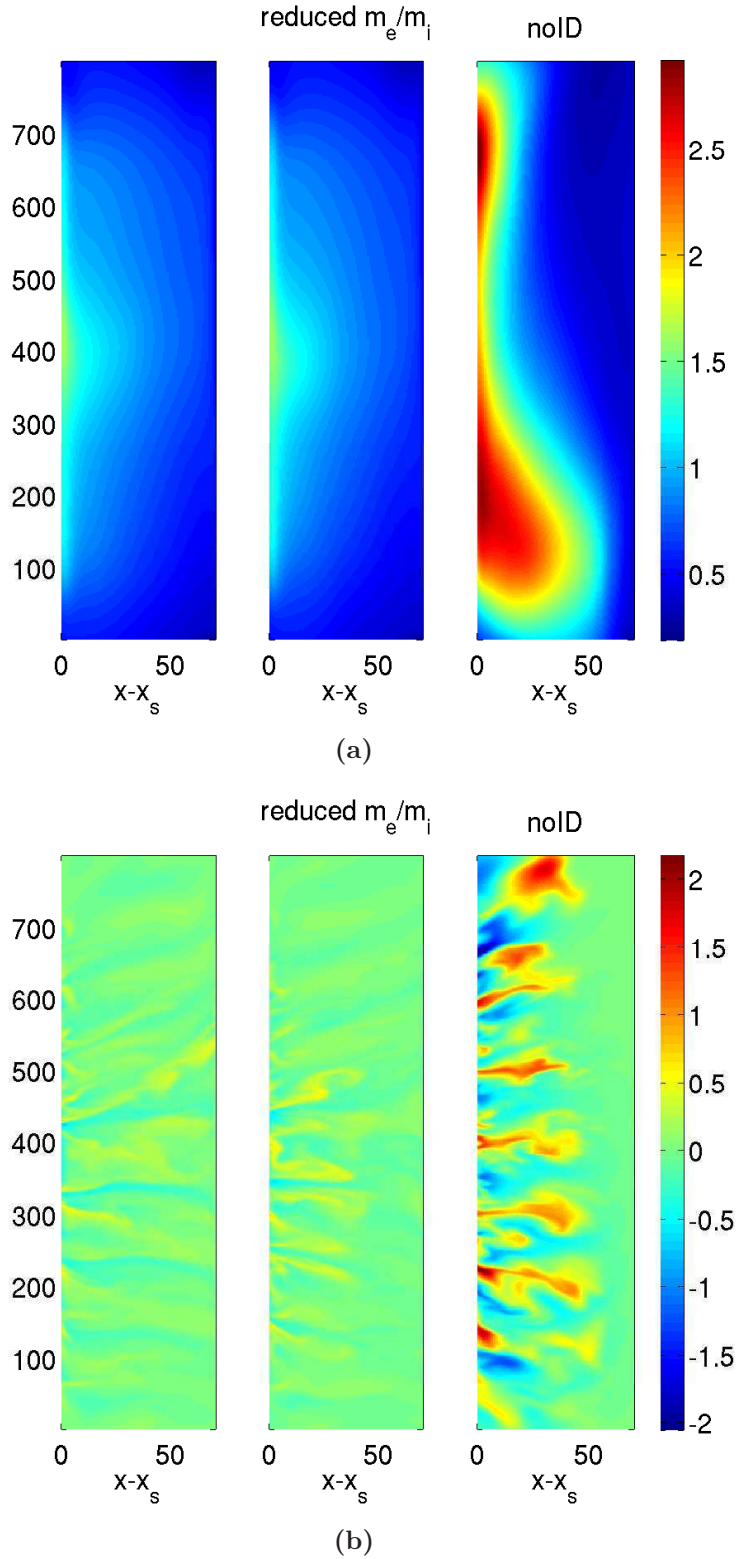
Figure 4.4: *Pressure equilibrium profile (top panels) and pressure fluctuation profile (bottom panels) in the $x - y$ plane for RBM simulation (left), the RBM with reduced m_e/m_i (center), and the RBM without ID (right). x_s is the radial position of the last closef flux surface, where the plasma source is located.*
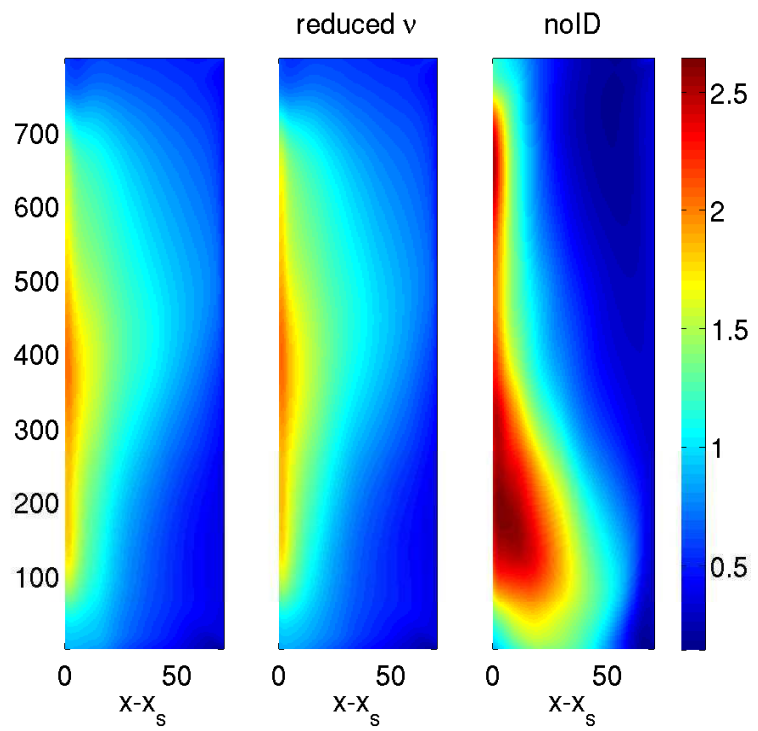
(a)
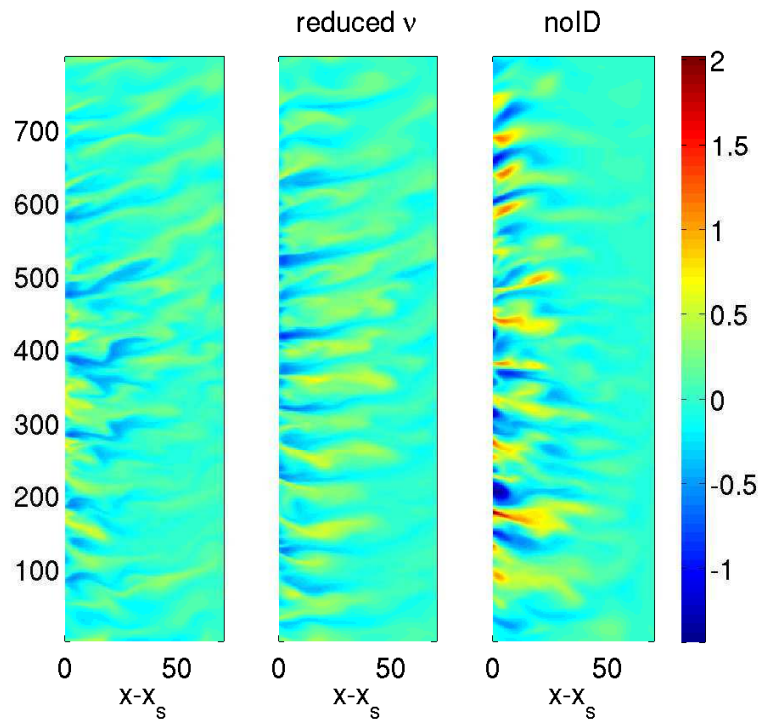
(b)

Figure 4.5: *Same as Fig. 4.4, for the InBM.*

(a)

(b)
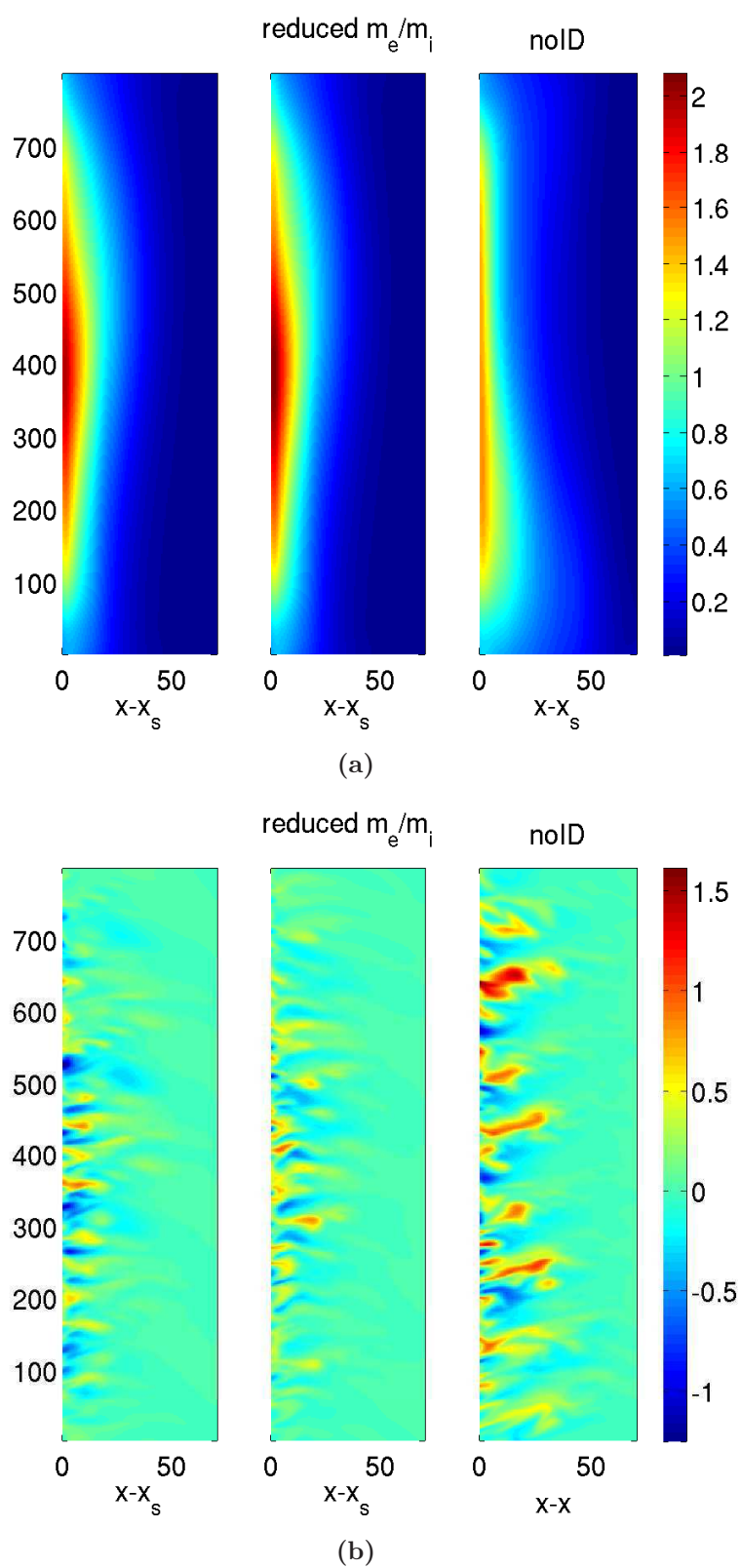
Figure 4.6: Same as Fig. 4.4, for the RDW.
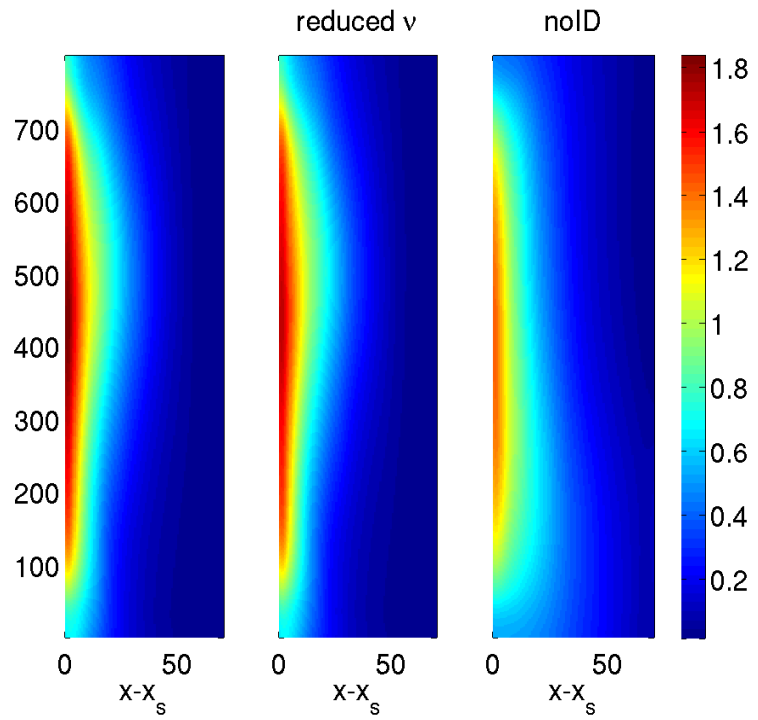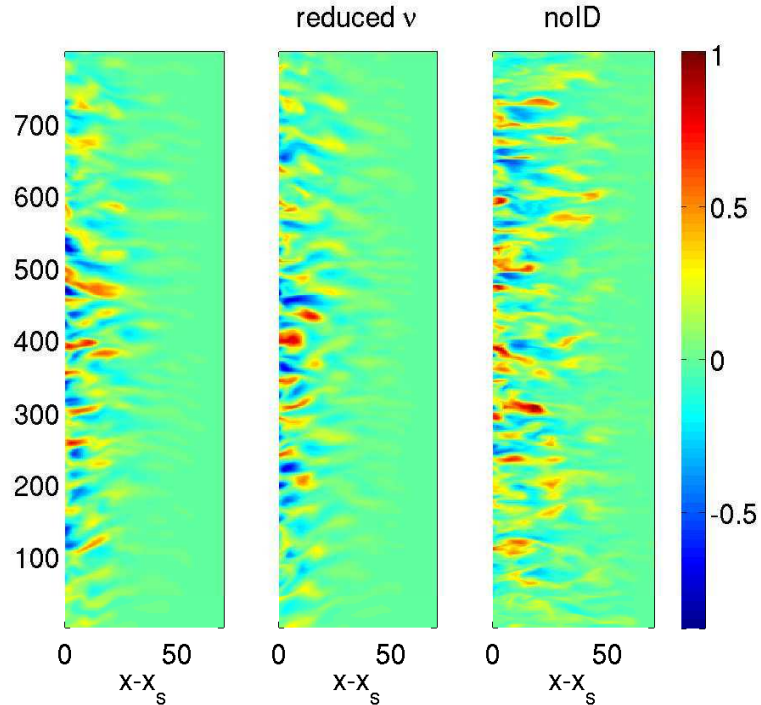
Figure 4.7: Same as Fig. 4.4, for the InDW.
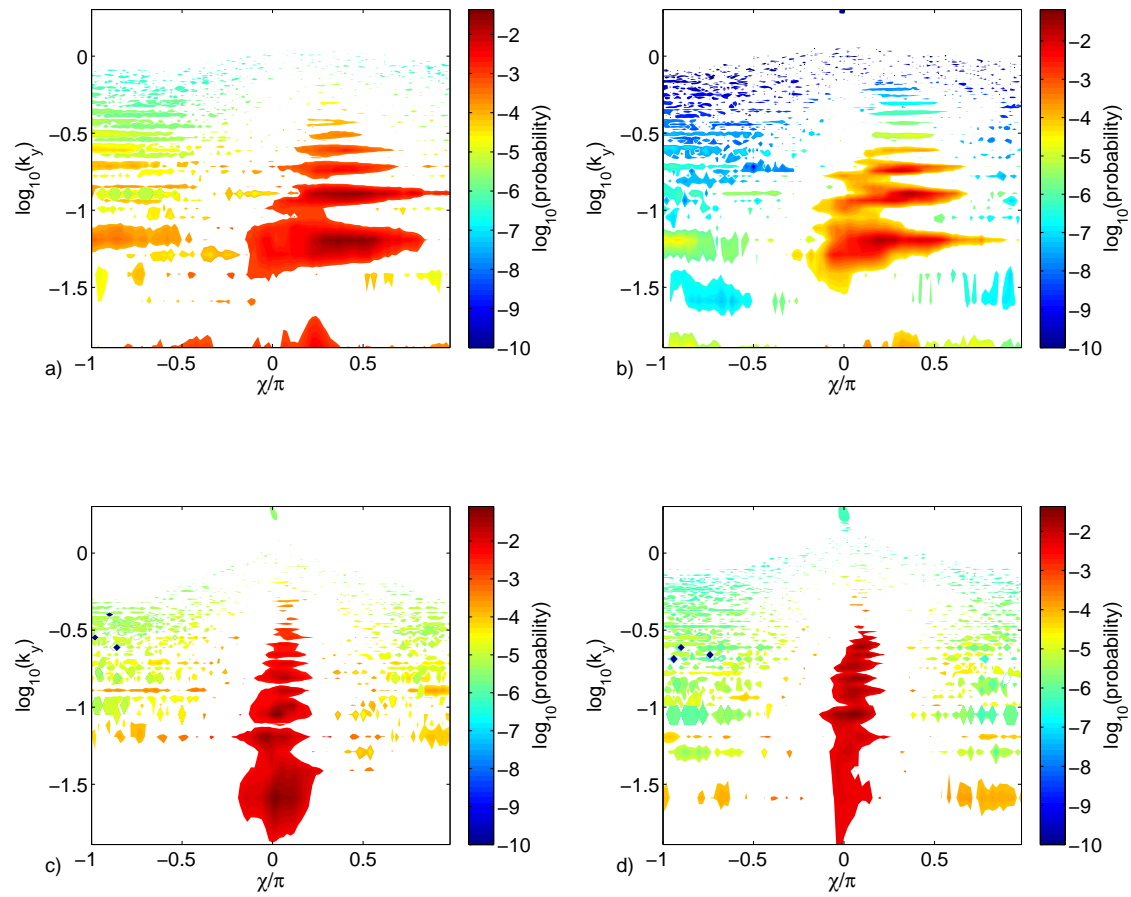
Figure 4.8: *Phase shift probability between ϕ and n weighted according to the power spectral density for the RBM (a), InBM (b), RDW (c), and InDW (d).*
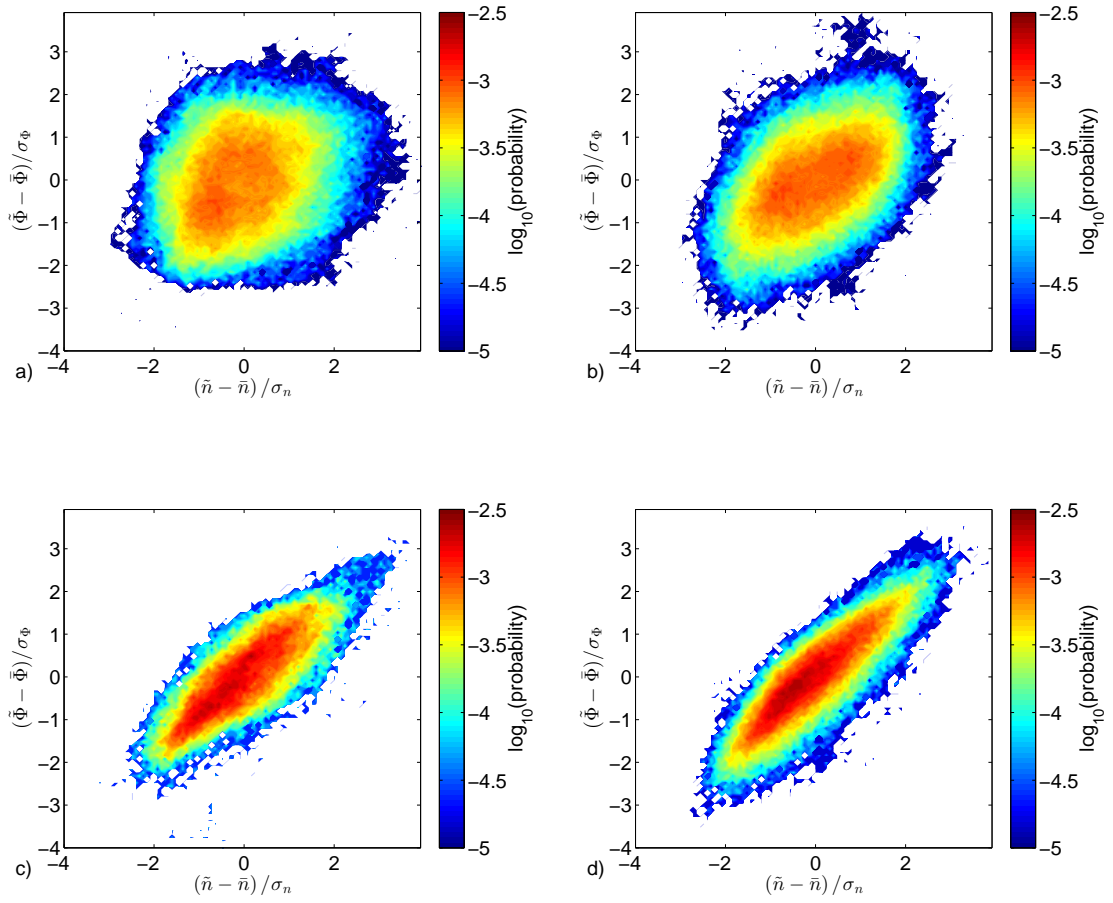
Figure 4.9: *Cross coherence between ϕ and n for the RBM (a), InBM (b), RDW (c), and InDW (d).*

simulation	ν	m_e/m_i	$\hat{s}$	q	ID	R/L_p simulation	R/L_p estimated	k_y simulation	k_y estimated	$k_{y,min}$ estimated	$k_{y,max}$ estimated	γ_{RBM}	γ_{InBM}	γ_{RDW}	γ_{InDW}
RBM	0.5	1/800	1	8	on	4.42	5.35	0.09	0.04	0.03	0.06	2.28	$\simeq 0$	0.12	$\simeq 0$
RBM reduced m_e/m_i	0.5	1/1600	1	8	on	7.26	/	/	/	/	/	/	/	/	/
RBM without ID	0.5	1/800	1	8	off	18.93	/	/	/	/	/	/	/	/	/
InBM	0.005	1/50	1	8	on	8.68	8.09	0.09	0.10	0.08	0.14	0.64	2.88	0.01	1.05
InBM reduced ν	0.0005	1/50	1	8	on	9.51	/	/	/	/	/	/	/	/	/
InBM without ID	0.005	1/50	1	8	off	18.94	/	/	/	/	/	/	/	/	/
RDW	0.05	1/800	-0.7	4	on	28.21	18.07	0.15	0.16	0.12	0.20	1.20	$\simeq 0$	1.46	$\simeq 0$
RDW reduced m_e/m_i	0.05	1/1600	-0.7	4	on	29.32	/	/	/	/	/	/	/	/	/
RDW without ID	0.05	1/800	-0.7	4	off	30.13	/	/	/	/	/	/	/	/	/
InDW	0.005	1/200	-1	4	on	28.72	16.90	0.18	0.17	0.14	0.21	0.13	$\simeq 0$	0.03	2.92
InDW reduced ν	0.0005	1/200	-1	4	on	28.39	/	/	/	/	/	/	/	/	/
InDW without ID	0.005	1/200	-1	4	off	22.79	/	/	/	/	/	/	/	/	/

Table 4.1: Parameters for the non-linear simulations. The domain dimensions are $L_y = 800$ and $L_x = 100$. The major radius is $R = 500$. The radial window over which the non-linear R/L_p and k_y are evaluated is $5 < x - x_s < 17$. The two values $k_{y,min}$ and $k_{y,max}$ are computed considering the k_y range corresponding to a 10% variation of the value γ/k_y with respect to its maximum at the R/L_p and k_y predicted.

Chapter 5

Hot ion effects on SOL turbulence

5.1 Introduction

Ion temperature determines the sputtering yields of the materials in contact with a plasma. Therefore, both in the steady state and during transient events (such as ELMs), understanding the mechanisms regulating the ion temperature in the tokamak SOL is important for estimating the lifetime of the materials of the first wall.

As a matter of fact, because of its critical role, in the last years an increased effort has been devoted to the ion temperature measurement in the tokamak edge. While most of the experimental campaigns are based on the use of retarding field analyzer probes (see Ref. [90] and references therein for a review of measurements before 2010, and Refs. [91, 92, 93, 94, 95] for more recent experimental campaigns), also other techniques are employed, such as the charge exchange recombination spectroscopy [96], the ion sensitive probe [97], or the pinhole probe [98]. In Ref. [90] a collection of T_i/T_e measurements from a number of tokamak SOL has been examined, showing values that range from the lower $T_i/T_e \sim 1$ to the extreme $T_i/T_e \sim 10$, with most of the data falling between 1 and 4 (see, *e.g.*, Ref. [90] and references therein for measurements taken before 2010, and, for more recent measurements, Ref. [92] for HL-2A, Ref. [93] for MAST, and Refs. [96, 97] for Alcator C-MOD). The ion temperature is therefore usually higher than T_e in the SOL. Moreover, in Ref. [90], the SOL e-folding lengths for T_e and T_i are shown for different tokamaks, indicating that the electron profile is usually steeper than the ion profile, leading to $\eta_e(= L_n/L_{T_e}) > \eta_i(= L_n/L_{T_i})$. The η_i value has been measured, *e.g.* during limited discharges in Tore Supra [99], and during diverted discharges in JFT-2M [100] resulting in $\eta_i < 1$ in both cases.

The numerical simulation of edge turbulence in the presence of ion temperature dynamics has been subject of numerous studies [6, 35, 60, 101, 22, 21, 25, 9, 102]. Ion temperature gradient is responsible for the rising of an instability called ion temperature gradient (ITG) (see, *e.g.*, Ref. [6]), which can drive cross-field transport

of particles and energy. Moreover, T_i effects have an impact on SOL instabilities that exist in the cold ion limit, as BM and DW instabilities. In general, both the ratio between the background ion and electron temperature, $\tau = T_{i0}/T_{e0}$, and η_i, are found to be the crucial parameters for determining the role of ITG turbulence in the SOL, and of the T_i effects on other instabilities. Zeiler et al. [35, 60, 6, 101], describe the linear and non-linear transition between RBM and ITG driven turbulence in the SOL by using a gradient-driven flux-tube code [22], identifying the non-linearly prevailing instability as a function of the gradient scale length and the α_d parameter, that represents the ratio between the diamagnetic frequency and the BM growth rate. It is found that at steep gradients the RBM drives turbulence when diamagnetic effects are negligible (small α_d) and it is overpowered by the non-linear drift wave instability for increasing values of α_d. The ITG instability dominates instead at high values of α_d and broad gradients. In a later study [101], Hallatschek and Zeiler focus on non-locality effects on the transition between RBM and ITG, finding a general quenching of the instability when the turbulence scale length becomes comparable to the gradient scale length (increasing non-locality). Scott et al. also developed a suite of numerical tools for the simulation of the SOL turbulence with ion dynamics; in particular, the fluid DALF code [21, 25] and the gyrofluid GEM code [25, 103]. The ITG signature is identified in large and dominant T_i fluctuations associated with a higher ion with respect to electron radial transport [21].

The goal of our investigation is to improve the understanding of the role of hot ions in SOL turbulence. First, we study T_i effects on the SOL linear instabilities that exist also in the cold ion limit, and we introduce the main properties of the ITG instability. Second, we identify the SOL turbulent regimes based on the instability that drive the non-linear transport as a function of the SOL operational parameters. The methodology we use to identify the non-linear SOL instability is supported by the analysis of GBS simulations. The GBS code represents an ideal tool to study T_i effects on SOL turbulence, as it is capable of simulating self-consistently the SOL instabilities and the formation of the plasma profile, allowing fluctuations of the same order of the background quantities.

The drift-reduced Braginskii model we use includes the effect of the polarisation drift in the T_i equation, that become important for $k_y \rho_s \sim 1$ (see Refs. [60] and [103]). Nevertheless, FLR effects contained in the stress tensor are neglected, and the electric potential is evaluated at the particle gyrocentre contrary to what it is done in gyrofluid models (see, *e.g.* Ref. [17]). We also remark that other effects present in collisionless plasmas, such as trapped particles and wave-particle resonances, are not contained in the Braginskii equations. Therefore our model does not describe accurately perturbations with a perpendicular wavelength of the order of ρ_i, or where kinetic effects are important. However, for typical SOL parameters, turbulence is dominated by modes with perpendicular scales much larger than ρ_i, and kinetic effects are expected to be negligible due to the large collisionality, justifying our model assumptions.

The present chapter is organized as follows. Section 5.2 discusses qualitatively the results of non-linear GBS simulations with hot ions. Ion temperature effects on the linear SOL instabilities are presented in Sec. 5.3. In Sec. 5.4 we first define the role of the ITG instability in SOL turbulence, defining under which conditions the RBM, the ITG, or the DW drive SOL turbulence. Then, we estimate the non-linear prevailing instability and we compare our expectations to the GBS results. Finally, in Sec. 5.5, we draw our conclusions.

5.2 Non-linear turbulence simulations with hot ions

In order to study the influence of the ion temperature on SOL turbulence, we perform a series of non-linear simulations, having set $\hat{s} = 0$, $\nu = 0.1$, $m_e/m_i = 1/200$, $L_y = 800$, $L_x = 100$, and $R = 500$, while τ is varied from 0 to 4. In Fig. 5.1 we present a poloidal cross section of the different fields evolved during the simulation with $\tau = 1$: the density, n, the electron temperature, T_e, the ion temperature, T_i, the vorticity, ω, the electron parallel velocity, $V_{\parallel e}$, and the ion parallel velocity, $V_{\parallel i}$.

The plasma injected from the core is transported radially by streamers elongated in the radial direction. This is visible in the ion temperature snapshot, which is similar to the electron temperature and the density snapshots (this in not surprising, since the nature of the equations governing these quantities is similar). The analysis of the ion and the electron parallel velocities show that the particles flow towards the limiter plates, although fluctuations of the electron parallel velocity field are larger than the ion ones, due to the higher electrons mobility.

In Table 5.1 we summarize the most important properties of our simulations, among which the pressure gradient length, R/L_p, and the mode number in the poloidal direction, k_y. We note that, in the present chapter, the pressure gradient is referred to the total pressure $p = p_e + p_i$. The comparison between the observed values and their estimates will be described later in the chapter. We observe that both R/L_p and k_y values are almost independent of τ.

In order to have a first insight into the nature of the turbulent transport, we compute the cross coherence between n and ϕ fluctuations in Fig. 5.2, and their phase shift in Fig. 5.3, for $\tau = 1, 2, 3, 4$, according to the methodology explained in Sec. 4.4. For all the considered values of τ, we observe that there is not a clear correlation between n and ϕ fluctuations; moreover, the phase shift between the two fluctuations is close to $\pi/2$. These results are the footprint of a ballooning type of instability (see Sec. 4.4). This is confirmed in Sec. 5.4, by using the gradient removal theory method presented in Chap. 4.

From these qualitative observations it emerges that T_i effects have a relatively minor influence on the turbulent properties. In the following, we explain the physics behind these observations.

τ	η_e	η_i	R/L_p simulation	R/L_p estimated	k_y simulation	k_y estimated	$k_{y,min}$ estimated	$k_{y,max}$ estimated	γ_{RBM}	γ_{IBM}	γ_{RDW}	γ_{IDW}	γ_{ITG}
0	0.72	/	12.34	11.94	0.13	0.18	0.13	0.26	2.35	$\simeq 0$	0.99	$\simeq 0$	/
1	0.64	0.59	12.34	11.30	0.11	0.17	0.11	0.24	2.94	$\simeq 0$	0.42	$\simeq 0$	0.01
2	0.61	0.49	12.56	10.88	0.09	0.15	0.11	0.22	3.70	$\simeq 0$	0.48	$\simeq 0$	0.36
3	0.57	0.42	12.56	10.59	0.09	0.15	0.10	0.20	4.07	$\simeq 0$	0.44	$\simeq 0$	0.45
4	0.55	0.31	12.78	10.34	0.09	0.14	0.10	0.19	4.66	$\simeq 0$	0.45	$\simeq 0$	0.51

Table 5.1: *Parameters for the non-linear simulations; $\hat{s} = 0$, $\nu = 0.1$, $m_e/m_i = 1/200$. The domain dimensions are $L_y = 800$ and $L_x = 100$. The major radius is $R = 500$. The major radius to the pressure gradient length ratio, R/L_p, is evaluated by fitting n, T_e, and T_i with an exponential function $0 < x - x_s < 70$. The radial window over which k_y is evaluated is $5 < x - x_s < 17$. The two values $k_{y,min}$ and $k_{y,max}$ are computed considering the k_y range corresponding to a 10% variation of the value γ/k_y with respect to its maximum at the R/L_p and k_y predicted.*

5.3 Linear instabilities in the presence of hot ions

In this section we present the main linear SOL instabilities in the presence of hot ions, focusing on the electrostatic limit. In Chap. 3 the resistive and inertial branches of the drift wave (RDW and InDW) and of the ballooning mode (RBM and InBM) instabilities are described in the cold ion limit, identifying the instability with the largest growth rate as a function of the SOL parameters. In the following, we first describe the impact of the hot dynamics on the forementioned instabilities. We then introduce an instability driven unstable by the presence of the ion temperature gradient, the so-called ion temperature gradient instability (ITG), with its slab (sITG) and toroidal (tITG) branches.

5.3.1 Drift waves instability with hot ions

The linear DW instability has been described in the cold ion limit in Sec. 3.2.2, by neglecting the sound wave coupling, *i.e.* by assuming $\gamma \gg k_{\parallel}$, the ballooning drive, and the compressibility terms in the continuity and temperature equations. By introducing hot ion dynamics, the system of Eqs. (3.11) is modified as follows:

$$\gamma n = i\omega_* \phi - \nabla_{\parallel} V_{\parallel e},$$
$$-k_{\perp}^2 \gamma \left(\phi + \tau T_i\right) = -\nabla_{\parallel} V_{\parallel e},$$
$$\frac{m_e}{m_i}\gamma V_{\parallel e} = -\nu V_{\parallel e} + \nabla_{\parallel}\left(\phi - n - 1.71 T_e\right),$$
$$\gamma T_e = i\omega_*\eta_e\phi - \frac{2}{3}1.71\nabla_{\parallel} V_{\parallel e},$$
$$\gamma T_i = i\omega_*\eta_i\phi - \frac{2}{3}\nabla_{\parallel} V_{\parallel e},$$

(5.1)

where we have neglected finite β effects. If we assume $\nabla_{\parallel} \to ik_{\parallel}$, we can reduce Eqs. (5.1) to an algebraic dispersion relation in the form

$$\gamma^3 a + \gamma^2 b + \gamma c + d = 0,$$

(5.2)

where the coefficients are:

$$a = -\frac{m_e}{m_i}k_y^2,$$
$$b = -k_y^2\left(\nu + i\tau\eta_i\frac{m_e}{m_i}\omega_*\right),$$
$$c = -k_{\parallel}^2\left(1 + 2.95k_y^2\right) - \tau k_y^2\left(i\eta_i\nu\omega_* + \frac{2}{3}k_{\parallel}^2\right),$$
$$d = ik_{\parallel}^2\omega_*\left(1 + 1.71\eta_e\right) + i\tau k_{\parallel}^2\omega_* k_y^2\left[\frac{2}{3}\left(1 + 1.71\eta_e\right) - 2.95\eta_i\right].$$

(5.3)

(a) density, n

(b) electron temperature, T_e

(c) ion temperature, T_i

(d) vorticity, ω

(e) electron parallel velocity, $V_{\parallel e}$
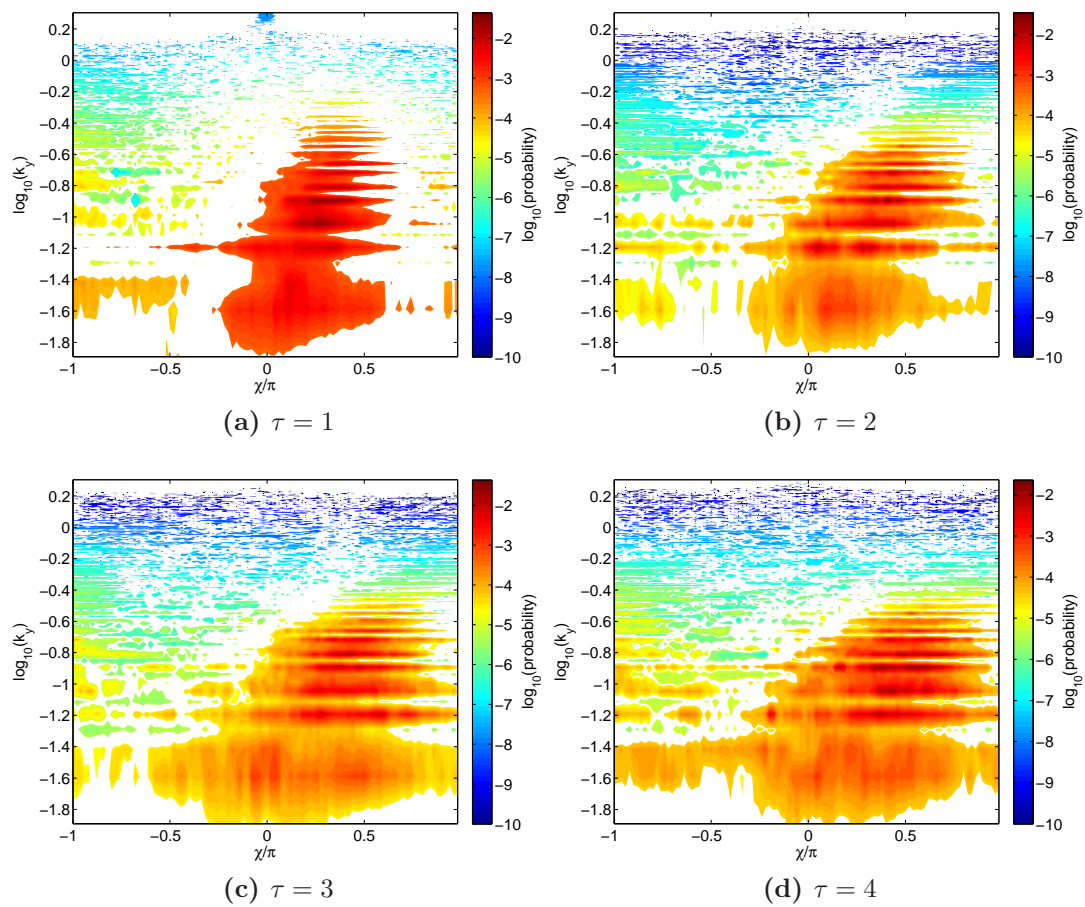
(f) ion parallel velocity, $V_{\parallel i}$
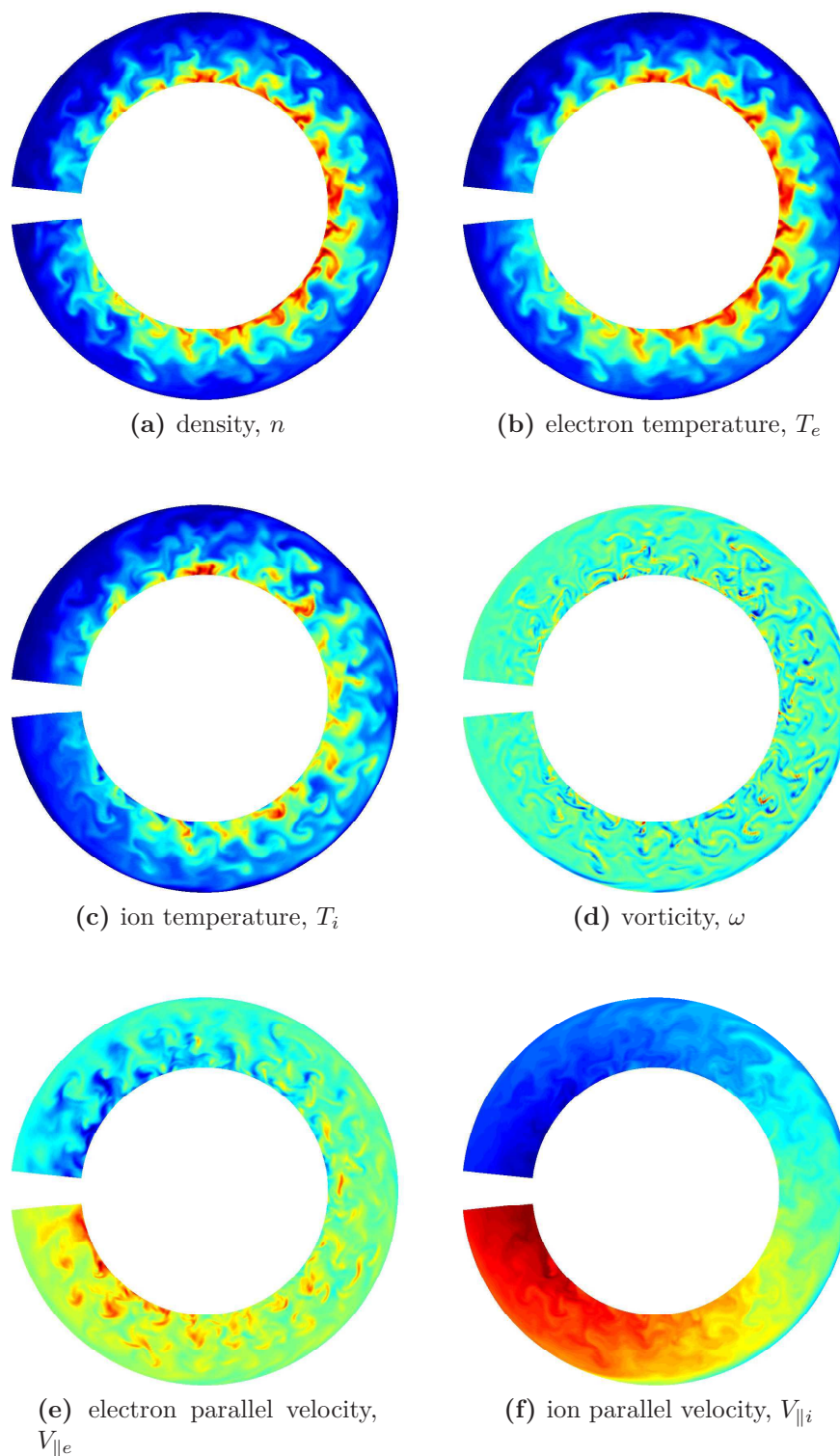
Figure 5.1: *Snapshots of density (a), electron temperature (b), ion temperature (c), vorticity (d), electron parallel velocity (e), and ion parallel velocity (f), in a poloidal cross section for the non-linear simulation with $\hat{s} = 0$, $\nu = 0.1$, $m_e/m_i = 1/200$, $\tau = 1$.*
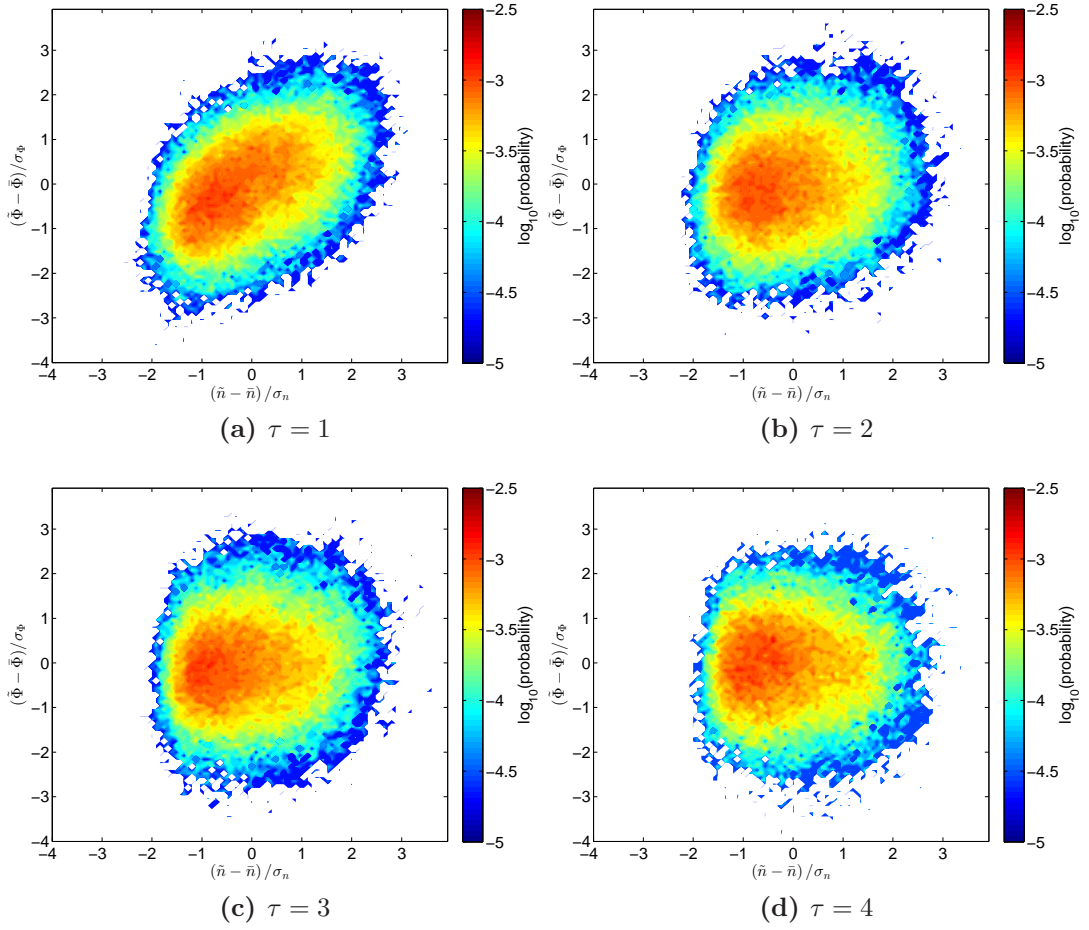
Figure 5.2: *Cross coherence between ϕ and n fluctuations for $\tau = 1$ (a), $\tau = 2$ (b), $\tau = 3$ (c), and $\tau = 4$ (d)*

(a) $\tau = 1$

(b) $\tau = 2$

(c) $\tau = 3$

(d) $\tau = 4$

Figure 5.3: *Phase shift between ϕ and n fluctuations for $\tau = 1$ (a), $\tau = 2$ (b), $\tau = 3$ (c), and $\tau = 4$ (d)*
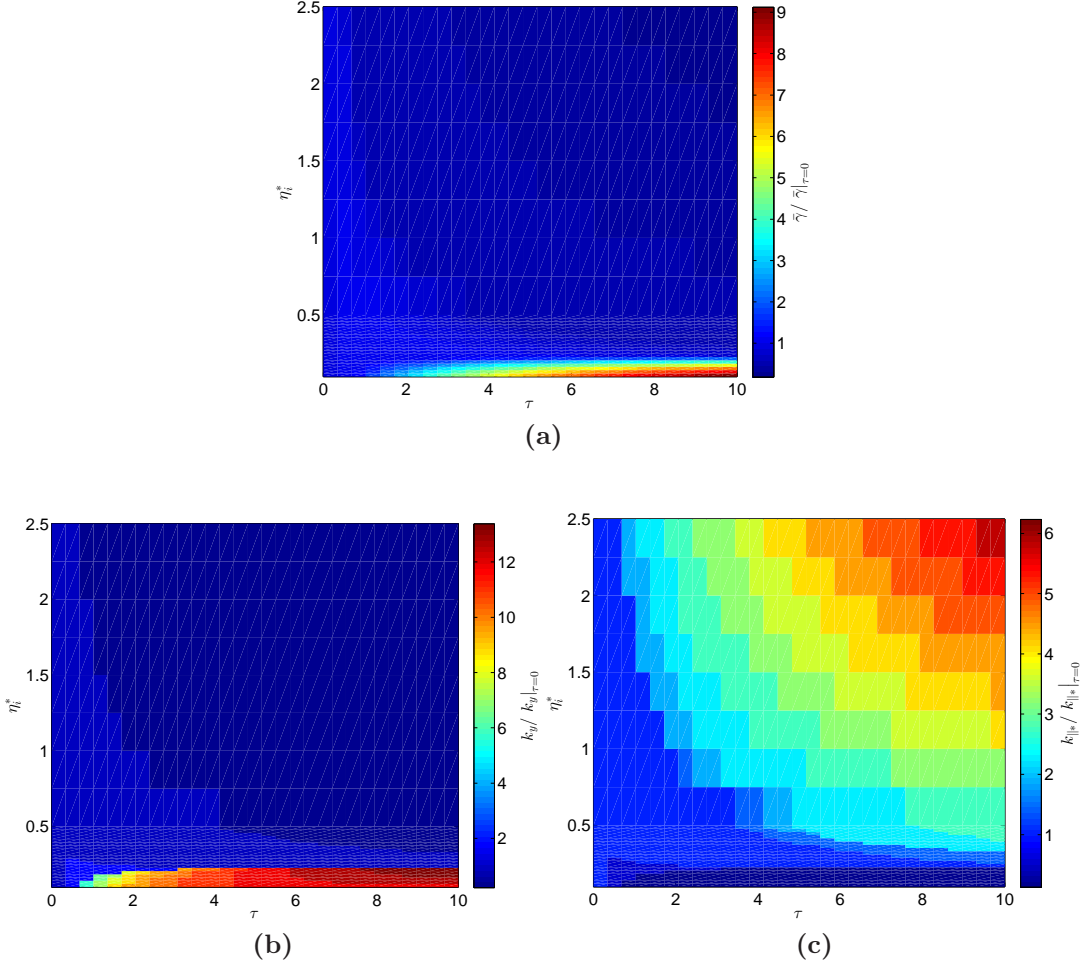
Figure 5.4: *Maximum $\check{\gamma}/\check{\gamma}|_{\tau=0}$, solution of the DW dispersion relation, Eq. (5.2), in the resistive limit (a), and corresponding $k_y/k_y|_{\tau=0}$ (b) and $k_\parallel^*/k_{\parallel*}|_{\tau=0}$ (c). The white surface indicates regions where the RDW is stable.*

First, we note that in the limit $\tau \to 0$, we retrieve the dispersion relation of the RDW, if $m_e/m_i \to 0$, or the dispersion relation of the InDW, if $\nu \to 0$. These dispersion relations are presented in Sec. 3.2.2. Second, we observe that, in the resistive limit, Eq. (5.2) can be rewritten by using only the following parameters: $\check{\gamma} = \gamma/[R/L_n(1+1.71\eta_e)]$, $k_{\parallel*}^2 = k_\parallel^2/[k_y^2\nu\omega_*(1+1.71\eta_e)]$, k_y, $\eta_{i*} = \eta_i/(1+1.71\eta_e)$, and τ. For $\tau = 0$ we retrieve the cold ion limit results: peak growth rate at $k_y \simeq 0.57$ and $k_{\parallel*} \simeq 0.56$, with $\check{\gamma} = \check{\gamma}_0 \simeq 0.085$ (see Sec. 3.2.2). In Fig. 5.4a we show $\check{\gamma}/\check{\gamma}_0$, solution of Eq. (5.2), in the resistive limit, maximized over $k_{\parallel*}$ and k_y, as a function of τ and η_{i*}. In Figs. 5.4b and 5.4c we present k_y and $k_{\parallel*}$ at the maximum growth rate. The maximum growth rate decreases with η_{i*} and this effect is more evident at large τ. The η_{i*} terms in the d and c coefficients of Eq. (5.3) are responsible for the decrease of the growth rate for $0.5 \lesssim \eta_i \lesssim 1$, and for $\eta_{i*} \gtrsim 1$, respectively.
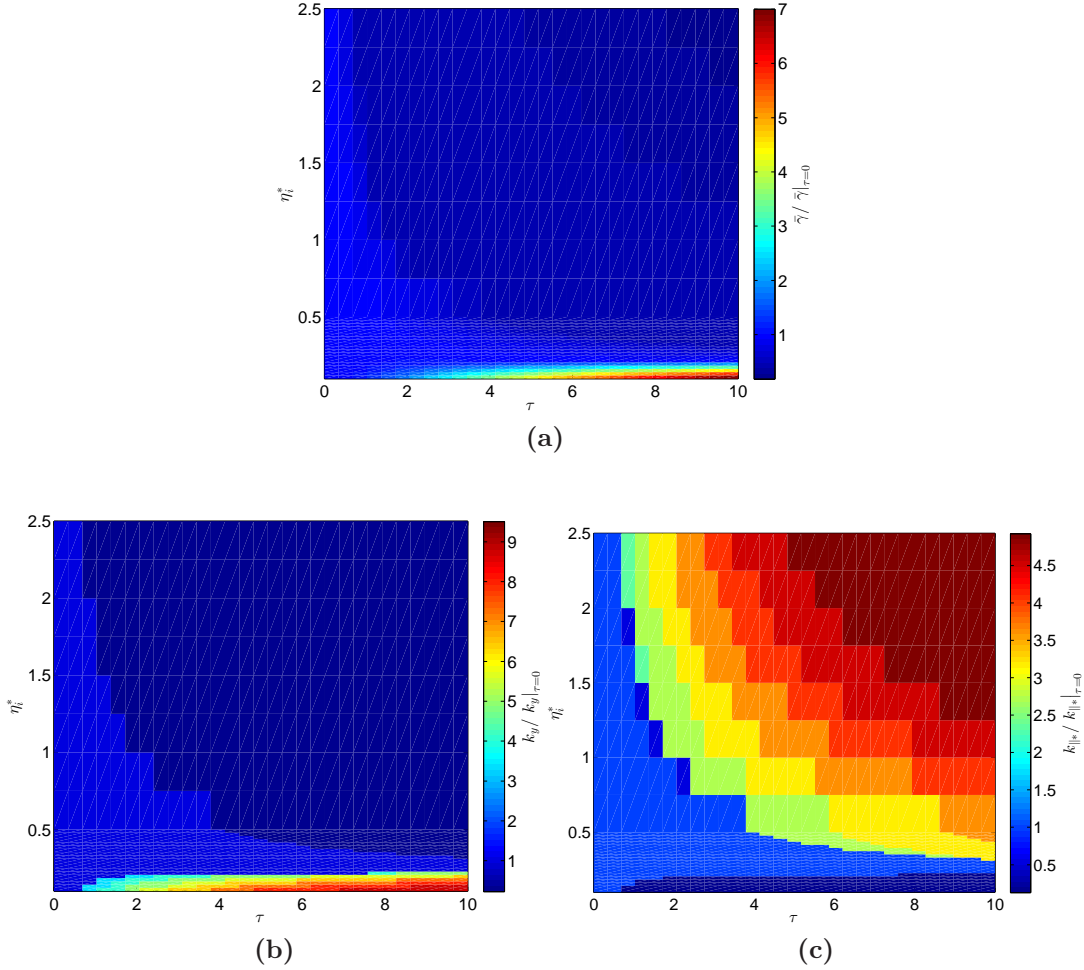
Figure 5.5: *Maximum $\bar{\gamma}/\left.\bar{\gamma}\right|_{\tau=0}$, solution of the DW dispersion relation, Eq. (5.2), in the inertial limit (a), and corresponding $k_y/\left.k_y\right|_{\tau=0}$ (b) and $k_{\parallel}^*/\left.k_{\parallel*}\right|_{\tau=0}$ (c). The white surface indicates regions where the InDW is stable.*

Similarly, in the inertial limit, Eq. (5.2) can be rewritten by introducing $\bar{\gamma} = \gamma/\left[R/L_n(1+1.71\eta_e)\right]$, $k_{\parallel*}^2 = k_{\parallel}^2/\left[k_y^2\omega^{*2}m_e/m_i(1+1.71\eta_e)^2\right]$, and $\eta_{i*} = \eta_i/(1+1.71\eta_e)$. For $\tau = 0$ we retrieve the cold ion limit results: peak growth rate $\bar{\gamma} = \bar{\gamma}_0 \simeq 0.17$ at $k_y \simeq 0.57$ and $k_{\parallel*} \simeq 0.6$ (see Sec. 3.2.2). In Fig. 5.5a we show $\bar{\gamma}/\bar{\gamma}_0$, solution of Eq. (5.2), in the inertial limit, maximized over $k_{\parallel*}$ and k_y, as a function of τ and η_{i*}. In Figs. 5.5b and 5.5c we present k_y and $k_{\parallel*}$ at which the maximum growth rate is found. As in the resistive limit, the maximum growth rate decreases with η_{i*} and this effect is more evident at large τ. Moreover, as in the resistive limits, the η_{i*} term in the d coefficient of Eq. (5.2) is responsible for the decrease of the growth rate at $0.5 \lesssim \eta_i \lesssim 1$, while the η_{i*} term in b reduces the growth rate at $\eta_{i*} \gtrsim 1$.

5.3.2 Ballooning modes with hot ions

The BM instability is described in the cold ion limit in Sec. 3.2.1, by neglecting the coupling with sound waves, *i.e.* $\gamma \gg k_\parallel$, and compressibility terms in the continuity and temperature equations. Moreover, $\nabla_\parallel$ terms in the density and temperature equations, as well as the diamagnetic terms in Ohm's law are neglected, in order to avoid the coupling with DW. We describe the BM with hot ion dynamics generalizing Eqs. (3.3) to $T_i \neq 0$, but ignoring finite β effects, as:

$$\gamma n = i\omega_* \phi,$$
$$-k_\perp^2 \gamma \left(\phi + \tau T_i\right) = i\omega_\kappa \left[n\left(1 + \tau\right) + T_e + \tau T_i\right] - \nabla_\parallel V_{\parallel e},$$
$$\frac{m_e}{m_i}\gamma V_{\parallel e} = \nabla_\parallel \phi - \nu V_{\parallel e}, \tag{5.4}$$
$$\gamma T_e = i\omega_* \eta_e \phi,$$
$$\gamma T_i = i\omega_* \eta_i \phi,$$

where $\omega_\kappa = 2k_y \cos\theta$ is the frequency associated with the curvature and the gradient of the magnetic field. Assuming $\nabla_\parallel \to ik_\parallel$, we can obtain a dispersion relation in the form of a second order algebraic equation:

$$\gamma^2 a + \gamma b + c = 0, \tag{5.5}$$

where

$$a = 1,$$
$$b = i\frac{R}{L_n}k_y \tau \eta_i + \frac{1}{\nu}\frac{k_\parallel^2}{k_y^2}, \tag{5.6}$$
$$c = -2\frac{R}{L_n}\left(1 + \tau + \eta_e + \tau\eta_i\right) + \frac{m_i}{m_e}\frac{k_\parallel^2}{k_y^2},$$

which reduces to the results of Secs. 3.2.1, for $\tau = 0$. In the limit $k_\parallel/k_y \to 0$, the maximum growth rate of the BM is attained, $\gamma_B^{max} = \sqrt{2R/L_n \left(1 + \tau + \eta_e + \tau\eta_i\right)}$, which is larger than the cold ion growth rate because of the presence of the $(\tau\eta_i + \tau)$ term. Finite values of $k_\parallel/k_y$ reduce the growth rate. In the resistive case, this effect is ascribed to the $k_\parallel^2/(\nu k_y^2)$ term in the b coefficient of Eq. (5.6); in the inertial case this is due to the $m_i k_\parallel^2/(m_e k_y^2)$ term in the c coefficient of Eq. (5.6). Similarly to what observed in Sec. 3.2.1, we find that the BM are stabilized for $k_y < k_y^{min}$, where $k_y^{min} = k_\parallel/\sqrt{\gamma_B^{max}\nu}$ for the RBM, and $k_y^{min} = k_\parallel\sqrt{m_i}/(\gamma_B^{max}\sqrt{m_e})$ for the InBM.

We use the linear solver described in Sec. 2.5, to determine the eigenfunctions and γ, solution of the system (5.4) and, in particular, the dependence of the eigenfunctions on the parallel coordinate. In Figs. 5.6 and 5.8 we show γ/γ_B^{max}, solution of Eqs. (5.4), maximized over k_y, with $q = 4$, in the resistive ($\nu = 0.1$) and inertial ($m_e/m_i = 1/200$) limits, respectively. In Figs. 5.7 and 5.9 we present the k_y corresponding to the peak growth rate. For both RBM and InBM, the reduction of the
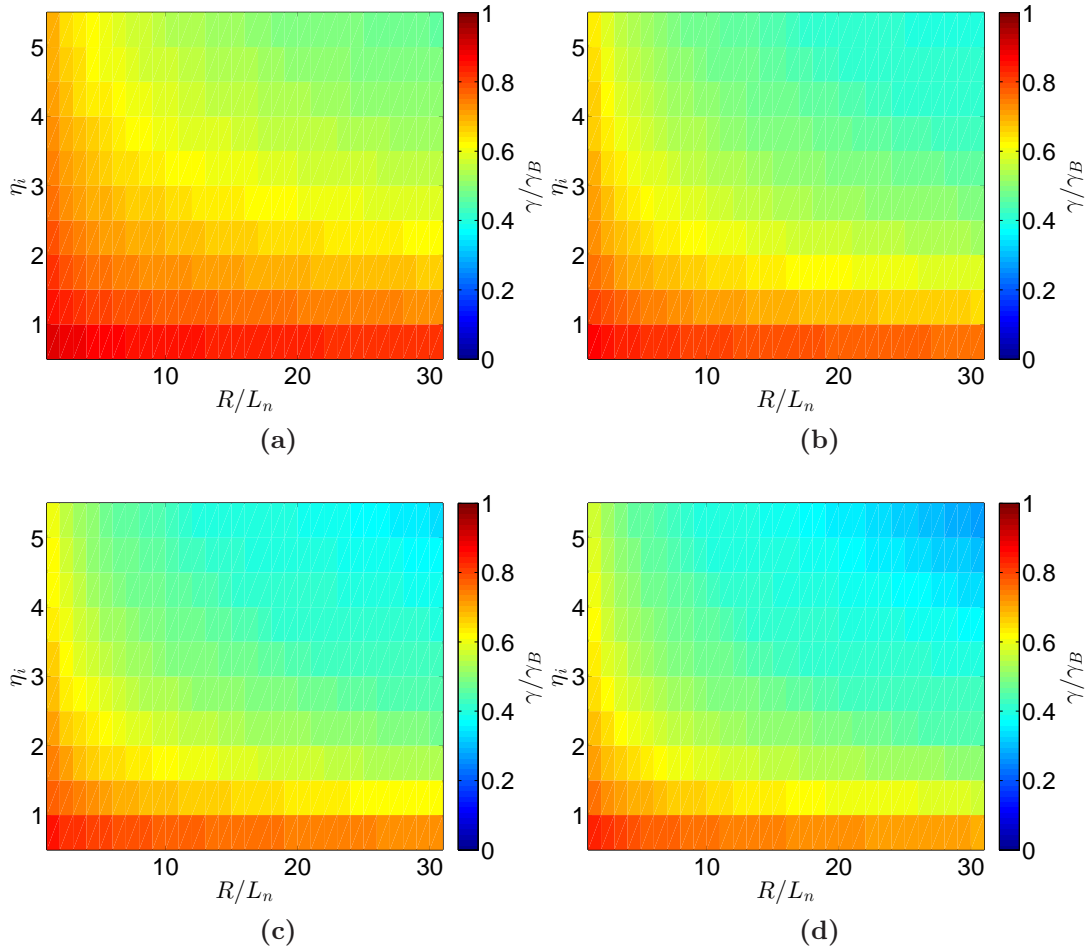
Figure 5.6: *Growth rate of the RBM, solution of Eqs. (5.4) for $\nu = 0.1$, $m_e/m_i \to 0$, $\eta_e = 0.67$, and for $\tau = 1$ (a), $\tau = 2$ (b), $\tau = 3$ (c), and $\tau = 4$ (d).*

growth rate observed at high η_i is due to finite $k_\parallel$ effects. In fact, at large η_i, γ peaks at low k_y, such that the term $k_\parallel^2/k_y^2$ in the b and c coefficients of Eq. (5.6) becomes larger, therefore reducing γ with respect to its maximum value. We remark that, for both RBM and InBM, the k_y corresponding to the maximum growth rate is large at low R/L_n, since k_y^{min} is a decreasing function of R/L_n. Finally, we observe that, for both RBM and InBM, the growth rate decreases with τ due to the term proportional to τ in the b coefficient of Eq. (5.5).

5.3.3 Ion temperature gradient instability

The presence of an ion temperature gradient can lead to the ITG instability, which has two branches, the slab and the toroidal ones (sITG and tITG). We can derive a simple dispersion relation that includes both branches of the ITG instability,
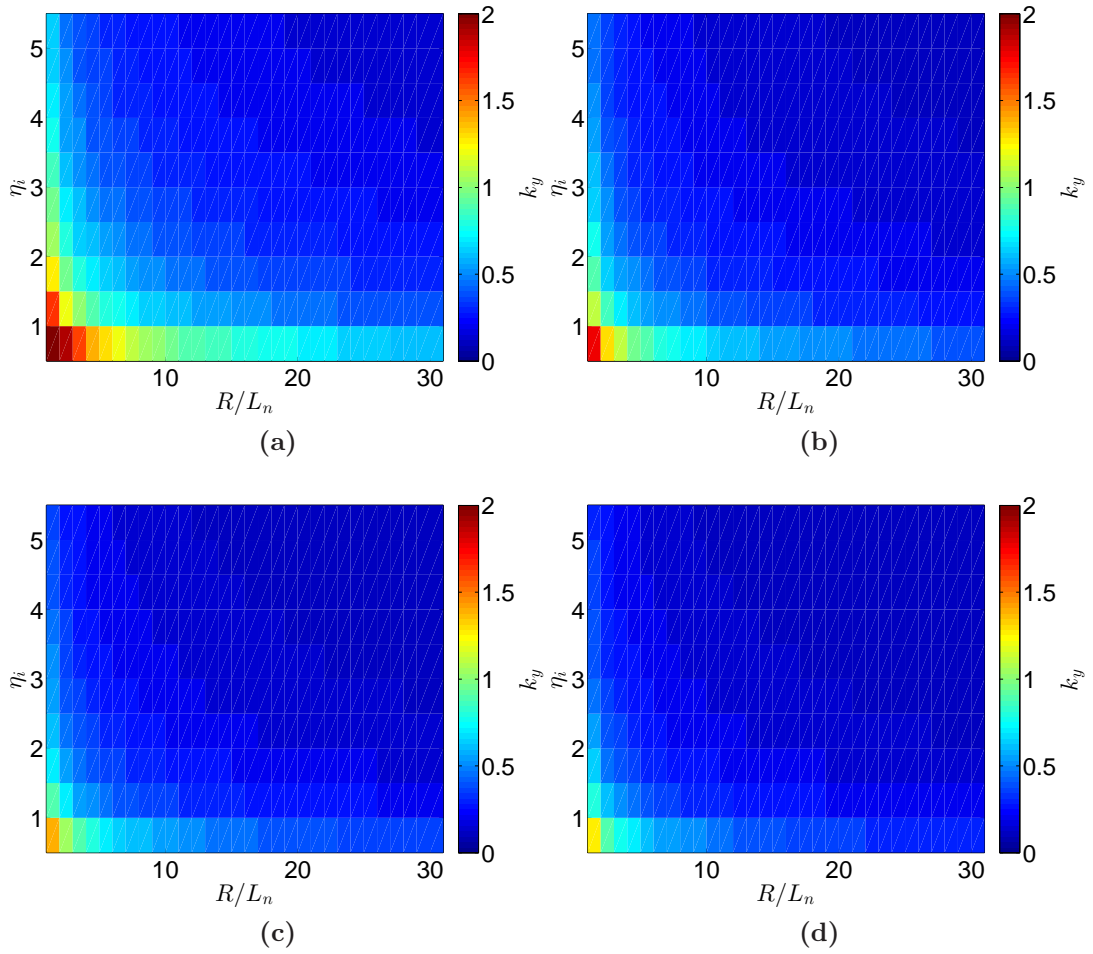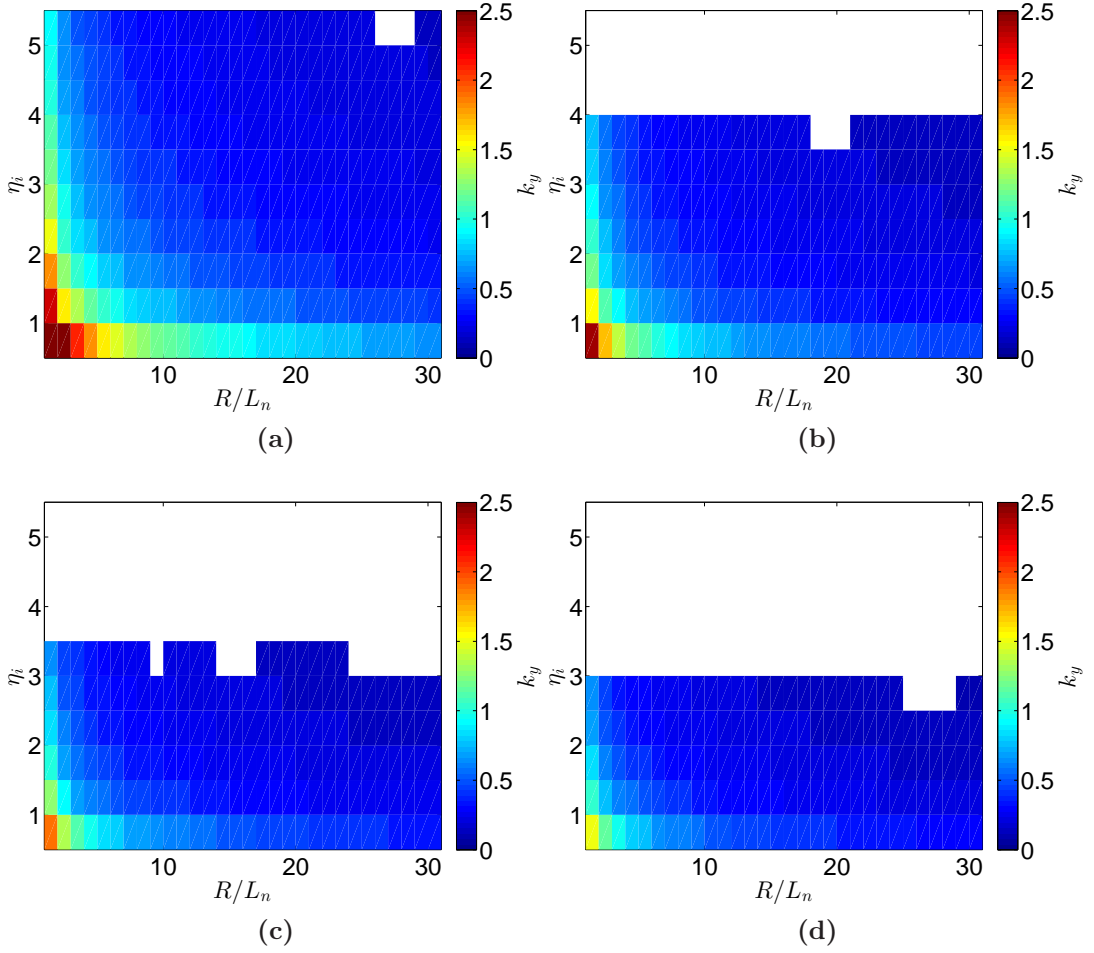
Figure 5.7: *Poloidal wavenumber k_y at the maximum RBM growth rate for $\nu = 0.1$, $m_e/m_i \rightarrow 0$, $\eta_e = 0.67$, and for $\tau = 1$ (a), $\tau = 2$ (b), $\tau = 3$ (c), and $\tau = 4$ (d).*
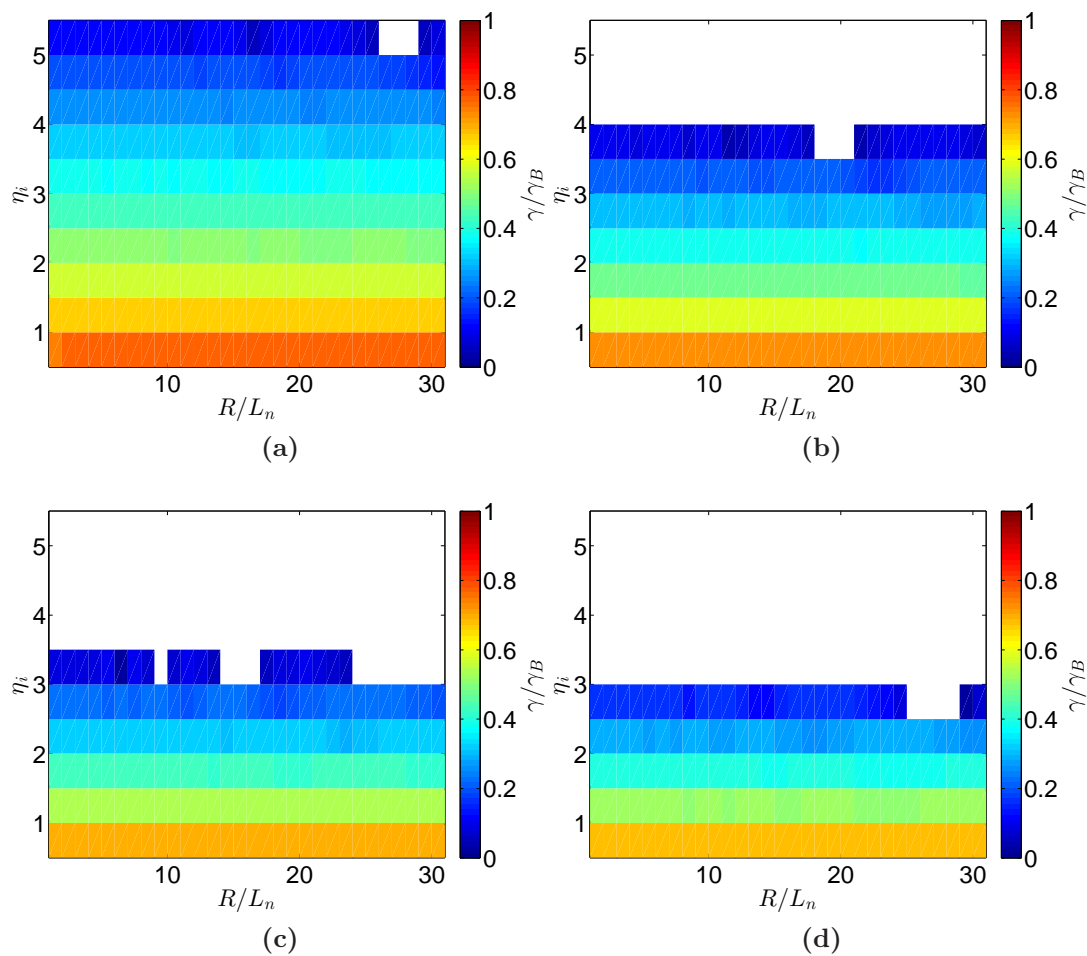
Figure 5.8: *Growth rate of the InBM, solution of Eqs. (5.4) for $\nu \to 0$, $m_e/m_i = 1/200$, $\eta_e = 0.67$, and for $\tau = 1$ (a), $\tau = 2$ (b), $\tau = 3$ (c), and $\tau = 4$ (d). The white surface indicates regions where the InBM is stable.*

Figure 5.9: *Poloidal wavenumber k_y at the maximum InBM growth rate for $\nu \to 0$, $m_e/m_i = 1/200$, $\eta_e = 0.67$, and for $\tau = 1$ (a), $\tau = 2$ (b), $\tau = 3$ (c), and $\tau = 4$ (d). The white surface indicates regions where the InBM is stable.*

within the hypothesis of isothermal electrons. We consider the continuity equation for electrons,

$$\gamma n = i\left(\omega_* - \omega_\kappa\right)\phi + i\omega_\kappa n - \frac{\partial V_{\|e}}{\partial z}, \tag{5.7}$$

the vorticity equation,

$$\gamma\left(k_\perp^2\phi + \tau k_\perp^2 T_i\right) = -i\omega_\kappa(1+\tau)n + \frac{\partial V_{\|e}}{\partial z} - \frac{\partial V_{\|i}}{\partial z} - i\omega_\kappa\tau T_i, \tag{5.8}$$

the adiabatic Ohm's law,

$$\frac{\partial n}{\partial z} = \frac{\partial \phi}{\partial z}, \tag{5.9}$$

the ion parallel velocity equation,

$$\gamma V_{\|i} = -\frac{\partial n}{\partial z}(1+\tau) - \frac{\partial T_i}{\partial z}\tau, \tag{5.10}$$

and the ion temperature equation,

$$\gamma T_i = i\frac{2}{3}\omega_\kappa n + \left(i\omega_*\eta_i - i\frac{2}{3}\omega_\kappa\right)\phi - \frac{2}{3}\frac{\partial V_{\|e}}{\partial z} - \frac{5}{3}\tau i\omega_\kappa T_i. \tag{5.11}$$

From Eqs. (5.7)-(5.11), assuming $\nabla_\| \to ik_\|$, we obtain the following dispersion relation:

$$a\gamma^3 + b\gamma^2 + c\gamma + d = 0, \tag{5.12}$$

where

$$a = 1 + k_y^2\left(1 + \frac{2}{3}\tau\right),$$
$$b = i\left\{\omega_*\left[-1 + k_y^2\tau\left(\eta_i - \frac{2}{3}\right)\right] + \omega_\kappa\left[1 + \frac{5}{3}\tau\left(2 + k_y^2\right)\right]\right\},$$
$$c = k_\|^2\left(1 + \frac{5}{3}\tau\right) + \omega_\kappa\tau\left[\omega_*\left(\frac{7}{3} - \eta_i\right) - \frac{5}{3}\omega_\kappa(1+\tau)\right],$$
$$d = ik_\|^2\tau\left[\omega_*\left(\eta_i - \frac{2}{3}\right) + \frac{5}{3}\omega_\kappa(1+\tau)\right], \tag{5.13}$$

which describes both the slab and toroidal branches of the ITG instability, analyzed below. As an aside, we note that a second instability developing at $k_y \gtrsim 1$, for small R/L_n and small η_i is also present in Eq. (5.12). This mode, dependent on the Boussinesq's approximation used in deducing the vorticity equation (5.8) and driven by magnetic curvature, is typically overpowered by the ITG instability. We exclude this mode for the analysis that follows, as it appears in a parameter regime that is not of relevance for SOL turbulence.

The dispersion relation of sITG is derived from Eqs. (5.7)-(5.12), by setting $\omega_\kappa = 0$. A simple description of the mechanism behind the growth of the sITG an be found in Ref. [6]. The sITG mode arises as a combination of plasma parallel compression and $\boldsymbol{E} \times \boldsymbol{B}$ convection, similarly to the DW instability (see Sec. 3.2.2),

in the absence of $\boldsymbol{B}$ gradient and curvature. The balance between $\boldsymbol{E} \times \boldsymbol{B}$ flow and parallel compression in the density equation, Eq. (5.7), leads to $i\omega_* \phi \simeq \partial_z V_{\|e}$, when $\omega_\kappa = 0$. Replacing this in the ion temperature equation, Eq. (5.11), and using the electron adiabaticity condition, in the long wavelength regime, such that the vorticity equation reduces to $\nabla_\| j_\| = 0$, one obtains $\gamma T_i \sim i\omega_* (\eta_i - 2/3)\phi$. This link between ϕ and T_i shows that the $\boldsymbol{E} \times \boldsymbol{B}$ radial transport, $\overline{\Gamma}_{T_i} \simeq k_y \overline{\tilde{\phi}\tilde{T_i}}$ decreases the T_i equilibrium gradient if $\eta_i > 2/3$. By removing free energy from the system, this provides the drive for the sITG instability. Therefore it is the parallel compression of the plasma, that in a homogeneous plasma simply develops a parallel sound wave, that in a inhomogeneous plasma drives the ITG instability.

An estimate of the peak value of γ for the ITG instability, and of the corresponding $k_\|$, can be found by simplifying the dispersion relation Eq. (5.12). Beside neglecting ω_κ in Eq. (5.12) and assuming $\nabla_\| j_\| = 0$, we suppose $\omega_* \ll \gamma$ and $\eta_i \gg 1$. The ITG dispersion relation becomes

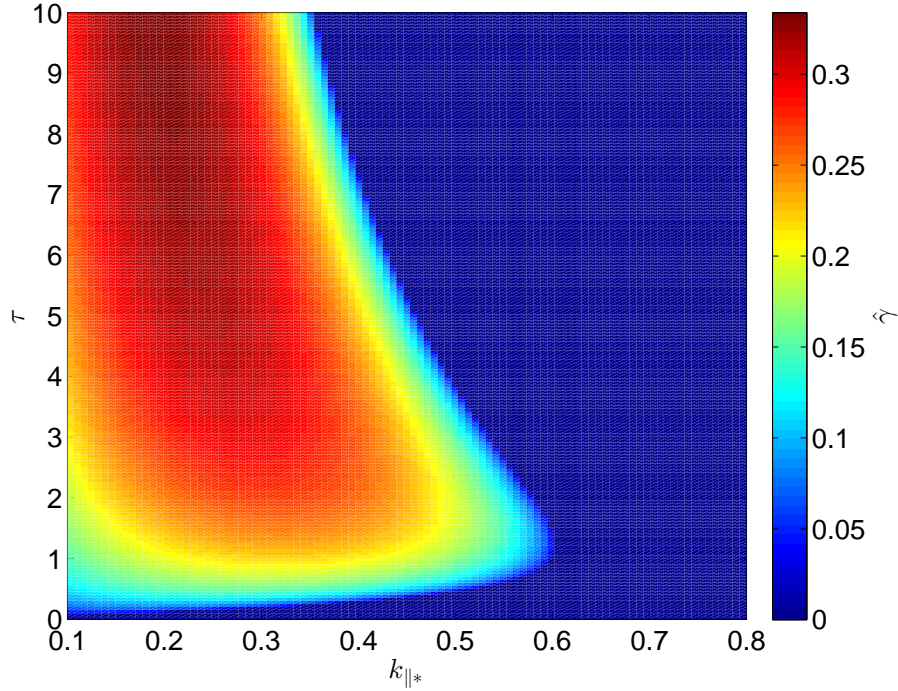$$\hat{\gamma}^3 + \left(1 + \frac{5}{3}\tau\right) k_{\|*}^2 \hat{\gamma} + i k_{\|*}^2 \tau = 0, \tag{5.14}$$

where $\hat{\gamma} = \gamma/(\omega_* \eta_i)$ and $k_{\|*} = k_\|/(\omega_* \eta_i)$. Therefore, the peak growth rate can be written as $\gamma_{max} \simeq g(\tau)\omega_* \eta_i$, and it occurs at $k_\| \simeq f(\tau)\omega_* \eta_i$. The $\hat{\gamma}$, solution of Eq. (5.14), is shown in Fig. 5.10.

We now consider the tITG branch. The tITG instability is a curvature driven instability, similarly to the BM and contrary to the sITG, due to the presence of an ion temperature gradient in the plasma. The instability mechanism is similar to the one of the BM (see Fig. 3.1) but, while the drive of the BM, leading to a charge separation, is a density fluctuation, for the tITG this is provided by T_i fluctuations. In fact, since the diamagnetic velocities are proportional to the particles temperatures (see Eqs. (2.50) and (2.51)), hot and cold particles drift at different speeds, generating a charge separation and, hence an $\boldsymbol{E} \times \boldsymbol{B}$ drift that, in the presence of a temperature gradient, amplifies the original temperature fluctuation. While, in case of BM, a $\pi/2$ shift between n and ϕ characterizes the instability, in case of tITG a $\pi/2$ shift between T_i and ϕ is maintained, and electrons can be adiabatic. With respect to the sITG, the tITG branch exists in the absence of $k_\|$ effects.

We can retrieve a simple dispersion relation of the tITG starting from Eq. (5.12), by neglecting the $\nabla_\|^2$ terms:

$$\gamma^2 \left[1 + k_\perp^2 \left(1 + \tau\frac{2}{3}\right)\right] + \gamma i \left[-\omega_* + \omega_\kappa \left(1 + \frac{10}{3}\tau\right)\right.$$
$$\left. + k_\perp^2 \tau \left(\omega_* \left(\eta_i - \frac{2}{3}\right) + \frac{5}{3}\omega_\kappa\right)\right] + \tag{5.15}$$
$$-\omega_\kappa \tau \left[\omega_* \left(\eta_i - \frac{7}{3}\right) + \frac{5}{3}\omega_\kappa (1 + \tau)\right].$$

Figure 5.10: $\hat{\gamma}$, *solution of Eq.* (5.14)

We note that the tITG mode follows the scaling derived in the adiabatic limit, even when resistivity is introduced in the model. We also remark that this results is different from the ITG dispersion relation in Ref. [60] because of the different Boussinesq's approximation of the ion density fluctuations used in the evaluation of the polarisation drift in the vorticity equation. Since the coefficient of the quadratic term in Eq. (5.15) is always positive, a necessary condition for an instability is given by setting $\omega_\kappa = 2k_y$, *i.e.* focusing on the dynamics at the equatorial outboard mid plane:

$$\omega_\kappa \tau \left[\omega_* \left(\eta_i - \frac{7}{3} \right) + \frac{5}{3} \omega_\kappa \left(1 + \tau \right) \right] > 0, \tag{5.16}$$

leading to

$$\eta_i > \frac{7}{3} - \frac{5}{3} \frac{\omega_\kappa}{\omega_*} \left(1 + \tau \right). \tag{5.17}$$

It is also possible to verify (see Ref. [60]) that the modes with the largest growth rate are the ones for which the linear term of Eq. (5.15) is close to 0. Since $\omega_\kappa/\omega_* \sim L_n/R \ll 1$, this can be written as:

$$k_\perp^2 \simeq \frac{1}{\tau \left(\eta_i - \frac{2}{3} \right)}. \tag{5.18}$$

Having described the two branches of the ITG instability, we now analyze the solu-

tion of the full ITG dispersion relation, Eq. (5.12), that includes both the slab and the toroidal branches. In Fig. 5.11 we show the growth rate, solution of Eq. (5.12), again for $\omega_\kappa = 2k_y$, normalized to $\eta_i R/L_n$, $i.e.$ $\hat{\gamma}k_y = \gamma/(\eta_i R/L_n)$, as suggested by Eq. (5.14), and maximized over k_y and $k_\parallel$, as a function of R/L_n and η_i, and for τ ranging from 1 to 4. The normalized growth rate $\hat{\gamma}k_y$ can be estimated, following the results for the sITG, as $g(\tau)k_y$, where $g(\tau)$(see Fig. 5.10) is an increasing function of τ. We find that the normalized growth rate decreases with τ, despite the fact that $g(\tau)$ increases with τ. This is in fact due to the decrease of k_y with τ.

In Figs. 5.12 and 5.13 we show k_y and $k_{\parallel*}k_y = k_\parallel/(\eta_i R/L_n)$ at the maximum growth rate. The normalized parallel wavenumber, $k_\parallel/(\eta_i R/L_n)$, can be estimated as $f(\tau)k_y$, where both $f(\tau)$ (from Fig. 5.10), as well as k_y, are decreasing functions of τ. We also observe that both the normalized growth rate, $\gamma/(\eta_i R/L_n)$ and the normalized parallel wavenumber, $k_\parallel/(\eta_i R/L_n)$ are almost independent of η_i and R/L_n for $\eta_i \gtrsim 1$. The poloidal wavenumber, k_y, decreases with τ and η_i, according to Eq. (5.18), which predicts the k_y at the maximum growth rate to be inversely proportional to both $\sqrt{\tau}$ and $\sqrt{\eta_i}$. Finally, we remark that, according to Fig. 5.11, the ITG instability is unstable above a certain η_i threshold, that decreases with R/L_n, and for values $R/L_n \gtrsim 15$ it is $\eta_i \simeq 1$.
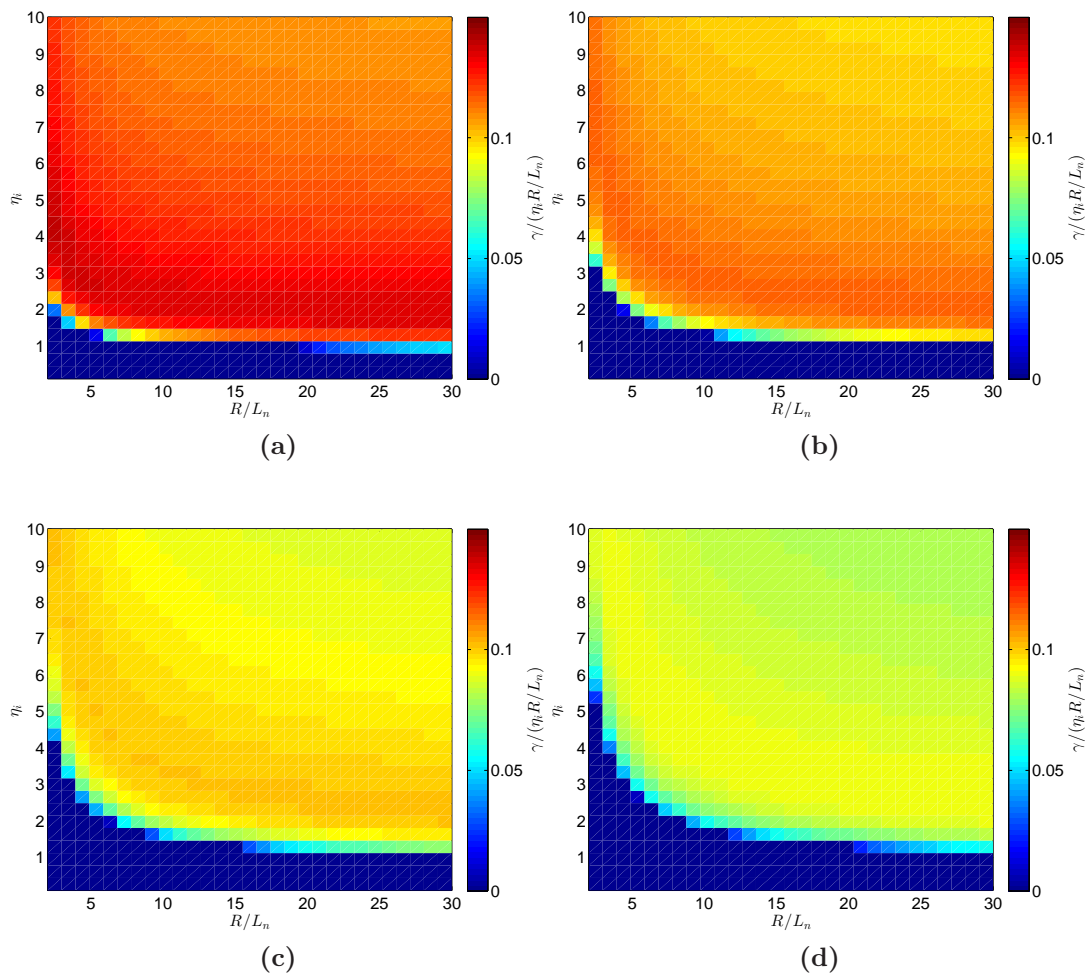
5.4   Turbulent regimes in the presence of hot ions

We now determine the instability driving turbulence and transport in the SOL, by identifying the turbulent regimes in the τ and ν parameter space. We use the same methodology described in Chap. 4, based on the gradient removal theory [87,88,44, 43], which assumes that turbulence saturation occurs when the background time-averaged pressure radial gradient is comparable to the perturbed pressure radial gradient, $k_x\tilde{p} \sim \overline{p}/L_p$. The range of applicability of the gradient removal hypothesis in estimating the turbulent saturation level, versus other mechanism, $i.e.$ Kelvin-Helmholtz secondary instability, is discussed in Ref. [87].

From a time, toroidal, and poloidal average of the pressure equation, it is possible to write a balance between radial transport and parallel losses, $\partial_x \overline{\Gamma}_x \sim \overline{p}\,\overline{c_s}/(qR)$. Estimating the radial flux, appearing in the balance, as $\overline{\Gamma}_x \sim k_y\widetilde{\phi\tilde{p}}$, the potential fluctuations from the leading term of the pressure equation, $\gamma\tilde{p} \sim ik_y\tilde{\phi}R/L_p$, and the density fluctuations from the gradient removal hypothesis, we can derive an estimate of L_p:

$$L_p^2 = \frac{\gamma q}{k_x^2 c_s \sqrt{1+\tau}}. \tag{5.19}$$

Equation (5.19) constitutes the equation that provides L_p as a function of the SOL operational parameters. The calculation of the linear growth rate, γ, appearing in Eq. (5.19), requires the estimate of the η_e and η_i values. The derivation of these estimates is the subject of Sec. 5.4.1. Thanks to these estimates, it is possible to
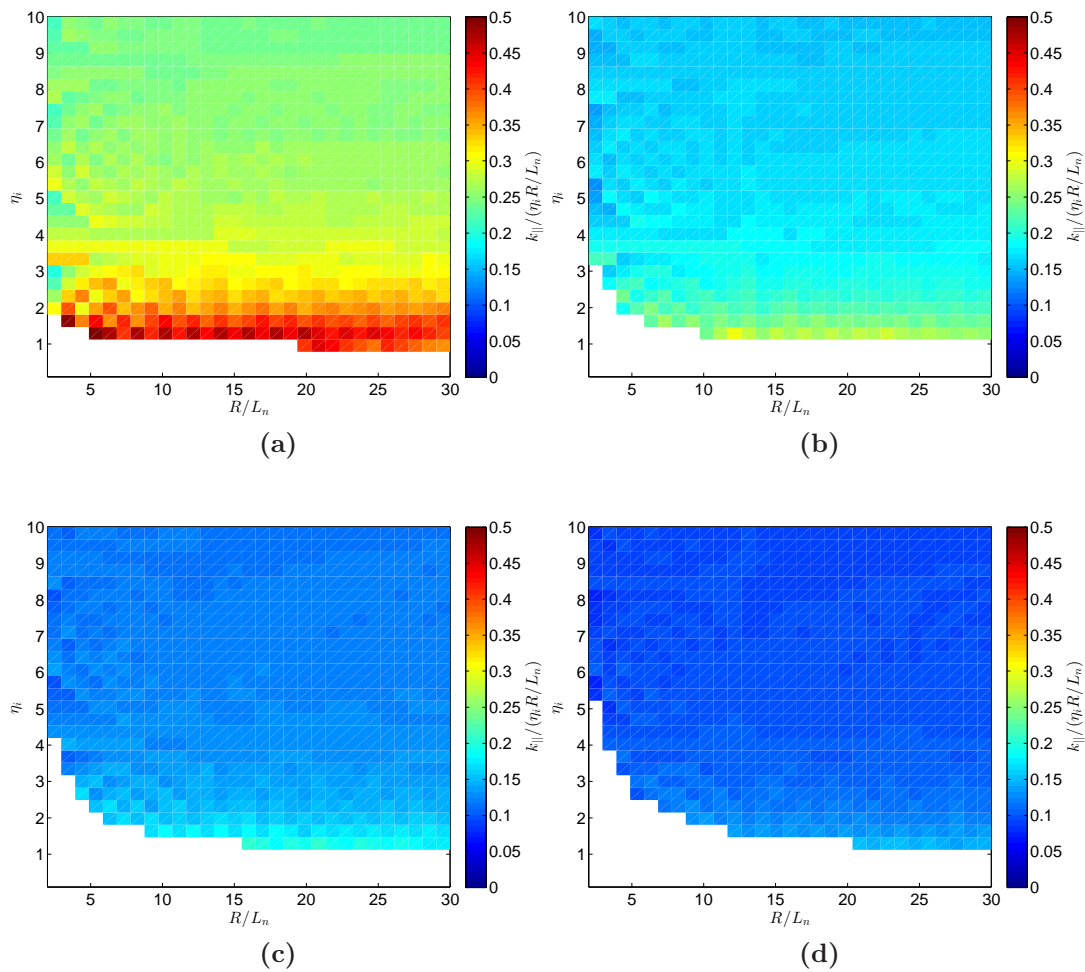
Figure 5.11: *Normalized growth rate $\hat{\gamma} k_y = \gamma/(\eta_i R/L_n)$ for the ITG mode as a function of η_i and R/L_n for $\tau = 1$ (a), $\tau = 2$ (b), $\tau = 3$(c), and $\tau = 4$ (d).*

(a)

(b)

(c)

(d)
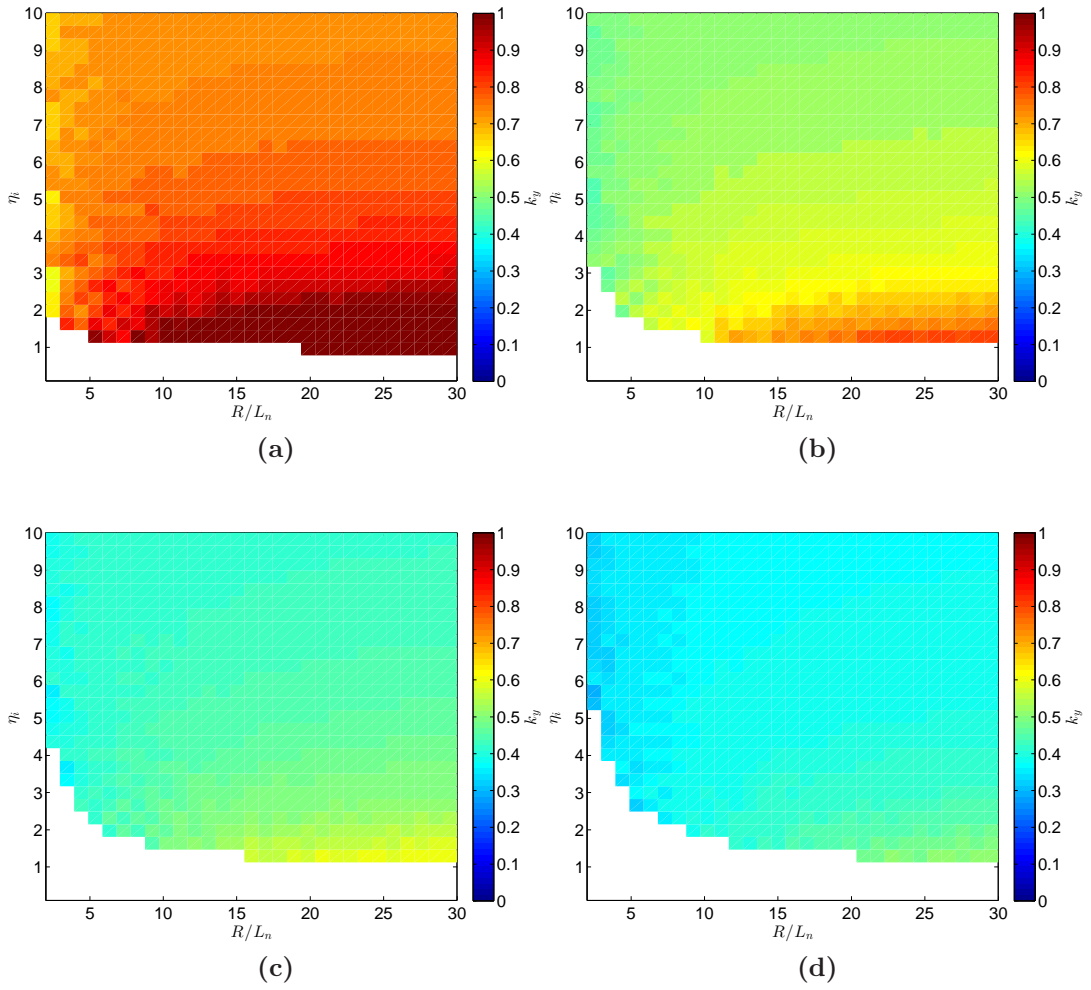
Figure 5.12: *Poloidal wavenumber k_y at the maximum growth rate of the ITG mode as a function of η_i and R/L_n for $\tau = 1$ (a), $\tau = 2$ (b), $\tau = 3$ (c), and $\tau = 4$ (d).*

Figure 5.13: *Normalized parallel wavenumber $k_{\parallel *} k_y = k_\parallel/(\eta_i R/L_n)$ at the maximum growth rate of the ITG mode as a function of η_i and R/L_n for $\tau = 1$ (a), $\tau = 2$ (b), $\tau = 3$ (c), and $\tau = 4$ (d).*

deduce the role of the hot ions in the SOL turbulence (Sec. 5.4.2), and determine the turbulence regimes as a function of τ, ν, and η_i.

5.4.1 Estimates of η_e and η_i

In Table 5.1 the values of η_e and η_i computed from non-linear simulation results are listed. We note that, η_e decreases from $\eta_e \sim 0.72$ to $\eta_e \sim 0.55$, for τ from $\tau = 0$ to $\tau = 4$, while η_i decreases from 0.59, for $\tau = 1$, to 0.31, for $\tau = 4$. We now theoretically estimate the η_e and η_i values by generalizing the method described in Ref. [36], by considering the leading terms in the density, the electron temperature, and the ion temperature equations, neglecting curvature and diffusion contributions, since much smaller than the radial $\boldsymbol{E} \times \boldsymbol{B}$ turbulent transport and the parallel advection terms. We can therefore write, by time, toroidally and poloidally averaging the density equation:

$$\frac{\partial \overline{\Gamma}_n}{\partial x} \simeq -\frac{1}{2\pi q R} \left. \overline{nV_{\parallel e}} \right|_{\text{limiter}},\tag{5.20}$$

where $\partial_x \overline{\Gamma}$ is the radial flux, toroidally and poloidally averaged. We note that $\left. \overline{nV_{\parallel e}} \right|_{\text{limiter}}$ is the toroidally and time averaged parallel flux of n evaluated at the two limiter plates. The same notation is used for the T_e and T_i parallel fluxes, i.e. $\left. \overline{T_e V_{\parallel e}} \right|_{\text{limiter}}$ and $\left. \overline{T_i V_{\parallel e}} \right|_{\text{limiter}}$. Similarly, for the electron temperature equation:

$$\frac{\partial \overline{\Gamma}_{T_e}}{\partial x} \simeq -\frac{2}{3} \frac{1}{2\pi q R} \left. \overline{T_e V_{\parallel e}} \right|_{\text{limiter}}.\tag{5.21}$$

In the ion temperature equation, we keep a curvature term, which, although negligible for small values of τ, can become important for increasing values of τ, as confirmed by the analysis of non-linear simulation results.

$$\frac{\partial \overline{\Gamma}_{T_i}}{\partial x} \simeq -\frac{2}{3} \frac{1}{2\pi q R} \left. \overline{T_i V_{\parallel e}} \right|_{\text{limiter}} - \frac{10}{3R} \tau \overline{T_i C\left(T_i\right)},\tag{5.22}$$

The parallel outflow terms appearing in Eq. (5.22) can be estimated as follows:

$$\frac{2}{3} \frac{1}{2\pi q R} \left. \overline{T_i V_{\parallel e}} \right|_{\text{limiter}} \sim \frac{2}{3} \frac{1}{2\pi q R} \overline{T_i} \sqrt{\overline{T_e}(1 + \tau)},\tag{5.23}$$

while for the curvature term we have:

$$\frac{10}{3R} \tau \overline{T_i} C\left(T_i\right) \sim \frac{10\tau}{3R} \frac{\overline{T_i}^2}{2\pi L_{T_i}},\tag{5.24}$$

where the poloidal gradient of T_i has been neglected with respect to the radial gradient. The ratio of the parallel outflow term with respect to the curvature term

---

is $L_{T_i}\sqrt{1+\tau}/(5q\tau)$. Since, from non-linear simulations results, $L_{T_i} \sim 200$, and typically $q \sim 4$, the curvature term is ~ 10 times smaller than the parallel outflow term for $\tau \simeq 1$, but the two terms can become comparable at large τ. In the following analysis we neglect the curvature term, and we discuss its role later while comparing our analytical estimates with the simulation results.

From Ref. [36], we can write the radial density flux, Γ_n, as:

$$\overline{\Gamma}_n = k_y \overline{\tilde{n}\tilde{\phi}}, \qquad (5.25)$$

The density fluctuations, $\tilde{n}$, are estimated from the leading order term of the continuity equation as $\tilde{n} \sim \tilde{\phi}\overline{n}Rk_y/(\gamma L_n)$. The electric potential fluctuations, $\tilde{\phi}$, can be estimated as $\tilde{\phi} \sim \gamma\tilde{p}L_p/(\overline{p}Rk_y)$, from the leading order terms of the pressure balance, which is obtained by summing up the n, T_e, and T_i equations. Finally, according to the gradient removal theory, $\tilde{p}/\overline{p} = 1/(k_x L_p)$. Inserting these approximations in Eq. (5.25), the radial density turbulent flux becomes therefore:

$$\overline{\Gamma}_n \sim \frac{\gamma\overline{n}}{k_x^2 RL_n}, \qquad (5.26)$$

and analogous expressions can be written for $\overline{\Gamma}_{T_e} \sim \gamma\overline{T_e}/(k_x^2 RL_{T_e})$ and $\overline{\Gamma}_{T_i} \sim \gamma\overline{T_i}/(k_x^2 RL_{T_i})$. We assume that n admits solutions in the form $\overline{n} = n_{max}\exp[(x-x_s)/L_n]$, in the SOL, for $x > x_s$, where x_s is the radial position of the source, and corresponds to the location of the LCFS. Analogous assumptions are made for T_e and T_i. Moreover, we write the linear growth rate as $\gamma = f\overline{T_e}^{1/2}$, where $f = f(R/L_p, \eta_e, \eta_i)$, and depends also on the SOL operational parameters. This representation is valid for all the linear instabilities under investigation. Substituting the expressions for $\overline{n}$, $\overline{T_e}$, $\overline{T_i}$ and for γ into Eq. (5.26), we obtain:

$$\frac{\partial\overline{\Gamma}_n}{\partial x} = \frac{f\overline{n}_{max}\overline{T}_{e,max}^{1/2}}{k_x^2 RL_n}\left(\frac{1}{L_n} + \frac{1}{2L_{T_e}}\right)\exp\left[(x-x_s)\left(\frac{1}{L_n} + \frac{1}{2L_{T_e}}\right)\right], \qquad (5.27)$$

and analogous expressions can be written for $\partial_x\Gamma_{T_e}$ and $\partial_x\Gamma_{T_i}$. Inserting Eq. (5.27), and the analogous expressions for $\partial_x\Gamma_{T_e}$ and $\partial_x\Gamma_{T_i}$ into Eqs. (5.20)-(5.22), we obtain:

$$\frac{f}{k_x^2 L_n}\left(\frac{1}{L_n} + \frac{1}{2L_{T_e}}\right) = \frac{1}{2\pi q},$$

$$\frac{3f}{2k_x^2 L_{T_e}^2} = \frac{1}{3\pi q}, \qquad (5.28)$$

$$\frac{f}{k_x^2 L_{T_i}}\left(\frac{1}{L_{T_i}} + \frac{1}{2L_{T_e}}\right) = \frac{1}{3\pi q},$$

where we have approximated $\overline{nV_{\|e}}\Big|_{\text{limiter}} \sim n_{max}T_{e,max}^{1/2}\exp\left[(x-x_s)\left(\frac{1}{L_n} + \frac{1}{2L_{T_e}}\right)\right]$. Similar estimates are used for $\overline{T_eV_{\|e}}\Big|_{\text{limiter}}$ and $\overline{T_iV_{\|e}}\Big|_{\text{limiter}}$. Combining Eqs. (5.28),

we obtain that $\eta_e = \eta_i$ and that η_e is the solution of a second order equation in the form:

$$\eta_e^2 - \frac{2}{9}\eta_e - \frac{4}{9} = 0. \tag{5.29}$$

We retrieve the result of Ref. [36], $\eta_e = \eta_i = 0.79$. By comparing these estimates with the η_e and η_i values from non-linear simulations, reported in Table 5.1, we observe that they are in reasonable agreement. In particular, while the theoretical estimate is definitely good for η_e, the simulation values of η_i are in general smaller than the theoretical estimate, particularly at large τ, when the curvature term in Eq. (5.22) becomes important.

5.4.2 Role of ITG in the SOL turbulence

According to the analysis of Sec. 5.4.1 and the simulation results, η_i in the SOL is below the ITG linear instability threshold. In fact, as showed in Fig. 5.11, based on the linear analysis, the ITG is unstable for $\eta_i \gtrsim 1$. We therefore expect the ITG to play a negligible role in SOL turbulence. This statement is confirmed by our non-linear results. In the following, we demonstrate that the ITG instability is non-linearly overpowered by the RBM instability for a wide range of parameters. We compare the ITG instability with the RBM, as RBM is the instability expected to drive turbulence, according to our estimate in the $T_i \to 0$ limit, at the typical SOL resistivity [43]. We therefore calculate the estimate of L_p for the ITG instability ($L_{p,ITG}$), according to Eq. (5.19), and we compare it to the estimate for the RBM ($L_{p,RBM}$). The instability driving turbulence in the SOL is expected to be the one leading to the largest L_p, since it allows the system to relax to the state with the lowest turbulent drive.

To calculate $L_{p,ITG}$ according to Eq. (5.19), we first estimate the ITG typical radial extension of the unstable mode, k_x. Applying the non-local linear method outlined in Ref. [104], we write the dispersion relation of the ITG, taken Eq. (5.12), for simplicity in the $k_\parallel \to 0$ limit, as:

$$\frac{\partial^2 \phi}{\partial x^2} - k_y^2 \left[1 + G(x)\right] \phi = 0, \tag{5.30}$$

where

$$G(x) = \frac{-\gamma - 2ik_y(1+\tau) + ik_y R/L_n - \frac{2ik_y\tau[2\gamma + i(-2+3\eta_i)k_y R/L_n]}{3\gamma + 10ik_y\tau}}{\gamma k_y^2 \left\{1 + \frac{\tau[2\gamma + i(-2+3\eta_i)k_y R/L_n]}{3\gamma + 10ik_y.\tau}\right\}} \tag{5.31}$$

Then, we Taylor expand $G(x)$ around x_0, the point of steepest gradient:

$$G(x) \simeq G_0 + G_0''(x - x_0)^2/2, \tag{5.32}$$

obtaining a harmonic oscillator equation, $\partial_x^2 \phi - k_y^2 \left[1 + G_0 + G_0''(x - x_0)^2/2 \right] \phi = 0$, whose solution can be written as:

$$\phi \sim \exp \left[\frac{-a(x - x_0)^2}{2} \right], \tag{5.33}$$

being

$$a = k_y \sqrt{\frac{|G_0''|}{2}}, \tag{5.34}$$

and where $G_0'' = \partial_x^2 G(x)$ at $x = x_0$. The estimate of the ITG radial eddy extension is $k_x = \sqrt{a}$. The $L_{p,ITG}$, evaluated according to Eq. (5.19), is showed in Fig. 5.14, where γ is evaluated from Eq. (5.12), in the $k_\parallel \to 0$ limit, and G_0'' has been evaluated by deriving Eq. (5.31) to estimate k_x^2. A simplified scaling law for $L_{p,ITG}$ can be analytically obtained to explain qualitatively the results in Fig. 5.14. The growth rate, γ, solution of Eq. (5.12), is developed to the lowest order in k_y, and in the limit $R/L_n \gg 1$, it is:

$$\gamma = k_y \left(\frac{iR}{2L_n} + \frac{1}{6} \sqrt{ -\frac{9R^2}{L_n^2} + \frac{72\eta_i R\tau}{L_n} - 160\tau^2 } \right). \tag{5.35}$$

The k_x estimate is obtained from Eq. (5.34), in the limit $R/L_n \gg 1$, and considering only the lowest order terms in k_y. This gives:

$$k_x^2 = \sqrt{ \frac{9(1 + \eta_i \tau)}{2L_n^2(3 + 2\tau)^2} }. \tag{5.36}$$

Substituting Eqs. (5.35) and (5.36) into Eq. (5.19), we obtain a polynomial equation for L_p, that reads as:

$$aL_p^4 + cL_p^2 + dL_p + e = 0, \tag{5.37}$$

$$\begin{aligned}
a &= 18(1 + \tau)(1 + \eta_i \tau), \\
c &= 160/9k_y^2 q^2 (3 + 2\tau)^2 (1 + \eta_i)^2 \tau^2, \\
d &= -8k_y^2 q^2 R\eta_i \tau (3 + 2\tau)^2 (1 + \eta_i), \\
e &= 4k_y^2 q^2 R^2 (3 + 2\tau)^2.
\end{aligned} \tag{5.38}$$

For large τ, the L_p estimate can be evaluated as a balance between the 2nd and the 1st order terms, leading to:

$$L_{p,ITG} \sim \frac{9R\eta_i}{20\tau(1 + \eta_i)}. \tag{5.39}$$

Equation (5.39) describes qualitatively the $L_{p,ITG}$ estimates showed in Fig. 5.14: $L_{p,ITG}$ decreases with τ, and increases with η_i, becoming weakly dependent on η_i
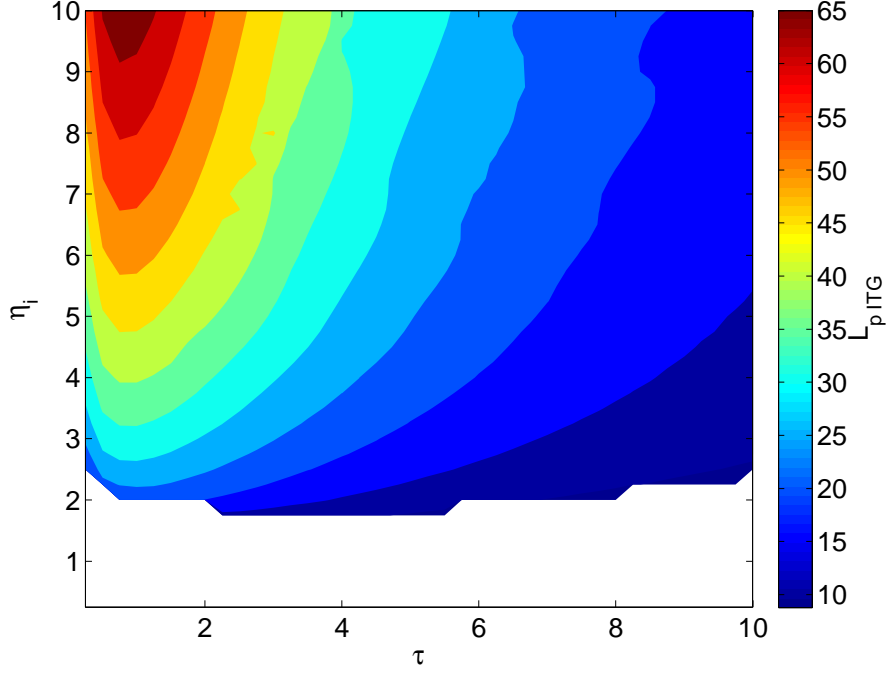
Figure 5.14: *Estimate of the equilibrium pressure scale length, L_{pITG}, from Eq. (5.19), in the hypothesis of ITG modes driving turbulence and transport.*

at large values of η_i.

Finally, we proceed to the comparison between $L_{p,ITG}$ and $L_{p,RBM}$ and to the estimate of the parameters where turbulence is driven by the ITG or the RBM. A scaling law for $L_{p,RBM}$ has been obtained in Ref. [44]. Starting from Eq. (5.19) and assuming $\gamma \simeq \gamma_B^{max}$, $k_x = \sqrt{k_y/L_p}$, and $k_y \simeq k_y^{min}$ (see Sec. 5.3.2), the following scaling law $L_{p,RBM}$ is derived:

$$L_{p,RBM} = R^{3/7}2^{3/7}q^{8/7}(1+\tau)^{1/7}\nu^{2/7}. \tag{5.40}$$

In Fig. 5.15 we show the ratio between $L_{p,ITG}$ and $L_{p,RBM}$, evaluated according to the results showed for the ITG case in Fig. 5.14, and Eq. (5.40). For the RBM case, we consider $\nu = 0.1$. We observe that the ITG leads to larger pressure scale lengths at small values of τ and large values of η_i. The white area represents a region in which Eq. (5.19) has no solution.

In general we expect that turbulence will be driven by the ITG when $L_{p,ITG} > L_{p,RBM}$. Figure 5.15 shows that this occurs when η_i overcomes a certain threshold. As $L_{p,RBM}$ depends on ν, the η_i threshold at which $L_{p,ITG} = L_{p,RBM}$ depends on ν. In Fig. 5.16 we show the η_i threshold above which $L_{pITG} > L_{pRBM}$ as a function of τ and ν. At low τ and ν, turbulence is driven by ITG modes at $\eta_i \gtrsim 2$: the η_i threshold increases with τ and ν. Finally, in the white area, for high τ and ν, the RBM always drives transport. This analysis confirms therefore our predictions
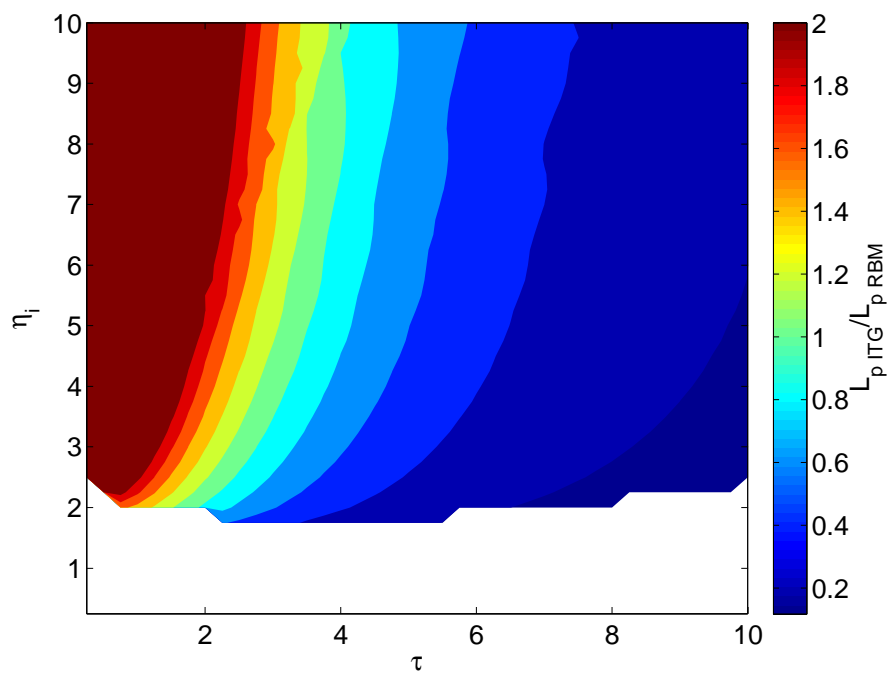
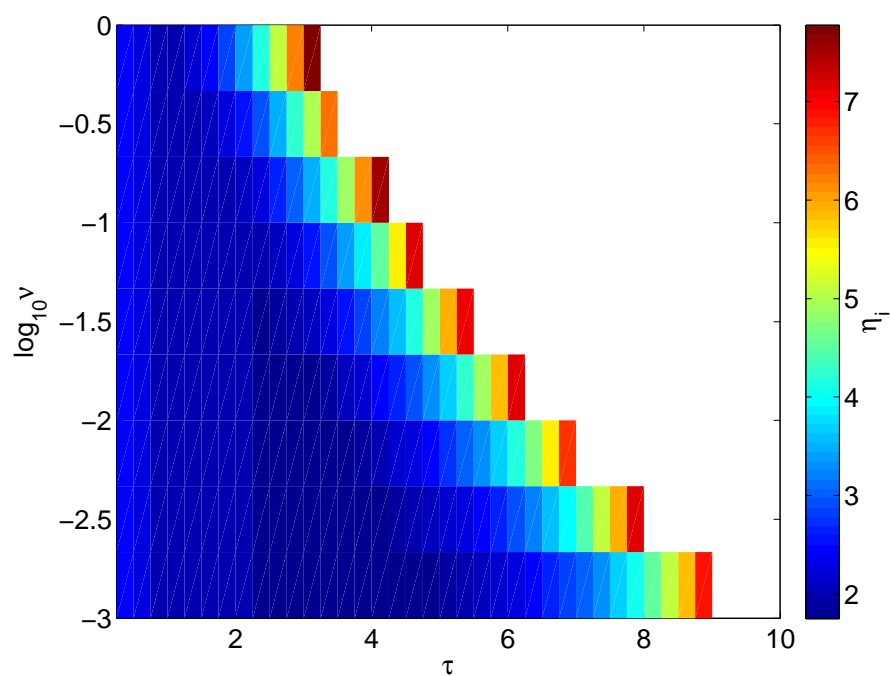**Figure 5.15:** L_{pITG}/L_{pRBM} at $\nu = 0.1$.

Figure 5.16: η_i threshold above which the turbulence is driven by the ITG.

based on the linear result: the ITG instability is active in the SOL when η_i overcomes a threshold that depends on τ and ν, being in any case $\eta_i \gtrsim 2$ necessary to have development of ITG-driven turbulence.

5.4.3 Scrape-off layer turbulent regimes with hot ions

The findings of Sec. 5.4.2 confirm that RBM overcomes the ITG for the η_i values observed in the non-linear simulations. As a matter of fact, this also proves that the ITG mode is sub-dominant with respect to the DW in the case the latter dominates over the RBM. We now identify the SOL turbulent regimes in the presence of hot ions following the same technique described in Sec. 4.2, concentrating on DW and BM only. We first calculate the equilibrium pressure gradient length resulting from the interplay of turbulent tranport and parallel losses using Eq. (5.19). Since we focus on DW and BM only, we can estimate the radial wavenumber as $k_x \simeq \sqrt{k_y/L_p}$, as discussed in Refs. [50], [36], and [39]. Equation (5.19) results in:

$$L_p \sim \frac{q}{c_s\sqrt{1+\tau}} \left(\frac{\gamma}{k_y} \right)_{max} . \tag{5.41}$$

We consider the theoretically estimated values $\eta_e = 0.79$ and $\eta_i = 0.79$, ν varying between 10^{-3} and 1, $m_e/m_i = 1/200$ (the value used in the GBS simulations), τ varying between 0 and 5, and $q = 4$. The estimated values of R/L_p are shown in Fig. 5.17a. Finally, we use the values of R/L_p and k_y previously determined to calculate the growth rate of the four instabilities: RBM, InBM, RDW, and InDW. The instability driving turbulence is the one with the largest growth rate. The result of this calculation is shown in Fig. 5.17b. We observe that for $\nu \gtrsim 10^{-2}$ RBM drives turbulence while, for lower values of ν, InDW overcomes the other instabilities and, finally, the InBM appears at the lowest value of ν and the largest value of τ. A similar calculation is performed by considering the experimental relevant value $m_e/m_i = 1/1836$, with the same other parameters. In Fig. 5.18a and Fig. 5.18b we show the estimated values of R/L_p and the instability driving turbulence, respectively. The RBM drives turbulence for $\nu \gtrsim 5 \times 10^{-3}$, while for lower values of ν the InDW prevails. The RDW appears at $\nu = 10^{-2}$ and $\tau = 0$.

In order to test the validity of our predictions, we compare R/L_p and k_y of the non-linear simulations described in Sec. 5.2 to the gradient removal estimates in Table 5.1. The maximum difference of R/L_p between our estimate and the simulation results is of order 10%. The uncertainty affecting k_y is estimated by considering a 10% variation of the γ/k_y value with respect to its maximum at the predicted R/L_p, and evaluating the k_y range corresponding to this variation. In Table 5.1 we also list the growth rates of each instability separately, in order to identify the instability regime of the non-linear simulations. We observe that turbulence is RBM driven in all simulations. This result is in agreement with the
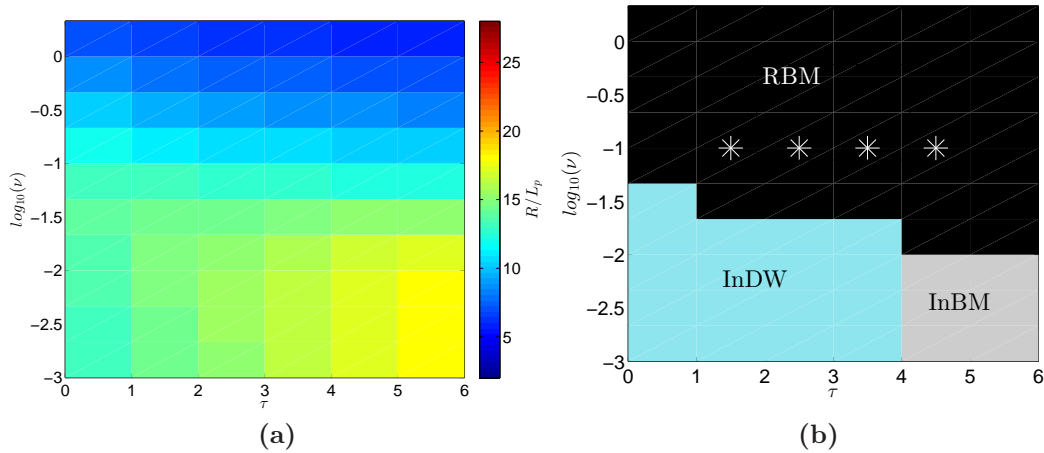
Figure 5.17: R/L_p *estimate (a) and turbulent regimes (b) at $m_i/m_e = 200$; different colors identify different regimes: RBM (black), InBM (grey), InDW (light blue). The white star symbols indicate the parameters at which non-linear simulations have been performed.*

results illustrated in Fig. 5.17b, where the four non-linear simulations are indicated by a white star symbol falling in the RBM regime.

5.5 Conclusions

In the present chapter we discuss the effects of hot ion dynamics on SOL turbulence, by using the drift-reduced Braginskii equations, in the electrostatic limit. This study is motivated by experimental observations that show $T_i \gtrsim T_e$ in the SOL. Hot ion dynamics introduces the ITG mode, and modifies the properties of the instabilities that exist in the cold ion limit, like the inertial and resistive branches of the DW, and of the BM.

First, we present the results of a set of non-linear GBS simulations with hot ions, for τ ranging from 1 to 4. By means of the cross coherence analysis between ϕ and n fluctuations, and their phase shift, we conclude that the observed instability has the typical footprint of a BM, being ϕ and n weakly correlated and exhibiting a phase shift close to $\pi/2$.

Second, we investigate the effect of hot ion dynamics on the linear SOL instabilities. Both the RDW and the InDW instabilities show a decreasing growth rate for increasing η_i. For the two branches of the BM instability, the introduction of hot ions increases the maximum growth rate with respect to the cold ion limit. As in the cold ion limit, the BM instability is damped for $k_y < k_y^{min}$, where k_y^{min} is determined by the stabilization due to the parallel dynamics. At large η_i, finite $k_\parallel$ effects decrease the growth rate with respect to its maximum. Then, we describe the ITG instability, discussing its slab and toroidal branches. The ITG mode is
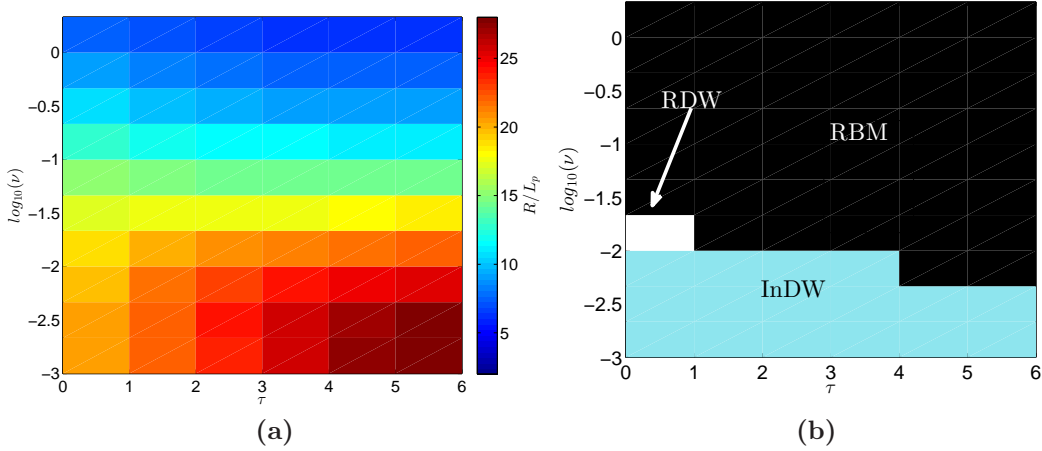
Figure 5.18: R/L_p estimate (a) and turbulent regimes (b) at $m_i/m_e/1836$; different colors identify different regimes: RBM (black), RDW (white), InDW (light blue).

unstable at η_i above a threshold that decreases with R/L_n and it is $\eta_i \simeq 1$ for $R/L_n \gtrsim 15$. Ion temperature gradient modes show a growth rate $\gamma \sim \eta_i \omega_*$ and a corresponding $k_\parallel \sim \eta_i \omega_*$. The k_y corresponding to the maximum growth rate is inversely proportional to both $\sqrt{\tau}$ and $\sqrt{\eta_i}$.

The η_i observed in the non-linear simulations of Sec. 5.2 and theoretically estimated, also in agreement with experimental observations [99, 100], is smaller than the linear threshold for ITG instability. Therefore we expect ITG to have a negligible role on SOL turbulence. This is confirmed by the analysis of the SOL turbulent regimes. Indeed, by comparing L_p estimates for the ITG and for the BM, obtained by means of the gradient removal theory, we show that the ITG is either not active, or overcome by the BM, unless η_i exceeds a threshold that is an increasing function of τ and ν, being its lowest value ~ 2. As a consequence, we conclude that, in the SOL scenario considered here, the ITG instability is expected to play a negligible role in driving and regulating SOL turbulence.

Chapter 6

Conclusions and outlook

Understanding the plasma dynamics in the tokamak SOL region is of crucial importance for the success of the entire fusion program. Scrape-off layer physics determines the boundary conditions for the plasma in the whole machine, it is expected to play a role in the L-H transition, and it regulates the power exhaust. In the SOL region, plasma is lost to the divertor, or the limiter, by streaming along the magnetic field lines, while it is transported in the perpendicular direction because of turbulence driven by different free energy sources present in the SOL. It is therefore important to identify the SOL turbulent regimes and their main features in order to predict, and eventually control, plasma behaviour in the SOL. The present thesis is focused on the investigation of the turbulent regimes in the tokamak SOL by identifying the mechanisms driving turbulence depending on the SOL parameters. Our investigations are limited to the cases where $\boldsymbol{E} \times \boldsymbol{B}$ velocity shear does not play a significant role in stabilizing turbulence.

In Chap. 2 we present the model we use throughout the thesis, based on the drift-reduced Braginskii equations, considering a limited plasma configuration in $s - \alpha$ equilibrium. We also derive a new set of boundary conditions to apply to these equations at the magnetic presheath entrance, including hot ion dynamics.

In Chap. 3, we describe the main linear instabilities included in our model, in the cold ion limit, identifying the inertial and resistive DW, and the resistive, inertial and ideal BM branches. In general the DWs have a larger growth rate than BMs for steep gradients, being the R/L_n threshold dependent on the two parameters $\sigma_R = 1/(\gamma_B^{max} k_y^2 q^2 \nu)$ and $\sigma_{In} = \sqrt{m_i}/\left(\gamma_B^{max} k_y q \sqrt{m_e}\right)$, describing the competition between parallel and perpendicular dynamics. The transition between RDW and InDW is governed by the $\delta = \nu L_n m_i/(R m_e)$ parameter and it occurs at $\delta \simeq 3.55$ for $\hat{s} = 0$, with the transition value of δ decreasing with the increase of $|\hat{s}|$. The regions of influence of the RBM and the InBM has been evaluated as a function of σ_R and σ_{In}, the boundary between those is independent of $\hat{s}$ for most of the values of σ_R and σ_{In}. The electromagnetic effects cause a damping of the DW instabilities at high R/L_n and the appearance of the IdBM instability, when the

$\alpha_{MHD} = q^2 \beta (1 + \eta_e) R/L_n$ threshold is overcome. Since in existing tokamaks R/L_n spans one order of magnitude and ν two orders of magnitude (see, e.g. Refs. [68, 69, 70, 71, 67, 72, 73, 74, 75]), we expect the behaviour of the SOL to change remarkably in these wide intervals of parameters. Our parameter space analysis of the linear SOL instabilities has been conceived as a first stage tool to be used in the understanding of turbulence in the SOL of tokamaks, necessary to interpret the results of non-linear simulations.

The analysis presented in Chap. 4 extends the results of Chap. 3 to the non-linear dynamics, identifying the SOL turbulent parameter space in the electrostatic limit. We ascribe the saturation of linear modes in the SOL to the *gradient removal* mechanism, which is active in standard SOL scenarios (see Ref. [87]). Saturation occurs when the radial derivative of the background pressure gradient is comparable to the radial derivative of the pressure fluctuations. This allows us to predict the time-averaged plasma gradient length, which is proportional to γ/k_y, where γ is the linear growth rate and k_y the poloidal wavenumber of the instability that dominates the non-linear dynamics. We build a map in the parameter space, where we identify the transport regime, depending on the driving instability as a function of the magnetic shear, $\hat{s}$, and the resistivity, ν, having fixed the mass ratio, m_e/m_i, and the safety factor, q. We observe that DWs drives turbulence at negative shear, InDW dominates at low ν, while positive shear and high q are favourable for BMs. We investigate the transition among the different instabilities (the RBM-InBM, the RBM-InDW, the RBM-RDW, and the RDW-InDW transitions) determining, in general, the threshold value of ν at which they take place. Being the transition between InBM and InDW independent of ν, we estimate the value of q at which this transition takes place as a function of $\hat{s}$. The validity of our methodology is verified by performing a set of non-linear simulations carried out with the GBS code, and we present four of those, each belonging to a different instability regime. For each set of SOL parameters of the non-linear simulations, we predict the instability regime, R/L_p, and the k_y of the saturated non-linear mode, according to the gradient removal hypothesis. The predictions and the results of the non-linear simulations show reasonable agreement. In particular, the analysis of the turbulence properties shows the capability of our methodology to identify the non-linear turbulent regimes.

In Chap. 5 we further develop our model by including the hot ion dynamics. We analyse the effect of hot ions on the linear SOL instabilities existing in the cold ion limit. Both RDW and InDW show a decreasing growth rate for increasing η_i. Hot ion dynamics increases the BM growth rate with respect to the cold ion limit. Similarly to what is observed in the cold ion limit, the BM is damped for $k_y < k_y^{min}$, where k_y^{min} is determined by the stabilization due to the parallel dynamics. We also describe the ITG instability with its slab and toroidal branches. The ITG mode is unstable when η_i overcomes a threshold that decreases with R/L_n, and it is $\eta_i \simeq 1$ at $R/L_n \gtrsim 15$. Ion temperature gradient modes show a growth rate $\gamma \sim \omega_* \eta_i$ and a corresponding $k_\parallel \sim \omega_* \eta_i$. The k_y at the maximum growth rate is inversely proportional to $\sqrt{\tau \eta_i}$. Since non-linear simulations including hot ion

dynamics and theoretical estimates, in agreement with experimental results, show that η_i is below the linear instability threshold for ITG, we expect ITG to play a negligible role in SOL turbulence. This result is confirmed by the analysis of the SOL turbulent regimes by means of the gradient removal theory: the comparison between L_p obtained for ITG and for BM regimes show that ITG is overcome by BM, unless η_i is larger than a threshold which, in turn, is an increasing function of τ and ν and whose minimum value is around 2. Moreover, a weak cross coherence and a phase shift around $\pi/2$ between the density and the potential fluctuations in the non-linear simulations show the typical footprint of the BM regime, supporting the evidence that BM is driving SOL turbulence in typical operating conditions.

To conclude, the present thesis identifies the main SOL turbulent regimes in a toroidally limited configuration, in $s - \alpha$ geometry, using a drift-reduced Braginskii model, and defines the regime driving turbulent transport as a function of the magnetic shear, $\hat{s}$, the resistivity, ν, the ion to electron temperature ratio, τ, the safety factor, q, and the electron to ion mass ratio, m_e/m_i. The work focuses on the gradient removal as the mechanism causing non-linear turbulent saturation, by which the gradient length, L_p, and the poloidal mode number, k_y, are estimated. The methodology for the turbulent regimes identification is supported by comparisons against non-linear simulation results performed with the GBS code. The main turbulent regimes identified are the resistive and inertial branches of the DW and of the BM modes, and the ITG mode.

Future extensions of the present work include the analysis of the coupling of the SOL dynamics with the closed flux surface region, in order to achieve full understanding of the turbulent regimes in the tokamak edge. This will allow us to address the physics related to the $\boldsymbol{E} \times \boldsymbol{B}$ shear suppression and approach the study of the L-H transition. Moreover, more complicated magnetic topologies, which include the X-point geometry and the presence of divertor plates, need to be considered for the analysis of the reactor relevant configurations. In this work we consider a convection limited scenario, in which ionization takes place in the tokamak core, and neutral dynamics is neglected. The introduction of the latter effects in GBS, in order to achieve a high-recycling and detached regimes, is currently under implementation.

Appendix A

Boundary conditions at the magnetic presheath entrance of non-isothermal plasmas

The derivation of boundary conditions at the magnetic presheath entrance, including hot ion dynamics, in the limit of isothermal ions and electrons, has been the subject of Sec. 2.4.4. We now relax the isothermal hypothesis and we verify that the boundary conditions derived in Sec. 2.4.4 are reasonable. For this purpose, we follow a derivation similar to the one presented in the Appendix of Ref. [49]. We include both non-isothermal ions and electrons. For sake of simplicity, we consider the case of no gradients along the x direction. We consider the ion continuity equation, the ion and electron parallel velocity equations, and the electron and ion temperature equations. We use the adimensionalization introduced in Sec. 2.4.4. The ion continuity equation, Eq. (2.115) holds also in the case of non-isothermal ions and electrons. The ion parallel momentum equation, Eq. (2.118), is modified as follows:

$$nV'_{si}\partial_s V_{\|i} + \sin\alpha\left(n\partial_s\phi + \tau T_i\partial_s n\right) + \sin\alpha\tau n\partial_s T_i = S_{\|m_i}, \tag{A.1}$$

the last term on the left hand side representing the non-isothermal ion contribution. The electron parallel velocity equation, Eq. (2.120), is also modified, obtaining:

$$\mu\sin\alpha T_e\partial_s n - \mu\sin\alpha n\partial_s\phi + 1.71\mu n\sin\alpha\partial_s T_e = S_{\|m_e}, \tag{A.2}$$

the last term on the left hand side representing the non-isothermal electron contribution. The electron temperature equation is derived from Eq. (2.89), in steady state, neglecting inertia, diffusion and resistivity effects:

$$nV_{\|e}\sin\alpha\partial_s T_e + \frac{2}{3}T_e\left[1.71n\sin\alpha\partial_s V_{\|e} - 0.71n\sin\alpha\partial_s V_{\|i}\right] +$$
$$-0.71\left(V_{\|i} - V_{\|e}\right)\sin\alpha\partial_s n + \frac{2}{3}\sin\alpha\partial_s q_e = S_{T_e}. \tag{A.3}$$

Chapter A. Boundary conditions at the magnetic presheath entrance of non-isothermal plasmas

The last term on the left hand side represents the microscopic heat flux and it takes into account the heat flux associated to a non-Maxwellian velocity distribution function. In fact, when a plasma is in contact with an absorbing wall, a non-neutral sheath develops, where the electrostatic potential drops, causing the repulsion of the electrons. As the electrons having an energy higher than the potential barrier can flow out of the system, without being reflected, the electron population can be described as a truncated maxwellian. The heat flux in the direction parallel to the magnetic field, associated with the truncated maxwellian distribution, can be expressed as (see Ref. [105]):

$$q_e = \frac{nT_e^{3/2}}{\sqrt{2\pi}I(\eta)}\left(\frac{m_i}{m_e}\right)^{1/2}\left[e^{-\eta}\left(\eta - \frac{1}{2}\right) + \frac{3}{2}\sqrt{\frac{\eta}{\pi}}\frac{e^{-2\eta}}{I(\eta)} + \frac{e^{-3\eta}}{2\pi I^2(\eta)}\right], \qquad (A.4)$$

where $\eta = \phi/T_e$, and $I(\eta) = \left[1 + \text{erf}(\sqrt{\eta})\right]$. The last term on the left hand side of Eq. (A.3) can therefore be expressed as:

$$\frac{2}{3}\sin\alpha\partial_s q_e = \frac{2}{3}\sin\alpha\frac{1}{T_e}\partial_s\phi\partial_\eta q_e. \qquad (A.5)$$

Introducing Eq. (A.4) into Eq. (A.5), we obtain:

$$\frac{2}{3}\sin\alpha\partial_s q_e = \frac{2}{3}\sin\alpha\frac{1}{\sqrt{2\pi}}n\sqrt{T_e}\sqrt{\frac{m_i}{m_e}}A_1\partial_s\phi, \qquad (A.6)$$

where A_1 is:

$$A_1 = \frac{\partial}{\partial\eta}\left(\frac{1}{I(\eta)}\left[e^{-\eta}\left(\eta - \frac{1}{2}\right) + \frac{3}{2}\sqrt{\frac{\eta}{\pi}}\frac{e^{-2\eta}}{I(\eta)} + \frac{e^{-3\eta}}{2\pi I^2(\eta)}\right]\right). \qquad (A.7)$$

Finally, the ion temperature equation is derived from Eq. (2.69), where $\boldsymbol{V}_{pol}$ has been neglected in $\boldsymbol{V}_{\perp i}$:

$$\frac{2}{3}T_i\sin\alpha\partial_s V_{\|i} + V_{\|i}\sin\alpha\partial_s T_i = S_{T_i}. \qquad (A.8)$$

Equations (2.115), (A.1), (A.2), (A.3), and (A.8) can be written as a linear system of equations, $M\boldsymbol{X} = \boldsymbol{S}$, where $\boldsymbol{X} = \left(\partial_s n, \partial_s V_{\|i}, \partial_s\phi, \partial_s T_e, \partial_s T_i\right)$, $\boldsymbol{S}$ is the source vector, and the M matrix is:

$$M = \begin{pmatrix} V'_{si} & n\sin\alpha & 0 & 0 & 0 \\ \sin\alpha\tau T_i & nV'_{si} & n\sin\alpha & 0 & \sin\alpha\tau n \\ \mu\sin\alpha T_e & 0 & -\mu n\sin\alpha & 1.71\mu n\sin\alpha & 0 \\ \begin{matrix}2/3\,0.71T_e\sin\alpha V_{\|e}+ \\ -2/3\,0.71T_e\sin\alpha V_{\|i}\end{matrix} & -2/3\,0.71nT_e\sin\alpha & \begin{matrix}2/3\,1.71c_\phi nT_e\sin\alpha+ \\ +n\sqrt{T_e}A_2\sin\alpha\end{matrix} & \begin{matrix}2/3\,1.71c_{T_e}nT_e\sin\alpha+ \\ +nV_{\|e}\sin\alpha\end{matrix} & 0 \\ 0 & 2/3T_i\sin\alpha & 0 & 0 & V_{\|i}\sin\alpha \end{pmatrix},$$

$$\qquad (A.9)$$

Annamaria Mosetto – CRPP/EPFL

where $A_2 = 2A_1\sqrt{m_i}/(3\sqrt{2\pi m_e})$. In Eq. (A.9) we have assumed that $\partial_s V_{\|e} = c_\phi \partial_s \phi + c_{T_e} \partial_s T_e$, where $c_\phi = \partial_\phi V_{\|e}$ and $c_{T_e} = \partial_{T_e} V_{\|e}$ are assumed to be known functions. Imposing again $\det M = 0$ at the magnetic presheath entrance, we find:

$$V_{\|i}^2 = T_e \frac{0.19 + 1.14 \hat{c_{T_e}} + \tau \tau_f \left[3.25 \hat{c_\phi} + 3.1 \hat{c_{T_e}} + 5/3 + 2.85 A_2 \right]}{1.14 \left(1.71 \hat{c_\phi} + \hat{c_{T_e}} \right) + 1 + 1.71 A_2}. \tag{A.10}$$

where $\tau_f = T_i/T_e$, $\hat{c_\phi} = c_\phi T_e / V_{\|e} = -1$, and $\hat{c_{T_e}} = c_{T_e} T_e / V_{\|e} = 0.5 + \phi/T_e \simeq 0.5 + \Lambda$. For $\Lambda = 3$, and $m_i/m_e = 1836$, $V_{\|i}/c_s$ is a decreasing function of τ, at $\tau = 0$ its value is 1.70, at $\tau = 1$ its value is 1.51, and its limit for $\tau \to \infty$ is 1.29. The previous result shows therefore that the Bohm-Chodura criterion, $V_{\|i} = c_s$ at the magnetic presheath entrance does not hold perfectly, even in the $\tau = 0$ limit, when non-isothermal ion and electron dynamics is taken into account. Finally, we can obtain an expression for $\partial_s T_i$:

$$\partial_s T_i = \partial_s \phi \frac{\tau_f}{F 3/2 - 5/2 \tau \tau_f} \simeq 0.23 \, \partial_s \phi, \tag{A.11}$$

where $F = V_{\|i}^2 / T_e$. We remark that the value of $\partial_s T_i$ does not depend on τ. Analogously, we obtain for $\partial_s T_e$:

$$\partial_s T_e = \partial_s \phi \frac{1.71 + 3/2 \, A_2 - 0.71/(F - \tau \tau_f)}{1.71(0.5 + \Lambda) + 3/2}. \tag{A.12}$$

The function $\partial_s T_e$ increases with τ. At $\tau = 0$ we find $\partial_s T_e / \partial_s \phi \simeq 1 \times 10^{-3}$, at $\tau = 1$ $\partial_s T_e / \partial_s \phi \simeq 0.015$, and in the limit $\tau \to \infty$, it is $\partial_s T_e / \partial_s \phi \simeq 0.04$. According to Eqs. (A.11) and (A.12), $\partial_s T_i$ and $\partial_s T_e$ can be therefore neglected in comparison with $\partial_s \phi$, confirming the validity of the derivation of the boundary conditions presented in Sec. 2.4.4.

Bibliography

[1] O. A. Hurricane, D. A. Callahan, D. T. Casey, P. M. Celliers, C. Cerjan, E. L. Dewald, T. R. Dittrich, T. Doppner, D. E. Hinkel, L. F. Berzak Hopkins, J. L. Kline, S. Le Pape, T. Ma, A. G. MacPhee, J. L. Milovich, A. Pak, H.-S. Park, P. K. Patel, B. A. Remington, J. D. Salmonson, P. T. Springer, and R. Tommasini. Fuel gain exceeding unity in an inertially confined fusion implosion. *Nature*, 506:343, 2014.

[2] Wikipedia. ITER, 2014.

[3] A. Loarte, B. Lipschultz, A.S. Kukushkin, G.F. Matthews, P.C. Stangeby, N. Asakura, G.F. Counsell, G. Federici, A. Kallenbach, K. Krieger, A. Mahdavi, V. Philipps, D. Reiter, J. Roth, J. Strachan, D. Whyte, R. Doerner, T. Eich, W. Fundamenski, A. Herrmann, M. Fenstermacher, P. Ghendrih, M. Groth, A. Kirschner, S. Konoshima, B. LaBombard, P. Lang, A.W. Leonard, P. Monier-Garbet, R. Neu, H. Pacher, B. Pegourie, R.A. Pitts, S. Takamura, J. Terry, E. Tsitrone, the ITPA Scrape-off Layer, and Divertor Physics Topical Group. Chapter 4: Power and particle control. *Nuclear Fusion*, 47(6):S203, 2007.

[4] J. W. Connor and H. R. Wilson. A review of theories of the L-H transition. *Plasma Physics and Controlled Fusion*, 42(1):R1, 2000.

[5] S. I. Braginskii. Transport processes in a plasma. *Reviews of plasma physics*, 1:205, 1965.

[6] A. Zeiler. Tokamak edge turbulence. *Max-Planck-Institut für Plasmaphysik*, (IPP 5/88), 1999.

[7] O. E. Garcia, V. Naulin, A. H. Nielsen, and J. Juul Rasmussen. Computations of intermittent transport in scrape-off layer plasmas. *Phys. Rev. Lett.*, 92:165003, 2004.

[8] D. A. Russell, J. R. Myra, and D. A. D'Ippolito. Saturation mechanisms for edge turbulence. *Physics of Plasmas*, 16(12):122304, 2009.

[9] N. Bisai, R. Singh, and P. K. Kaw. Scrape-off layer tokamak plasma turbulence. *Physics of Plasmas*, 19(5):052509, 2012.

[10] F. Militello, W. Fundamenski, V. Naulin, and A. H. Nielsen. Simulations of edge and scrape off layer turbulence in mega ampere spherical tokamak plasmas. *Plasma Physics and Controlled Fusion*, 54(9):095011, 2012.

[11] B. Scott. Three-dimensional computation of drift Alfvén turbulence. *Plasma Physics and Controlled Fusion*, 39(10):1635, 1997.

[12] B.D. Dudson, M.V. Umansky, X.Q. Xu, P.B. Snyder, and H.R. Wilson. Bout++: A framework for parallel plasma fluid simulations. *Computer Physics Communications*, 180(9):1467, 2009.

[13] P. Tamain, Ph. Ghendrih, E. Tsitrone, V. Grandgirard, X. Garbet, Y. Sarazin, E. Serre, G. Ciraolo, and G. Chiavassa. TOKAM-3D: A 3D fluid code for transport and turbulence in the edge plasma of tokamaks. *Journal of Computational Physics*, 229(2):361, 2010.

[14] V. Naulin, T. Windisch, and O. Grulke. Three-dimensional global fluid simulations of cylindrical magnetized plasmas. *Physics of Plasmas*, 15(1):012307, 2008.

[15] P. Beyer, X. Garbet, and P. Ghendrih. Tokamak turbulence with stochastic field lines. *Physics of Plasmas*, 5(12):4271, 1998.

[16] G. Fuhr, P. Beyer, S. Benkadda, and X. Garbet. Evidence from numerical simulations of transport-barrier relaxations in tokamak edge plasmas in the presence of electromagnetic fluctuations. *Phys. Rev. Lett.*, 101:195001, 2008.

[17] W. Dorland and G. W. Hammett. Gyrofluid turbulence models with kinetic effects. *Physics of Fluids B: Plasma Physics (1989-1993)*, 5(3):812, 1993.

[18] M. A. Beer and G. W. Hammett. Toroidal gyrofluid equations for simulations of tokamak turbulence. *Physics of Plasmas*, 3(11):4046, 1996.

[19] B. Scott. Free-energy conservation in local gyrofluid models. *Physics of Plasmas*, 12(10):102307, 2005.

[20] P. Ricci, F. D. Halpern, S. Jolliet, J. Loizu, A. Mosetto, A. Fasoli, I. Furno, and C. Theiler. Simulation of plasma turbulence in scrape-off layer conditions: the GBS code, simulation results and code validation. *Plasma Physics and Controlled Fusion*, 54(12):124047, 2012.

[21] B. Scott. The nonlinear drift wave instability and its role in tokamak edge turbulence. *New Journal of Physics*, 4(1):52, 2002.

[22] A. Zeiler, D. Biskamp, J. F. Drake, and P. N. Guzdar. Three-dimensional fluid simulations of tokamak edge turbulence. *Physics of Plasmas*, 3(8):2951, 1996.

[23] B. N. Rogers and J. F. Drake. Enhancement of turbulence in tokamaks by magnetic fluctuations. *Phys. Rev. Lett.*, 79:229, 1997.

[24] B. N. Rogers, J. F. Drake, and A. Zeiler. Phase space of tokamak edge turbulence, the L-H transition, and the formation of the edge pedestal. *Phys. Rev. Lett.*, 81:4396, 1998.

[25] B. Scott. Drift wave versus interchange turbulence in tokamak geometry: Linear versus nonlinear mode structure. *Physics of Plasmas*, 12(6):062314, 2005.

[26] J. F. Drake, A. Zeiler, and D. Biskamp. Nonlinear self-sustained drift-wave turbulence. *Phys. Rev. Lett.*, 75:4222, 1995.

[27] B. LaBombard, J .W. Hughes, D. Mossessian, M. Greenwald, B. Lipschultz, J. L. Terry, and the Alcator C-Mod Team. Evidence for electromagnetic fluid drift turbulence controlling the edge plasma state in the Alcator C-Mod tokamak. *Nuclear Fusion*, 45(12):1658, 2005.

[28] P. N. Guzdar, R. G. Kleva, A. Das, and P. K. Kaw. Zonal flow and zonal magnetic field generation by finite β drift waves: A theory for low to high transitions in tokamaks. *Phys. Rev. Lett.*, 87:015001, 2001.

[29] S. Tsai, F. W. Perkins, and T. H. Stix. Thermal conductivity and low frequency waves in collisional plasmas. *Physics of Fluids (1958-1988)*, 13(8):2108, 1970.

[30] F. L. Hinton and C. W. Horton. Amplitude limitation of a collisional drift wave instability. *Physics of Fluids (1958-1988)*, 14(1):116, 1971.

[31] W. Horton and R. D. Estes. Fluid simulation of ion pressure gradient driven drift modes. *Plasma Physics*, 22(7):663, 1980.

[32] J. F. Drake and T. M. Antonsen. Non-linear reduced fluid equations for toroidal plasmas. *Physics of Fluids (1958-1988)*, 27(4):898, 1984.

[33] R. D. Hazeltine, C. T. Hsu, and P. J. Morrison. Hamiltonian four field model for nonlinear tokamak dynamics. *Physics of Fluids (1958-1988)*, 30(10):3204, 1987.

[34] W. Horton. Nonlinear drift waves and transport in magnetized plasma. *Physics Reports*, 192(1-3):1, 1990.

[35] A. Zeiler, J. F. Drake, and B. Rogers. Non-linear reduced Braginskii equations with ion thermal dynamics in toroidal plasma. *Physics of Plasmas*, 4(6):2134, 1997.

[36] P. Ricci, B. N. Rogers, and S. Brunner. High- and low-confinement modes in simple magnetized toroidal plasmas. *Phys. Rev. Lett.*, 100:225002, 2008.

[37] B. N. Rogers and P. Ricci. Low-frequency turbulence in a linear magnetized plasma. *Phys. Rev. Lett.*, 104:225002, 2010.

[38] A. Fasoli, B. Labit, M. McGrath, S. H. Müller, G. Plyushchev, M. Podestà, and F. M. Poli. Electrostatic turbulence and transport in a simple magnetized plasmaa. *Physics of Plasmas*, 13(5):055902, 2006.

[39] P. Ricci and B. N. Rogers. Three-dimensional fluid simulations of a simple magnetized toroidal plasma. *Physics of Plasmas*, 16(9):092307, 2009.

[40] P. Ricci and B. N. Rogers. Turbulence phase space in simple magnetized toroidal plasmas. *Phys. Rev. Lett.*, 104:145001, 2010.

[41] P. Ricci, C. Theiler, A. Fasoli, I. Furno, B. Labit, S. H. Müller, M. Podestà, and F. M. Poli. Langmuir probe-based observables for plasma-turbulence code validation and application to the TORPEX basic plasma physics experiments. *Physics of Plasmas*, 16(5):055703, 2009.

[42] P. Ricci, C. Theiler, A. Fasoli, I. Furno, K. Gustafson, D. Iraji, and J. Loizu. Methodology for turbulence code validation: Quantification of simulation-experiment agreement and application to the TORPEX experiment. *Physics of Plasmas*, 18(3):032109, 2011.

[43] A. Mosetto, F. D. Halpern, S. Jolliet, J. Loizu, and P. Ricci. Turbulent regimes in the tokamak scrape-off layer. *Physics of Plasmas*, 20(9):092308, 2013.

[44] F. D. Halpern, P. Ricci, B. Labit, I. Furno, S. Jolliet, J. Loizu, A. Mosetto, G. Arnoux, J. P. Gunn, J. Horacek, M. Kočan, B. LaBombard, C. Silva, and JET-EFDA Contributors. Theory-based scaling of the sol width in circular limited tokamak plasmas. *Nuclear Fusion*, 53(12):122001, 2013.

[45] G. Q. Yu, S. I. Krasheninnikov, and P. N. Guzdar. Two-dimensional modelling of blob dynamics in tokamak edge plasmas. *Physics of Plasmas*, 13(4):042508, 2006.

[46] S. Jolliet, F. D. Halpern, J. Loizu, A. Mosetto, and P. Ricci. Aspect ratio effects on limited scrape-off layer plasma turbulence. *Physics of Plasmas*, 21(2):022303, 2014.

[47] X. Lapillonne, S. Brunner, T. Dannert, S. Jolliet, A. Marinoni, L. Villard, T. Gorler, F. Jenko, and F. Merz. Clarifications to the limitations of the s-alpha equilibrium model for gyrokinetic computations of turbulence. *Physics of Plasmas*, 16(3):032308, 2009.

[48] A. Arakawa. Computational design for long-term numerical integration of the equations of fluid motion: Two-dimensional incompressible flow. Part I. *Journal of Computational Physics*, 1(1):119, 1966.

[49] J. Loizu, P. Ricci, F. D. Halpern, and S. Jolliet. Boundary conditions for plasma fluid models at the magnetic presheath entrance. *Physics of Plasmas*, 19(12):122307, 2012.

[50] B. N. Rogers and W. Dorland. Noncurvature-driven modes in a transport barrier. *Physics of Plasmas*, 12(6):062511, 2005.

[51] E. Anderson, Z. Bai, C. Bischof, S. Blackford, J. Demmel, J. Donngarra, A. Greenbaum J. Du Croz, S. Hammarling, A. McKenney, and D. Sorensen. *LAPACK User's Guide*. Third Edition, SIAM, Philadelphia, 1999.

[52] N. J. Higham. The scaling and squaring method for the matrix exponential revisited. *SIAM Journal on Matrix Analysis and Applications*, 26(4):1179, 2005.

[53] J. W. Connor, R. J. Hastie, and J. B. Taylor. Shear, periodicity, and plasma ballooning modes. *Phys. Rev. Lett.*, 40:396, 1978.

[54] G. Bateman and D. B. Nelson. Resistive-ballooning-mode equation. *Phys. Rev. Lett.*, 41:1804, 1978.

[55] D. R. McCarthy, P. N. Guzdar, J. F. Drake, Jr. T. M. Antonsen, and A. B. Hassam. Stability of resistive and ideal ballooning modes in the texas experimental tokamak and diii-d. *Physics of Fluids B: Plasma Physics*, 4(7):1846, 1992.

[56] S. V. Novakovskii, P. N. Guzdar, J. F. Drake, C. S. Liu, and F. L. Waelbroeck. New unstable branch of drift resistive ballooning modes in tokamaks. *Physics of Plasmas*, 2(3):781, 1995.

[57] T. Rafiq, G. Bateman, A. H. Kritz, and A. Y. Pankin. Development of drift-resistive-inertial ballooning transport model for tokamak edge plasmas. *Physics of Plasmas*, 17(8):082511, 2010.

[58] T. Rafiq, C. C. Hegna, J. D. Callen, and A. H. Kritz. Unified theory of resistive and inertial ballooning modes in three-dimensional configurations. *Physics of Plasmas*, 16(10):102505, 2009.

[59] A. Zeiler, D. Biskamp, and J. F. Drake. Three-dimensional collisional drift-wave turbulence: Role of magnetic shear. *Physics of Plasmas*, 3(11):3947, 1996.

[60] A. Zeiler, D. Biskamp, J. F. Drake, and B. N. Rogers. Transition from resistive ballooning to η_i driven turbulence in tokamaks. *Physics of Plasmas*, 5(7):2654, 1998.

[61] A. Kendl and B. D. Scott. Magnetic shear damping of dissipative drift wave turbulence. *Phys. Rev. Lett.*, 90:035006, 2003.

[62] K. Mima and A. Hasegawa. Nonlinear instability of electromagnetic drift waves. *Physics of Fluids*, 21(1):81, 1978.

[63] M. Wakatani and A. Hasegawa. A collisional drift wave description of plasma edge turbulence. *Physics of Fluids*, 27(3):611, 1984.

[64] H. Sugama, M. Wakatani, and A. Hasegawa. Study of resistive drift and resistive interchange modes in a cylindrical plasma with magnetic shear. *Physics of Fluids*, 31(6):1601, 1988.

[65] W. Horton. Drift waves and transport. *Rev. Mod. Phys.*, 71:735, 1999.

[66] P. H. Diamond, A. Hasegawa, and K. Mima. Vorticity dynamics, drift wave turbulence, and zonal flows: a look back and a look ahead. *Plasma Physics and Controlled Fusion*, 53(12):124001, 2011.

[67] B. LaBombard, J. W. Hughes, N. Smick, A. Graf, K. Marr, R. McDermott, M. Reinke, M. Greenwald, B. Lipschultz, J. L. Terry, D. G. Whyte, S. J. Zweben, and Alcator C-Mod Team. Critical gradients and plasma flows in the edge plasma of Alcator C-Mod. *Physics of Plasmas*, 15(5):056106, 2008.

[68] O. E. Garcia, R. A. Pitts, J. Horacek, A. H. Nielsen, W. Fundamenski, J. P. Graves, V. Naulin, and J. Juul Rasmussen. Turbulent transport in the TCV SOL. *Journal of Nuclear Materials*, 363–365(0):575, 2007.

[69] V. Mukhovatov, M. Shimada, A. N. Chudnovskiy, A. E. Costley, Y. Gribov, G. Federici, O. Kardaun, A. S. Kukushkin, A. Polevoi, V. D. Pustovitov, Y. Shimomura, T. Sugie, M. Sugihara, and G. Vayakis. Overview of physics basis for iter. *Plasma Physics and Controlled Fusion*, 45(12A):A235, 2003.

[70] C. Gormezano, A. C. C. Sips, T. C. Luce, S. Ide, A. Becoulet, X. Litaudon, A. Isayama, J. Hobirk, M. R. Wade, T. Oikawa, R. Prater, A. Zvonkov, B. Lloyd, T. Suzuki, E. Barbato, P. Bonoli, C.K. Phillips, V. Vdovin, E. Joffrin, T. Casper, J. Ferron, D. Mazon, D. Moreau, R. Bundy, C. Kessel, A. Fukuyama, N. Hayashi, F. Imbeaux, M. Murakami, A. R. Polevoi, and H. E. St John. Chapter 6: Steady state operation. *Nuclear Fusion*, 47(6):S285, 2007.

[71] Y. Igitkhanov, G. Janeschitz, G. W. Pacher, M. Sugihara, H. D. Pacher, D. E. Post, E. Solano, J. Lingertat, A. Loarte, T. Osborne, O. P. Pogutse, M. Shimada, and W. Suttrop. Edge parameter operational space and trajectories for iter. *Plasma Physics and Controlled Fusion*, 40(5):837, 1998.

[72] F. Militello and W. Fundamenski. Multi-machine comparison of drift fluid dimensionless parameters. *Plasma Physics and Controlled Fusion*, 53(9):095002, 2011.

[73] D. A. Mossessian, R. J. Groebner, R. A. Moyer, T. H. Osborne, J. W. Hughes, M. Greenwald, A. Hubbard, and T. L. Rhodes. Edge dimensionless identity experiment on DIII-D and Alcator C-Mod. *Physics of Plasmas*, 10(3):689, 2003.

[74] M. Groth, J. A. Boedo, N. H. Brooks, R. C. Isler, A. W. Leonard, G. D. Porter, J. G. Watkins, W. P. West, B. D. Bray, M. E. Fenstermacher, R. J. Groebner, R. A. Moyer, D. L. Rudakov, J. H. Yu, and L. Zeng. Effect of cross-field drifts on flows in the main scrape-off-layer of DIII-D L-mode plasmas. *Nuclear Fusion*, 49(11):115002, 2009.

[75] M. N. A. Beurskens, T. H. Osborne, L. D. Horton, L. Frassinetti, R. Groebner, A. Leonard, P. Lomas, I. Nunes, S. Saarelma, P. B. Snyder, I. Balboa, B. Bray, K .Crombé, J. Flanagan, C. Giroud, E. Giovannozzi, M. Kempenaars, N. Kohen, A. Loarte, J. Lönnroth, E. de la Luna, G. Maddison, C. Maggi, D. McDonald, G. McKee, R. Pasqualotto, G. Saibene, R .Sartori, E. R. Solano, W. Suttrop, E. Wolfrum, M. Walsh, Z. Yan, L. Zabeo, D. Zarzoso, and JET-EFDA contributors. Pedestal width and ELM size identity studies in JET and DIII-D; implications for ITER. *Plasma Physics and Controlled Fusion*, 51(12):124051, 2009.

[76] J. R. Myra, D. A. D'Ippolito, X. Q. Xu, and R. H. Cohen. Resistive modes in the edge and scrape-off layer of diverted tokamaks. *Physics of Plasmas*, 7(11):4622, 2000.

[77] J. W. Connor, R. J. Hastie, H. R. Wilson, and R. L. Miller. Magnetohydrodynamic stability of tokamak edge plasmas. *Physics of Plasmas*, 5(7):2687, 1998.

[78] D. D. Ryutov and R. H. Cohen. Instability driven by sheath boundary conditions and limited to divertor legs. *Contributions to plasma physics*, 44(1-3):168, 2004. 9th International Workshop on Plasma Edge Theory in Fusion Devices, Univ Calif, San Diego, San Diego, CA, Sep. 03-05, 2003.

[79] A. Mosetto, Federico D. Halpern, S. Jolliet, and P. Ricci. Low-frequency linear-mode regimes in the tokamak scrape-off layer. *Physics of Plasmas*, 19(11):112103, 2012.

[80] S. Brunner. Waves and instabilities in inhomogeneous plasmas. PhD course notes, CRPP, EPFL, Lausanne.

[81] Jr. T. M. Antonsen, J. F. Drake, P. N. Guzdar, A. B. Hassam, Y. T. Lau, C. S. Liu, and S. V. Novakovskii. Physical mechanism of enhanced stability from negative shear in tokamaks: Implications for edge transport and the L-H transition. *Physics of Plasmas*, 3(6):2221, 1996.

[82] J. F. Drake, Y. T. Lau, P. N. Guzdar, A. B. Hassam, S. V. Novakovski, B. Rogers, and A. Zeiler. Local negative shear and the formation of transport barriers. *Phys. Rev. Lett.*, 77:494, 1996.

[83] D. Dobrott, D. B. Nelson, J. M. Greene, A. H. Glasser, M. S. Chance, and E. A. Frieman. Theory of ballooning modes in tokamaks with finite shear. *Phys. Rev. Lett.*, 39:943, 1977.

[84] T. M. Antonsen. Stability of bound eigenmode solutions for the collisionless universal instability. *Phys. Rev. Lett.*, 41:33, 1978.

[85] P. N. Guzdar, L. Chen, P. K. Kaw, and C. Oberman. Effect of magnetic shear on dissipative drift-wave instabilities. *Phys. Rev. Lett.*, 40:1566, 1978.

[86] S. Coda for the TCV team. Progress and scientific results in the tcv tokamak. *Nuclear Fusion*, 51(9):094017, 2011.

[87] P. Ricci and B. N. Rogers. Plasma turbulence in the scrape-off layer of tokamak devices. *Physics of Plasmas*, 20(1):010702, 2013.

[88] F. D. Halpern, S. Jolliet, J. Loizu, A. Mosetto, and P. Ricci. Ideal ballooning modes in the tokamak scrape-off layer. *Physics of Plasmas*, 20(5):052306, 2013.

[89] F. D. Halpern, P. Ricci, S. Jolliet, J. Loizu, and A. Mosetto. Theory of the scrape-off layer width in inner-wall limited tokamak plasmas. *Nuclear Fusion*, 54(4):043003, 2014.

[90] M. Kočan, J. P. Gunn, S. Carpentier-Chouchana, A. Herrmann, A. Kirk, M. Komm, H. W. Müller, J.-Y. Pascal, R. A. Pitts, V. Rohde, and P. Tamain. Measurements of ion energies in the tokamak plasma boundary. *Journal of Nuclear Materials*, 415(1, Supplement):S1133, 2011. Proceedings of the 19th International Conference on Plasma-Surface Interactions in Controlled Fusion.

[91] S. Y. Allan, S. Elmore, A. Kirk, M. Kočan, and P. Tamain. Ion energy measurements on MAST using a midplane RFEA. *Journal of Nuclear Materials*, 438, Supplement(0):S1192, 2013. Proceedings of the 20th International Conference on Plasma-Surface Interactions in Controlled Fusion Devices.

[92] K. Kreuger, Z. H. Huang, M. Jiang, G. S. Xu, W. Zhang, H. Q. Wang, J. Cheng, W. Y. Hong, L. W. H. Yan, and C. Xiao. Simultaneous ion temperature and flow measurements using a retarding field analyzer in the HL-2A tokamak. *Radiation Effects and Defects in Solids*, 160(10):776, 2013.

[93] P. Tamain, M. Kočan, J. Gunn, A. Kirk, J.-Y. Pascal, and M. Price. Ion energy measurements in the scrape-off layer of MAST using a retarding field analyzer. *Journal of Nuclear Materials*, 415(1, Supplement):S1139, 2011. Proceedings of the 19th International Conference on Plasma-Surface Interactions in Controlled Fusion.

[94] M. Kočan, S. Y. Allan, S. Carpentier-Chouchana, P. de Marné, S. Elmore, T. Franke, J. P. Gunn, A. Herrmann, A. Kirk, M. Kubič, T. Lunt, H. W. Müller, R. A. Pitts, V. Rohde, and the ASDEX Upgrade Team. Ion energies and currents of type I and mitigated ELMs in the ASDEX Upgrade far scrape-off layer. *Nuclear Fusion*, 52(2):023016, 2012.

[95] M. Kočan, F. P. Gennrich, A. Kendl, H. W. Müller, and the ASDEX Upgrade Team. Ion temperature fluctuations in the ASDEX Upgrade scrape-off layer. *Plasma Physics and Controlled Fusion*, 54(8):085009, 2012.

[96] D. Brunner, B. LaBombard, R. M. Churchill, J. Hughes, B. Lipschultz, R. Ochoukov, T. D. Rognlien, C. Theiler, J. Walk, M. V. Umansky, and D. Whyte. An assessment of ion temperature measurements in the boundary of the Alcator C-Mod tokamak and implications for ion fluid heat flux limiters. *Plasma Physics and Controlled Fusion*, 55(9):095010.

[97] D. Brunner, B. LaBombard, R. Ochoukov, and D. Whyte. Scanning ion sensitive probe for plasma profile measurements in the boundary of the Alcator C-Mod tokamak. *Review of Scientific Instruments*, 84(5):053507, 2013.

[98] I. S. Nedzelskiy, C. Silva, P. Duarte, and H. Fernandes. Simultaneous measurements of the parallel and perpendicular ion temperature with a pinhole probe in the scrape-off-layer of the tokamak ISTTOK. *Review of Scientific Instruments*, 83(3):033505, 2012.

[99] M. Kočan and J. P. Gunn. Comparison of scrape-off layer profiles in outboard-versus inboard-limited plasmas in Tore Supra. *Plasma Physics and Controlled Fusion*, 52(4):045010, 2010.

[100] K. Uehara, T. Kawakami, H. Amemiya, K. Höthker, A. Cosler, and W. Bieger. Measurements of ion temperature and flow velocity using symmetric and asymmetric double probes in the boundary plasma of the JFT-2M tokamak. *Nuclear Fusion*, 38(11):1665, 1998.

[101] K. Hallatschek and A. Zeiler. Nonlocal simulation of the transition from ballooning to ion temperature gradient mode turbulence in the tokamak edge. *Physics of Plasmas*, 7(6):2554, 2000.

[102] N. Bisai and P. K. Kaw. Role of ion temperature on scrape-off layer plasma turbulence. *Physics of Plasmas*, 20(4):042509, 2013.

[103] B. Scott. Computation of electromagnetic turbulence and anomalous transport mechanisms in tokamak plasmas. *Plasma Physics and Controlled Fusion*, 45(12A):A385, 2003.

[104] P. Ricci and B. N. Rogers. Transport scaling in interchange-driven toroidal plasmas. *Physics of Plasmas*, 16(6):062303, 2009.

[105] J. Loizu, P. Ricci, and C. Theiler. Existence of subsonic plasma sheaths. *Phys. Rev. E*, 83:016406, 2011.

Acknowledgements

These four years of PhD have been a very tough, but fruitful period, and many are the people I wish to thank. First of all I thank my parents, without whom all this would have been simply impossible. I thank my mother for the endless talks on the phone and for always cheering me up, my father for his calm rational look at the world and his gentle words when I was in difficulties. I thank my sister for always being there, despite the kilometers in between and for always keeping our relationship very strong.

At CRPP I have been welcomed by Paolo, whom I thank for having given me the opportunity of doing this PhD and for always believing I had the skills to achieve it. I thank him for the long hours of discussion, for the careful guidance and for his availability. His office was always open for asking questions and clarifying doubts. He has been also a great host for very nice get-togethers that contributed to glue our working group. I thank a lot Federico and Sebastien for having helped me with those boring technicalities nobody wants to deal with, for having explained me a lot of physics and for always having welcomed me with a smile in their office. I also thank the rest of our group, Joaquim, Christoph and Fabio, for the familiar environment they created, that made the work less tough. A special thank to Joaquim, who shared with me a lot of the years at CRPP, for his smile, for his brightness as a scientist, for his spending time explaining me stuff when he was at the end of his thesis, and for his very spontaneous way of approaching people and life.

I thank Janos for having been a good officemate, sometimes a bit loud...but always available if I needed help and a good talk. I was also very lucky with my second officemate Julien, whom I thank for his positive attitude and the pauses of chatting.

I thank Lucia, with whom I built a very fulfilling friendship, made of sharing coffees and complaints and mountain hikes and cycling rides and canoe descents and much more. She has become a very important reference for my life in Lausanne, a very good companion.

I thank Mariia, who has been one of the first friends I met during this stay in Lausanne, for her constant presence, for the evenings of talking, for the laughs, for the stupid politically incorrect opinions we shared, and because with her I know I can always be myself.

Curriculum Vitae

Annamaria Mosetto

Chemin des Aubépines 16
1004 Lausanne
Switzerland
☏ +41 (0) 786598232
☎ +41 (0) 216936544
✉ annamaria.mosetto@gmail.com
date of birth 03/04/1983, residence permit B

Objective

Position in Energetic and Nuclear Engineering, R&D

Education

04/2010–expected in 05/2014	**PhD in Plasma Physics**, *École Polytechnique Fédérale de Lausanne*, Lausanne, Switzerland.
10/2005–05/2008	**Master in Energetic and Nuclear Engineering**, *Politecnico di Torino*, Torino, Italy, *with distinction*.
10/2002–10/2005	**Bachelor in Energetic Engineering**, *Politecnico di Torino*, Torino, Italy, *with distinction*.

Academic experience

04/2010–expected in 05/2014	**Theoretical and Computational Physicist**, *École Polytechnique Fédérale de Lausanne, Lausanne, Switzerland*. PhD project in Plasma Physics: "Global two-fluid simulations of tokamak scrape-off layer turbulence": **modeling**, **simulation** and **data analysys**
03/2009–03/2010	**Research assistant in Nuclear Engineering**, *Politecnico di Torino, Torino, Italy*. Intrumentation selection for the measurement of the two-phase flow rates for the IRIS reactor test campaign: **instrumentation evaluation**, **modeling**, **data analysis**

Work experience

09/2008–02/2009	**Research assistant in Energetic Engineering**, *Politecnico di Torino, Torino, Italy*. Development of a dynamic model for the cogeneration plants based on PEM fuel cells for the production of electricity and heat in civil and naval application: **modeling** and **simulation** of the system, **performance optimisation**
10/2007–04/2008	**Internship in Nuclear Engineering R&D**, *Westinghouse Electric Company, Pittsburgh, PA, USA*. Six months internship for the development of the Master thesis "Two-phase flow instrumentation for the simulation of the IRIS nuclear reactor": **instrumentation review**, **modeling** and **simulation** of the system, **data analysis**

Skills

Programming	Matlab, basic knowledge of C++ and Fortran
Office	Latex, Microsoft Office package, Libre Office package
Software	CFX for computational fluid dynamics, Matlab analysis tools, Simulink

Languages

Italian	**native**
English	**fluent (C1)**
French	**fluent (B2)**

First author publications and participations to conferences

- *A. Mosetto*, F. D. Halpern, S. Jolliet, J. Loizu and P. Ricci, *Turbulent regimes in the tokamak scrape-off layer*, Physics of Plasmas, vol. 20, num. 9, p. 092308, 2013.
- *A. Mosetto*, F. D. Halpern, S. Jolliet and P. Ricci, *Low-frequency linear-mode regimes in the tokamak scrape-off layer*, Physics of Plasmas, vol. 19, num. 11, p. 112103, 2012.
- *A. Mosetto*, F. D. Halpern, S. Jolliet, J. Loizu and P. Ricci, *Turbulent regimes in the tokamak scrape-off layer*, poster presented at the EPS conference on Plasma Physics, Espoo, Finnland, 01/07-05/07/2013.
- *A. Mosetto*, F. D. Halpern, S. Jolliet and P. Ricci, *Global two-fluid simulations of tokamak scrape-off layer turbulence*, poster presented at the Sherwood Fusion Theory Conference, Atlanta (GA), USA, 31/03-03/04/2012.
- *A. Mosetto*, F. D. Halpern and P. Ricci, *Global two-fluid simulations of tokamak scrape-off layer turbulence*, poster presented at the European Fusion Theory Conference, Frascati, Italia, 26/09-29/09/2011.

Other publications

- F. D. Halpern, P. Ricci, S. Jolliet, J. Loizu and A. Mosetto, *Theory of the scrape-off layer width in inner-wall limited tokamak plasmas*, Nuclear Fusion, vol. 54, num. 4, p. 043003, 2014.
- S. Jolliet, F. D. Halpern, J. Loizu, A. Mosetto and P. Ricci, *Aspect ratio effects on limited scrape-off layer plasma turbulence*, Physics of Plasmas, vol. 21, num. 2, p. 022303, 2014.
- J. Loizu, P. Ricci, F. D. Halpern, S. Jolliet and A. Mosetto, *On the electrostatic potential in the scrape-off layer of magnetic confinement devices*, Plasma Physics and Controlled Fusion, vol. 55, num. 12, p. 124019, 2013.
- F. D. Halpern, P. Ricci, B. Labit, I. Furno and S. Jolliet et al., *Theory-based scaling of the SOL width in circular limited tokamak plasmas*, Nuclear Fusion, vol. 53, num. 12, p. 122001, 2013.
- F. D. Halpern, S. Jolliet, J. Loizu, A. Mosetto and P. Ricci, *Ideal ballooning modes in the tokamak scrape-off layer*, Physics of Plasmas, vol. 20, num. 5, p. 052306, 2013.
- P. Ricci, F. D. Halpern, S. Jolliet, J. Loizu and A. Mosetto et al.,*Simulation of plasma turbulence in scrape-off layer conditions: the GBS code, simulation results and code validation*, Plasma Physics and Controlled Fusion, vol. 54, num. 12, p. 124047, 2012.

Interests

Sport (running, cycling, mountaneering), Travelling, Cinema